Preparing Multimetallic Architectures to Control the Behaviour of Multiple Excited States

A thesis submitted for the degree of

Doctor of Philosophy

In Inorganic Chemistry

Cameron Richard Alex Gray

Trinity College, University of Oxford

May 2024

ABSTRACT

Preparing Multimetallic Architectures to Control the Behaviour of Multiple Excited States

Multimetallic lanthanide complexes offer properties not afforded by their monometallic analogues e.g. multimodal imaging agents, or qubit gates. Exploiting these properties offers new opportunities in bio-medical imaging, luminescent sensors, and quantum information science.

The preparation of multimetallic lanthanide complexes, with long-term solution stability, remains challenging. The chemical similarity of the lanthanide series precludes chemoselective syntheses. The lanthanide contraction remains the most significant physical difference between the lanthanide ions; size-selective chelators have been reported in the literature. Where multimetallic complexes have been prepared, the inherent lability of most lanthanide-chelator bonds results in a 'scrambling' of ions in solution. The use of kinetically inert substituted DO3A derivatives can afford access to multimetallic lanthanide complexes with long-term solution stability.

Chapter 1 provides background information on general lanthanide chemistry and describes the current literature on multimetallic lanthanide complexes.

Chapter 2 describes the preparation of dicopper(II) and multimetallic copper(II)-zinc(II) complexes of a bis-cyclen ligand, and the EPR study of their magnetic properties. These complexes act as model systems for analogous lanthanide complexes.

Chapter 3 describes the preparation of multimetallic lanthanide complexes from a ligand containing two kinetically inert chelators, derived from DO3A. Bis-europium(III) and bis-terbium(III) complexes are prepared, and the hydrolysis of a pendant acetyl ester allows for comparison of phenolate-bridged and non-bridged species, investigating the effects of intermetallic communication. The multimetallic europium(III)-terbium(III) and lutetium(III)-gadolinium(III) complexes are investigated for their luminescence and magnetic properties respectively.

Chapter 4 describes the preparation of a kinetically inert lanthanide chelators, derived from DO3A, with a pendant salicylate motif. Self-assembly of the lanthanide(III) complexes thereof with lanthanide acetylacetonates enables access to multimetallic complexes. The luminescence properties and energy transfer mechanics are investigated for the europium(III) and terbium(III) derivatives.

Chapter 5 describes the preparation of tetranuclear europium(III) and lutetium(III) complexes of 5-Me-HXTA, a lanthanide chelator, and a novel benzophenone-octaacetic acid derivative. The photophysics of these complexes are explored. Preparation of larger architectures with different ratios of lanthanide(III) ion and a novel benzophenone-octaacetic acid derivative is explored.

Chapter 6 contains a summary of the conclusions of this thesis.

Chapter 7 contains the experimental procedures and relevant characterisation data to support structural determination are appended in chapter 8.

ACKNOWLEDGEMENTS

Without Prof. Stephen Faulkner, his guidance, support, and expertise none of this work could have succeeded. I would like to thank all the members of the Faulkner group for the help, support and friendship. Special thanks to Dani, Debs, Carlson, Grace, Louis, Charlotte, Charlie, and Jonny.

My thanks go to Prof. Christiane Timmel and her group, whose collaboration on all things EPR made so much of this thesis possible. Especially to Ashley Redman and Filip Ivanovic who conducted many of the EPR experiments.

My thanks go to Dr Nick Rees, Dr Victor Mikhailov, and Dr John Walsby-Tickle for all their assistance with NMR spectroscopy and mass spectrometry.

My thanks go to my family for supporting me whilst I carried out and wrote up this work. Especially to my Mum and Dad who supported me in advancing my academic dreams.

My biggest thanks go to Nikkita for all the love and support during my DPhil. Without your endless support and encouragement none of this would have been possible.

CONTENTS

ABSTRACT III

ACKNOWLEDGEMENTS VI

CONTENTS VII

ABBREVIATIONS XI

1. INTRODUCTION 13

1.1: THE LANTHANIDES 13

1.2: GENERAL CHEMISTRY OF THE LANTHANIDES 14

1.3: ELECTRONIC STRUCTURE OF THE LANTHANIDES 17

1.4: SPIN-ORBIT COUPLING 20

1.5: LIGAND FIELD SPLITTING 20

1.6: LANTHANIDE LUMINESCENCE 21

1.7: ENERGY TRANSFER MECHANISMS 27

1.8: SOLVENT QUENCHING 29

1.9: NUCLEAR MAGNETIC RESONACE 31

1.10: PARAMAGNETIC NUCLEAR MAGNETIC RESONANCE 32

1.11: ELECTRON PARAMAGNETIC RESONANCE 34

1.12: MULTIMETALIC LANTHANIDE COMPLEXES 35

1.13: THERMODYNAMIC CONTROL 36

1.14: KINETIC CONTROL 40

1.15: AIMS 44

1.16: REFERENCES.....46

2. DICOPPER(II) AND MULTIMETALLIC COPPER(II)-ZINC(II) COMPLEXES AS SIMPLE SPIN MODELS FOR PHENOLATE-BRIDGED SYSTEMS.....51

2.1: INTRODUCTION.....51

2.2: SYNTHESIS OF H2.1, $[Cu_2 2.1][NO_3]_3$, AND $[CuZn2.1][NO_3]_3$.....53

2.3: ELECTRON PARAMAGNETIC RESONANCE (EPR) SPECTROSCOPY OF $[Cu_2 2.1][NO_3]_3$ AND $[CuZn2.1][NO_3]_3$.....58

2.4: COMPLEX CONFORMATION.....61

2.5: SYNTHESIS OF $[Cu_2 2.1][BF_4]_3$ AND $[CuZn2.1][BF_4]_3$.....62

2.6: ELECTRON PARAMAGNETIC RESONANCE (EPR) SPECTROSCOPY OF $[Cu_2 2.1][BF_4]_3$ AND $[CuZn2.1][BF_4]_3$.....63

2.7: CONCLUSIONS.....70

2.8: REFERENCES.....71

3. A STATISTICAL APPROACH TO SYMMETRIC MULTIMETALLIC LANTHANIDE COMPLEXES AND MODULATING THE INTERMETALLIC COMMUNICATION VIA BRIDGING PHENOLATE COORDINATION.....73

3.1: SYNTHESIS OF LIGANDS $H_6 3.3$ AND $H_7 3.1$.....75

3.2: SYNTHESIS AND CHARACTERISATION OF $Ln_2 3.3$.....77

3.3: SYNTHESIS AND CHARACTERISATION OF $[Na][Ln_2 3.1]$.....80

3.4: HYDROLYSIS OF PHENYL ACETATE ESTER OF $Ln_2 2.5$ AND MANIPULATION OF INTERMETALLIC COMMUNICATION.....82

3.5: LUMINESCENCE SPECTROSCOPY OF $[Na][Ln_2 3.1]$ AND $[Na][Ln_2 3.3]$.....83

3.6: SYNTHESIS OF MULTIMETALLIC LANTHANIDE(III) COMPLEXES [Na][LnLn'3.1].....89

3.7: LUMINESCENCE SPECTROSCOPY OF [Na][EuTb3.1] 94

3.8: ELECTRON PARAMAGNETIC RESONANCE SPECTROSCOPY OF [Na][GdLu3.1] 95

3.9: CONCLUSIONS 96

3.10: REFERENCES 97

4. A SELF-ASSEMBLY APPROACH TO MULTIMETALLIC LANTHANIDE(III) COMPLEXES USING A SALICYLIC ACID APPENDED DO3A DERIVATIVE 99

4.1: SYNTHESIS OF $H_5$4.1 101

4.2: SYNTHESIS OF H_2Ln4.1 103

4.3: SELF-ASSEMBLY OF H_2Ln4.1 AND Ln'$(acac)_3$ 106

4.4: PHOTOPHYSICS OF $[Na]_2$[Ln'$(acac)_3$].[Ln4.1] 108

4.5: SELF-ASSEMBLY OF H_2Ln4.1 WITH OTHER LANTHANIDE CONTAINING SYSTEMS 118

4.6: CONCLUSIONS 119

4.7: REFERENCES 120

5. SYNTHESIS AND PHOTOPHYSICAL CHARACTERISATION OF POLYNUCLEAR LANTHANIDE(III) COMPLEXES DERIVED FROM 5-Me-HXTA AND A NOVEL POLY-ACETIC ACID FUNCTIONALISED BENZOPHENONE DERIVATIVE 123

5.1: SYNTHESIS OF $[Na]_4$[5-Me-HXTA] AND $Na_8H_2$5.1 124

5.3: SYNTHESIS OF $[Na]_8[Ln_4(5.1)(5\text{-Me-HXTA})_2]$ 126

5.3: UV-VISIBLE SPECTROSCOPY OF $[Na]_8[Ln_4(5.1)(5\text{-Me-HXTA})_2]$ 129

5.4: LUMINESCENCE SPECTROSCOPY OF $[Na]_8[Ln_4(5.1)(5\text{-Me-HXTA})_2]$ 131

5.5: SYNTHESIS OF LARGER ARCHITECTURES WITH $Na_8H_2$5.1 134

5.6: UV-VISIBLE AND LUMINESCENCE SPECTROSCOPY OF Eu$(5.1)_n$ 136

5.7: CONCLUSIONS 140

5.8: REFERENCES..... 141

6. CONCLUSIONS..... 143

7. EXPERIMENTAL DETAILS..... 146

7.1: GENERAL EXPERIMENTAL CONSIDERATIONS..... 146

7.2: SYNTHETIC PROCEDURES..... 150

7.3: REFERENCES..... 178

8. APPENDIX I: NMR SPECTRA..... 180

9. APPENDIX 2: LIFETIME KINETIC TRACES..... 202

acac	acetylacetonate
CNOT	Controlled NOT
cyclen	1,4,7,10-tetraazacyclododecane
cwEPR	continuous wave Electron Paramagnetic Resonance
DMSO	dimethylsulfoxide
DO3A	1,4,7,10-tetraazacyclododecane-1,4,7-triacetic acid
DOTA	1,4,7,10-tetraazacyclododecane-1,4,7,10-tetraacetic acid
DTPA	diethylenetriamine pentaacetic acid
EPR	Electron Paramagnetic Resonance
ESI	ElectroSpray Ionisation
FRET	Fluorescence Resonance Energy Transfer
HMRS	High Resolution Mass Spectrometry
HPLC	High Performance Liquid Chromatography
i.d.	inner diameter
LCMS	Liquid Chromatography Mass Spectroscopy
Ln	Lanthanide
LRMS	Low Resolution Mass Spectrometry
MALDI	Matrix Assisted Laser Desorption Ionisation
MRI	Magnetic Resonance Imaging
NMR	Nuclear Magnetic Resonance
o.d.	outer diameter
RET	Resonance Energy Transfer
SAP	Square AntiPrismatic
TSAP	Twisted Square AntiPrismatic

1. INTRODUCTION

1.1: THE LANTHANIDES

The lanthanides, or lanthanoids, (Ln) refers to the elements from cerium to lutetium[1]. These elements most readily form their trivalent oxidation state and are characterised by their 4f valence electrons. In the trivalent oxidation state, the electronic configuration is $[Xe]4f^n$ ($n = 1$ — 14, cerium(III) — lutetium(III)). There is a significant separation between this and $[Xe]4f^{n-1}5d^1$ ($\Delta E > 32000\ cm^{-1}$).[2, 3]

Lanthanum also forms the trivalent oxidation state and is often discussed alongside the lanthanides, having a comparable ionic radius.[2] Lanthanum(III) has a $4f^0$ configuration and hence many of the intrinsic properties of the lanthanide ions do not apply to lanthanum. The lighter members of group 3, yttrium and scandium may sometimes be discussed with the lanthanides. [2, 4]

The historical term 'rare earths' is often used to encompass the lanthanides and group 3.[2] These elements are in fact more abundant that some transition metals.[2, 5] Thulium, the least abundant lanthanide, is more abundant than silver, mercury, gold, platinum and rhodium. Cerium, lanthanum and neodymium are more abundant than cobalt and lead.[5]

The lanthanides and their compounds have found use as: NMR shift reagents,[6-8] MRI contrast agents,[9-14] luminescent sensors,[15-21] optical imaging agents,[22-27] single molecule magnets,[28-31] and as qubits for quantum information science.[32-35]

The 4f orbitals are radially contracted; the filled 6s and 5p orbitals both possess a larger radial expansion. Consequently, the 4f valence electrons are "inner orbitals" and are shielded from environmental perturbations.[36] Figure 1.1 shows the radial distribution function of the hydrogenic 4f, 5d and 6s orbitals of cerium(0).[36]

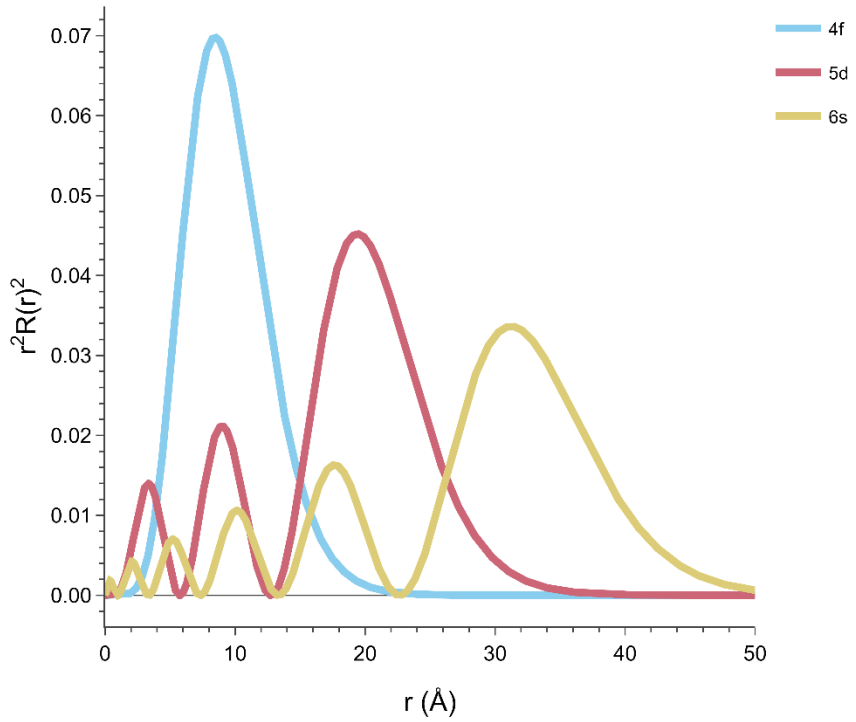

Figure 1.1.1: Radial distribution function of the hydrogenic 4f orbitals compared to the hydrogenic 5d and 6s orbitals for a cerium(0) atom. Drawn using waveplot.[37]

Whereas, for transition metals, the valence d orbitals can extend past the periphery of the ion to interact with ligand orbitals, for the lanthanide ions the 4f orbitals do not.[2] Hence, for the lanthanide ions, the bonding is primarily electrostatic.[2, 38-40] The 5f elements have a greater degree of covalency than the 4f elements, due to the further protrusion of the 5f orbitals.[4] There

is limited covalency in the 4f elements, though the further understanding of this is a burgeoning field.[40]

A further consequence of the radially contracted orbitals and minimal covalency is that all the lanthanides exhibit similar chemical behaviour.[38] The elements are most commonly found in the trivalent (3+) oxidation state.[2] Figure 1.2 shows the third ionisation energy (I_3) and the fourth ionisation energy (I_4) across the lanthanide series. The third ionisation energy (I_3) is greatest for europium and ytterbium. The divalent ions of europium and ytterbium have half and completely filled 4f shells, and are comparatively stabilised by exchange.[4] Gadolinium and lutetium, one atomic number on from europium and ytterbium have half or completely filled 4f shells in the trivalent ion and have comparatively low third ionisation energies.[4]

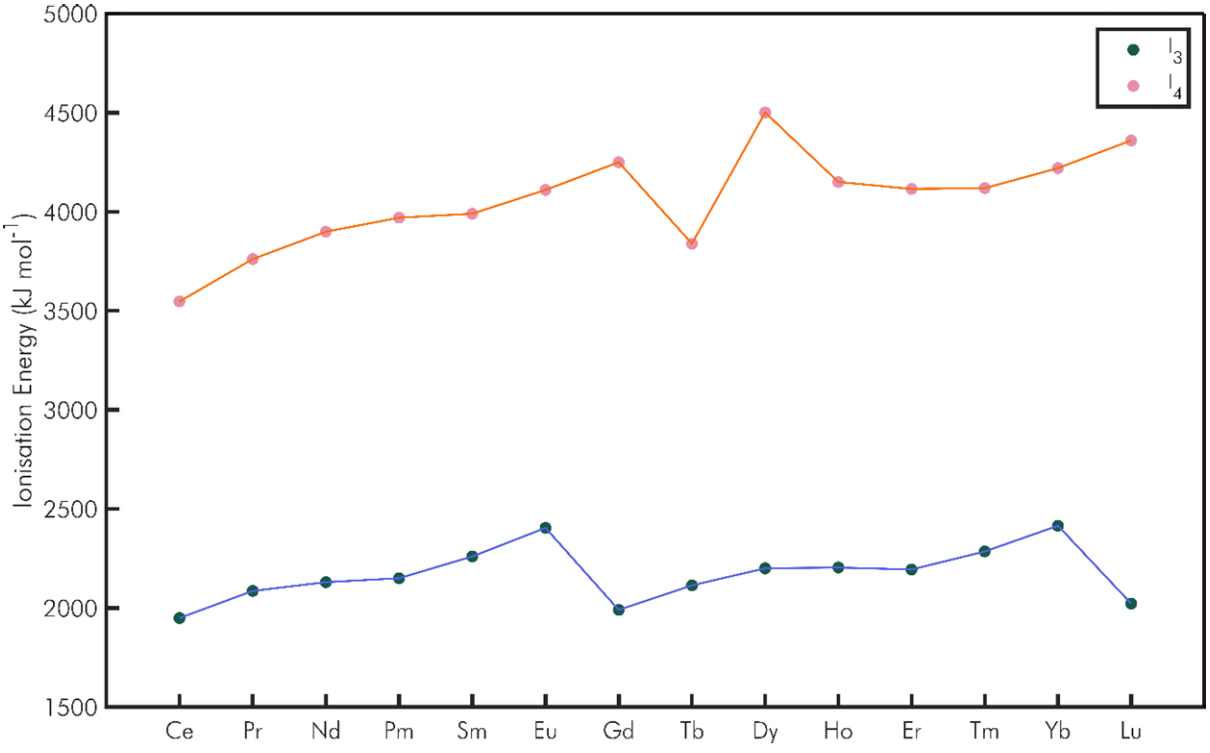

Figure 1.1.2: Third ionisation energy (green dots, blue line) and fourth ionisation energy (pink dots, orange line) for the lanthanide metals. Redrawn from reference 4.[4]

Compounds of the divalent (2+) oxidation state are known for the entire lanthanide series (except the radioactive promethium).[5, 42-46] Divalent lanthanide complexes are generally challenging to access, typically requiring a strong reducing agent. In the solid state divalent lanthanide compounds can be prepared. Lanthanide(II) iodide compounds are known to be prepared from the parent lanthanide(0) and lanthanide(III) iodide with high temperatures and long reaction times for all the lanthanides except the radioactive promethium.[45] Molecular divalent lanthanide species require strong reducing agents and stabilising ligand systems, a common approach is substituted cyclopentadienyl rings.[5, 45, 46] Samarium(II), europium(II) and ytterbium(II) are easiest to access, and have been explored most extensively, though europium (II) is the only free divalent ion that is stable in water.[5] Formally lanthanide(0) complexes were prepared from the parents lanthanide(0) and 1,3,5-tris(tert-butyl)benzene by Cloke and co-workers.[47, 48]

Compounds of the tetravalent (4+) oxidation state are known but challenging to access. Cerium(IV) is readily accessible.[49] Praseodymium(IV), neodymium(IV), dysprosium(IV) and terbium(IV) have been observed in solid-state compounds. Recently molecular complexes of terbium(IV)[50-52] and praseodymium(IV)[53] have been isolated.[49]

Moving across the lanthanide series from lower to greater atomic number, the ionic radius of the trivalent oxidation state decreases, known as the *lanthanide contraction*. Lutetium(III) (r_{ion} = 98 pm) is about 15% smaller than cerium(III) (r_{ion} = 114 pm).[4, 36] This is a result of one electron not perfectly shielding another in the same shell. Whilst, when moving across the series the nuclear charge increases by one, this is not completely counteracted by the additional electron, so the effective nuclear charge increases.[36] Hence, as one moves across the series and the effective nuclear charge increases, the 4f orbitals contract further.[2, 4]

The large ionic radius and lack of orbital overlap requirements means the coordination number and geometry of complexes of the lanthanide ions is primarily driven by electrostatics.[4] Coordination numbers between 2 and 12 are known.[29, 54] The larger early lanthanides tend to adopt 9-coordinate geometries, whereas the smaller late lanthanides tend to adopt 8-coordinate geometries.[39] Bulky ligands are required to enforce lesser coordination numbers.[4]

As a result of the small ionic radius and trivalent oxidation state, the trivalent lanthanide ions are hard Lewis acids.[4] As the ionic radii decrease across the series, the lanthanide ions become comparatively harder Lewis acids. The lanthanide ions typically form strong complexes with hard Lewis bases.[2]

As a consequence of the primarily electrostatic interactions with ligands, complexes of the lanthanide ions are typically labile.[38] For the aquo ions the lifetime for exchange of water ligands is on the order of nanoseconds.[4]

1.3: ELECTRONIC STRUCTURE OF THE LANTHANIDES

These elements most readily form their trivalent oxidation state and are characterised by their 4f valence electrons. We will therefore limit our discussion to the trivalent oxidation state. The electronic configuration is $[Xe]4f^n$ (n = 1 — 14, cerium(III) — lutetium(III)).[2, 3] There is a significant separation between this and $[Xe]4f^{n-1}5d^1$ ($\Delta E > 32000$ cm^{-1}).[3] This discussion will initially consider a free Ln(III) ion i.e. no applied ligand field.

Several *quantum numbers* are used to describe electrons and the orbitals in which they may be found. n is the *principal quantum number* and describes they shell in which an electron or orbital sits. ℓ is the *orbital angular momentum* and takes the values 0 — (n -1). ℓ is represented by integers (0, 1, 2, 3 …) or letters (*s, p, d, f, …*). For the lanthanide ions the valence electrons are in the 4f orbitals i.e. they have values of n=4, ℓ=3. m_ℓ is the projection of ℓ onto the z axis and represents the orientation of the orbital in space, m_ℓ takes the integer values of - ℓ — ℓ . For f orbitals, this results in 7 orbitals ℓ = -3, -2 … +2, +3. Each electron has a spin angular momentum, s, with a value of $\frac{1}{2}$. m_s is the projection of s onto the z axis and takes values $\pm \frac{1}{2}$. The Pauli exclusion principle states that no two electrons may have the same set of quantum numbers, hence, each orbital can house two electrons. Correspondingly, the 4f subshell can house 14 electrons.[3]

The trivalent lanthanide ions all have the electronic configuration [Xe]$4f^n$ (n = 0 — 14, La(III) — Lu(III)). There are a number of ways the electrons and orbitals can be associated. For any value of $4f^n$:[3]

$$number\ of\ configurations = \frac{14!}{n!\,(14-n)!}$$

Each of these configurations is called a *microstate*. These microstates are characterised by overall quantum number M_L and M_S. These overall quantum numbers are derived from the projections of the sum of the angular momenta. All the microstates which correspond to the projections of one L and S value are grouped together in a spectroscopic term of form ${}^{(2S+1)}L$.

The multiplicity of a term, how many microstates it regroups, is determined by $(2S+1) \times (2L+1)$.[2-4] The term of the ground state can be determined by Hund's rules:

1. The term giving the highest spin multiplicity (i.e. fewest paired electrons)
2. The term giving the largest orbital multiplicity

Table 1.1 gives the ground-state terms for each trivalent lanthanide ion and some associated information.

Table 1.1: Electronic configuration, number of configurations, ground state term and multiplicity[4].

Ln(III)	$4f^n$	Number of configurations	Ground State Term	Multiplicity
Ce	1	14	^2F	14
Pr	2	91	^3H	33
Nd	3	364	^4I	52
Pm	4	1001	^5I	65
Sm	5	2002	^6H	121
Eu	6	3003	^7F	49
Gd	7	3432	^8S	8
Tb	8	3003	^7F	49
Dy	9	2002	^6H	121
Ho	10	1001	^5I	65
Er	11	364	^4I	52
Tm	12	91	^3H	33
Yb	13	14	^2F	14
Lu	14	1	^1S	1

1.4: SPIN-ORBIT COUPLING

The spin angular momentum and orbital angular momentum of the electrons are not independent and couple, termed *spin-orbit coupling*. The Russel-Saunders formalism is used here, where the spin and orbital angular momenta couple give a total angular momentum, J. J takes the values [(L + S), (L + S -1), … , (L – S)]. There is a spin-orbit coupling constant, λ, associated with this, λ is positive for $4f^n$ n= 1 — 7, and the lowest value of J is the lowest in energy. For $4f^n$ n= 8 — 14 λ is negative, the greatest value of J is lowest in energy. Each $^{(2S+1)}L$ term is split into a number of spectroscopic levels, $^{(2S+1)}L_J$. Each spectroscopic level is (2J + 1)-fold degenerate.[3]

1.5: LIGAND FIELD SPLITTING

The above treatment considers a free ion. The spherical symmetry (isotropy) of a free ion is removed when in a chemical environment. Consequently, the (2J + 1) degeneracy of the J levels is partially lifted, this is a *ligand field splitting*.[3] Owing to the inner orbital nature of the 4f valence electrons,[2, 4] ligand field splitting effects are small, typically 100s of cm^{-1}.[3] Ligand field splitting effects for transition metals are much larger, up to 35,000 cm^{-1}.[28] As the effect is so small, it can be treated last when considering the electronic structure of the lanthanide ions. To simplify the situation, the ligands can be thought of as negative point charges, this generates an electrostatic ligand (or crystal) field. This ligand field interacts with the 4f electrons, splitting the $^{(2S+1)}L_J$ into (2J+1) m_J states.[28]

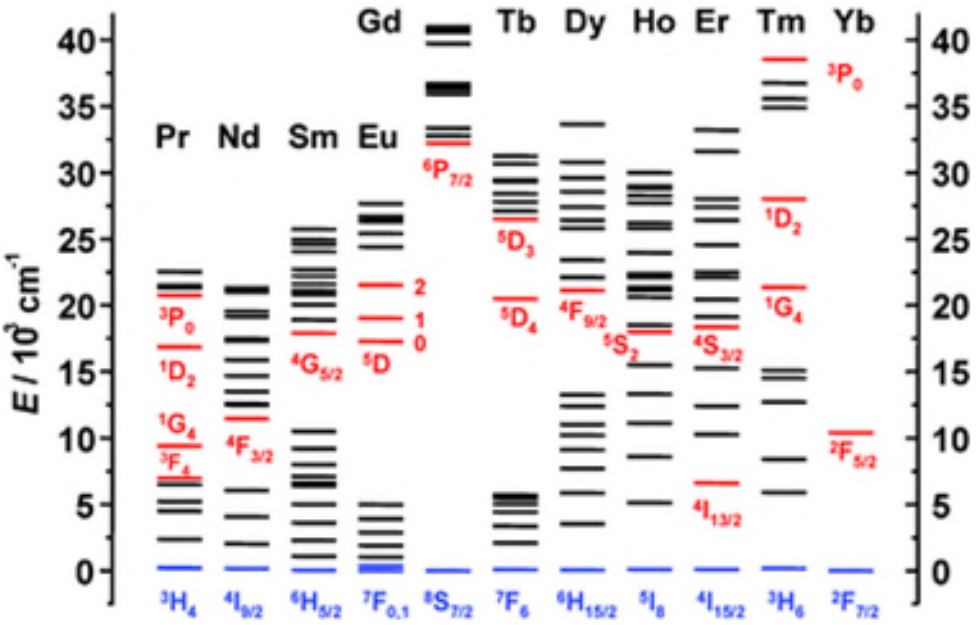

Figure 1.1.3: Partial energy level diagram showing the ground state (blue) and excited states of the lanthanide ions (except the radioactive promethium) including ligand field splitting. Emissive states are highlighted in red. Taken from reference 23. [23]

For those ions with odd $4f^n$ electron counts, ligand field splitting does not completely remove the degeneracy of the $^{(2S+1)}\Gamma_J$ levels.[3] The ligand field sub-levels are at least doubly degenerate, termed *Kramer's doublets*. The degeneracy of these doublets is only lifted by an applied magnetic field.[3] Figure 1.3 shows a partial energy diagram for the aquo complexes of the lanthanide(III) ions, including ligand field splitting.[23]

1.6: LANTHANIDE LUMINESCENCE

The open-shell lanthanide ions, cerium(III) — ytterbium(III), display distinctive photophysical behaviour. This is a result of the 4f valence electrons. The observed transitions are *intraconfigurational* 4f — 4f transitions representing a rearrangement of the electrons around the lanthanide ion, from one configuration (and term) to another, higher energy one. 4f — 4f transitions are partially parity forbidden, hence absorption is weak with low molar extinction

coefficients.[3, 23] Similarly, the low transition probability means emission is slow, giving long luminescence lifetimes.[22] The inner-orbital nature of the 4f orbitals, and weak interaction with their environment, means the emission wavelengths vary minimally with chemical environment and emission bands are sharp.[2, 4]

The lanthanide ions can be either fluorescent ($\Delta S = 0$) or phosphorescent ($\Delta S \neq 0$) depending on the ion in question and the states involved in the transition.[22] The terms luminescent and luminescence encompass both and will be used from here.

Table 1.2 lists the ground state, excited state(s) and approximate transition wavelengths for the lanthanide(III) ions. The excited state of cerium(III) is unique among the lanthanides; being a 4f — 5d transition. The first excited state of gadolinium(III) is too high in energy for sensitisation to be readily feasible. Lutetium(III), $4f^{14}$, does not have any 4f — 4f transitions available due to a full 4f subshell.[3]

Table 1.2: Table showing the ground and excited state terms, and the emissive transitions and characteristic wavelengths for the trivalent lanthanide ions (except the radioactive promethium). Data taken from reference 3.[3]

Ln(III)	Ground State	Excited State	Final State	Wavelength (nm)
Ce	$^2F_{\frac{5}{2}}$	5d	$^2F_{\frac{5}{2}}$	300 – 450
		$^1D_2$	$^3F_4$, $^1G_4$, $^3H_4$, $^3H_5$	1000,1440,600, 690
Pr	$^3H_4$	$^3P_0$	^3H_J (J = 4 – 6)	490, 545, 615, 640
		$^3P_0$	^3F_J (J = 4 – 6)	700, 725
Nd	$^4I_{\frac{9}{2}}$	$^4F_{\frac{3}{2}}$	^4I_J ($J = \frac{9}{2} - \frac{13}{2}$)	900, 1060, 1350
			^6H_J ($J = \frac{5}{2} - \frac{13}{2}$)	560, 595, 640, 700, 775
Sm	$^6H_{\frac{5}{2}}$	$^4G_{\frac{5}{2}}$	^6F_J ($J = \frac{1}{2} - \frac{9}{2}$)	870, 887, 926, 1010, 1150
			$^6H_{\frac{13}{2}}$	877
Eu	$^7F_0$	$^5D_0$	^7F_J (J = 0 – 6)	580, 590, 615, 650, 720, 750, 820
Gd	$^8S_{\frac{7}{2}}$	$^6P_{\frac{7}{2}}$	$^8S_{\frac{7}{2}}$	315
Tb	$^7F_6$	$^5D_4$	^7F_J (J = 6 – 0)	490, 540, 580, 620, 650, 660, 675
Dy	$^6H_{\frac{15}{2}}$	$^4F_{\frac{9}{2}}$	^6H_J ($J = \frac{15}{2} - \frac{9}{2}$)	475, 570, 660, 750
		$^4I_{\frac{15}{2}}$	^6H_J ($J = \frac{15}{2} - \frac{9}{2}$)	455, 540, 615, 695
Ho	$^5I_8$	$^5S_2$	^5I_J (J = 8,7)	545, 750
		$^5F_5$	$^5I_8$	650
		$^5F_5$	$^5I_7$	965
Er	$^4I_{\frac{15}{2}}$	$^4S_{\frac{3}{2}}$	^4I_J ($J = \frac{15}{2}, \frac{13}{2}$)	545, 850
		$^4F_{\frac{9}{2}}$	$^4I_{\frac{15}{2}}$	660
		$^4I_{\frac{9}{2}}$	$^4I_{\frac{15}{2}}$	810
		$^4I_{\frac{13}{2}}$	$^4I_{\frac{15}{2}}$	1540
Tm	$^3H_6$	$^1D_2$	$^3F_4$, $^3H_4$, $^3F_3$, $^3F_2$	450, 650, 740, 775
		$^1G_4$	$^3H_6$, $^3F_4$, $^3H_5$	470, 650, 770
		$^3H_4$	$^3H_6$	800
Yb	$^2F_{\frac{7}{2}}$	$^2F_{\frac{5}{2}}$	$^2F_{\frac{7}{2}}$	980

As a result of the low absorption of the, partially forbidden, 4f — 4f transitions, exciting a lanthanide(III) compound sufficiently to observe significant luminescence can be a challenge. To circumvent this, a proximate chromophore can, once excited, undergo energy transfer to the lanthanide(III) ion (see Figure 1.4). This is sometimes referred to as the *antenna effect*, or, *sensitisation*.[3, 23, 37]

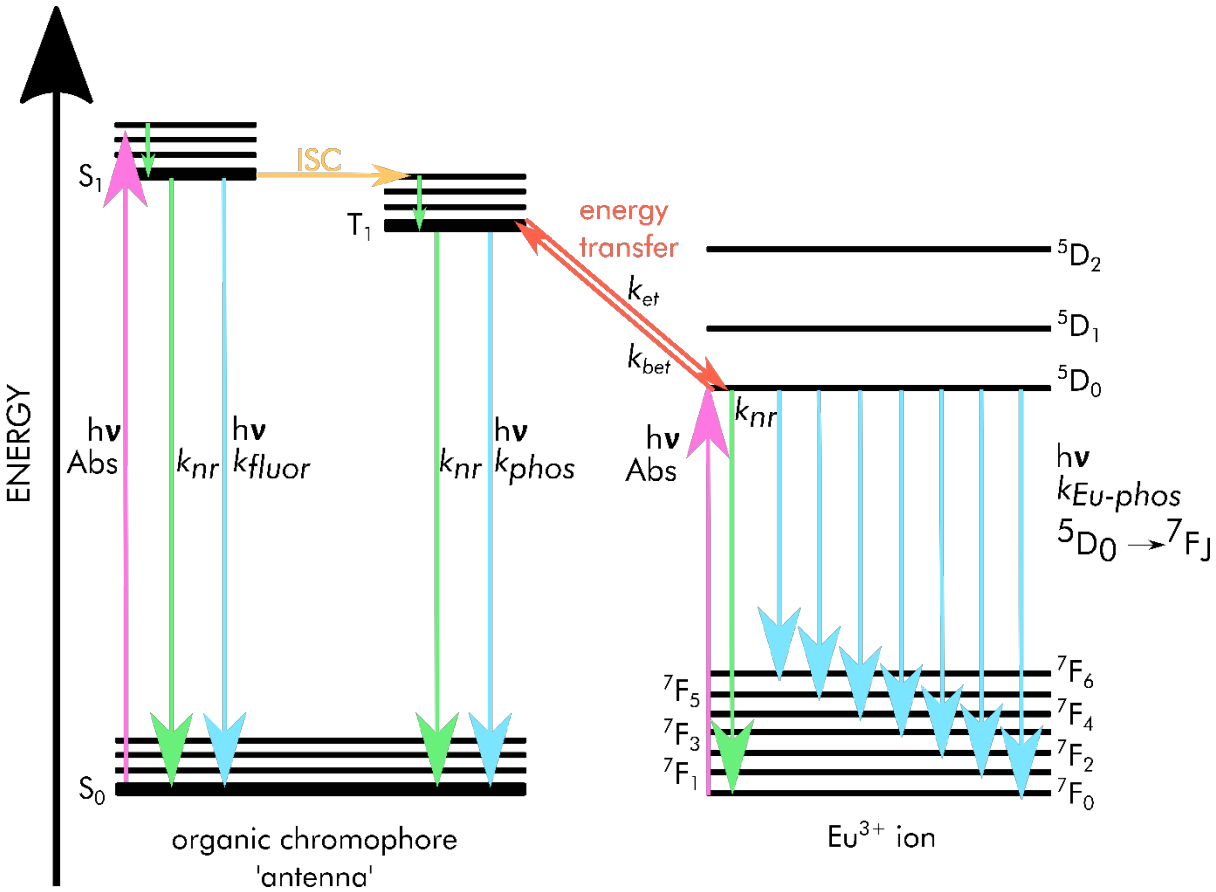

Figure 1.1.4: Jablonski diagram showing the potential photophysical processes for a europium(III) ion with a proximate organic chromophore. Absorptive (pink) processes, radiative (blue) and non-radiative (green) decay, inter-system crossing (yellow) and energy transfer (red). Energy transfer may occur via a FRET or Dexter exchange mechanism.

The Jablonski diagram (Figure 1.4) shows the major photophysical processes which can occur, both those leading to lanthanide luminescence and competing deactivation pathways of the excited states, for a hypothetical europium(III) complex with an organic sensitising chromophore. The processes discussed are general, energy levels will vary with chemical identity. There are two absorptive processes available, excitation of the sensitising chromophore from the singlet ground state to the singlet excited state, or excitation from the lanthanide ground state ($^7F_0$) to the lanthanide excited state ($^5D_0$), leading to population of the lanthanide excited state, $^5D_0$. Excitation from S_0 to S_1 of the sensitising chromophore leads to population of singlet excited state of the chromophore, rapid intersystem crossing leads to population of the lower lying triplet excited state, T_1. Intersystem crossing occurs rapidly and with near unity efficiency due to the heavy atom effect. Excitation from S_0 to T_1 is not typically observed, being formally forbidden, due to the spin change of the transition, it has a much lower excitation coefficient than S_0 to S_1. Radiative (fluorescence) and non-radiative deactivation of S_1 are possible. Radiative (phosphorescence) and non-radiative deactivation of T_1 are possible. Energy transfer (via Dexter or FRET mechanism) from T_1 to the lanthanide $^5D_0$ excited state is possible, if the energy levels align correctly. This pathway allows for population of a europium(III) centred excited state, $^5D_0$, by excitation of the S_0-S_1 transition of a proximate chromophore.[3, 22-24, 37, 55]

The $^5D_0$ excited state can emit a photon to deactivate radiatively, giving observable luminescence. Non-radiative deactivation is also feasible. In the case of europium(III) emission is observed from $^5D_0$ to each of the ^7F_J ($J = 6 – 0$) sublevels, each is observed as a narrow band in the emission spectrum. For the other lanthanide(III) ions, the same excitation pathway is possible, however, the states and (relative) energy levels of the ground and excited states will vary (see Figure 1.3 and Table 1.2).[3, 22, 23, 37, 55]

When $\Delta E(T_1–Ln(III)ES)$ is within KT (< 2000 cm^{-1}), back-energy transfer from the excited state of the lanthanide(III) ion to the triplet excited state (T_1) of the chromophore can occur. As triplet excited states are readily quenched by oxygen ($^3O_2$ ground state), this can reduce quantum yield in oxygenated environments.[22]

The following guidelines for suitable sensitising chromophores have been laid out:[22]

1. A high molar absorptivity
2. A triplet excited state, lower in energy than the singlet excited state
3. The antenna triplet state must lie > 2000 cm^{-1} above the accepting excited states of the lanthanide(III) ion, to prevent back energy transfer

The majority of antenna groups in the literature are organic chromophores, though there are examples of d-block sensitising chromophores in the literature. There are reported systems where energy transfer from one lanthanide ion to another is observed, however, this doesn't offer a significant improvement in excitation efficiency.[56, 57]

Energy transfer from a ligand centred chromophore (generally the triplet excited state) to a lanthanide(III) centred excited state can occur via two mechanisms: Dexter exchange, or fluorescence resonance energy transfer, FRET. FRET is also known as resonance energy transfer (RET) and Förster resonance energy transfer (FRET). Figure 1.5 illustrates the difference between the two mechanisms. Dexter exchange is a through-bond, double electron exchange, which requires overlap of the sensitising chromophore and 4f orbitals. FRET is a through-space, dipole-diploe interaction, in which the dipole moment of the T_1 excited state and the dipole moment of the 4f orbitals couple. When the energy transfer mechanism is primarily dipolar, the rate of energy transfer is given by:[3, 58]

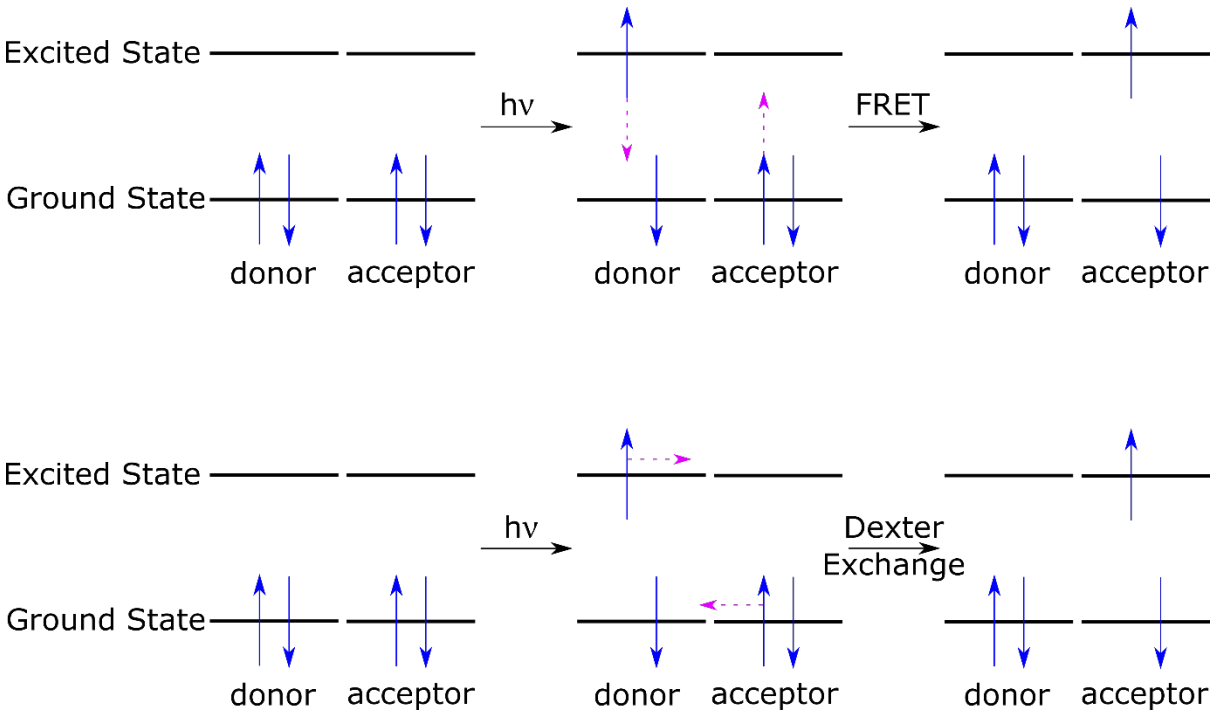

Figure 1.1.5: Top: Diagram illustrating the mechanism of fluorescence resonance energy transfer (FRET) from a donor species to an acceptor species Bottom: Diagram illustrating the mechanism of Dexter exchange from a donor species to an acceptor species

$$k_{ET}(FRET) = \frac{1}{\tau_D}\left(\frac{R_0}{r}\right)^6$$

Hence, the efficiency of the energy transfer drops with r^{-6} where r is the donor-acceptor distance. R_0 is the distance for 50% energy transfer, usually lies between 5 and 20 Å, and is specific to the donor-acceptor pair. R_0 is dependent on the quantum yield of the donor (Q_D); overlap integral of the donor emission spectrum and acceptor absorption spectrum (J); refractive index (n) and an orientation factor (κ) and is given by:[3, 58]

$$R_0 = 8.75 \times 10^{-25}(\kappa^2 Q_D n^{-4} J)$$

For Dexter exchange, a double electron exchange process, orbital overlap is key, requiring the wavefunctions of the donor and acceptor to overlap. Dexter exchange probability is proportional to $e^{-\beta r}$ and hence falls off more rapidly with distance than FRET.[3, 59]

It remains unclear which mechanism is dominant in lanthanide(III) complexes. In systems where the sensitising chromophore is directly coordinated to the lanthanide(III) ion it seems likely Dexter exchange will be operational. Given the narrow spectral linewidth of lanthanide(III) transitions the spectral overlap integral, upon which FRET efficiency depends, is likely low. Collisional Dexter exchange may occur.

The energy of the lanthanide(III) excited states is such that proximate XH oscillators can quench the excited state. Quenching occurs when the energy level of the lanthanide excited state overlaps with vibrational overtones of proximate XH oscillators (X = C, N, O).[3] The more phonons required to bridge the energy gap, the less efficient this quenching is. Consequently, the smaller the energy gap, between excited and ground state multiplets, the more sensitive the transition is to quenching.[3, 60-62]

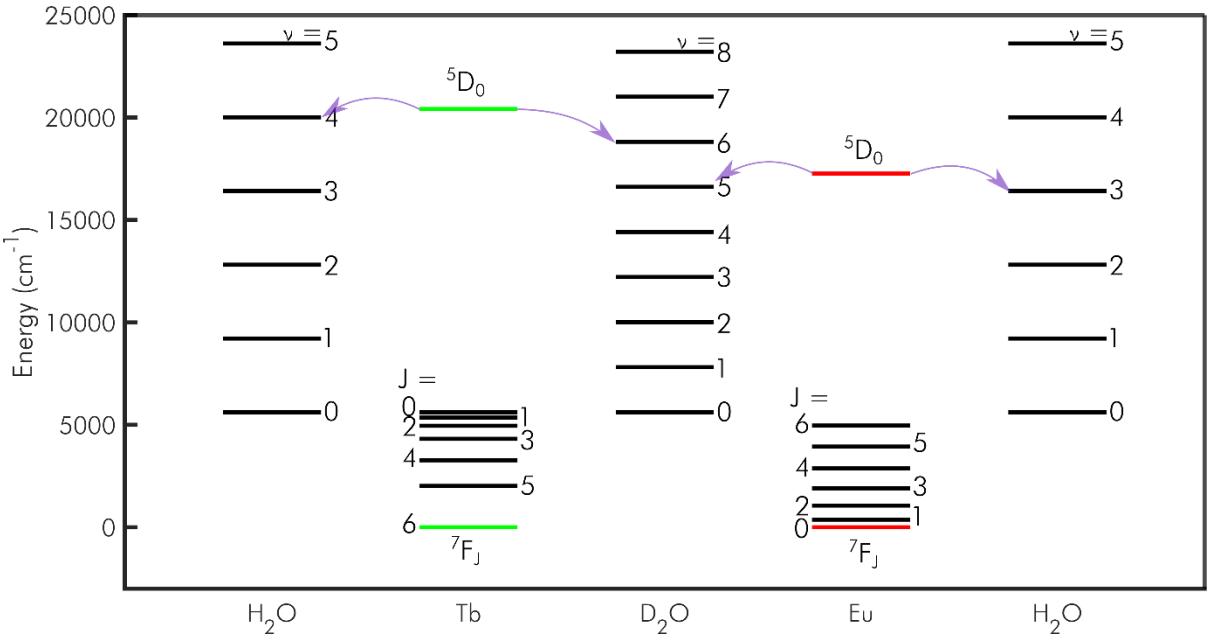

Figure 1.1.6: Partial energy level diagram comparing the vibrational overtones of H_2O and D_2O with the emissive and ground state multiplets of terbium(III) and europium(III). The ground state multiplets are of the aquo complex. [3, 37, 63-65]

Coordinated water molecules can efficiently quench the excited state. D_2O has lower energy vibrational modes (2200 cm^{-1}) compared to H_2O (3600 cm^{-1}).[3] Hence, quenching by D_2O requires more phonons to bridge the energy gap and is less efficient that quenching by H_2O.[3] Figure 1.6 shows the comparison of the excited states of europium(III) and terbium(III) with the

vibrational overtones of H_2O and D_2O. The number of coordinated water molecules, q, can be determined from comparing the lifetimes in protic and deuterated solvent with the modified Horrocks equation:[60-62]

$$q = A(k_{H_2O} - k_{D_2O} - B)$$

Where k_{H_2O} is the rate constant of radiative deactivation in H_2O, k_{D_2O} is the rate constant of radiative deactivation in D_2O. These are the reciprocal of the experimentally measured luminescence lifetime in a given solvent. A and B are empirically derived constants, and are ion dependant. Table 1.3 gives values of A and B for select ions.[60] This equation assumes quenching by proximate XH oscillators is the only significant mechanism of quenching.

The values of q, the hydration number of a lanthanide complex, should be treated with caution. There is inherent error of ± 0.5q in the measurements and approximation. The equation assumes solvent quenching to be the only significant quenching pathway. Where other quenching mechanisms, such as intermetallic quenching, are significant this assumption break down.[66]

Table 1.3: Table showing the empirical parameters A and B for europium(III) and terbium(III). [60]

	A	B
Eu(III)	1.2	0.25
Tb(III)	5.0	0.06

All nuclei have a *spin* quantum number, I. If we consider the simplest case of a ^{1}H nucleus, a single proton, $I = \frac{1}{2}$. The nucleus can take one of two m_i states, $+\frac{1}{2}$ or $-\frac{1}{2}$. In the absence of a magnetic field, these two states are degenerate. Application of a magnetic field, B, will lower this degeneracy.[67-69]

Figure 1.7 shows the extent of Zeeman splitting for a ^{1}H nucleus with magnetic field up to 9.4 T. Applying radiation of the same energy as the difference between spin states will cause transitions between spin energy levels. This frequency is known as the *Larmor frequency*, 400 MHz for our ^{1}H nucleus in a 9.4 T field.[67-69]

Following the above treatment, it would appear all ^{1}H nuclei would come into resonance at the same frequency, regardless of chemical identity and environment. Shielding, the extent to which local electron density alters the effective magnetic field a nucleus experiences, results in slightly different resonant frequencies. Thus, chemically different protons resonate at slightly different frequencies. [67-69]

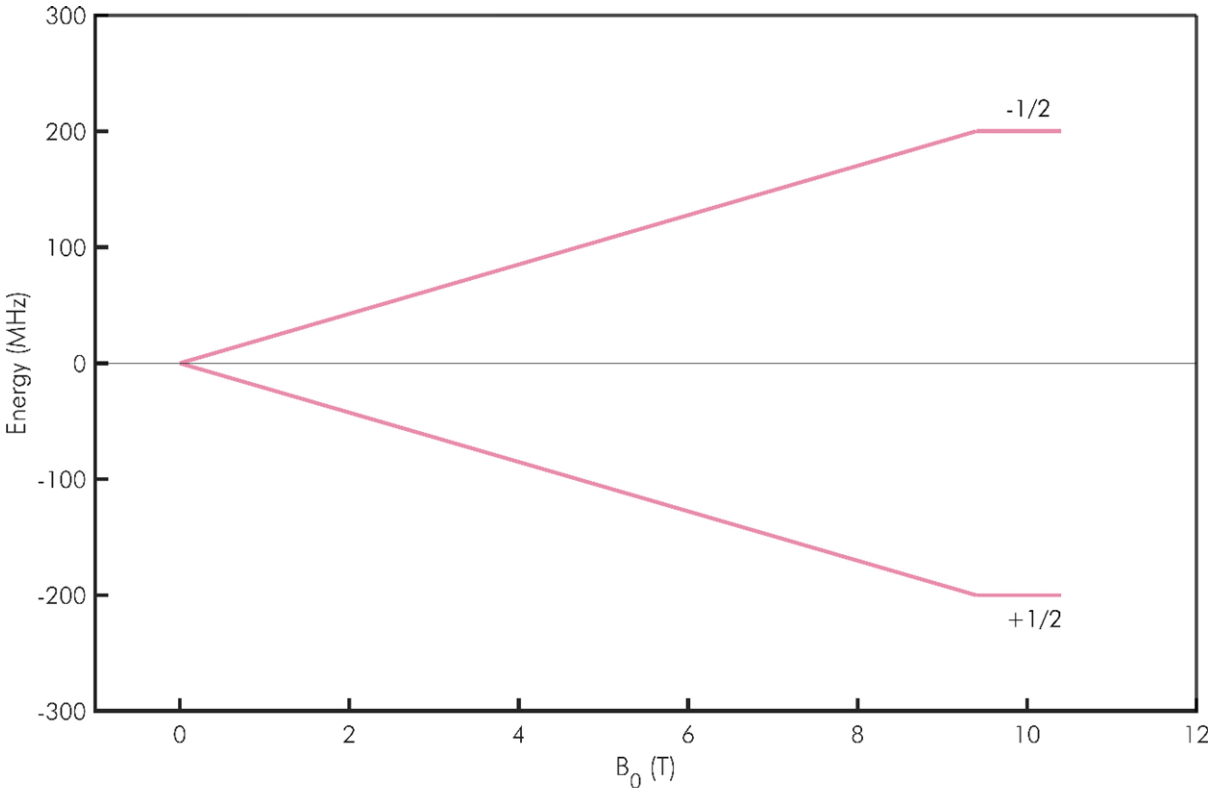

Figure 1.1.7: Plot of Zeeman interaction for a free ^{1}H nucleus with increasing field to 9.4 T.

The *spin* quantum number may take other values than $\frac{1}{2}$. When I = 0, the nuclei have no angular momentum and consequently have no zeeman interaction nor NMR spectra. A noteable case is ^{12}C. ^{13}C has I = $\frac{1}{2}$, and a natural abundance ca. 1%, as such any carbon NMR spectra are acquired on the ca. 1% of ^{13}C nuclei in a sample. When I > $\frac{1}{2}$, the nuclei can take values of m_i = -I, (-I+1) … +I.[67-69]

1.10: PARAMAGNETIC NUCLEAR MAGNETIC RESONANCE

The open-shell lanthanide(III) ions are paramagnetic and have a magnetic moment.[2, 4] This magnetic moment can cause large changes in chemical shift for proximate nuclei, a lanthanide induced shift (Δ). This comprises three components: a diamagnetic shift (Δ_d), a contact shift (Δ_c)

and pseudo-contact shift (Δ_p). The diamagnetic shift originates from conformational changes and modulating the electronics of the ligand. The contact shift originates from through-bond transfer of spin density to the measured nucleus. The pseudo-contact shift is the through space dipolar interaction between the magnetic moments of the ion and the measured nucleus.[70]

The pseudo-contact shift typically dominates for an observed nucleus and, as a consequence of the anisotropic electron distribution and associated magnetic susceptibility,[31] is orientation dependant.[70] This orientation dependence can imply structural information and is described by McConnell's equation:[71]

$$\Delta_p = \frac{1}{12\pi r^3}[\chi_{\mathrm{ax}}(3\cos^2\theta - 1) + 3\chi_{rh}\sin^2\theta\, cos2\varphi$$

Where θ, φ, and r are the polar coordinates describing the position of the nucleus in question relative to the lanthanide(III) ion. χ is the magnetic susceptibility tensor, with axial and rhombic components.[70] Bleaney's theory links the axiality and rhombicity of the magnetic susceptibility tensor with the ligand field parameters.[72]

Europium(III) has a ground state term of $^7F_0$, implying the total angular momentum of the ion is 0. Due to low-lying $^7F_1$ and $^7F_2$ states, which are thermally populated at NMR experiment temperatures, the ion is functionally paramagnetic.

1.11: ELECTRON PARAMAGNETIC RESONANCE

Electron paramagnetic resonance (EPR) spectroscopy, sometimes called electron spin resonance (ESR) spectroscopy, is a magnetic resonance technique for unpaired electron spin. Electrons have a spin quantum number $S = \frac{1}{2}$ and can take $m_s \pm\frac{1}{2}$. The degeneracy of these states is lifted by an applied magnetic field, the Zeeman interaction, as shown in Figure 1.8. Comparison with Figure 1.7 will show the magnitude of the electron Zeeman interaction is orders of magnitude greater than the nuclear Zeeman interaction for a proton. EPR spectrometers operate at a range of frequencies in the microwave region. The frequencies are referred to as bands, the most common being X-band, at ca. 9.5 GHz. As sweeping microwave frequencies is more technically challenging than for radiowaves, EPR spectra are typically acquired by sweeping the magnetic field with a fixed microwave frequency. When the applied field is such that the resonance frequency of the electron is equal to the frequency of applied radiowaves, the electron spin comes into resonance and can transition between energy levels. Hence, most spectra are presented as a function of applied field in Gauss or mT.[73]

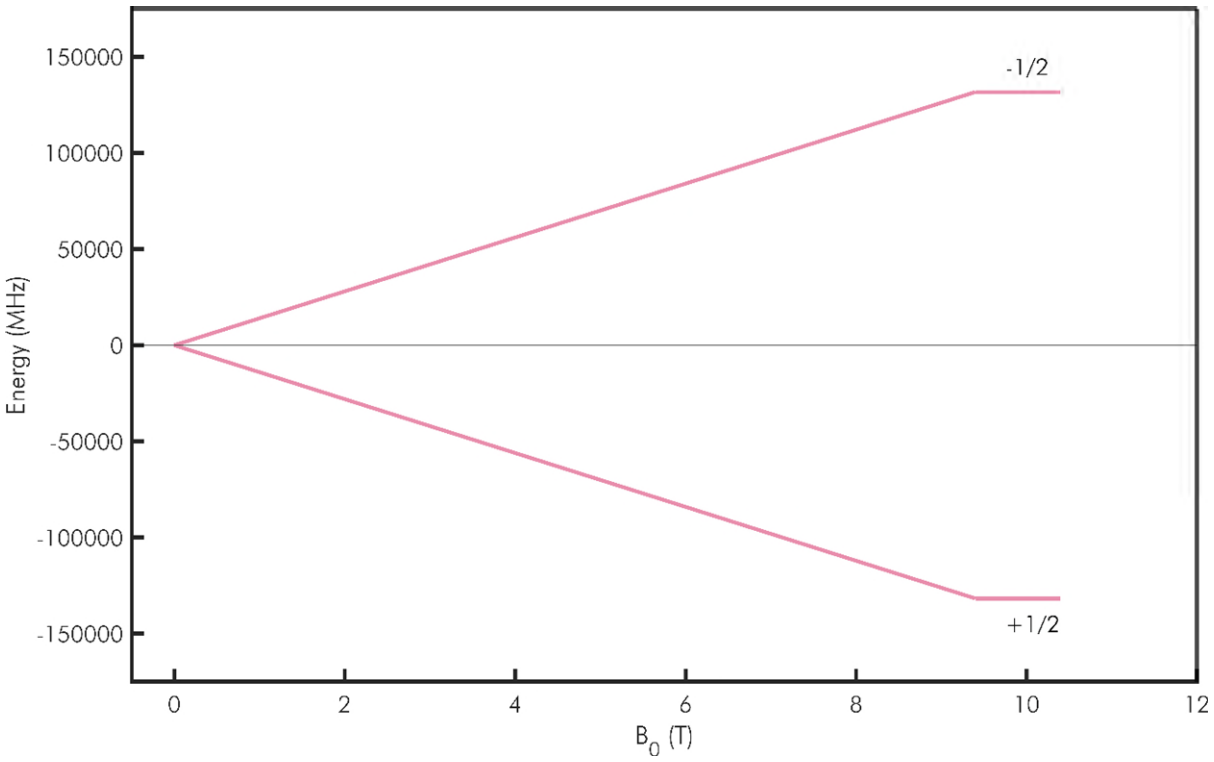

Figure 1.1.8: Plot of the Zeeman interaction for a free electron with increasing field up to 9.4 T.

1.12: MULTIMETALIC LANTHANIDE COMPLEXES

The synthesis of polynuclear lanthanide complexes, i.e. those with multiple metal atoms of the same element, have yielded wheels,[74] cages,[75-78] helicates[79-84] and more.[85-89] The preparation of heteromultimetallic complexes, i.e. those with multiple metal atoms of different elements, remains a synthetic challenge. The similarity in chemical behaviour of the lanthanide ions precludes the preparation of multimetallic complexes through the use of different chemical interactions, in stark contrast to the chemistry of transition metal complexes.[90-93] The inherent lability of complexes of the lanthanide elements can lead to '*scrambling*' where a pure heterometallic system returns, over time, to the equilibrium position of a mixture of multimetallic and polynuclear species.[38, 39]

There are two broad approaches to multimetallic lanthanide complexes: thermodynamic control and kinetic control. Under thermodynamic control, ligand architectures are designed to take advantage of small differences in chemical behaviour, such as the lanthanide contraction, to enforce site-selective complexation. Under kinetic control, kinetically inert chelators are employed to prevent scrambling and allow multimetallic architectures to constructed.[38]

Lanthanide coordination bonds, being primarily electrostatic, are inherently labile.[4] Hence, lanthanide complexes are more labile than their d-block analogues.[4] Kinetically inert lanthanide complexes can be prepared by employing rigid, preorganised macrocyclic ligands with 7 or 8 donors. Substituted DO3A derivatives meet these criteria and have been employed as gadolinium(III) MRI contrast agents, where the high thermodynamic stability and kinetic inertness are required to prevent nephrogenic systemic fibrosis.[22]

1.13: THERMODYNAMIC CONTROL

There are several reports in the literature of ligand systems which can enforce selective multimetallic complexation by exploiting the lanthanide contraction, the approximately 15% decrease in ionic radius across the lanthanide series from cerium(III) to lutetium(III). These reports all prepare and study the complexes in the solid state.

Aromí and co-workers have reported a series of ligands and corresponding hetero-multimetallic complexes in which two different sized binding pockets impart size selectivity.[57, 94, 95, 97-100] Aromí and co-workers have extended this concept to prepare trinuclear complexes of the type $Ln_2Ln'L$.[96, 101] The complexes are prepared in a one-pot reaction from the corresponding ligand and lanthanide(III) nitrate salts in pyridine, with a non-polar solvent layered to yield single crystals.[94, 97, 98] The authors observe solution scrambling by mass spectrometry which they attribute to the loss of terminal nitrate, water and pyridine ligands in solution.[97] Single crystal x-ray diffraction patterns are equally well solved by both hetero-multimetallic and homometallic structures for most pairs of ions.[98]

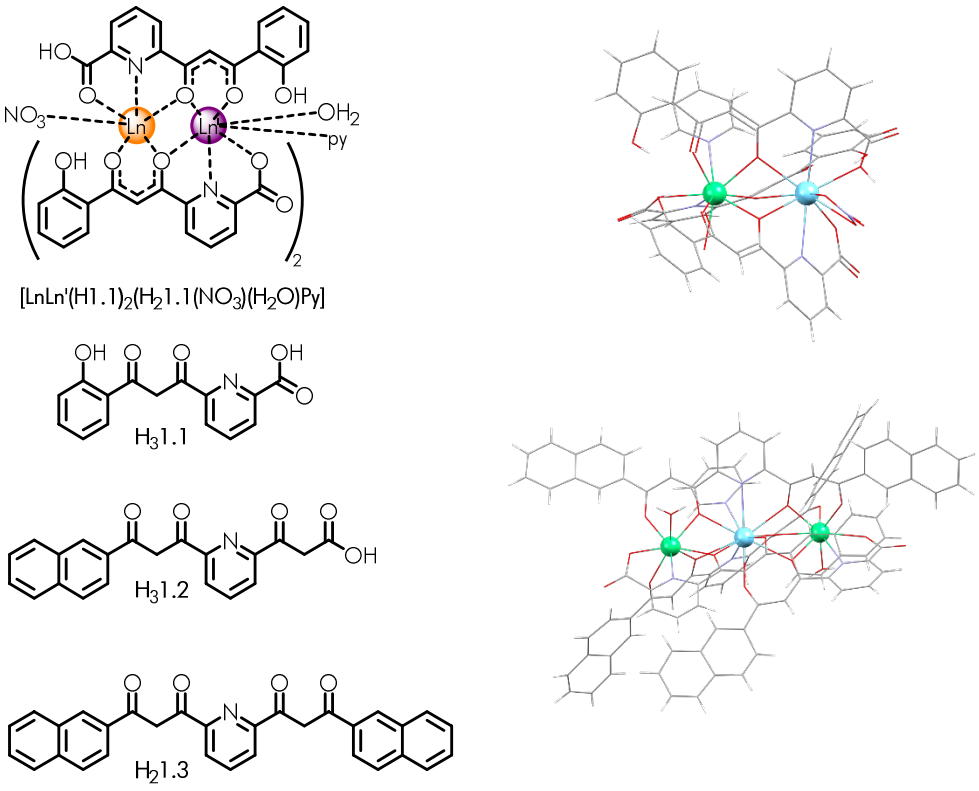

Figure 1.1.9: Chemical structure of ***[LnLn'1.1]***$^{+}$ *reported by Aromí and co-workers. B) Single-crystal x-ray diffraction structure of* ***[ErLa1.1]***$^{+}$ *reported by Aromí and co-workers.*[94] *C) Chemical structures of* ***1.1***, ***1.2*** *and* ***1.3*** *ligands reported by Aromí and co-workers for the preparation of multimetallic lanthanide complexes.*[95] *D) Single-crystal x-ray diffraction structure of* ***[Er2La1.3]***$^{+}$ *reported by Aromí and co-workers.*[96]

[CeEr1.1]$^{+}$ has been applied as a molecular CNOT quantum information gate.[94] A CNOT gate is one where the target bit is switched only when a control bit is in a particular state.[95, 102] The cerium(III) and erbium(III) ions both have doubly degenerate ground states and each can be addressed individually. The whole molecule has 4 discreet Zeeman states. When the applied magnetic field is chosen such that only one transition is in resonance, the molecule acts as a CNOT gate.[94] **[Er$_2$Ce1.3]**$^{+}$ has been applied in a similar manner to **[CeEr1.1]**$^{+}$, however, the introduction of a third ion enables error correction for the CNOT gate.[96] **[Tb$_2$1.1]**$^{+}$, a homometallic analogue of **[CeEr1.1]**$^{+}$ has been applied as a molecular CNOT and a SWAP quantum information gate.[95, 103] Continuous wave EPR measurements at 6 K on frozen solution samples showed that SWAP and CNOT gate operations could be caried out when the applied magnetic field was chosen such that each transition was resonant with the X-band photons.[32, 94, 95]

Aromí and co-workers investigated Ln(III)-to-Ln(III) energy transfer in heterometallic derivatives of **1.1**.[100] When **[EuYb1.1]**$^{+}$ was investigated, dual emission from europium(III) and ytterbium(III) was observed, excitation spectra suggested all sensitisation was from the ligand centred triplet excited state. The ligand centred triplet excited state was found to be close in energy to the $^5D_0$ and $^5D_1$ excited states of europium(III) and back energy transfer was observed. When **[NdYb1.1]**$^{+}$ was investigated, dual emission from neodymium(III) and ytterbium(III) was observed. Both neodymium(III) and ytterbium(III) can be sensitised efficiently without back energy transfer to the ligand triplet excited state. The excited state decay curve for ytterbium(III) centred emission (λ_{em} = 980 nm) in **[NdYb1.1]**$^{+}$ shows a short rise-time which the authors attribute to energy transfer from neodymium(III) centred excited states, following direct excitation of neodymium(III) (λ_{ex} = 584 nm). This rise-time is not present following excitation of the ligand chromophore.[100] The wavelength of light used to excite neodymium(III) (λ_{ex} = 584 nm) overlaps

with the triplet excited state of the ligand, back energy transfer and non-directional energy transfer to neodymium(III) or ytterbium(III) may occur.

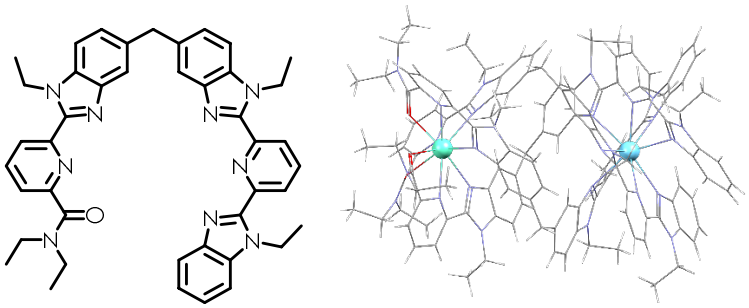

Figure 1.1.10: Left: Ligand structure of **1.4** *reported by Piguet, Bünzli and co-workers for the preparation of heterometallic helicates[104]Right: Single-crystal x-ray diffraction structure of* **[EuLa(1.4)$_3$][ClO$_4$]$_6$** *reported by Piguet, Bünzli and co-workers[104]*

Piguet, Bünzli and co-workers have reported several hetero- and homo-metallic lanthanide helicates.[39, 104] The ligand which displays the greatest selectivity, **1.4**, for the heterometallic pairing is shown in Figure 1.10. The complex is prepared from **1.4** and the parent lanthanide(III) perchlorate salts in acetonitrile to afford complex **[LnLn'(1.4)$_3$][ClO$_4$]$_6$**. The heterometallic selectivity is attributed to the differently sized coordination pockets, and the differing radius of the lanthanide(III) ions. The greatest heterometallic selectivity is observed for **[LaLu(1.4)$_3$][ClO$_4$]$_6$** at 90% heterometallic complex. Relative concentrations were determined by ^{1}H NMR spectroscopy and electrospray ionisation mass spectrometry. The authors comment that whilst the heterometallic complexes can be isolated in the solid state, in acetonitrile solution the complexes scramble to an equilibrium mixture.[104]

The authors propose the heterometallic complexes for imaging applications, with **[EuTb(1.4)$_3$][ClO$_4$]$_6$** being the most useful. However, the authors determine the heterometallic

selectivity a europium(III)-terbium(III) pair as 51%, approaching the statistical yield for a completely non-selective system of 50%.[104]

Piligkos and co-workers prepared multimetallic lanthanide-cryptate complexes. Stepwise preparation, via a Schiff base reaction, and metalation of cryptate chelators enable access to pure multimetallic complexes.[105] A similar approach has been employed by Williams and co-workers for the preparation of multimetallic complexes containing one d-block metal and one group 1 or 2 metal for catalysis.[106-110]

Kitigawa et al. report a terbium(III)-neodymium(III) multimetallic complex prepared from the corresponding lanthanide(III) acetylacetonates and a bis-phosphineoxide linker. The authors do not comment on multimetallic purity.[111]

1.14: KINETIC CONTROL

To overcome the challenges of 'scrambling' in solution Faulkner and Sørenson have proposed using kinetically inert lanthanide chelators.[38] Whilst most lanthanide complexes are labile,[4] the use of rigid, preorganised, macrocyclic chelators with 7 or 8 donors can prepare kinetically and thermodynamically inert complexes. These mostly take the form of substituted DO3A ligands, with the 4th N-substituent being bulky and/or coordinating. Faulkner and Sørenson propose a rate constant of dissociation lower than 10^{-6} s^{-1} under the experimental conditions to allow long-term storage of kinetically inert lanthanide complexes.[38]

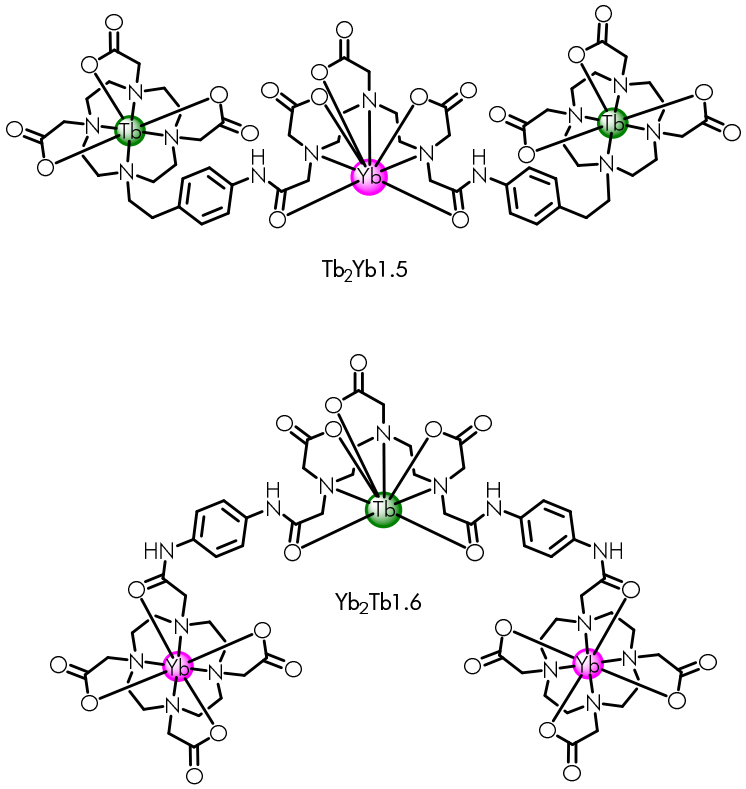

Figure 1.1.11: Top: The multimetallic lanthanide complex reported by Faulkner and Pope, ***Tb₂Yb1.5*** *[56] Bottom: The multimetallic lanthanide complex reported by Natrajan and co-workers,* ***Yb₂Tb1.6*** *[112]*

Faulkner and Pope reported lanthanide sensitised lanthanide luminescence in a trimetallic **$Tb_2Yb_1$1.5** complex.[56] Utilising a kinetically inert terbium(III) complex with a pendant amine group as a building block, treatment with diethylenetriamine pentaacetic acid (DTPA) dianhydride links the two building blocks and unlocks a DTPA chelator. Further treatment with an ytterbium(III) source affords the trimetallic complex. Solution scrambling is avoided by use of kinetically inert terbium(III) units. Emission from ytterbium(III) centred excited states is observed following direct excitation of terbium(III) centred excited states (λ_{em} = 488 nm).[56] Natrajan and co-workers employed the same synthetic strategy to access a series multimetallic lanthanide complexes; **Yb_2Tb1.6** and **Yb_2Eu1.6** exhibit dual visible near-infra red emission.[112]

Trembley and Sames modified the approach of Faulkner and Pope[56] for the preparation of bimetallic lanthanide complexes.[112] Treatment of a free ligand containing both DO3A and DTPA chelators with excess terbium(III) salts metalates both chelators. Subsequent selective demetalation of the labile DTPA chelator affords the monometallic complex. Further treatment with a lanthanide(III) source allows access to high purity bimetallic complexes.[113]

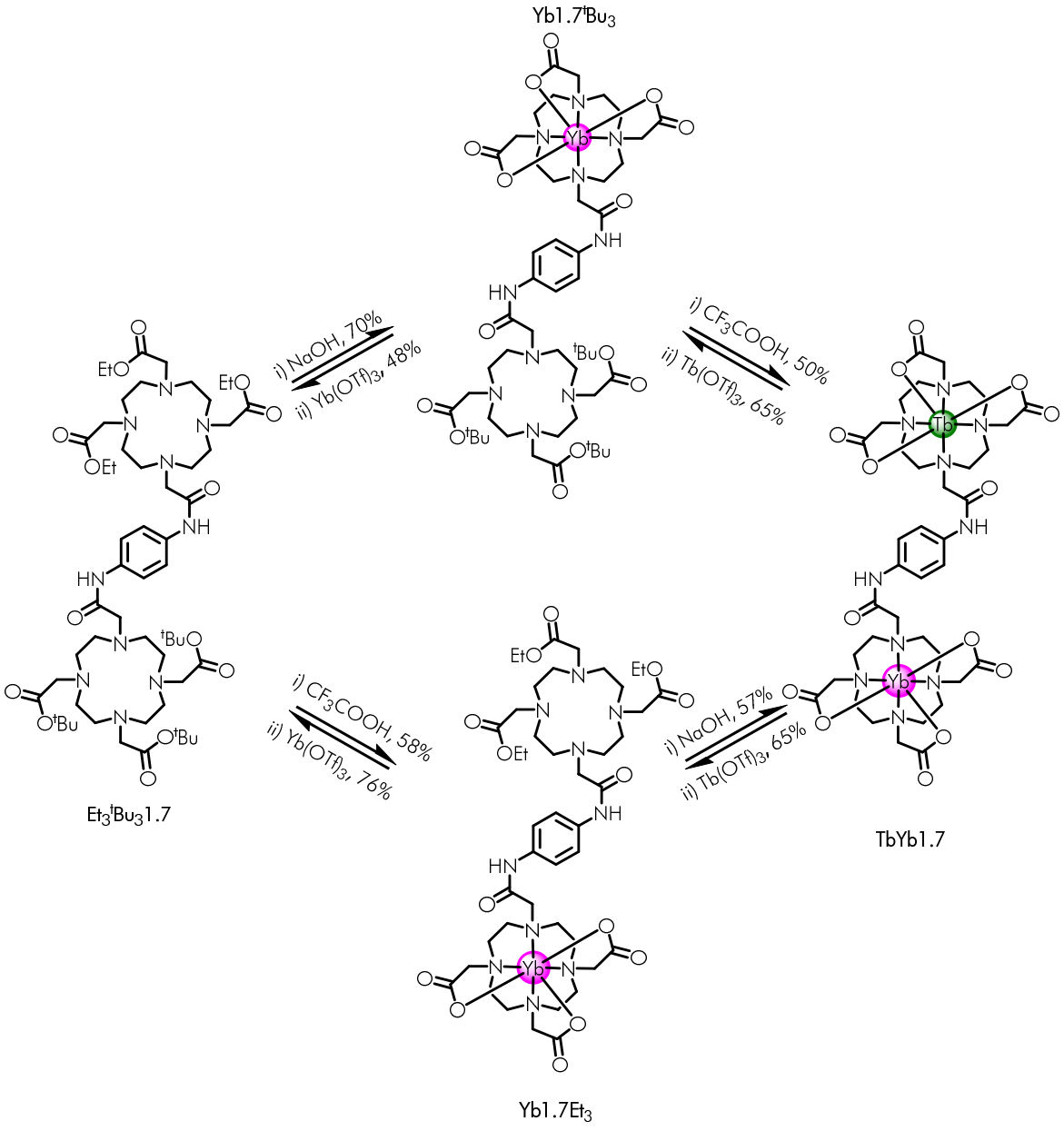

Figure 1.1.12: The orthogonal protection strategy employed by Natrajan et al. to access symmetrical multimetallic complexes.[114]

Natrajan et al. reported the use of orthogonal protection strategies to subsequently deprotect and metalate kinetically inert chelators, allowing access to high purity bimetallic complexes.[114] Figure 1.12 shows the two routes of sequential deprotection, metalation reactions to afford heterometallic complexes.

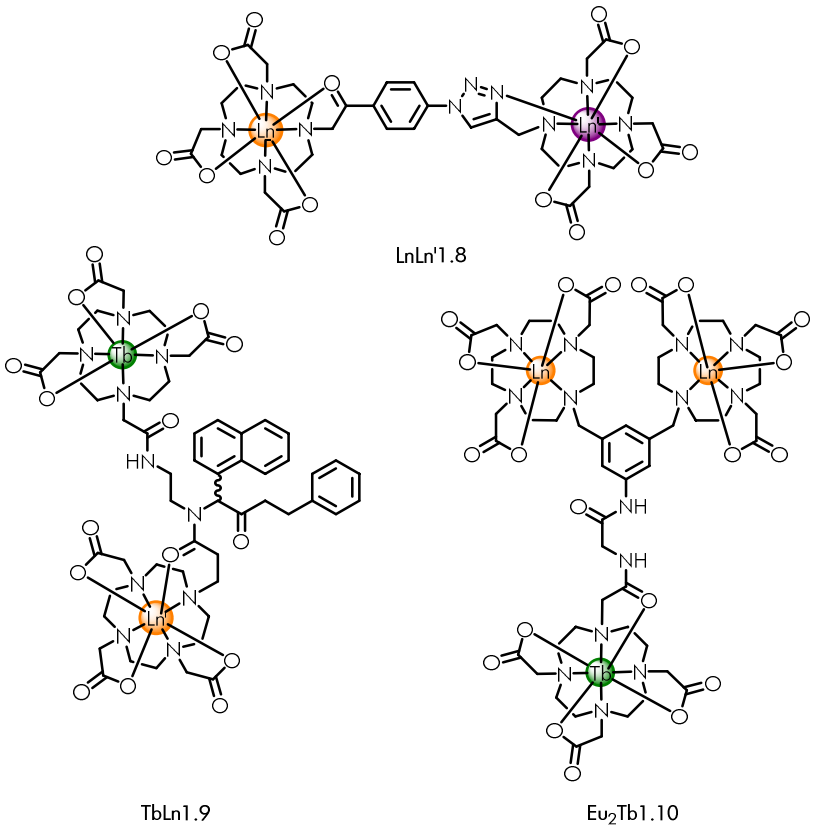

Figure 1.1.13: Top: The multimetallic lanthanide complex prepared by Faulkner and co-workers via an alkyne-azide cycloaddition, ***LnLn'1.8***[115] *Bottom Left: The multimetallic lanthanide complex prepared by Faulkner and co-workers via an Ugi reaction* ***TbLn1.9***[116] *Bottom Right: The multimetallic lanthanide complex prepared by Faulkner and co-workers via peptide coupling* ***$Ln_2Tb1.10$***.[117]

Faulkner and co-workers have reported several structurally distinct multimetallic complexes prepared from kinetically inert lanthanide(III) complexes coupled with high yielding reactions. Tropiano et al. reported a bimetallic lanthanide complex prepared from an alkyne-azide cycloaddition 'click' reaction.[115] Faulkner and co-workers have reported bimetallic, trimetallic

and tetrametallic complexes prepared via Ugi reactions.[116-119] Faulkner and co-workers have reported trimetallic complexes prepared via peptide coupling reactions.[117]

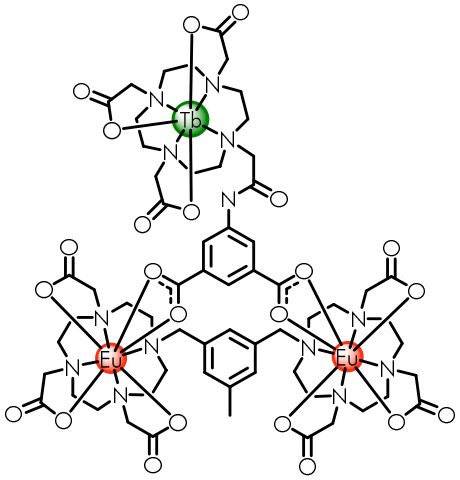

[Tb1.11]$^{-}$. [$Eu_2$1.12]

Figure 1.1.14: Self-assembly of ***[Tb1.11]$^{2-}$*** *with* ***$Eu_2$1.12*** *to afford a multimetallic architecture, as reported by Faulkner and co-workers.*[120]

Faulkner and co-workers have investigated the self-assembly of terbium(III) derivatives with pendant isophthalate groups with bis-europium(III) complexes, to allow access to multimetallic architectures.[120] The self-assembly of carboxylic acid derivatives with bimetallic complexes has been expanded to more complex structures, such as transition-metal chromophores[121] and surfaces.[122] Sørenson et al. have investigated the self-assembly of meta-xylyl derivatives under different conditions, with isophthalate showing the strongest binding.[123]

1.15: AIMS

This thesis will aim to extend the literature examples of kinetically inert lanthanide complexes and explore the photophysical properties of such complexes.

The principal aim of chapter 2 is to prepare d-block complexes to act as simple $S=\frac{1}{2}$ models of phenolate-bridged lanthanide complexes. The EPR spectroscopy of dicopper(II) and copper(II)-zinc(II) complexes will be explored. Exchange coupling in copper(II) complexes has previously been explored, with varying intermetallic communication pathways affecting observed coupling strength.

The principal aim of chapter 3 is to prepare two bis-macrocyclic ligands with a p-cresol bridging unit and the lanthanide complexes thereof. Multimetallic lanthanide complexes will be prepared via a statistical complexation and HPLC separation route, aided by ligand symmetry. Binuclear complexes with a covalent block on phenolate-bridging will be explored, hydrolysis to afford phenolate-bridged complexes will be explored to understand intermetallic communication facilitated by a bridging phenolate group.

The principal aim of chapter 4 is to prepare multimetallic lanthanide complexes from the self-assembly of one kinetically inert lanthanide complex with lanthanide acetylacetonate complexes. The photophysical properties that result for a set of europium(III)-terbium(III) complexes will be explored.

The principal aim of chapter 5 is to prepare tetranuclear lanthanide complexes with a bridging phenolate from a novel benzophenone derivative. The photophysics of these complexes will be explored. The preparation of larger architectures will be investigated.

1.16: REFERENCES

1. N. N. Greenwood. and A. Earnshaw, Chemistry of the Elements, Butterman-Heinemann, Boston, USA, 1997.
2. C. Housecroft and A. Sharpe, Inorganic Chemistry, Pearson Education, Limited, Harlow, UNITED KINGDOM, 2018.
3. J.-C. G. Bünzli and S. V. Eliseeva, in Lanthanide Luminescence: Photophysical, Analytical and Biological Aspects, eds. P. Hänninen and H. Härmä, Springer Berlin Heidelberg, Berlin, Heidelberg, 2011, pp. 1-45.
4. N. Kaltsoyannis and P. Scott, The f elements, Oxford University Press, Oxford, 1999.
5. W. J. Evans, *Inorg. Chem.*, 2007, 46, 3435-3449.
6. C. F. G. C. Geraldes, in Methods in Enzymology, Academic Press, 1993, vol. 227, pp. 43-78.
7. C. C. Hinckley, *J. Am. Chem. Soc.*, 1969, 91, 5160-5162.
8. H. C. Aspinall, *Chem. Rev.,* 2002, 102, 1807-1850.
9. K. W.-Y. Chan and W.-T. Wong, *Coord. Chem. Rev.*, 2007, 251, 2428-2451.
10. S. M. Pinto, V. Tomé, M. J. F. Calvete, M. M. C. A. Castro, É. Tóth and C. F. G. C. Geraldes, *Coord. Chem. Rev.*, 2019, 390, 1-31.
11. J. Wahsner, E. M. Gale, A. Rodríguez-Rodríguez and P. Caravan, *Chem. Rev.*, 2019, 119, 957-1057.
12. S. Shuvaev, E. Akam and P. Caravan, *Investigative Radiology*, 2021, 56.
13. S. Zhang, M. Merritt, D. E. Woessner, R. E. Lenkinski and A. D. Sherry, *Acc. Chem. Res.* , 2003, 36, 783-790.
14. P. Harvey, A. M. Blamire, J. I. Wilson, K.-L. N. A. Finney, A. M. Funk, P. K. Senanayake and D. Parker, *Chem. Sci.*, 2013, 4, 4251-4258.
15. C. M. G. dos Santos, A. J. Harte, S. J. Quinn and T. Gunnlaugsson, *Coord. Chem. Rev.*, 2008, 252, 2512-2527.
16. M. L. Aulsebrook, B. Graham, M. R. Grace and K. L. Tuck, *Coord. Chem. Rev.*, 2018, 375, 191-220.
17. S. J. Butler and D. Parker, *Chem. Soc. Rev.*, 2013, 42, 1652-1666.
18. S. E. Bodman and S. J. Butler, *Chem. Sci.*, 2021, 12, 2716-2734.
19. A. B. Aletti, D. M. Gillen and T. Gunnlaugsson, *Coord. Chem. Rev.*, 2018, 354, 98-120.
20. D. Parker, Coord. *Chem. Rev.*, 2000, 205, 109-130.
21. D. Parker, J. D. Fradgley and K.-L. Wong, *Chem. Soc. Rev.*, 2021, 50, 8193-8213.
22. A. J. Amoroso and S. J. A. Pope, *Chem. Soc. Rev.*, 2015, 44, 4723-4742.
23. J.-C. G. Bünzli and C. Piguet, *Chem. Soc. Rev.*, 2005, 34, 1048-1077.
24. J.-C. G. Bünzli, *Chem. Rev.*, 2010, 110, 2729-2755.
25. U. Cho and J. K. Chen, *Cell Chem. Biol.*, 2020, 27, 921-936.

26. M. C. Heffern, L. M. Matosziuk and T. J. Meade, *Chem. Rev.*, 2014, 114, 4496-4539.
27. Y. Ning, G.-Q. Jin, M.-X. Wang, S. Gao and J.-L. Zhang, *Curr. Opin. Chem. Biol.*, 2022, 66, 102097.
28. C. A. P. Goodwin, *Dalton Trans.*, 2020, 49, 14320-14337.
29. C. A. P. Goodwin, F. Ortu, D. Reta, N. F. Chilton and D. P. Mills, *Nature*, 2017, 548, 439-442.
30. N. F. Chilton, *Annu. Rev. Mater. Res.*, 2022, 52, 79-101.
31. J. D. Rinehart and J. R. Long, *Chem. Sci.,* 2011, 2, 2078-2085.
32. G. Aromí, F. Luis and O. Roubeau, in Lanthanides and Actinides in Molecular Magnetism, 2015, pp. 185-222.
33. M. R. Wasielewski, M. D. E. Forbes, N. L. Frank, K. Kowalski, G. D. Scholes, J. Yuen-Zhou, M. A. Baldo, D. E. Freedman, R. H. Goldsmith, T. Goodson, M. L. Kirk, J. K. McCusker, J. P. Ogilvie, D. A. Shultz, S. Stoll and K. B. Whaley, *Nature Rev. Chem.*, 2020, 4, 490-504.
34. D. W. Laorenza and D. E. Freedman, *J. Am. Chem. Soc*, 2022, 144, 21810-21825.
35. A. Gaita-Ariño, F. Luis, S. Hill and E. Coronado, *Nat. Chem.*, 2019, 11, 301-309.
36. J.-C. G. Bünzli and C. Piguet, *Chem. Rev.*, 2002, 102, 1897-1928.
37. J. Kragskow, waveplot, waveplot.com
38. J.-C. G. Bünzli, *Acc. Chem. Res.*, 2006, 39, 53-61.
39. T. J. Sørensen and S. Faulkner, *Acc. Chem. Res.* , 2018, 51, 2493-2501.
40. C. Piguet and J.-C. G. Bünzli, *Chem. Soc. Rev.*, 1999, 28, 347-358.
41. M. L. Neidig, D. L. Clark and R. L. Martin, *Coord. Chem. Rev.*, 2013, 257, 394-406.
42. M. R. MacDonald, J. E. Bates, J. W. Ziller, F. Furche and W. J. Evans, *J. Am. Chem. Soc.*, 2013, 135, 9857-9868.
43. M. R. MacDonald, J. W. Ziller and W. J. Evans, *J. Am. Chem. Soc.*, 2011, 133, 15914-15917.
44. M. R. MacDonald, J. E. Bates, M. E. Fieser, J. W. Ziller, F. Furche and W. J. Evans, *J. Am. Chem. Soc.* , 2012, 134, 8420-8423.
45. F. Nief, *Dalton Trans.*, 2010, 39, 6589-6598.
46. P. B. Hitchcock, M. F. Lappert, L. Maron and A. V. Protchenko, *Angew. Chem. Int. Ed.*, 2008, 47, 1488-1491.
47. J. G. Brennan, F. G. N. Cloke, A. A. Sameh and A. Zalkin, *J. Chem. Soc., Chem. Commun.*, 1987, 1668-1669.
48. W. A. King, S. Di Bella, G. Lanza, K. Khan, D. J. Duncalf, F. G. N. Cloke, I. L. Fragala and T. J. Marks, *J. Am. Chem. Soc.*, 1996, 118, 627-635.
49. A. R. Willauer, I. Douair, A.-S. Chauvin, F. Fadaei-Tirani, J.-C. G. Bünzli, L. Maron and M. Mazzanti, *Chem. Sci,*, 2022, 13, 681-691.
50. N. T. Rice, I. A. Popov, D. R. Russo, J. Bacsa, E. R. Batista, P. Yang, J. Telser and H. S. La Pierre, *J. Am. Chem. Soc.*, 2019, 141, 13222-13233.
51. T. P. Gompa, S. M. Greer, N. T. Rice, N. Jiang, J. Telser, A. Ozarowski, B. W. Stein and H. S. La Pierre, *Inorg. Chem.*, 2021, 60, 9064-9073.

52. A. R. Willauer, C. T. Palumbo, R. Scopelliti, I. Zivkovic, I. Douair, L. Maron and M. Mazzanti, *Angew. Chem. Int. Ed.*, 2020, 59, 3549-3553.

53. A. R. Willauer, C. T. Palumbo, F. Fadaei-Tirani, I. Zivkovic, I. Douair, L. Maron and M. Mazzanti, *J. Am. Chem. Soc.* , 2020, 142, 5538-5542.

54. X. Li, W. Liu, Z. Guo and M. Tan, *Inorg. Chem.*, 2003, 42, 8735-8738.

55. S. Faulkner, S. J. A. Pope and B. P. Burton-Pye, *Appl. Spectrosc. Rev.*, 2005, 40, 1-31.

56. S. Faulkner and S. J. A. Pope, *J. Am. Chem. Soc.* , 2003, 125, 10526-10527.

57. L. Abad Galán, D. Aguilà, Y. Guyot, V. Velasco, O. Roubeau, S. J. Teat, M. Massi and G. Aromí, *Chem. Eur. J.*, 2021, n/a.

58. J. R. Lakowicz, Principles of Fluorescence Spectroscopy, Springer US, New York, NY, 3rd 2006. edn., 2006.

59. D. L. Dexter, *J. Chem. Phys.*, 1953, 21, 836-850.

60. A. Beeby, I. M. Clarkson, R. S. Dickins, S. Faulkner, D. Parker, L. Royle, A. S. de Sousa, J. A. Gareth Williams and M. Woods, *J. Chem. Soc. Perkin Trans. 2*, 1999, 493-504.

61. W. D. Horrocks, Jr. and D. R. Sudnick, *Acc. Chem. Res.*, 1981, 14, 384-392.

62. W. D. Horrocks, Jr. and D. R. Sudnick, *J. Am. Chem. Soc.*, 1979, 101, 334-340.

63. L. M. Manus, R. C. Strauch, A. H. Hung, A. L. Eckermann and T. J. Meade, *Anal. Chem.*, 2012, 84, 6278-6287.

64. W. T. Carnall, P. R. Fields and K. Rajnak, *J. Chem. Phys.*, 1968, 49, 4447-4449.

65. W. T. Carnall, P. R. Fields and K. Rajnak, *J. Chem. Phys.*, 1968, 49, 4412-4423.

66. M. Tropiano, O. A. Blackburn, J. A. Tilney, L. R. Hill, T. Just Sørensen and S. Faulkner, *J. Lumin.*, 2015, 167, 296-304.

67. P. J. Hore, Nuclear magnetic resonance, Oxford University Press, Oxford, Second edition. edn., 2015.

68. J. A. Iggo and K. V. Luzyanin, NMR spectroscopy in inorganic chemistry, Oxford University Press, Oxford, Second edition. edn., 2020.

69. H. Friebolin and J. K. Becconsall, Basic one- and two-dimensional NMR spectroscopy, Wiley-VCH, Weinheim, 4th rev. edn., 2005.

70. J. A. Peters, J. Huskens and D. J. Raber, *Prog. Nucl. Magn. Reson. Spectrosc.*, 1996, 28, 283-350.

71. H. M. McConnell, *J. Chem. Phys.*, 1957, 27, 226-229.

72. B. Bleaney, *J. Mag. Res.,* 1972, 8, 91-100.

73. V. Chechik, E. Carter and D. Murphy, Electron paramagnetic resonance, Oxford University Press, Oxford, 2016.

74. Y. Bretonnière, M. Mazzanti, J. Pécaut and M. M. Olmstead, *J. Am. Chem. Soc.*, 2002, 124, 9012-9013.

75. J. Xu and K. N. Raymond, *Angew. Chem. Int. Ed.*, 2000, 39, 2745-2747.

76. L.-L. Yan, C.-H. Tan, G.-L. Zhang, L.-P. Zhou, J.-C. Bünzli and Q.-F. Sun, *J. Am. Chem. Soc*, 2015, 137, 8550-8555.

77. X. Tang, D. Chu, W. Gong, Y. Cui and Y. Liu, *Angew. Chem. Int. Ed.*, 2021, 60, 9099-9105.

78. K. S. Jeong, Y. S. Kim, Y. J. Kim, E. Lee, J. H. Yoon, W. H. Park, Y. W. Park, S.-J. Jeon, Z. H. Kim, J. Kim and N. Jeong, Angew. Chem. Int. Ed., 2006, 45, 8134-8138.

79. J. Hamacek, C. Besnard, T. Penhouet and P.-Y. Morgantini, *Chem. Eur. J.*, 2011, 17, 6753-6764.

80. M. Elhabiri, R. Scopelliti, J.-C. G. Bünzli and C. Piguet*, J. Am. Chem. Soc*., 1999, 121, 10747-10762.

81. J. Lu, X.-L. Li, C. Jin, Y. Yu and J. Tang, *New J. Chem*., 2020, 44, 994-1000.

82. J. Lu, V. Montigaud, O. Cador, J. Wu, L. Zhao, X.-L. Li, M. Guo, B. Le Guennic and J. Tang, *Inorg. Chem*., 2019, 58, 11903-11911.

83. J. J. Lessmann and W. D. Horrocks, *Inorg. Chem*., 2000, 39, 3114-3124.

84. T. K. Ronson, H. Adams, L. P. Harding, S. J. A. Pope, D. Sykes, S. Faulkner and M. D. Ward, *Dalton. Trans.*, 2007, 1006-1022.

85. Y. Bretonnière, M. Mazzanti, R. Wietzke and J. Pécaut, *Chem. Commun*., 2000, 1543-1544.

86. J. Hamacek and A. Vuillamy, *Eur. J. Inorg. Chem*., 2018, 2018, 1155-1166.

87. S. Swavey and R. Swavey, *Coord. Chem. Rev.,* 2009, 253, 2627-2638.

88. O. A. Blackburn, M. Tropiano, L. S. Natrajan, A. M. Kenwright and S. Faulkner, *Chem. Commun*., 2016, 52, 6111-6114.

89. S. J. A. Pope, A. M. Kenwright, V. A. Boote and S. Faulkner, *Dalton Trans.*, 2003, 3780-3784.

90. J. Campos, *Nature Rev. Chem.*, 2020, 4, 696-702.

91. M. Navarro, J. J. Moreno, M. Pérez-Jiménez and J. Campos, *Chem. Commun*., 2022, 58, 11220-11235.

92. W. T. Diment, W. Lindeboom, F. Fiorentini, A. C. Deacy and C. K. Williams, *Acc. Chem. Res*., 2022, 55, 1997-2010.

93. P. Buchwalter, J. Rosé and P. Braunstein, *Chem. Rev*., 2015, 115, 28-126.

94. D. Aguilà, L. A. Barrios, V. Velasco, O. Roubeau, A. Repollés, P. J. Alonso, J. Sesé, S. J. Teat, F. Luis and G. Aromí, *J. Am. Chem. Soc.*, 2014, 136, 14215-14222.

95. D. Aguilà, O. Roubeau and G. Aromí, *Dalton. Trans*., 2021, 50, 12045-12057.

96. E. Macaluso, M. Rubín, D. Aguilà, A. Chiesa, L. A. Barrios, J. I. Martínez, P. J. Alonso, O. Roubeau, F. Luis, G. Aromí and S. Carretta, *Chem. Sci.*, 2020, 11, 10337-10343.

97. J. Gónzalez-Fabra, N. A. G. Bandeira, V. Velasco, L. A. Barrios, D. Aguilà, S. J. Teat, O. Roubeau, C. Bo and G. Aromí, *Chem. Eur. J*, 2017, 23, 5117-5125.

98. D. Aguilà, V. Velasco, L. A. Barrios, J. González-Fabra, C. Bo, S. J. Teat, O. Roubeau and G. Aromí, *Inorg. Chem*., 2018, 57, 8429-8439.

99. F. Luis, P. J. Alonso, O. Roubeau, V. Velasco, D. Zueco, D. Aguilà, J. I. Martínez, L. A. Barrios and G. Aromí, *Commun. Chem.*, 2020, 3, 176.

100. L. Abad Galán, D. Aguilà, Y. Guyot, V. Velasco, O. Roubeau, S. J. Teat, M. Massi and G. Aromí, *Chem. Eur. J*, 2021, 27, 7288-7299.

101. D. Maniaki, A. Sickinger, L. A. Barrios Moreno, D. Aguilà, O. Roubeau, N. S. Settineri, Y. Guyot, F. Riobé, O. Maury, L. A. Galán and G. Aromí, *Inorg. Chem*., 2023, 62, 3106-3115.

102. D. Aguilà, O. Roubeau and G. Aromí, *Dalton Trans.*, 2021, 50, 12045-12057.

103. F. Luis, A. Repollés, M. J. Martínez-Pérez, D. Aguilà, O. Roubeau, D. Zueco, P. J. Alonso, M. Evangelisti, A. Camón, J. Sesé, L. A. Barrios and G. Aromí, *Phys. Rev. Lett.*, 2011, 107, 117203.

104. N. André, R. Scopelliti, G. Hopfgartner, C. Piguet and J.-C. G. Bünzli, *Chem. Commun.*, 2002, 214-215.

105. C. D. Buch, S. H. Hansen, D. Mitcov, C. M. Tram, G. S. Nichol, E. K. Brechin and S. Piligkos, *Chem. Sci.*, 2021.

106. A. C. Deacy, C. B. Durr and C. K. Williams, *Dalton Trans.*, 2020, 49, 223-231.

107. W. Lindeboom, D. A. X. Fraser, C. B. Durr and C. K. Williams, *Chem. Eur. J.*, 2021, 27, 12224-12231.

108. N. V. Reis, A. C. Deacy, G. Rosetto, C. B. Durr and C. K. Williams, *Chem. Eur. J.*, 2022, 28.

109. F. Fiorentini, W. T. Diment, A. C. Deacy, R. W. F. Kerr, S. Faulkner and C. K. Williams, *Nat. Commun.*, 2023, 14, 4783.

110. W. T. Diment, G. Rosetto, N. Ezaz-Nikpay, R. W. F. Kerr and C. K. Williams, *Green Chem.,* 2023, 25, 2262-2267.

111. Y. Kitagawa, K. Matsuda, P. P. F. da Rosa, K. Fushimi and Y. Hasegawa, *Chem. Commun.*, 2021.

113. M. E. Thornton, J. Hemsworth, S. Hay, P. Parkinson, S. Faulkner and L. S. Natrajan, *Front. Chem.*, 2023, 11

113. M. S. Tremblay and D. Sames, *Chem. Commun.*, 2006, 4116-4118.

114. L. S. Natrajan, A. J. L. Villaraza, A. M. Kenwright and S. Faulkner, *Chem. Commun.*, 2009, 6020-6022.

115. M. Tropiano, A. M. Kenwright and S. Faulkner, *Chem. Eur. J*, 2015, 21, 5697-5699.

116. T. J. Sørensen, A. M. Kenwright and S. Faulkner, *Chem. Sci.*, 2015, 6, 2054-2059.

117. M. Tropiano, O. A. Blackburn, J. A. Tilney, L. R. Hill, M. P. Placidi, R. J. Aarons, D. Sykes, M. W. Jones, A. M. Kenwright, J. S. Snaith, T. J. Sørensen and S. Faulkner, *Chem. Eur. J*, 2013, 19, 16566-16571.

118. T. J. Sørensen, M. Tropiano, A. M. Kenwright and S. Faulkner, *Eur. J. Inorg. Chem.*, 2017, 2017, 2165-2172.

119. T. J. Sørensen, M. Tropiano, O. A. Blackburn, J. A. Tilney, A. M. Kenwright and S. Faulkner, *Chem. Commun.*, 2013, 49, 783-785.

120. J. A. Tilney, T. J. Sørensen, B. P. Burton-Pye and S. Faulkner, *Dalton Trans.*, 2011, 40, 12063-12066.

121. L. R. Hill, O. A. Blackburn, M. W. Jones, M. Tropiano, T. J. Sørensen and S. Faulkner, *Dalton Trans.*, 2013, 42, 16255-16258.

122. J. Lehr, J. Bennett, M. Tropiano, T. J. Sørensen, S. Faulkner, P. D. Beer and J. J. Davis, *Langmuir*, 2013, 29, 1475-1482.

123. T. J. Sørensen, L. R. Hill and S. Faulkner, *ChemistryOpen*, 2015, 4, 509-515.

2. DICOPPER(II) AND MULTIMETALLIC COPPER(II)-ZINC(II) COMPLEXES AS SIMPLE SPIN MODELS FOR PHENOLATE-BRIDGED SYSTEMS

The work presented in chapter 2 was carried out in collaboration with the group of Prof. Christiane Timmel at the University of Oxford. Ashley Redman and Filip Ivanovic carried out the X-Band EPR experiments.

2.1: INTRODUCTION

We sought to design and prepare model systems to help further our understanding of the magnetic properties of phenolate-bridged bimetallic lanthanide complexes. We decided to investigate d-block analogues to act as model systems. We chose copper(II) for the $S = \frac{1}{2}$ ground state. We used zinc(II) as a diamagnetic ($S = 0$) analogue with a similar ionic radius and chemical behaviour.

Exchange coupling, J, is a convenient measure of through-bond electronic communication. Timmel and co-workers have explored the modulation of J in linear[1] and cyclic[2] polycopper(II) complexes. For a cyclic Cu_2Zn_4 porphyrin nanoring, Timmel and co-workers found constructive quantum interference when two parallel exchange pathways are present, offering a 4.5-fold enhancement of exchange coupling compared to a single exchange pathway.[2] An understanding of exchange coupling is important for the realisation of qubit gates.[3]

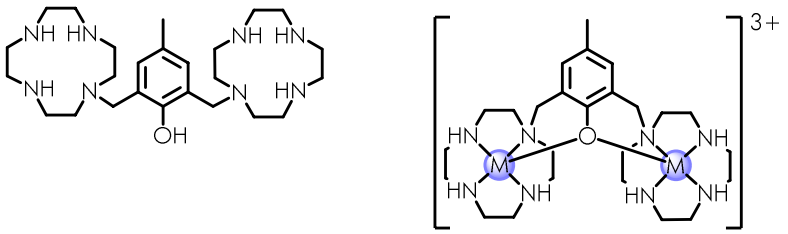

*Figure 2.1: Chemical structures of **H2.1** and **[M₂2.1]³⁺***

H2.1 was designed to have two chelators suitable for d-block metals whilst remaining structurally similar to **[Na][LnLn'3.1]** (see chapter 3), hence, two cyclen moieties were selected. The bridging p-cresol moiety was included to allow through-bond communication, and exchange coupling, between the two metal ions. Complexes of **2.1** are expected to have the phenolate bridge the two metal centres.

Copper(II), with a d^9 configuration and one unpaired electron, has a spin quantum number of $S = \frac{1}{2}$. A spin-half system is expected to simplify the electron paramagnetic resonance (EPR) experiments compared to systems with non-half spin quantum numbers, such as the lanthanide(III) ions under study in chapter 3. Zinc(II) has a d^{10} configuration and, hence, is diamagnetic ($S = 0$) and EPR silent.

Whilst the structure of the **$[M_2 2.1]^{3+}$** cation has been drawn with 5-coordiante copper(II) and zinc(II) centres, it is expected that either the anion or a coordinating solvent will fill the vacant coordination site, to create an octahedral geometry at each metal centre.

The inherent lability of copper(II) and zinc(II) complexes precluded the controlled preparation of **[CuZn2.1]$^{3+}$**; the resultant complexes would 'scramble' in solution. Given the diamagnetic nature of zinc(II), we decided to prepare **[CuZn2.1]$^{3+}$** via a statistical mixture of copper(II) and zinc(II) salts, with **[CuZn2.1]$^{3+}$** existing in diamagnetic a host of **[Zn$_2$2.1]$^{3+}$**.

The dicopper(II) complex of **H2.1** (with perchlorate counterions), **[Cu$_2$2.1][ClO$_4$]$_3$**, has been reported by Kodera et al. for DNA cleavage.[4] However, this report doesn't include the procedures for preparing the ligand. The cited literature for the synthetic procedure does not prepare **H2.1**. Previous work by the same group had prepared an amide analogue.[5] Hence, a novel synthetic procedure was devised. A solid-state structure determined by single-crystal x-ray diffraction is presented, however, no CIF file is included.

2.2: SYNTHESIS OF H2.1, [Cu$_2$2.1][NO$_3$]$_3$, AND [CuZn2.1][NO$_3$]$_3$

A synthetic route to **H2.1** is detailed in Scheme 2.1. Protection of 1,4,7,10-tetraazacyclododecane (cyclen) with 3 equivalents of di-*tert*butyl-dicarboxylate affords **2.2**. Purification via flash chromatography afforded pure **2.2** in 41% yield. **2.2** has a triply N-protected cyclen ring, with one secondary amine left free to further react.

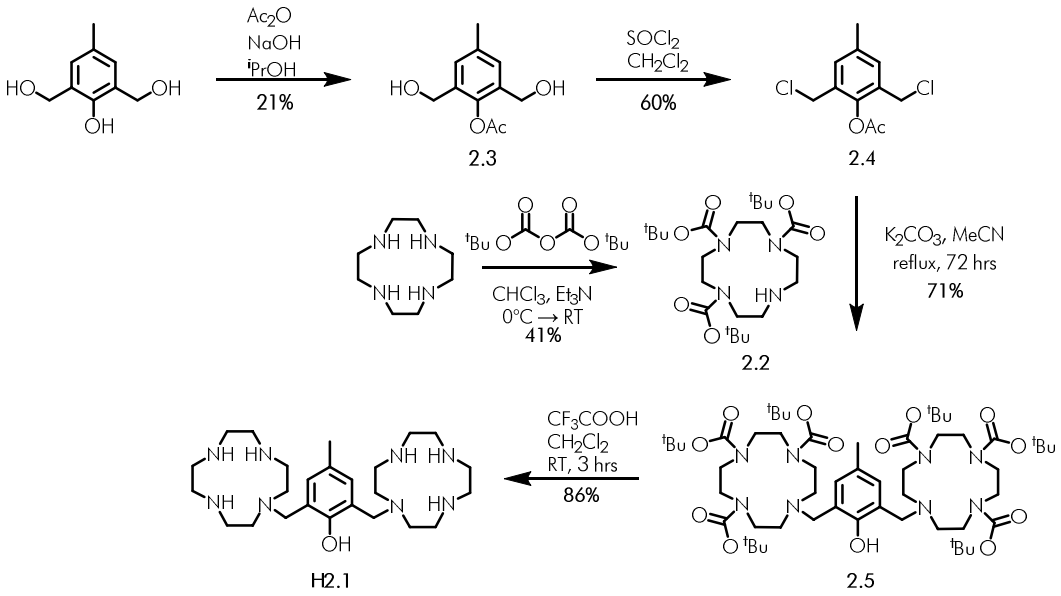

Scheme 2.1: Synthetic route to ***H2.1***

To prepare the p-cresol bridging unit, we first selectively protected the phenol group of 2,6-bis(hydroxymethyl)-4-methyl phenol with an acetyl ester, leaving the aliphatic alcohols unprotected. The method of Srivastava et. al. was used.[6] Treatment of 2,6-bis(hydroxymethyl)-4-methyl phenol with acetic anhydride in isopropanol, with addition of aqueous sodium hydroxide afforded a mixture of 2,6-bis(hydroxymethyl)-4-methyl phenol, **2.3** and more highly acetylated structures. Purification via flash chromatography afforded **2.3** in 21% yield. **2.3** was found to be unstable to standing under ambient conditions, and was prepared immediately before use.

Treatment of **2.3** with thionyl chloride in dichloromethane under argon for 72 hours afforded crude **2.4**. The target compound could be isolated with flash chromatography in 59% yield. Reaction for 72 hours was found to maximise yield. **2.4** was found to be stable to standing under ambient conditions, unlike the precursor **2.3**.

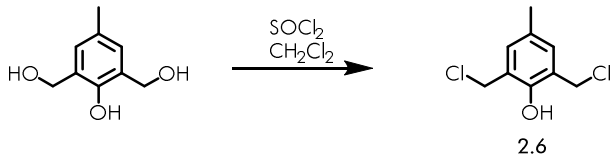

2.6

Scheme 2.2: Preparation of **2.6** *by direct chlorination of 2,6-bis(hydroxymethyl)-4-methyl phenol*

Direct treatment of 2,6-bis(hydroxymethyl)-4-methyl phenol with thionyl chloride in dichloromethane under argon (Scheme 2.2), as the method of Pope et. al.,[7] gave inconsistent yields of **2.6**. **2.6** was found to be unstable to standing under ambient conditions for prolonged periods of time. This is attributed to the phenolate group attacking the chloromethyl moiety, causing a polymerisation.

Substitution of the alkyl halide of **2.4** with the free amine of **2.2** was employed to prepare **2.5** Treatment of **2.2** with **2.4** in acetonitrile with potassium carbonate, with heating to reflux for 72 hours, afforded **2.5** in 71% yield. The reaction was found to afford **2.5** in sufficient purity to be taken forward without further purification. The reaction was found to hydrolyse the acetyl ester protecting group of the phenol moiety.

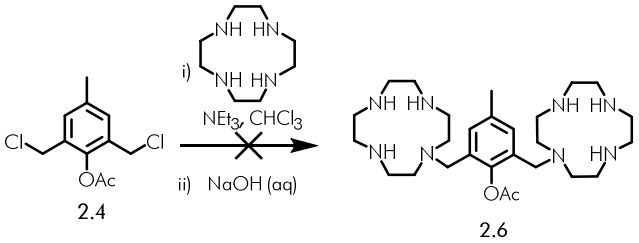

2.4 2.6

Scheme 2.3: Procedure for the direct preparation of **2.6** *according to the method of Gunnlaugsson and co-workers*[7]

Deprotection of the *tert*-butyl carboxylate protecting groups of **2.5** with trifluoroacetic acid in dichloromethane afforded the target ligand **H2.1**. The product was purified by recrystallisation

from a concentrated methanol solution with diethyl ether thrice, affording pure **H2.1** in 86% yield. Attempts to directly prepare **H2.1** or **2.6** from 1,4,7,10-tetraazacyclododecane and **2.4**, according to the generalised method of Gunnlaugsson and co-workers for the mono-alkylation of 1,4,7,10-tetraazacyclododecane, were unsuccessful (Scheme 2.3).[7]

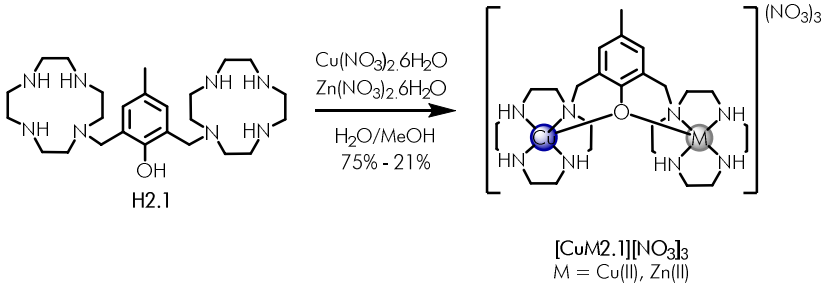

Scheme 2.4: Synthetic procedure for the preparation of ***[Cu$_2$2.1][NO$_3$]$_3$*** *and* ***[CuZn2.1][NO$_3$]$_3$***

[Cu$_2$2.1][NO$_3$]$_3$** was prepared as the nitrate salt from the copper(II) nitrate hydrate in water and methanol in 75% yield. **[CuZn2.1][NO$_3$]$_3$** was prepared as the nitrate salt from a mixture of copper(II) nitrate hydrate and zinc(II) nitrate hydrate in water and methanol. A kinetic control approach could not be taken, copper(II) and zinc(II) complexes are too labile and scramble in solution; hence, a statistical approach was taken. **[CuZn2.1][NO$_3$]$_3$** is always prepared as a statistical mixture of **[CuZn2.1][NO$_3$]$_3$**, **[Cu$_2$2.1][NO$_3$]$_3$**, and **[Zn$_2$2.1][NO$_3$]$_3$**. By using an excess of zinc(II) ions the mixture can become predominantly **[Zn$_2$2.1][NO$_3$]$_3$** and **[CuZn2.1][NO$_3$]$_3$**. As zinc(II) is diamagnetic, when recording the EPR spectra, we only observe magnetically dilute **[CuZn2.1][NO$_3$]$_3$**. A series of copper(II) doping levels were investigated, expressed as a percentage of metal ions: 1%, 4%, 8%, 10%, and 25%. **[CuZn2.1][NO$_3$]$_3$ was prepared for various ratios of copper(II) and zinc(II) ions, the complexes were afforded in 21 — 31% yield.

Figure 2.2 shows the frozen solution electron paramagnetic resonance (EPR) spectra of **[Cu$_2$2.1][NO$_3$]$_3$** and **[CuZn2.1][NO$_3$]$_3$** prepared with different copper(II) doping levels. Measurements were carried out in a 1:1 weight ratio of water and glycerol. The minor changes on moving from 4mol% to 1mol% suggest that any **[Cu$_2$2.1][NO$_3$]$_3$** present is such a minor component that it is non-observable; the spectrum can be treated as arising solely from the **[CuZn2.1][NO$_3$]$_3$**. The intermediate ratios can be well described as statistical convolution of the **[Cu$_2$2.1][NO$_3$]$_3$** and **[CuZn2.1][NO$_3$]$_3$** spectra. The EPR spectrum of **[Cu$_2$2.1][NO$_3$]$_3$** shows the signals arising from the **[Cu$_2$2.1]$^{3+}$** moiety. Good signal-to-noise ratio was observed with all mol% copper(II) loadings tested; hence, future experiments used a 1mol% copper(II) loading to prepare **[CuZn2.1][NO$_3$]$_3$** in a **[Zn$_2$2.1][NO$_3$]$_3$** matrix.

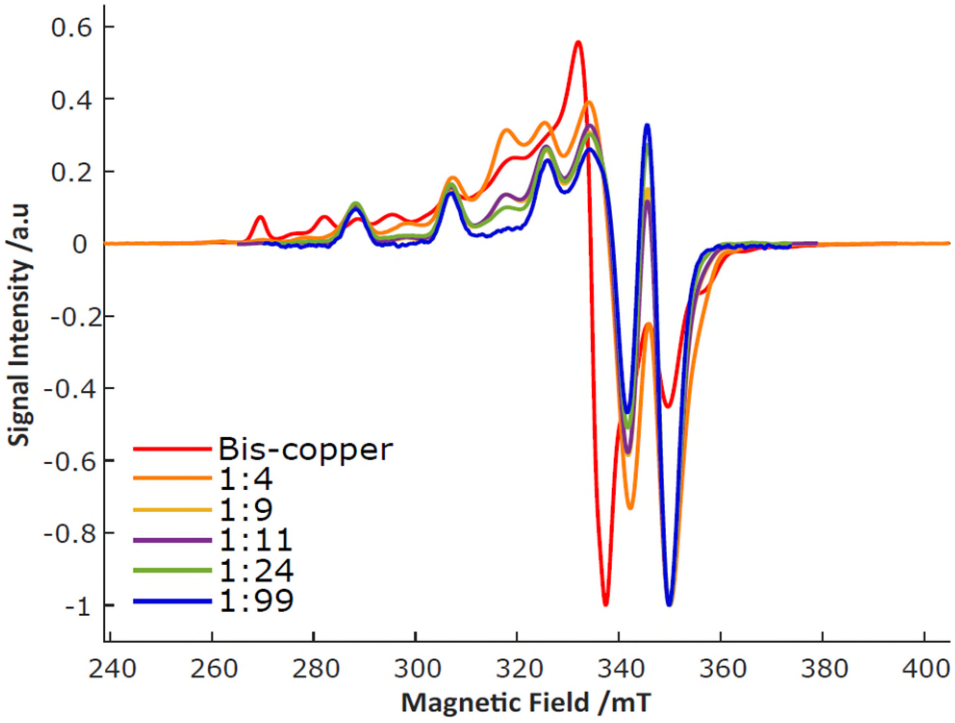

Figure 2.2: X-band cwEPR spectra of ***[Cu$_2$2.1][NO$_3$]$_3$*** *(red), and statistical mixtures with zinc(II):copper(II) of 4:1 (orange), 9:1 (yellow), 11:1 (purple), 24:1 (green) and 99:1 (blue).*

2.3: ELECTRON PARAMAGNETIC RESONANCE (EPR) SPECTROSCOPY OF $[Cu_2 2.1][NO_3]_3$ AND $[CuZn2.1][NO_3]_3$

All X-band cwEPR spectra were obtained using an EMX Micro spectrometer, using either an ER-4122SHQE or dual-mode ER-4116DM resonator. The spectra were frequency corrected to 9.75 GHz. 3.8 mm o.d., 2.7 mm i.d. Ilmasil tubes were used for all X-band measurements. cwEPR spectra were, where possible, simulated with the MATLAB package EasySpin by Filip Ivanovic.[9]

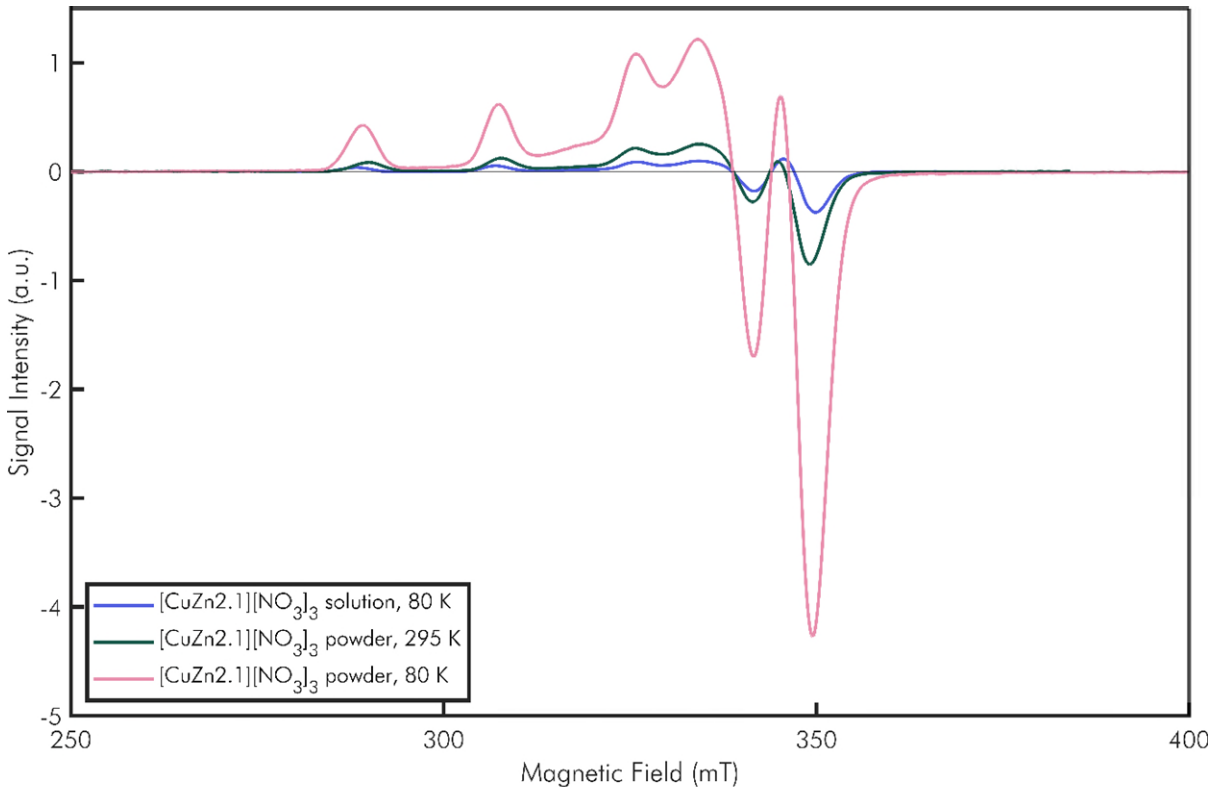

Figure 2.3:X-band cwEPR spectra of ***[CuZn2.1][NO$_3$]$_3$*** *in frozen 1:1 weight ratio water:glycerol at 80 K (blue), as a powder at 295 K (green), and as a powder at 80 K (pink).*

Electron paramagnetic resonance (EPR) spectroscopy was used to investigate the electronic structure of **[CuZn2.1][NO$_3$]$_3$**. Figure 2.3 shows the X-band EPR spectra of **[CuZn2.1][NO$_3$]$_3$** recorded as a powder sample and as a frozen solution in a 1:1 weight ratio water:glycerol solution. Spectra were recorded at 295 K and 80 K. The spectra are characteristic of a copper(II) complex, with the ^{64}Cu hyperfine visible.[2] The spectra indicate an axiality of the hyperfine and g-tensors. This would be consistent with the proposed structure. The spectra are qualitatively the same in both the solid state and solution. The powder sample is expected to be magnetically dilute, with a **[Zn$_2$2.1][NO$_3$]$_3$** matrix.

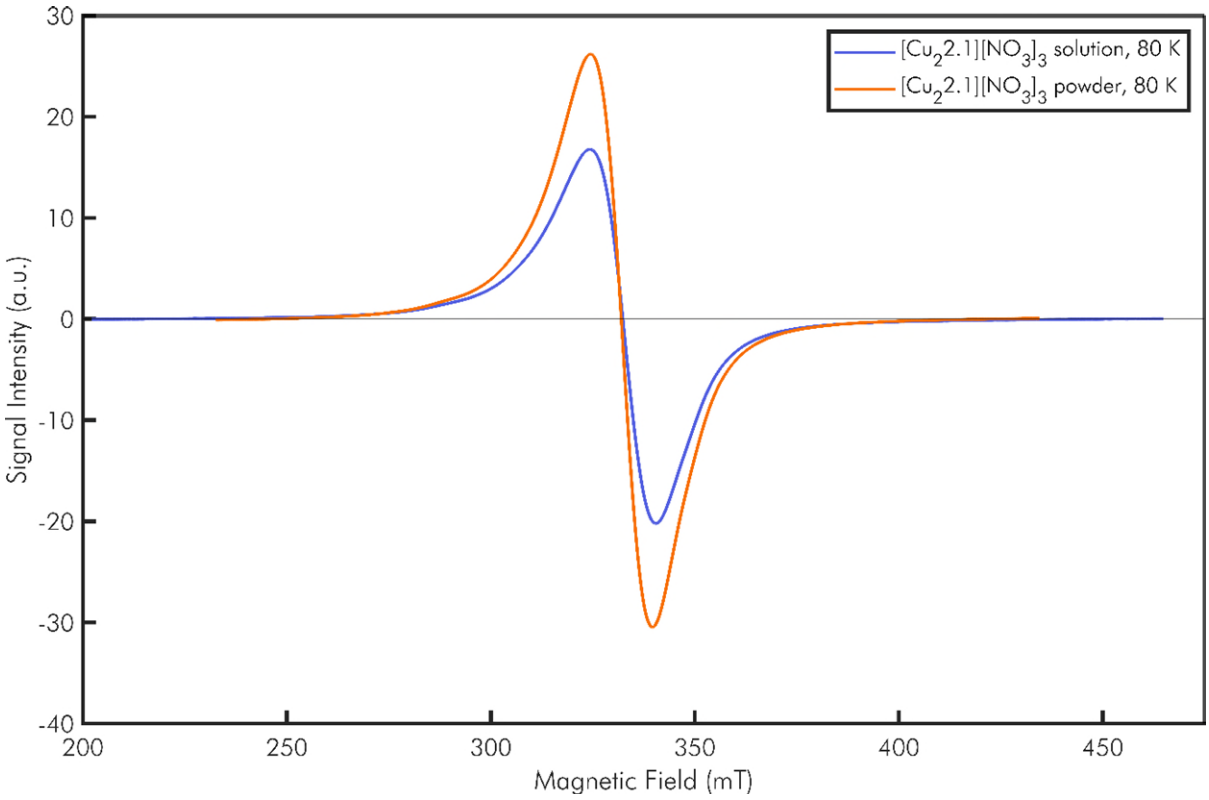

*Figure 2.4:X-band cwEPR spectra of **[Cu$_2$2.1][NO$_3$]$_3$** in a frozen 1:1 weight ratio water:glycerol mixture solution (blue), as a powder (orange) recorded at 80 K.*

Figure 2.4 shows the X-band EPR spectra of **[Cu$_2$2.1][NO$_3$]$_3$** as a powder and a frozen solution in a 1:1 weight ratio water:glycerol solution. Both spectra were recorded at 80 K. The spectra show a similar profile, a single broad resonance. There is no visible ^{64}Cu hyperfine, though this may be obscured by the wider linewidth. The spectra imply an isotropic g-tensor. The presence of an EPR signal implies that the two copper(II) ions do not couple to a singlet state. A half-field transition could not be observed, the spectrum is therefore only tentatively assigned as a triplet. The spectrum is the same in frozen solution and powder samples, implying the solution state structure is the same as the solid-state structure. For **[Cu$_2$2.1][NO$_3$]$_3$** the powder sample is not magnetically dilute.

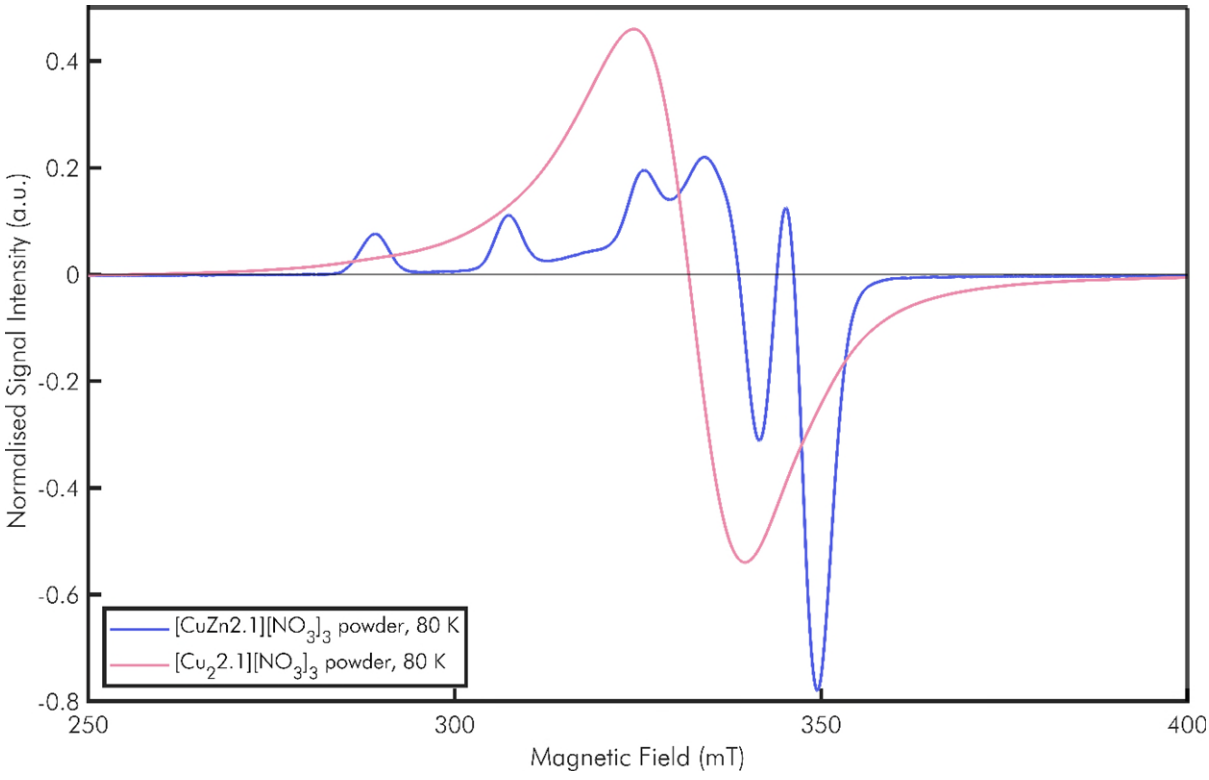

Figure 2.5: X-band cwEPR spectra of ***[CuZn2.1][NO$_3$]$_3$*** *(blue) and* ***[Cu$_2$2.1][NO$_3$]$_3$*** *(pink) as a powder recorded at 80 K.*

Figure 2.5 shows the normalised X-band EPR spectra of **[CuZn2.1][NO$_3$]$_3$** and **[Cu$_2$2.1][NO$_3$]$_3$** as powder samples at 80 K and 295 K (**[CuZn2.1][NO$_3$]$_3$** only). The spectra are clearly very different, the narrower linewidth and ^{64}Cu hyperfine of **[CuZn2.1][NO$_3$]$_3$** are not distinct from the single broad feature of **[Cu$_2$2.1][NO$_3$]$_3$**. One would expect that the **[Cu$_2$2.1][NO$_3$]$_3$** species would have a significantly altered electronic structure, with probable exchange coupling between the copper(II) centres.

2.4: COMPLEX CONFORMATION

The analogous lanthanide complexes (see chapter 3) are known to exhibit multiple confirmations, depending on the coordination mode of the phenol(ate) moiety. Scheme 2.5 illustrates the potential coordination confirmations for complexes of **2.1**. Where $M^1 = M^2$, conformers b and c are identical. In the case of **[CuZn2.1]$^{3+}$** these are distinct.

Supporting anions or solvents likely coordinate in all four conformations. The cyclen moiety cannot contort itself to support a tetrahedral geometry, thus, each metal centre likely has two more coordinating ligands to support an octahedral geometry. One of these may be the phenolate.

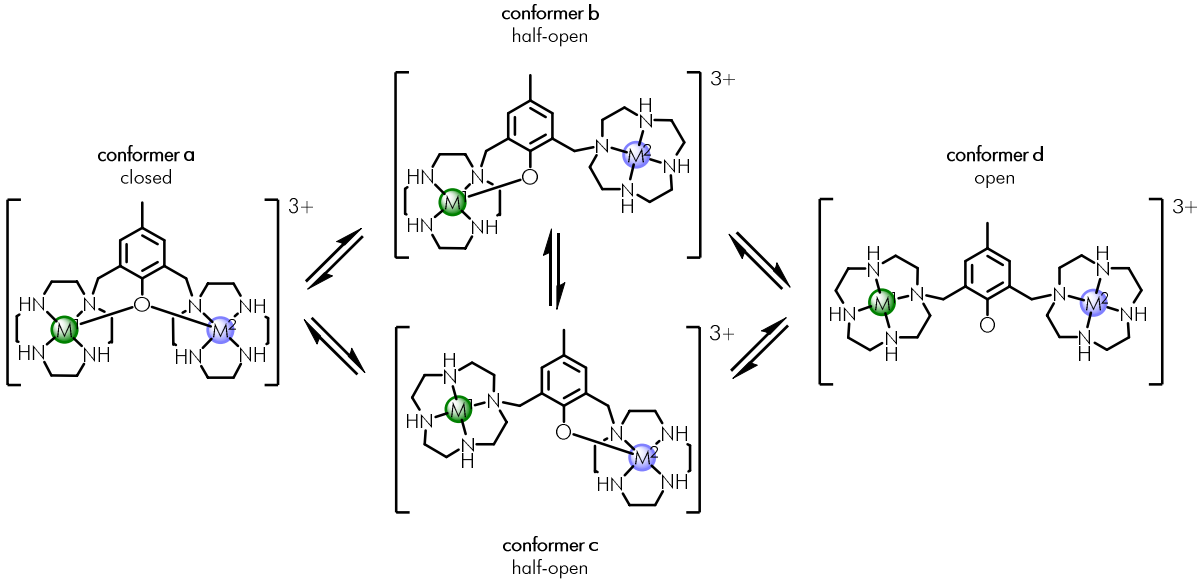

Scheme 2.5: possible conformations of $[M_2 2.1]^{3+}$

2.5: SYNTHESIS OF $[Cu_2 2.1][BF_4]_3$ AND $[CuZn2.1][BF_4]_3$

To further investigate whether supporting anions and coordinating solvents affect complex conformation, we prepared complexes with weakly coordinating counterions and using as weakly coordinating a solvent as possible. Tetrafluoroborate was chosen as the weakly coordinating anion for its low coordination ability. **$[Cu_2 2.1][BF_4]_3$** was prepared from copper(II) tetrafluoroborate in anhydrous acetonitrile. **$[CuZn2.1][BF_4]_3$** was prepared from a 1mol% mixture of copper(II) tetrafluoroborate and 99mol% zinc(II) tetrafluoroborate in anhydrous acetonitrile. Copper(II) tetrafluoroborate and zinc(II) tetrafluoroborate were dried under vacuum for several hours prior to use. Anhydrous acetonitrile was used as the solvent, less coordinating (and less polar) solvents proved incapable of dissolving **H2.1**. Standard Schlenk techniques were employed to exclude water, which may be affecting complex confirmation. Prepared

complexes were stored in a nitrogen glovebox. Solution phase measurements were carried out in anhydrous acetonitrile.

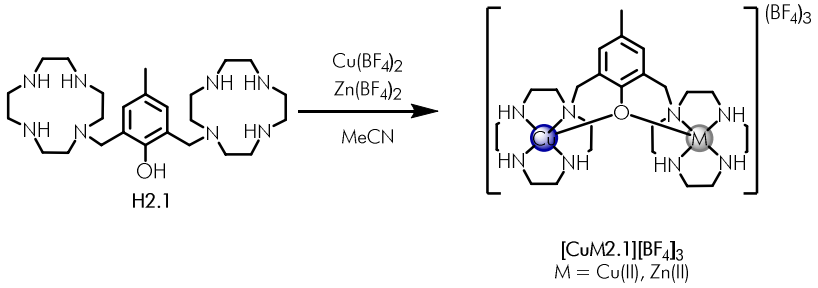

Scheme 2.6: Synthetic procedure for the preparation of ***[Cu$_2$2.1][BF$_4$]$_3$*** *and* ***[CuZn2.1][BF$_4$]$_3$***

2.6: ELECTRON PARAMAGNETIC RESONANCE (EPR) SPECTROSCOPY OF [Cu$_2$2.1][BF$_4$]$_3$ AND [CuZn2.1][BF$_4$]$_3$

Figure 2.6 shows the X-band EPR spectra of **[CuZn2.1][BF$_4$]$_3$** in powder form at 295 K and 80 K. A poor signal-to-noise ratio is observed even at 80 K. The spectra show an axial g-tensor with the ^{64}Cu hyperfine visible. Attempts to record a solution phase spectrum in acetonitrile were unsuccessful, the signal could not be reasonably differentiated from noise.

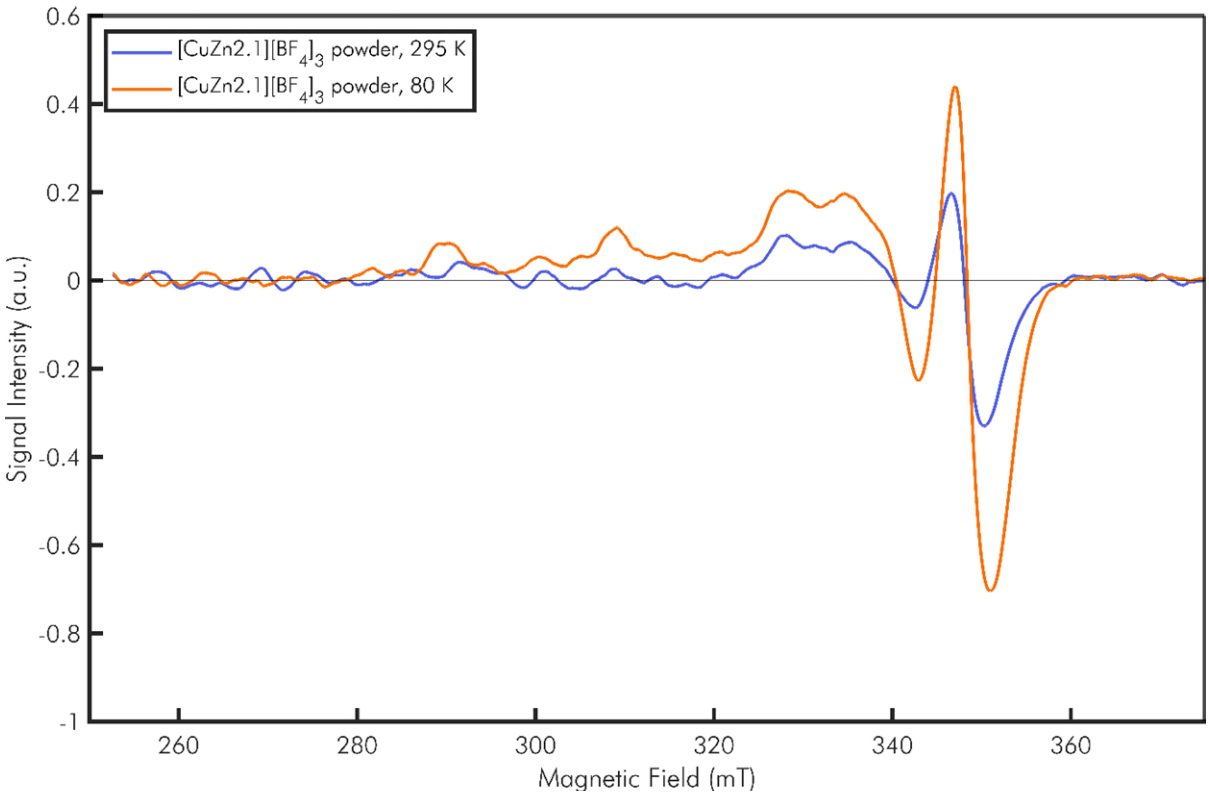

Figure 2.6: X-band cwEPR spectra of ***[CuZn2.1][BF$_4$]$_3$*** *in powder form at 295 K (blue) and 80 K (orange)*

Figure 2.7 shows the normalised X-band cwEPR spectra of **[Cu$_2$2.1][BF$_4$]$_3$** as an acetonitrile solution, at 100 K and 273 K, and as a powder at 295 K. The solution phase spectrum recorded at 100 K and the powder spectrum recorded at 295 K are qualitatively the same, with the ^{64}Cu hyperfine visible in both spectra. Both spectra imply an axial g-tensor. The solution phase spectrum recorded at 273 K, with far worse signal-to-noise ratio, shows a different spectral shape, with sharper features visible and no clear ^{64}Cu hyperfine. It's unclear whether this is a genuine temperature difference, indicative of a coupling interaction at low temperature, or a function of the poor signal-to-noise ratio caused by the higher temperature.

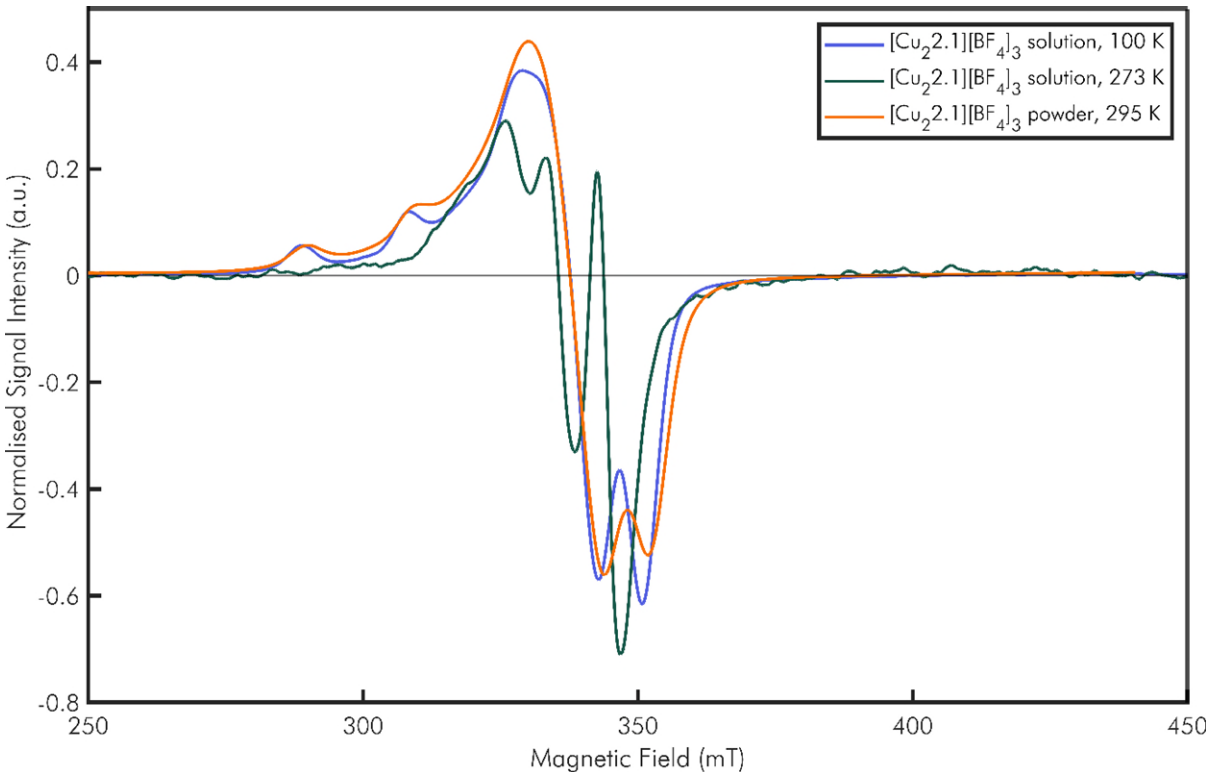

Figure 2.7: X-band cwEPR spectra of ***[Cu2.1][BF4]3*** *as an acetonitrile solution, at 100 K (blue) and 273 K (green), and as a powder at 295 K (orange).*

Figure 2.8 shows the normalised X-band EPR spectra of **[Cu2.1][BF4]3** in powder form at 295 K and **[CuZn2.1][BF4]3** in powder form at 295 K and at 80 K. Both **[Cu2.1][BF4]3** and **[CuZn2.1][BF4]3** show the ^{64}Cu hyperfine interaction. The signal-to-noise ratio of **[CuZn2.1][BF4]3** is worse than for **[Cu2.1][BF4]3**, which is expected as the paramagnetic **[CuZn2.1][BF4]3** is only 1% of the sample.

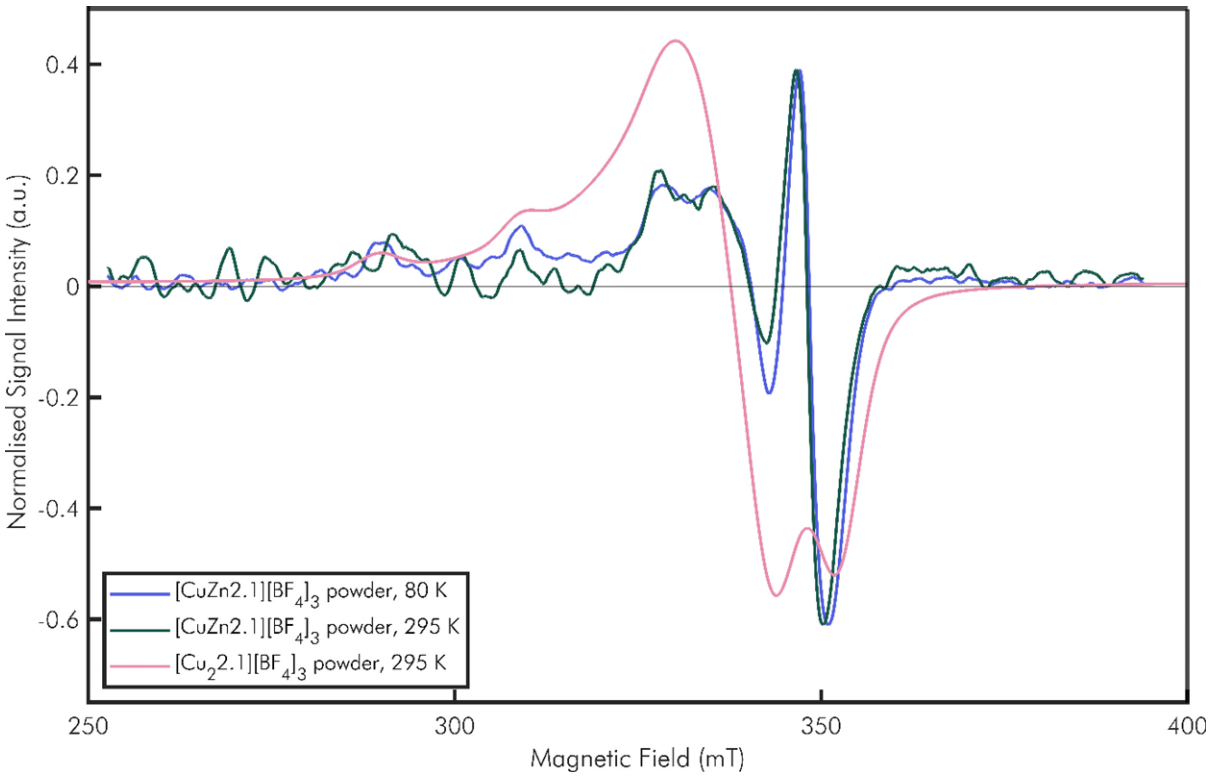

Figure 2.8: X-band cwEPR spectra of ***[Cu₂2.1][BF₄]₃*** *in powder form at 295 K (pink) and* ***[CuZn2.1][BF₄]₃*** *in powder form at 295 K (green) and at 80 K (blue).*

Figure 2.9 shows the X-band EPR spectra of $[Cu_2 2.1]^{3+}$ with tetrafluoroborate and nitrate counterions in acetonitrile and a 1:1weight ratio water:glycerol mixture respectively. As these are frozen solution measurements, it is hoped they are magnetically dilute and intermolecular interactions are effectively zero. As discussed in section 2.4 a number of confirmations are accessible by the $[Cu_2 2.1]^{3+}$ cation with supporting counterion or ligand coordination. Whereas the spectrum for $[Cu_2 2.1][NO_3]_3$ is very broad and does not feature observable ^{64}Cu hyperfine interaction, the spectrum for $[Cu_2 2.1][BF_4]_3$ has narrower line widths and the ^{64}Cu hyperfine interaction is observable. This suggests the two complexes do have different electronic structures in solution. $[Cu_2 2.1][BF_4]_3$ is similar to $[CuZn2.1][BF_4]_3$ suggesting any exchange coupling is weak. Attempts to locate the half-field transition were unsuccessful, however, as a formally forbidden transition it may be hidden in experimental noise. $[Cu_2 2.1][NO_3]_3$, significantly broadened line width, suggests a different ground state. It is possible that $[Cu_2 2.1][NO_3]_3$ has

stronger exchange coupling to a triplet ground state. Neither **[Cu$_2$2.1][NO$_3$]$_3$** nor **[Cu$_2$2.1][BF$_4$]$_3$** could be simulated satisfactorily in EasySpin.

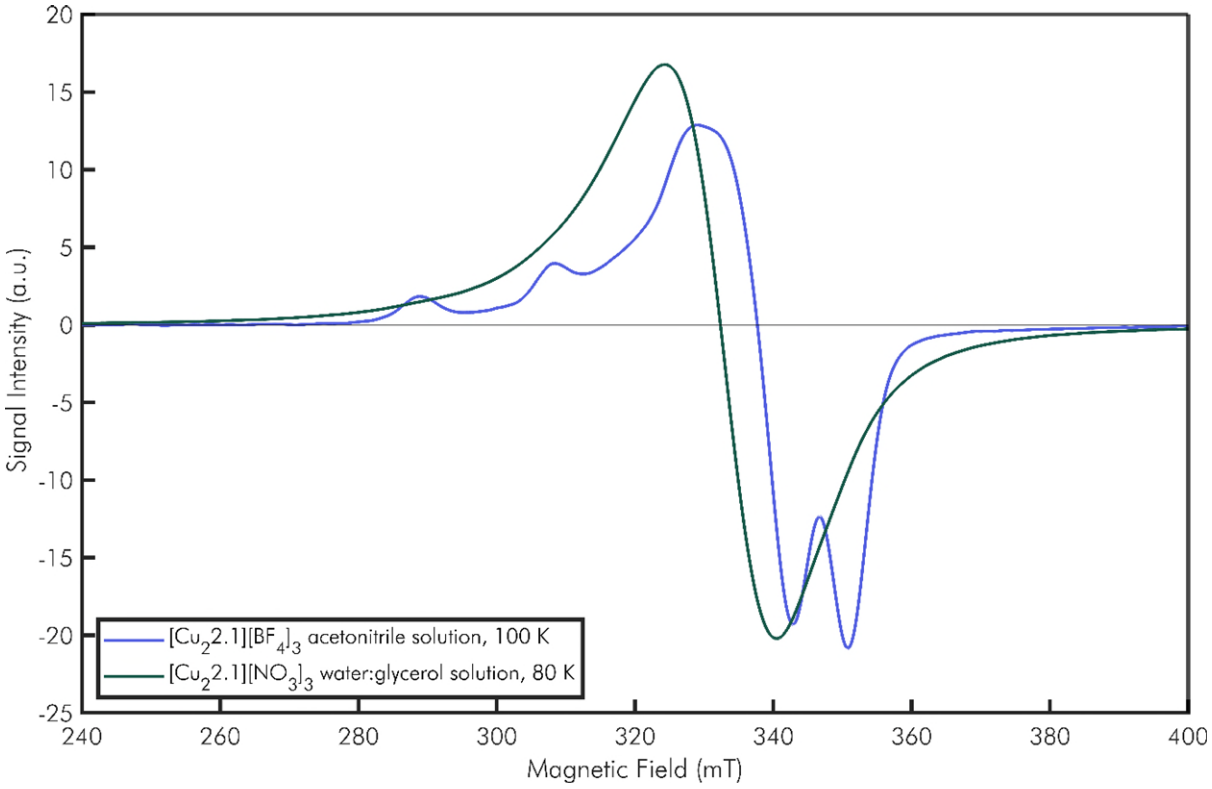

*Figure 2.9: X-band cwEPR spectra of **[Cu$_2$2.1][NO$_3$]$_3$** in 1:1 weight ratio water:glycerol solution at 80 K (green) and **[Cu$_2$2.1][BF$_4$]$_3$** in acetonitrile solution at 100 K (blue)*

Figure 2.10 shows the X-band EPR spectra of **[CuZn2.1]$^{3+}$** with tetrafluoroborate and nitrate counterions in powder forms. These measurements are taken on powder samples to maximise signal-to-noise ratio. These samples are magnetically dilute, with the **[CuZn2.1]$^{3+}$** complex diluted into a **[Zn$_2$2.1]$^{3+}$** complex, due to the synthesis method use (see section 2.2). The spectra are qualitatively similar, both showing the ^{64}Cu hyperfine interaction. The g-tensor is slightly shifted in the two complexes. This suggests for **[CuZn2.1]$^{3+}$** the counterion has a minimal impact.

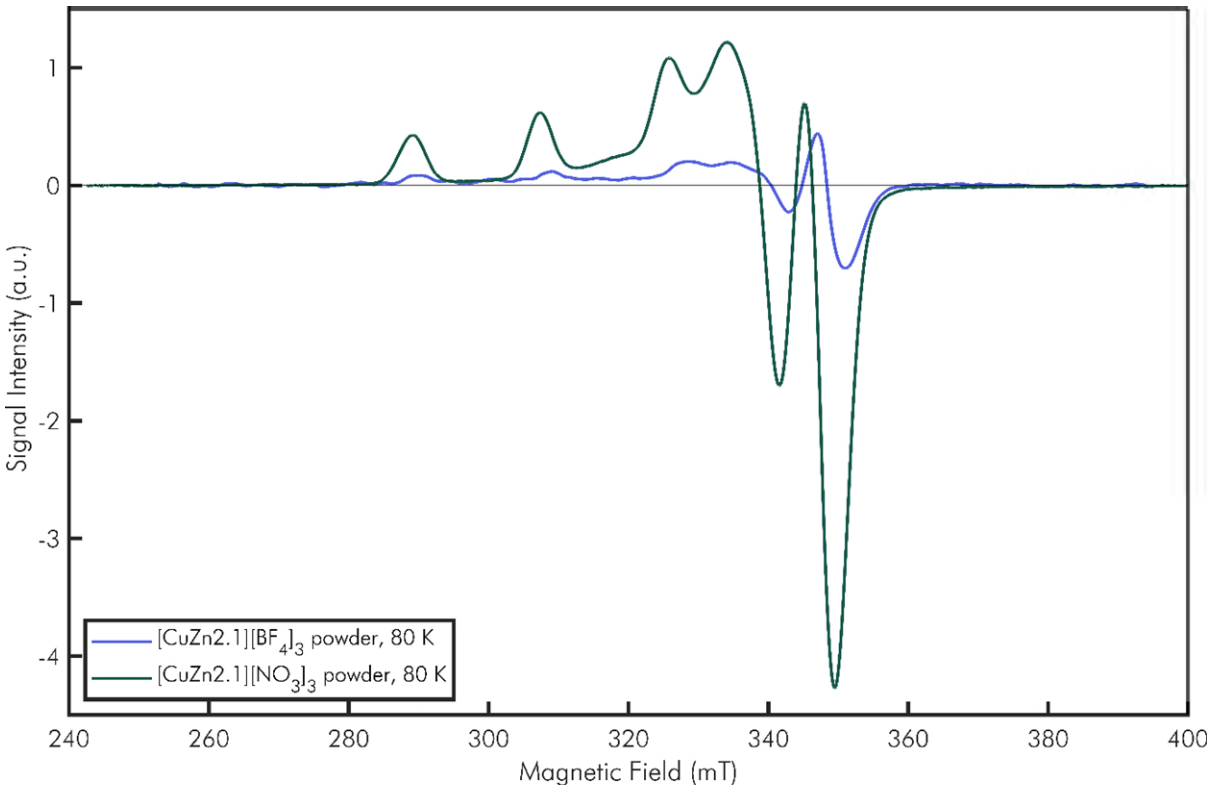

Figure 2.10: X-band cwEPR spectra of ***[CuZn2.1][NO$_3$]$_3$*** *in powder form (green) and* ***[CuZn2.1][BF$_4$]$_3$*** *in powder form (blue), both recorded at 80 K*

Table 2.1 shows the spectral parameters of the X-band EPR spectra of **[CuZn2.1][NO$_3$]$_3$** and **[CuZn2.1][BF$_4$]$_3$** obtained by least squares fitting. Figure 2.11 shows a comparison of fitted data to experimental spectrum. The least-squares fitting was conducted by Filip Ivanovic using the EasySpin package for MATLAB.[9] A substantial *HStrain* parameter was required to fit these data. *HStrain* is a parameter passed into EasySpin to account for unresolved hyperfine interactions, and the linewidth changes that result from these unresolved interactions. The g-tensor is axial for both complexes and very similar. The hyperfine tensor, A, is axial for both complexes and very similar between the two. These data support a similar local coordination environment for the complexes. Thus, it is unlikely that solvent and counterion effects impact copper(II)-zinc(II) complexes of **H2.1**.

Table 2.1: spectral parameters of ***[CuZn2.1][NO$_3$]$_3$*** *and* ***[CuZn2.1][BF$_4$]$_3$*** *obtained by least squares fitting*

	[CuZn2.1][NO$_3$]$_3$	**[CuZn2.1][BF$_4$]$_3$**
g	[2.0485 2.20]	[2.048 2.1875]
A (MHz)	[50 550]	[45 570]
HStrain (MHz)	[175 147.5]	[150 120]

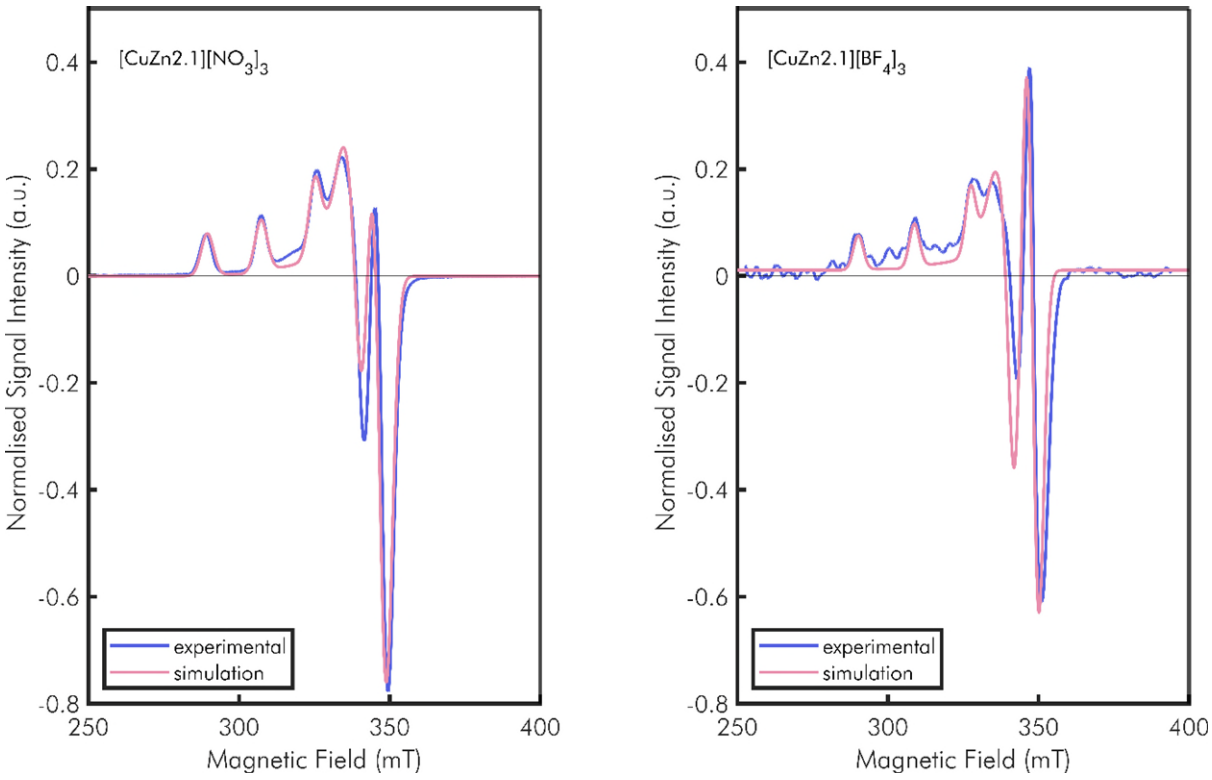

Figure 2.11: Experimental (blue) spectrum and EasySpin simulation (pink) for: left: ***[CuZn2.1][NO$_3$]$_3$*** *right:* ***[CuZn2.1][BF$_4$]$_3$****. Both simulations using the parameters listed in Table 2.1. Simulations and fitting were conducted by Filip Ivanovic.*

Despite considerable effort to fit the experimentally measured spectra of **$[Cu_2$2.1$][NO_3]_3$** and **$[Cu_2$2.1$][BF_4]$** to a variety of spin-systems with different degrees of coupling, no successful fits could be obtained.

2.7: CONCLUSIONS

We prepared dicopper(II) and copper(II)-zinc(II) complexes of a bis-macrocyclic ligand, **H2.1**, with nitrate and tetrafluoroborate counterions. EPR spectra of **$[CuZn$2.1$][NO_3]_3$** and **$[CuZn$2.1$][BF_4]_3$** are characteristic of a copper(II) complex, with well-resolved ^{64}Cu hyperfine interactions. The spectra can be simulated, and reveal very similar g- and hyperfine tensors. Suggesting that for **$[CuZn$2.1$]^{3+}$** counterion effects are insignificant. EPR spectra of **$[Cu_2$2.1$][NO_3]_3$** and **$[Cu_2$2.1$][BF_4]_3$** show significant differences suggesting counterion effects are more pronounced. **$[Cu_2$2.1$][BF_4]_3$** resembles a mono-copper(II), suggesting only weak exchange coupling. **$[Cu_2$2.1$][NO_3]_3$** has a spectral profile resembling a strongly exchange-coupled system. Neither system could be successfully simulated using EasySpin. These data suggest that the counterion, or solvent coordination may influence through-bond communication pathways. Dicopper(II) complexes appear to be a poor model for the magnetic properties of bis-lanthanide(III) complexes; the system was not acting as the simple model for **[Na][LnLn'3.1]** we intended to develop so we focused our efforts on lanthanide-containing complexes.

2.8: REFERENCES

1. S. Richert, I. Kuprov, M. D. Peeks, E. A. Suturina, J. Cremers, H. L. Anderson and C. R. Timmel, *Phys. Chem. Chem. Phys.,* 2017, 19, 16057-16061.
2. S. Richert, J. Cremers, I. Kuprov, M. D. Peeks, H. L. Anderson and C. R. Timmel, *Nat. Commun.*, 2017, 8, 14842.
3. E. J. Little, J. Mrozek, C. J. Rogers, J. Liu, E. J. L. McInnes, A. M. Bowen, A. Ardavan and R. E. P. Winpenny, *Nat. Commun.*, 2023, 14, 7029.
4. M. Kodera, Y. Kadoya, K. Aso, K. Fukui, A. Nomura, Y. Hitomi and H. Kitagishi*, Bull. Chem. Soc. Jpn*., 2019, 92, 739-747.
5. Y. Kadoya, K. Fukui, M. Hata, R. Miyano, Y. Hitomi, S. Yanagisawa, M. Kubo, M. Kodera, *Inorg. Chem*. 2019, 58, 14294–14298
6. V. Srivastava, A. Tandon and S. Ray, *Synth. Commun*., 1992, 22, 2703-2710
7. S. J. A. Pope, A. M. Kenwright, S. L. Heath and S. Faulkner, *Chem. Commun*., 2003, 1550-1551
8. J. Massue, S. E. Plush, C. S. Bonnet, D. A. Moore and T. Gunnlaugsson, *Tet. Lett.*, 2007, 48, 8052-8055.
9. S. Stoll and A. Schweiger, *J. Magn. Reson*., 2006, 178, 42-55.

3. A STATISTICAL APPROACH TO SYMMETRIC MULTIMETALLIC LANTHANIDE COMPLEXES AND MODULATING THE INTERMETALLIC COMMUNICATION VIA BRIDGING PHENOLATE COORDINATION

As discussed in section 1.12, access to solution-stable multimetallic lanthanide complexes requires the use of kinetically inert chelators. These chelators must have rigid, preorganised macrocyclic chelators with 7 or 8 donors, fulfilled by substituted DO3A derivatives with an additional donor.[1]

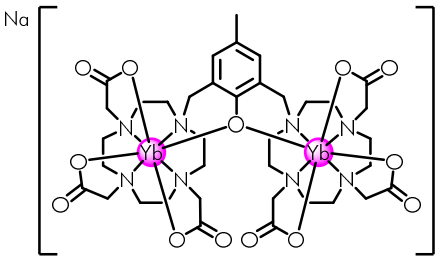

Na[$Yb_2$3.1]

Figure 3.1: Chemical structure of ***[Na][$Yb_2$3.1]***

[Na][$Yb_2$3.1], (Figure 3.1) was reported by Pope et al. for the preparation of bis-ytterbium(III) complexes. **[Na][$Yb_2$3.1]** was found to have two different emissive centres, implying non-symmetry in the complex. This was determined by the time-resolved ytterbium(III) emission spectrum fitting to a bi-exponential function.[2]

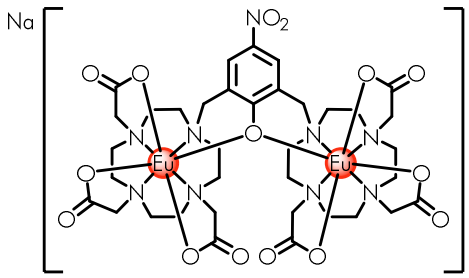

Na[$Eu_2$3.2]

Figure 3.2: Chemical structure of ***[Na][$Eu_2$3.2]***

Blackburn et. al. reported a 4-nitrophenol analogue of **3.2** (Figure 3.2). The authors found a pH dependence of the emission spectrum of **[Na][$Eu_2$3.2]**. This was attributed to conformational changes resulting from the phenol-phenolate equilibrium. This equilibrium was not observed for a monometallic analogue, implying both europium(III) ions are bridged by the coordinated phenolate.[3]

We sought to further investigate the effects of through-bond communication pathways by covalently blocking phenolate coordination with an acetyl group. This ensures the complex has only through-space intermetallic communication pathways. *In situ* cleavage of the acetyl ester with sodium carbonate in water opens up phenolate coordination and through-bond intermetallic coordination pathways (Figure 3.3).

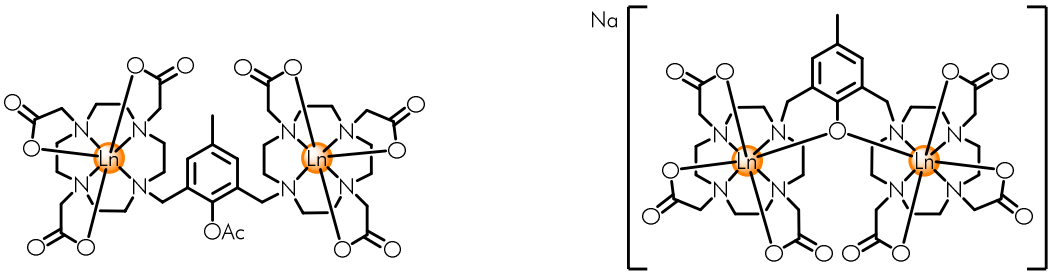

$Ln_2$3.3
Ln = Eu(III), Tb(III)

[Na][$Ln_2$3.1]
Ln = Eu(III), Tb(III)

Figure 3.3: Chemical structures of ***$Ln_2$2.5*** *and* ***[Na][$Ln_2$2.6]***

We sought to utilise the symmetry of **3.1** to prepare multimetallic complexes through a mono-metallic intermediate, **H_4Ln3.1** with further treatment with a second lanthanide(III) ion affording **[Na][LnLn'3.1]**. Purification of **H_4Ln3.1** from the resultant mixture of **$H_7$3.1**, **H_4Ln3.1,** and **[Na][$Ln_2$3.1]** requires high-performance liquid chromatography (HPLC).

3.1: SYNTHESIS OF LIGANDS $H_6$3.3 AND $H_7$3.1

$H_7$3.1 was previously reported by Pope et al.[2] Issues with the preparation of the dicholomethyl intermediate **2.6** led us to develop a synthesis employing an acetyl protecting group for the phenol motif, as discussed in section 2.2. **2.4** was prepared in 2-steps from the commercially available 2,6-bis(hydroxymethyl)-4-methyl phenol (see section 2.2).[4]

Treatment of 1,4,7,10-tetraazacyclododecane (cyclen) with *tert*-butyl bromoacetate in acetonitrile with sodium hydrogen carbonate afforded **3.4** in 39% yield, in accordance with literature procedures.[5] **3.4** allows access to a protected DO3A chelator with a fourth amine available for substitution reactions to allow functionalisation.

Treatment of **3.4** with **2.4** in acetonitrile with sodium carbonate at room temperature for 72 hours was found to afford **3.5**. Purification via flash chromatography afforded the target compound in 29% yield. The acetyl ester is stable to the reaction and purification conditions.

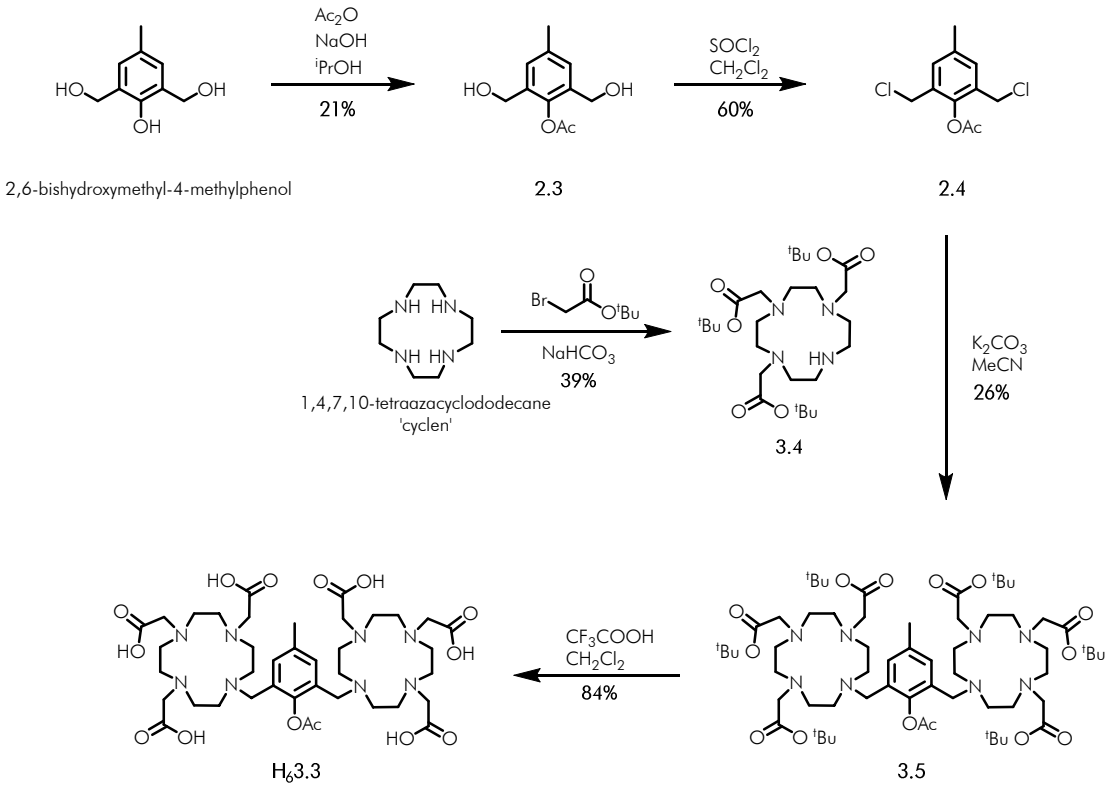

Scheme 3.1: Synthetic route to ***H₆3.3***

Treatment of **3.5** with a 1:1 volume ratio of trifluoroacetic acid and dichloromethane selectively hydrolyses the *tert*-butyl esters, leaving the acetyl ester intact. Purification via thrice repeated recrystallisation from concentrated methanol solution with diethyl ether afforded pure **$H_6$3.3** in 84% yield.

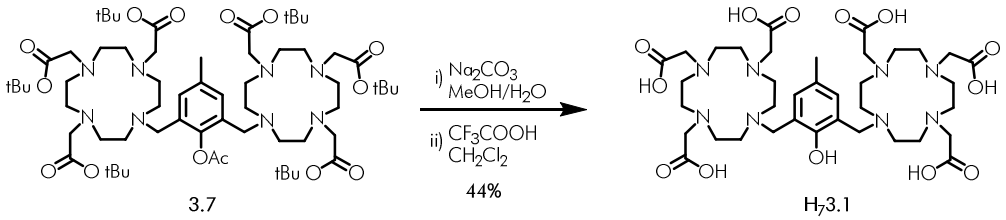

3.7 $H_7$3.1

Scheme 3.2: Preparation of ***$H_7$3.1*** *from* ***3.5***

$H_7$3.1 was prepared from **3.7** via sequential deprotections. The acetyl ester was hydrolysed by treatment of **3.7** with sodium carbonate. The tert-butyl esters were hydrolysed by treatment with trifluoroacetic acid in dichloromethane. The two-step procedure afforded **$H_7$3.1** in 44% yield.

3.2: SYNTHESIS AND CHARACTERISATION OF $Ln_2$3.3

To preserve the acetyl ester **$Eu_2$3.3** and **$Tb_2$3.3** were prepared by treatment of **$H_6$3.3** with the parent lanthanide(III) triflate salt in acetonitrile. After stirring at room temperature for 21 hours the resultant solution was evaporated to dryness under flowing nitrogen. The complexes were purified from residual **$H_6$3.3** and triflate salts by dialysis (FLOAT-A-LYZER G2 500 - 1000D CE) in distilled water. After membrane activation, the chamber was partially filled with an aqueous solution of **Ln3.3**. Immersion of the chamber in a large quantity distilled water (typically 2 L) allowed for purification. The external water was changed three times per day for three days. **$Eu_2$3.3** was afforded in 56% yield. **$Tb_2$3.3** was afforded in 37% yield.

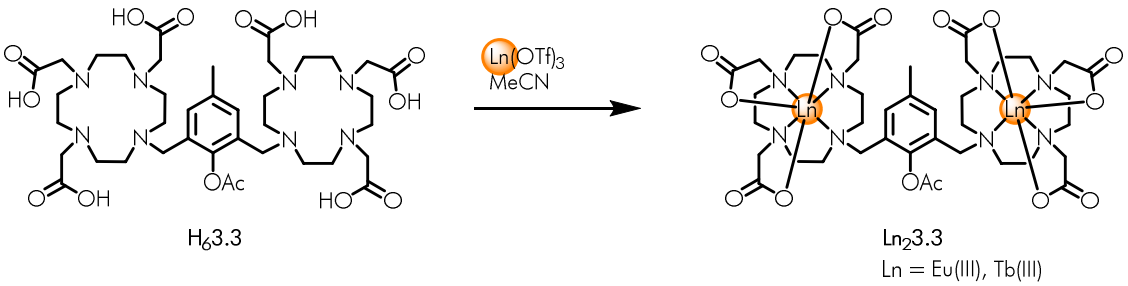

Scheme 3.3: Synthetic scheme for preparation of ***Eu$_2$3.3*** *and* ***Tb$_2$3.3***

Figure 3.4 shows the ^{1}H NMR spectra of **Tb$_2$3.3** in D_2O and CD_3OD. Only very broad resonances are observed in D_2O. In CD_3OD sharper resonances are observed at 113 ppm. These data support the proposed 7-coordinate complex structure.[3,6,7]

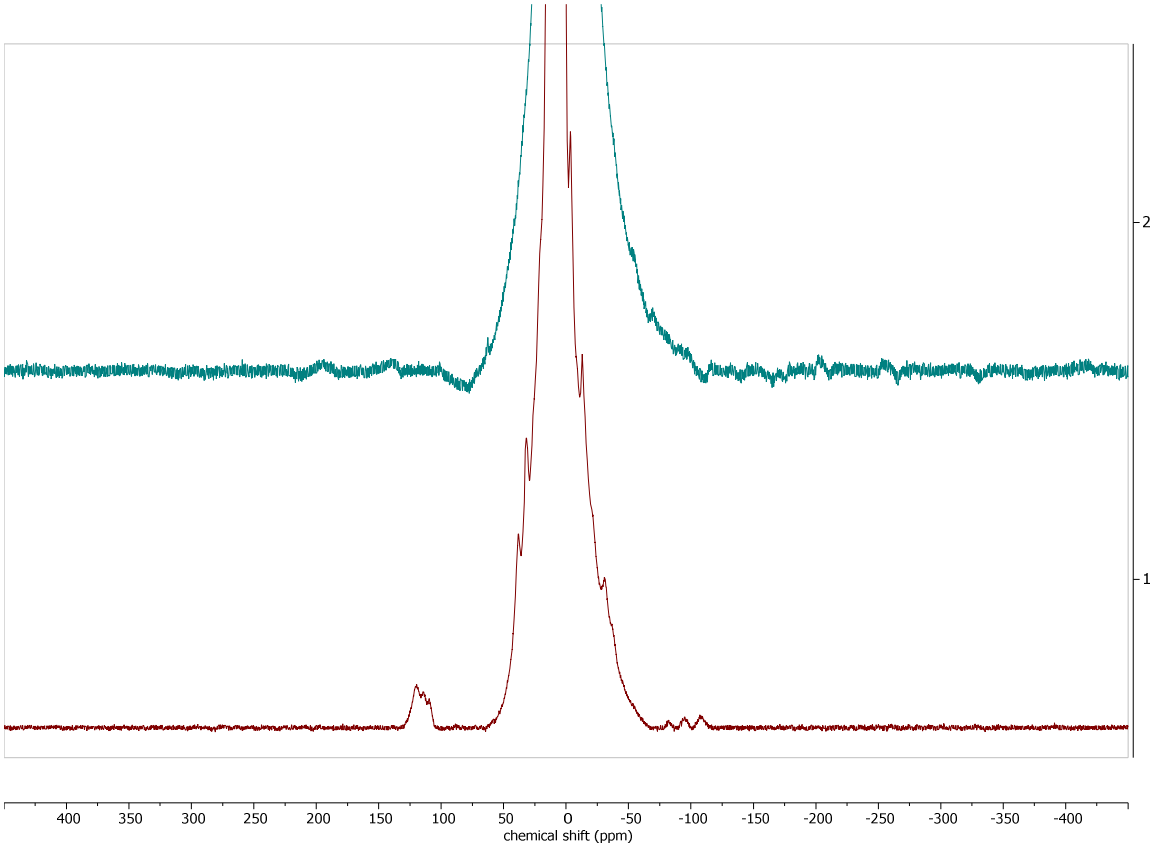

Figure 3.4: ^{1}H NMR spectrum of ***Tb$_2$3.3*** *recorded at 400 MHz. Top: Recorded in D_2O. Bottom: Recorded in CD_3OD*

Figure 3.5 shows the ^{1}H NMR spectrum of **$Eu_2$3.3** in D_2O and CD_3OD. The resonances sharpen in CD_3OD compared to D_2O. These data support the proposed 7-coordinate complex structure.[3,6,7] The ^{1}H NMR spectra of **$Eu_2$3.3** and **$Tb_2$3.3** show different rates of exchange, compared to the NMR timescale, with fast exchange in methanol and an intermediate rate of exchange in water.[3,6,7]

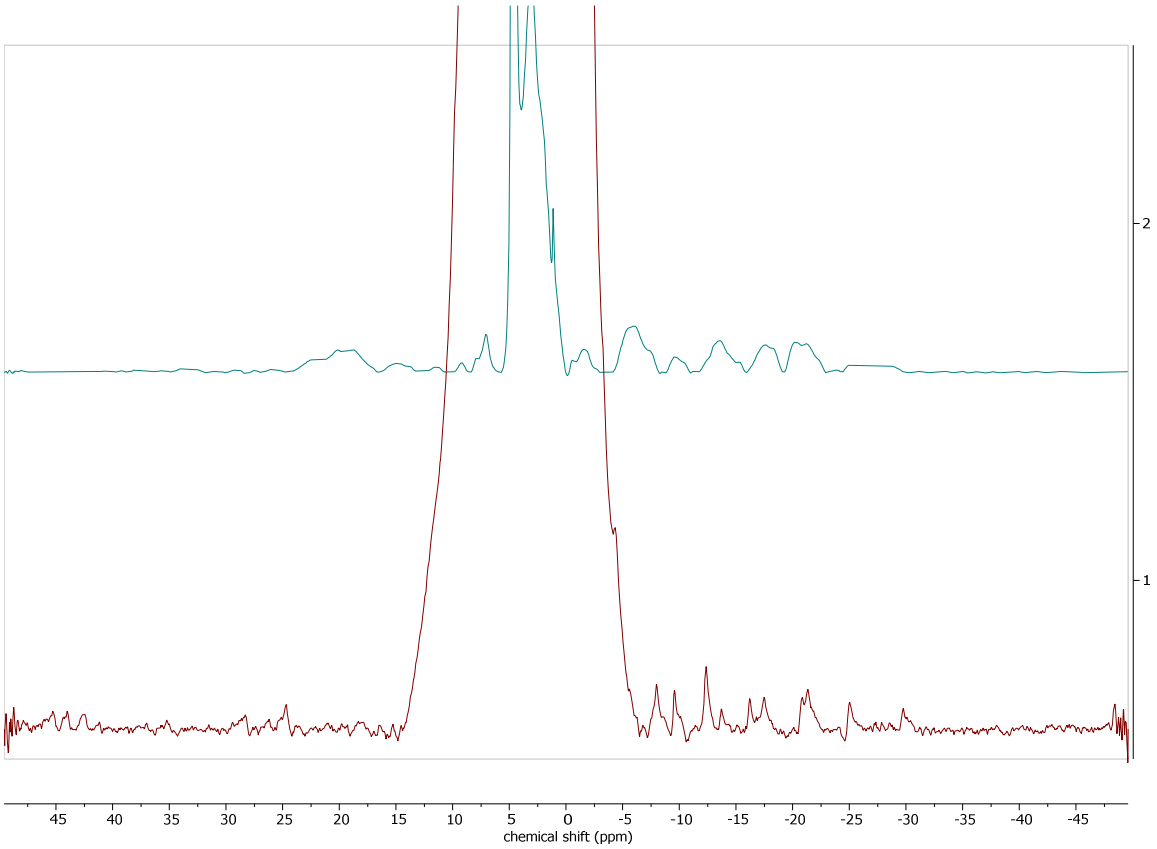

*Figure 3.5: ^{1}H NMR spectrum of **$Eu_2$3.3** recorded at 400 MHz Top: Recorded in D_2O. Bottom: Recorded in CD_3OD*

[Na][Eu$_2$3.1] and **[Na][Tb$_2$3.1]** were prepared from **H$_7$3.1** in a 1:1 volume ratio of water:methanol and the parent lanthanide(III) triflate. After heating for 16 hours, sodium hydroxide was added. Excess lanthanide(III) salt was expected to form insoluble lanthanide(III) hydroxide. After heating for a further 24 hours, the mixture was filtered to remove insoluble precipitate and the filtrate evaporated to dryness. The complexes were purified from residual **H$_7$3.1** and triflate salts by dialysis (FLOAT-A-LYZER G2 500 - 1000D CE), with four water changes over seven days. **[Na][Eu$_2$3.1]** was prepared in 18% yield. **[Na][Tb$_2$3.1]** was prepared in 24% yield.

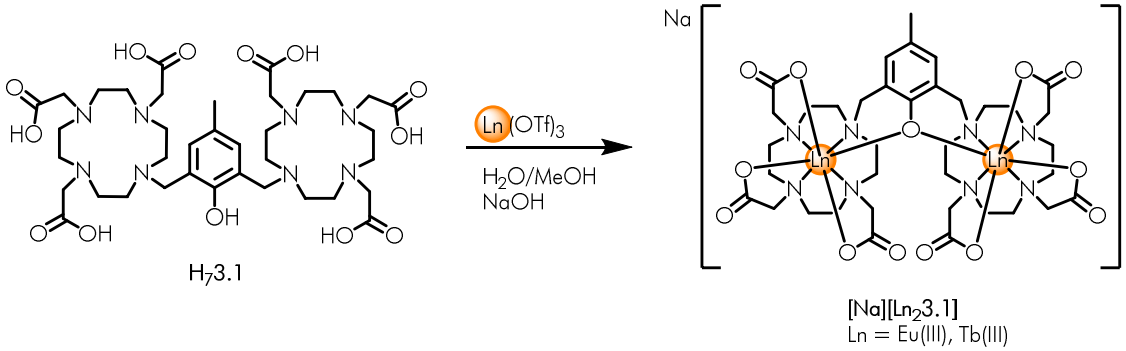

*Scheme 3.4: Preparation of **[Na][Ln$_2$3.1]** from **H$_7$3.1***

[Na][Eu$_2$3.1] was found as the [**Eu$_2$3.1**]$^-$ ion by electrospray ionisation mass spectrometry. **[Na][Tb$_2$3.1]** was found as the [**Tb$_2$3.1**]$^-$ ion by electrospray ionisation mass spectrometry. These data confirm the structural identity of the complexes.

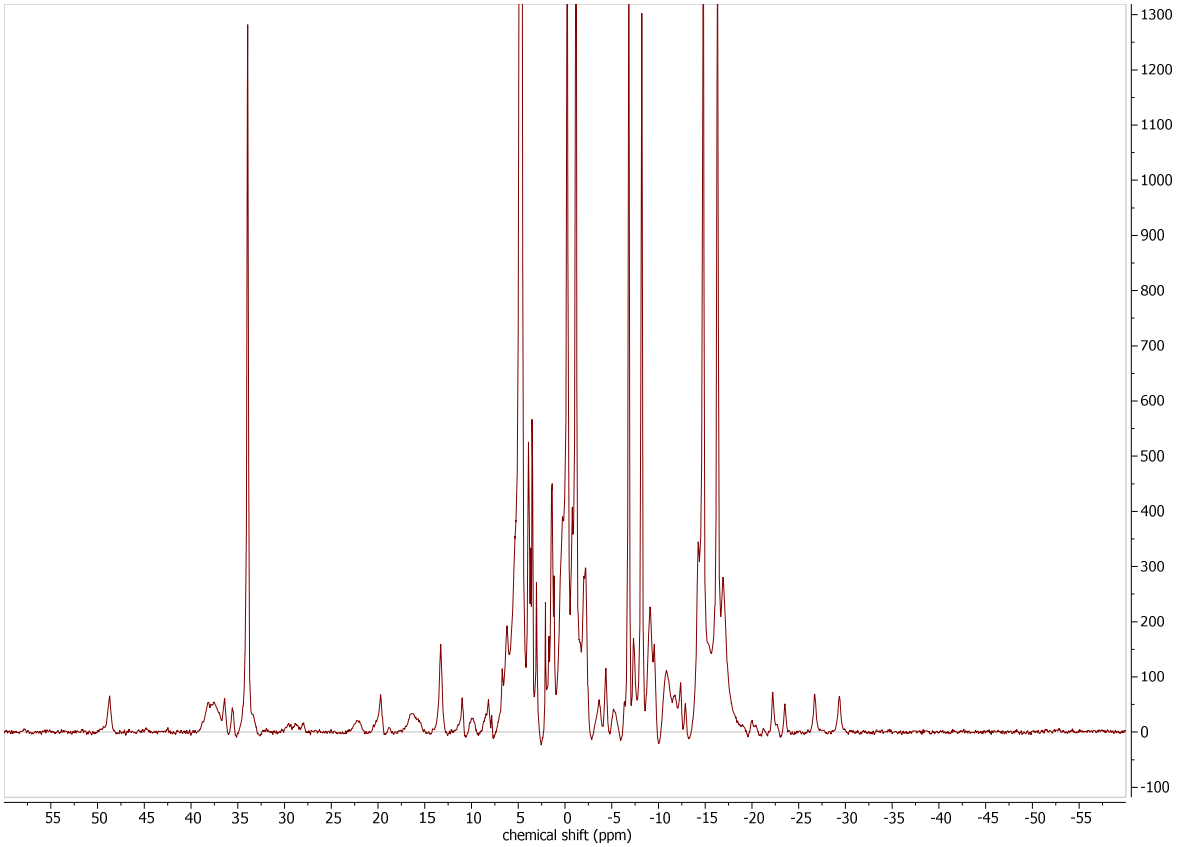

*Figure 3.6: ^{1}H NMR spectrum of **[Na][Eu$_2$3.1]** recorded at 400 MHz in D_2O.*

Figure 3.6 shows the ^{1}H NMR spectrum of **[Na][Eu$_2$3.1]** recorded at 400 MHz in D_2O. The sharp resonances suggest minimal interconversion between diastereomers in solution. The sharp resonance at 34 ppm is assigned to **[EuDOTA]$^-$** impurity, which persisted through purification.

Figure 3.7 shows the ^{1}H NMR spectrum of **[Na][Tb$_2$3.1]** recorded at 400 MHz in D_2O. The sharp resonances suggest minimal interconversion between isomers in solution. Both **[Na][Tb$_2$3.1]** and **[Na][Eu$_2$3.1]** have significantly sharper resonances than **Eu$_2$3.3** and **Tb$_2$3.3**. Suggesting a suppression of diastereomer interconversion with the bridging phenolate. The sharp resonance at 402 ppm is assigned to **[TbDOTA]$^-$** impurity, which persisted through purification.

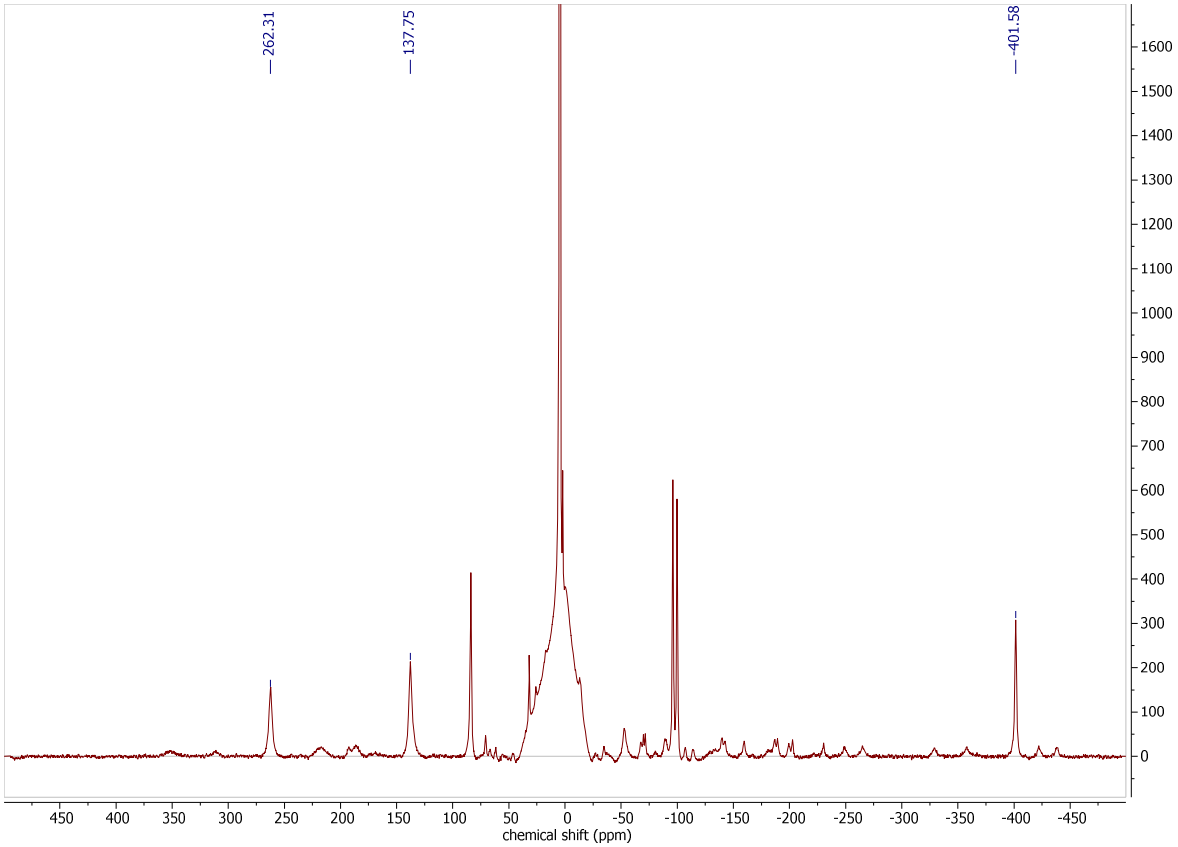

Figure 3.7 ^{1}H NMR spectrum of ***[Na][Tb$_2$3.1]*** *recorded at 400 MHz in D_2O.*

3.4: HYDROLYSIS OF PHENYL ACETATE ESTER OF Ln$_2$2.5 AND MANIPULATION OF INTERMETALLIC COMMUNICATION

We sought to investigate the manipulation of intermetallic communication in binuclear lanthanide(III) complexes with a molecular design in which through-bond communication can be switched-on. Hydrolysis of the acetyl ester of **Ln$_2$3.3**, with sodium carbonate in water, is expected to yield **[Na][Ln$_2$3.1]** in which the bridging phenolate affords a route for through-bond intermetallic communication, as shown in Scheme 3.5.

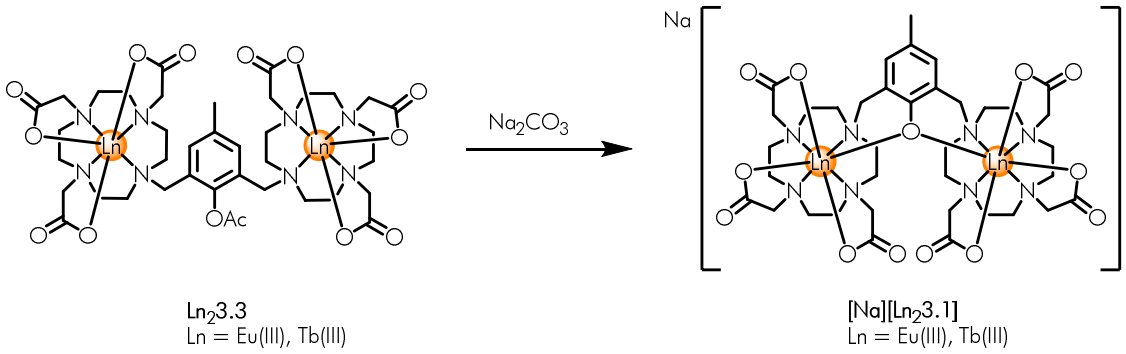

Scheme 3.5: Synthetic route to in situ preparation of ***[Na][Ln₂3.3]*** *from* ***Ln₂3.3***

Electrospray ionisation (ESI) mass spectrometry measurements on aqueous solutions of **[Na][Eu₂3.1]** formed *in situ* found the $[\mathbf{Eu_2 3.1}+Na+H]^+$ adduct.

3.5: LUMINESCENCE SPECTROSCOPY OF [Na][Ln₂3.1] AND [Na][Ln₂3.3]

Figure 3.8 shows the emission spectra of **Eu₂3.3** and **[Na][Eu₂3.1]. [Na][Eu₂3.1]** was prepared *in situ* by treatment of **Eu₂3.3** with 5 equivalents of sodium carbonate. Both complexes were recorded as 10^{-4} M solutions in H_2O. Both complexes were excited via the phenyl acetate/phenolate chromophore at λ_{ex} = 270 nm. A 400 nm high pass filter was used for both samples to remove any scattered excitation light. Both complexes display characteristic europium(III) centred emission with the $^5D_0 \rightarrow {}^7F_0$ (580 nm), $^5D_0 \rightarrow {}^7F_1$ (591 nm), $^5D_0 \rightarrow {}^7F_2$ (617 nm), $^5D_0 \rightarrow {}^7F_3$ (651 nm), and $^5D_0 \rightarrow {}^7F_4$ (692 nm) transitions observed. **[Na][Eu₂3.1]** shows an increase in emission intensity compared to **Eu₂3.3**. This is attributed to the direct coordination of the chromophore to the europium(III) centre and the resulting more efficient energy transfer, via a Dexter exchange mechanism.

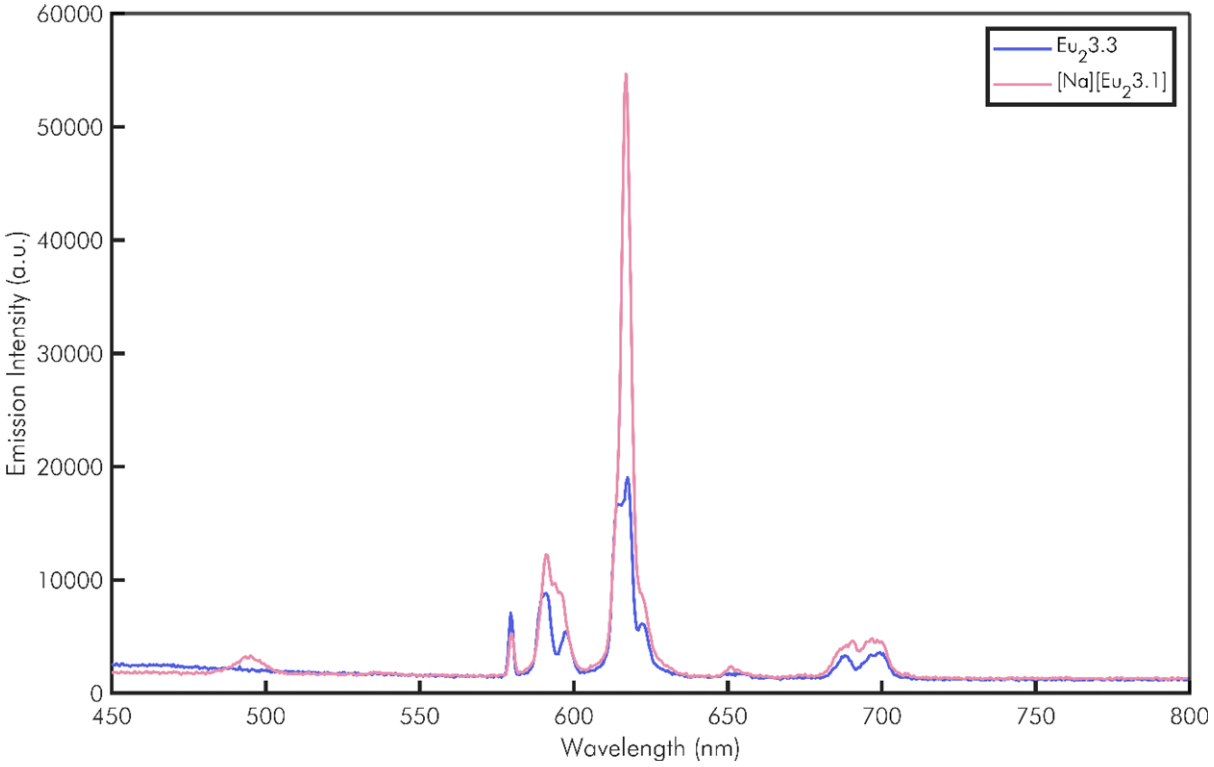

Figure 3.8: Emission spectra of ***Eu₂3.3*** *and* ***[Na][Eu₂3.1]****. Both recorded as 10^{-4} M solutions in H_2O with excitation via ligand centred absorption at λ_{ex} = 270 nm. Emission monochromator set to a bandpass of 1 nm.*

Figure 3.9 shows the full normalised emission spectra of **Eu₂3.3** and **[Na][Eu₂3.1]** and a closer look at the $^5D_0 \rightarrow {}^7F_0$ (580 nm), $^5D_0 \rightarrow {}^7F_1$ (592 nm), and $^5D_0 \rightarrow {}^7F_2$ (617 nm) transitions. It is clear that there is a different line-shape of the emission spectrum for **Eu₂3.3** compared to **[Na][Eu₂3.1]**. The hypersensitive $^5D_0 \rightarrow {}^7F_2$ transition (617 nm) changes in relative intensity to the $^5D_0 \rightarrow {}^7F_0$ (580 nm) and $^5D_0 \rightarrow {}^7F_1$ (592 nm) transitions. These data indicate a different coordination environment around the emissive europium(III) centre, supporting phenolate coordination.

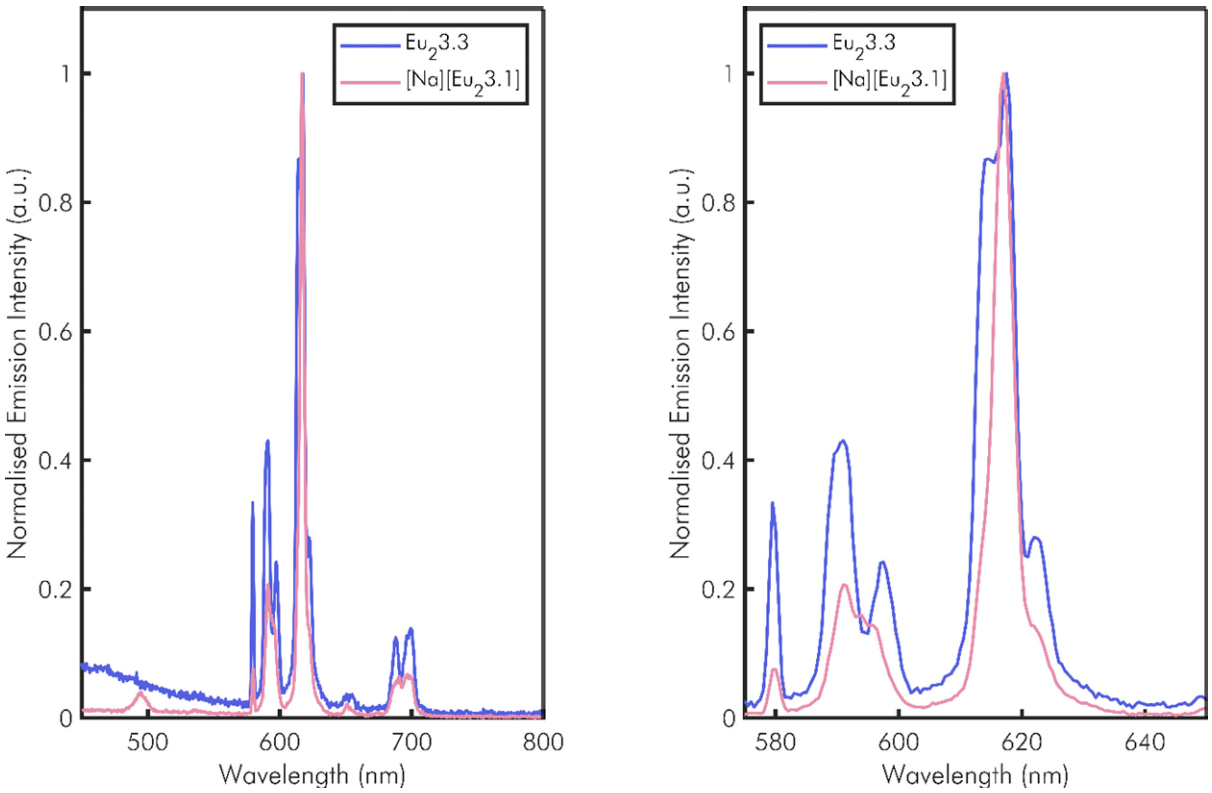

Figure 3.9: Normalised emission spectra of ***Eu₂3.3*** *and* ***[Na][Eu₂3.1]****. Both recorded as 10^{-4} M solutions in H_2O with excitation via ligand centred absorption at λ_{ex} = 270 nm. Right: Full measured emission window. Left: 575 to 650 nm only to show line-shape changes. Emission monochromator set to a bandpass of 1 nm.*

Figure 3.10 shows the emission spectra of **$Tb_2$3.3** and **[Na][$Tb_2$3.1]**. As with **[Na][$Eu_2$3.1]**, **[Na][$Tb_2$3.1]** was prepared *in situ* by treatment of **$Tb_2$3.3** with 5 equivalents of sodium carbonate. Both complexes were recorded as 10^{-5} M solutions in H_2O, and were excited at λ_{ex} = 270 nm, via ligand centred absorption bands. Both **$Tb_2$3.3** and **[Na][$Tb_2$3.1]** display characteristic terbium(III) centred luminescence with the $^5D_4 \rightarrow {}^7F_6$ (486 nm), $^5D_4 \rightarrow {}^7F_5$ (546 nm), $^5D_4 \rightarrow {}^7F_4$ (588 nm), and $^5D_4 \rightarrow {}^7F_3$ (620 nm) transitions observed. **[Na][$Tb_2$3.1]** displays significantly more intense emission under the same conditions. This is attributed to the increased efficiency of energy transfer with the direct coordination of sensitising chromophore.

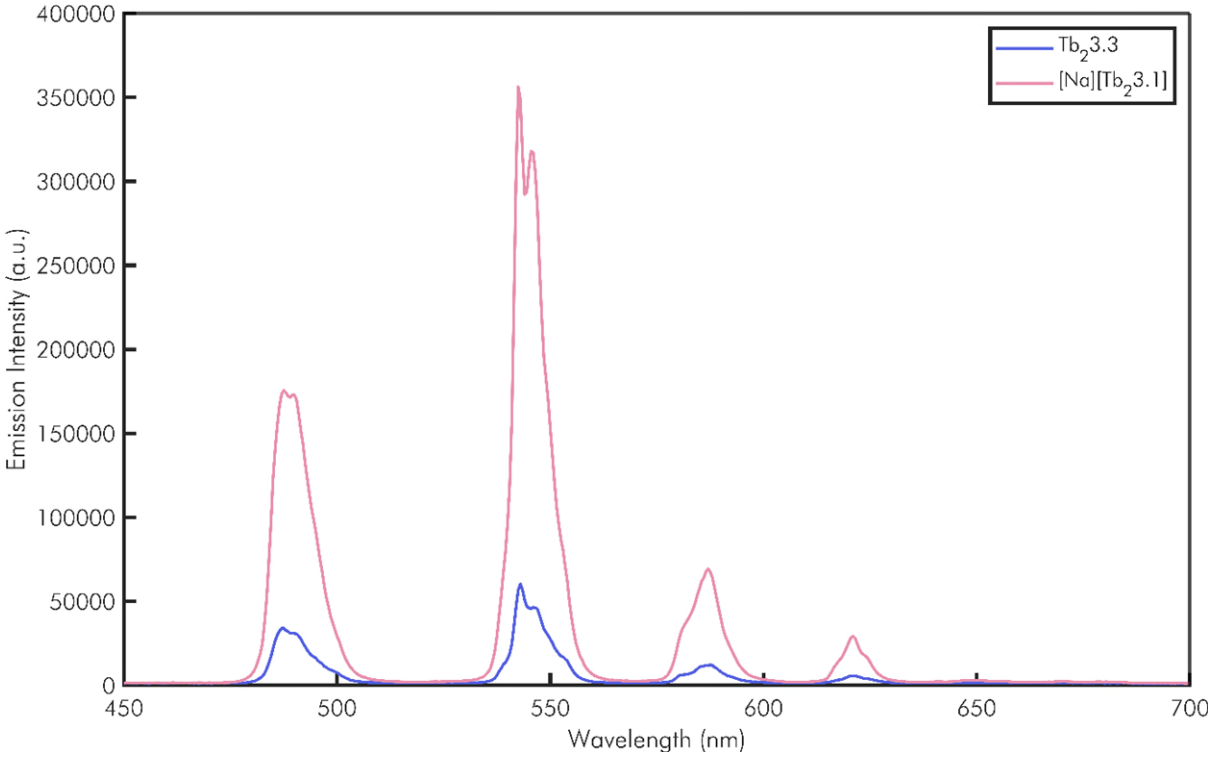

Figure 3.10: Emission spectra of ***Tb₂3.3*** *and* ***[Na][Tb₂3.1]****. Both recorded as 10^{-5} M solutions in H_2O with excitation via ligand centred absorption at λ_{ex} = 270 nm. Emission monochromator set to a bandpass of 1 nm.*

Figure 3.11 shows the normalised emission spectra of **Tb₂3.3** and **[Na][Tb₂3.1]**. Unlike with **Eu₂3.3** and **[Na][Eu₂3.1]** there is no difference in spectral line-shape between **Tb₂3.3** and **[Na][Tb₂3.1]**. Terbium(III) lacks a true hypersensitive transition, so changes in relative intensity of the different transitions are not as informative of local coordination environment than for europium(III).

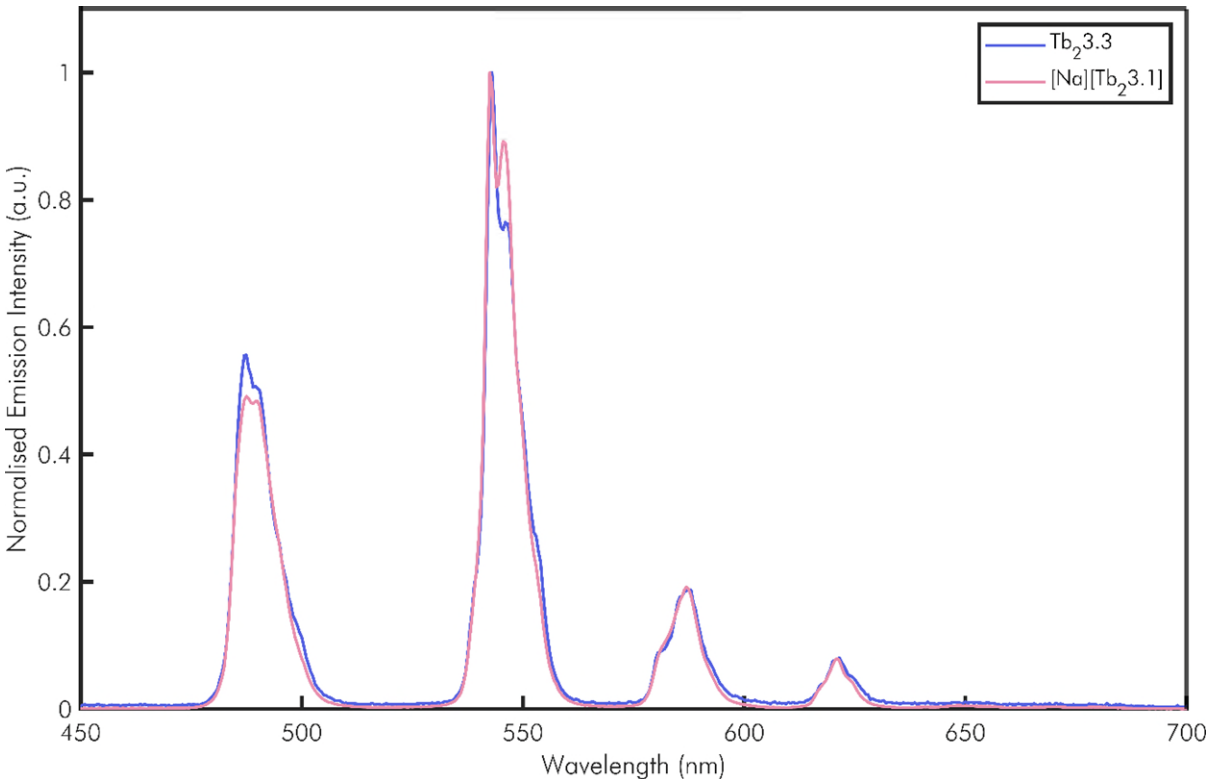

Figure 3.11: Normalised Emission spectra of ***Tb₂3.3*** *and* ***[Na][Tb₂3.1]****. Both recorded as 10^{-5} M solutions in H_2O with excitation via ligand centred absorption at λ_{ex} = 270 nm. Emission monochromator set to a bandpass of 1 nm.*

Table 3.1 shows the luminescence lifetimes of **Eu₂3.3**, **Tb₂3.3**, **[Na][Eu₂3.1]**, and **[Na][Tb₂3.1]** in H_2O. **Eu₂3.3** and **[Na][Eu₂3.1]** were recorded at 10^{-4} M, **Tb₂3.3** and **[Na][Tb₂3.1]** were recorded at 10^{-5} M. **Eu₂3.3** and **[Na][Eu₂3.1]** were recorded by monitoring the $^5D_0 \rightarrow {}^7F_2$ transition at λ_{em} = 617 nm, **Tb₂3.3** and **[Na][Tb₂3.1]** were recorded by monitoring the $^5D_4 \rightarrow F_6$ transition at λ_{em} = 546 nm. All complexes were excited via ligand centred absorptions at λ_{ex} = 270 nm.

Table 3.1: Luminescence lifetimes of ***$Eu_2$3.3****,* ***$Tb_2$3.3****,* ***[Na][$Eu_2$3.1]****, and* ***[Na][$Tb_2$3.1]*** *in H_2O*

	τ $Ln_2$3.3 (ms)	τ [Na][$Ln_2$3.1] (ms)
Ln = Eu(III)	0.4	0.6
Ln = Tb(III)	1.8	1.3

For **$Eu_2$3.3** and **[Na][$Eu_2$3.1]** the luminescence lifetime increases from 0.4 ms to 0.6 ms on hydrolysis of the phenyl acetate ester. This can be attributed to the exclusion of coordinating water, as the phenolate coordinates. The reduces the effect of quenching from proximate solvent oscillators. For **$Tb_2$3.3** and **[Na][$Tb_2$3.1]** the luminescence lifetime decreases from 1.8 ms to 1.3 ms on hydrolysis of the phenyl acetate ester. This is attributed to increased quenching of the terbium(III) centred excited state by a proximate terbium(III) centred excited state. The increased intermetallic communication, and option for through-bond energy transfer (Dexter exchange) increases the magnitude of this effect in **[Na][$Tb_2$3.1]** compared to **$Tb_2$3.3.** The difference between europium(III) and terbium(III) complexes can be rationalised by the more efficient quenching of europium(III) centred excited states by proximate solvent oscillators than of terbium(III) centred excited states (see section 1.8). Where solvent quenching is greater than quenching by proximate lanthanide(III) ions, the lifetime increases on hydrolysis of the phenyl acetate ester. When the reverse is true, the lifetime decreases.

The modified Horrocks equation, to determine the hydration number of emissive lanthanide(III) centres, is not suitable for lanthanide(III) complexes with significant quenching mechanisms beyond proximate solvent oscillators, owing to the possibilities for quenching one lanthanide through the manifold of another. Hence, we have not attempted to determine the hydration

number for **$Eu_2$3.3**, **$Tb_2$3.3**, **[Na][$Eu_2$3.1]**, and **[Na][$Tb_2$3.1]** as intermetallic communication provides a second significant quenching mechanism.

3.6: SYNTHESIS OF MULTIMETALLIC LANTHANIDE(III) COMPLEXES [Na][LnLn'3.1]

Scheme 3.6 shows the general approach to preparing multimetallic lanthanide complexes. The approach exploits the kinetic inertness of substituted DO3A derivatives. Treatment of a symmetric bis-macrocyclic ligand, **2.6**, with 1 equivalent of lanthanide(III) triflate affords a mixture of **$H_7$3.1**, **[Na][H_3Ln3.1]** and **[Na][$Ln_2$3.1]**. High-performance liquid chromatography (HPLC) can separate these components, allowing an isolation of **[Na][H_3Ln3.1]**. Further treatment of **[Na][H_3Ln3.1]** with 1 equivalent of lanthanide(III) triflate affords the multimetallic complex **[Na][LnLn'3.1]**.

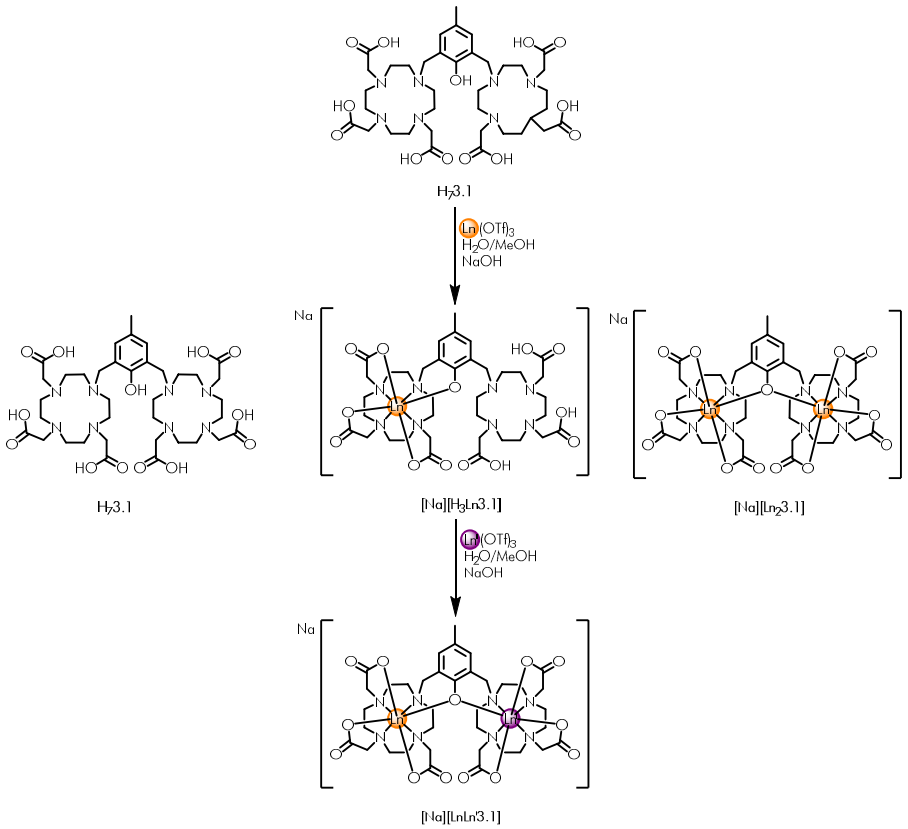

Scheme 3.6: Preparation of ***[Na][LnLn'3.1]*** *via preparation and isolation of* ***[Na][H3Ln3.1]***

[Na][H3Eu3.1] was isolated in 45% yield. HPLC separation using an eluent gradient from a high water content to a low water content eluted the compound after ca 1.75 minutes. LCMS was used to confirm the identity of the product and that a single species was isolated. Figure 3.12 shows the LCMS trace and the mass spectrum of the single peak.

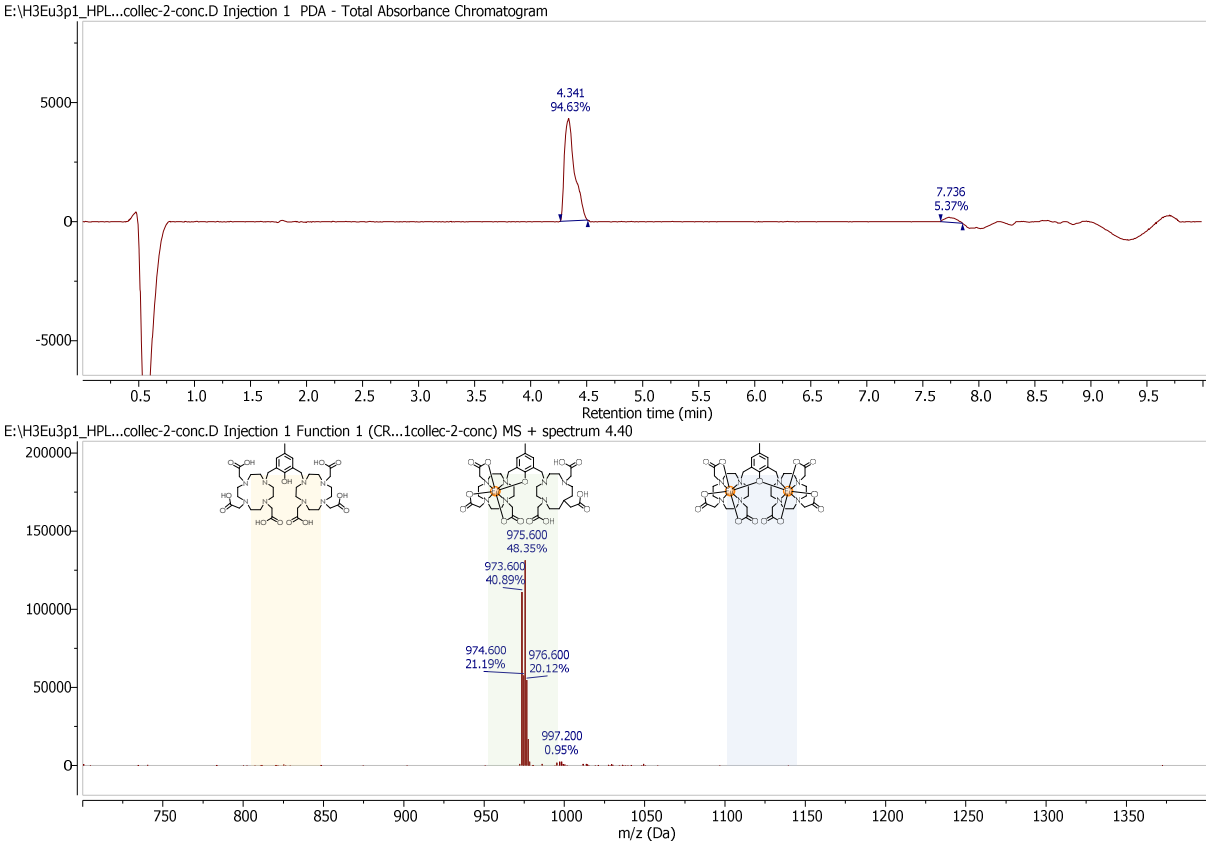

Figure 3.12: LCMS trace of ***[Na][H$_3$Eu3.1]****. The green box indicates the mass region associated with* ***[Na][H$_3$Eu3.1]****. The yellow box indicates the mass region associated with* ***H$_7$3.1****. The blue box indicates the mass region associated with* ***[Na][Eu$_2$3.1]****.*

Figure 3.13 shows the ^{1}H NMR spectrum of **[Na][H$_3$Eu3.1]** recorded in D_2O at 400 MHz. The resonances at 48 and 39 are assigned as the axial ring protons of the coordinated europium(III) ion. The resonance at 35 ppm is consistent with an **[EuDOTA]$^-$** impurity.

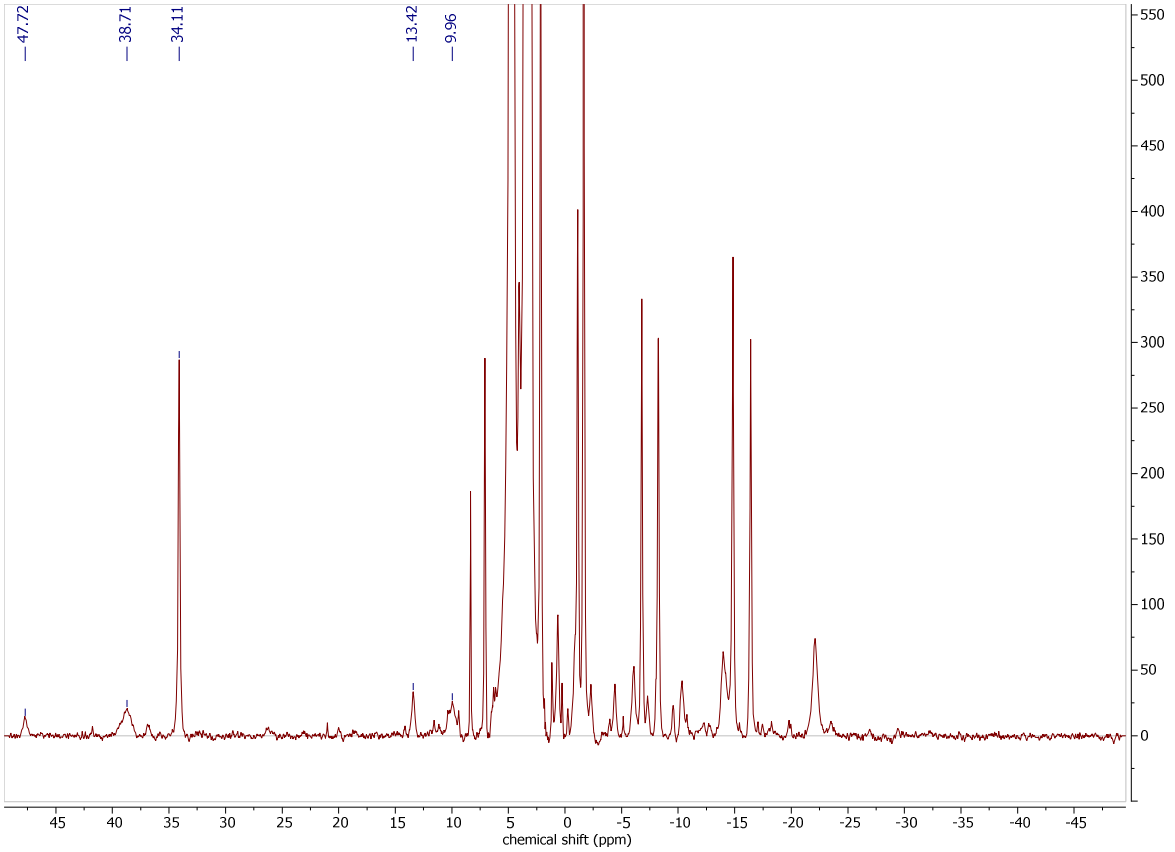

Figure 3.13: ^{1}H NMR spectrum in D_2O at 400 MHz of ***[Na][H$_3$Eu3.1]***

Further treatment of **[Na][H$_3$Eu3.1]** with terbium(III) triflate in water and methanol afforded **[Na][EuTb3.1]** in 99% yield. Figure 3.14 shows the ^{1}H NMR spectrum of **[Na][EuTb3.1]** in D_2O at 400 MHz. New resonances are observed upon coordination of terbium(III). These expand past the typical window for europium(III) complexes, owing to the greater magnetic moment of terbium(III). The resonances are tentatively assigned as the axial ring protons. No **[TbDOTA]$^-$** impurity is observed.

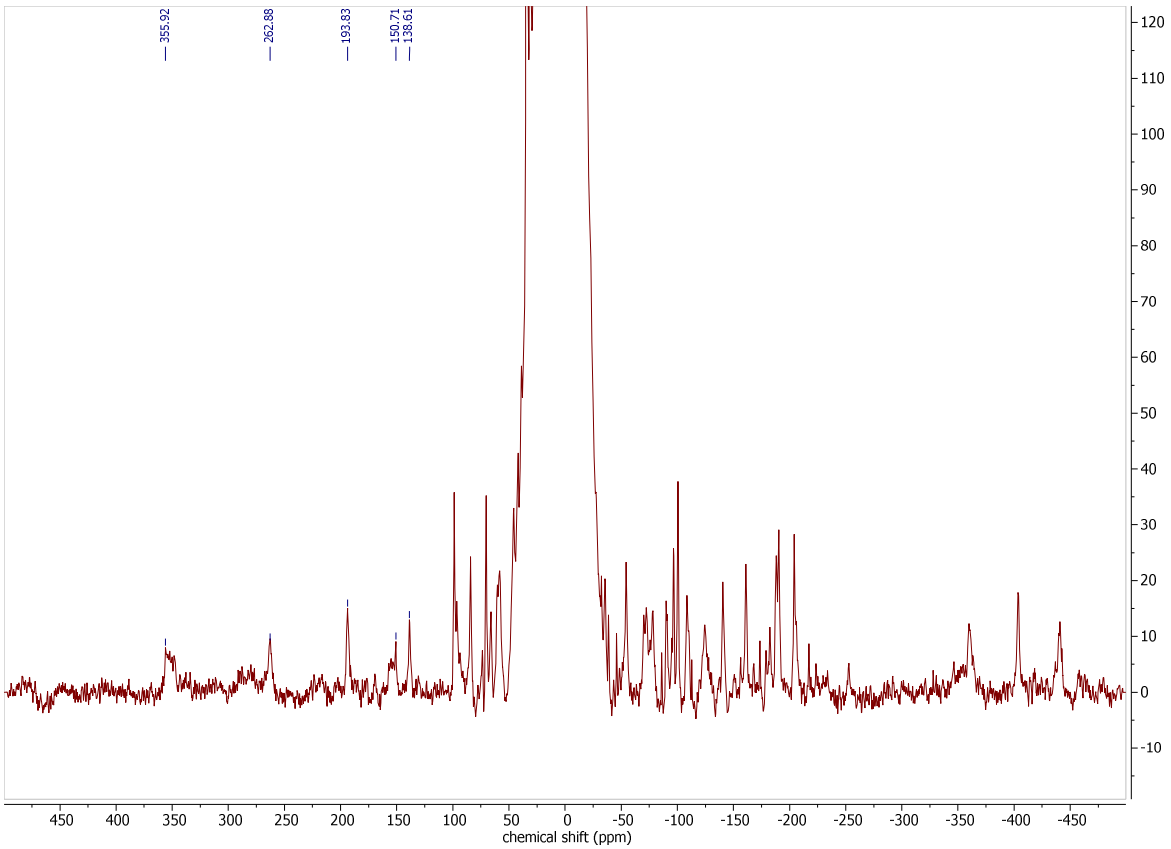

*Figure 3.14: ^{1}H NMR spectrum of **[Na][EuTb3.1]** in D_2O at 400 MHz*

Electrospray ionisation mass spectrometry found the [**EuTb3.1**]$^-$ ion at m/z = 1153.2215 confirming the species identity.

This approach was used to prepare **[Na][H_3Lu3.1]** in 37% yield and **[Na][LuGd3.1]** in 14% yield. The isotropic paramagnetism and rapid electronic relaxation of gadolinium(III) precluded characterisation of **[Na][LuGd3.1]** by NMR spectroscopy. Electron paramagnetic resonance (EPR) spectroscopy was used to characterise **[Na][LuGd3.1]** (see section 3.8).

Figure 3.15 shows the steady state emission spectrum of **[Na][EuTb3.1]** in water, at a concentration of 10^{-4} M, excited at $\lambda_{ex} = 290$ nm. When excited via ligand $\pi \rightarrow \pi^*$ transition, emission is seen from terbium(III) centred excited states and europium(III) centred excited states. The peak at 580 nm contains unfiltered incident light at double the excitation wavelength. The spectrum is dominated by emission from terbium(III) centred excited states, consistent with terbium(III) being less sensitive to solvent quenching.

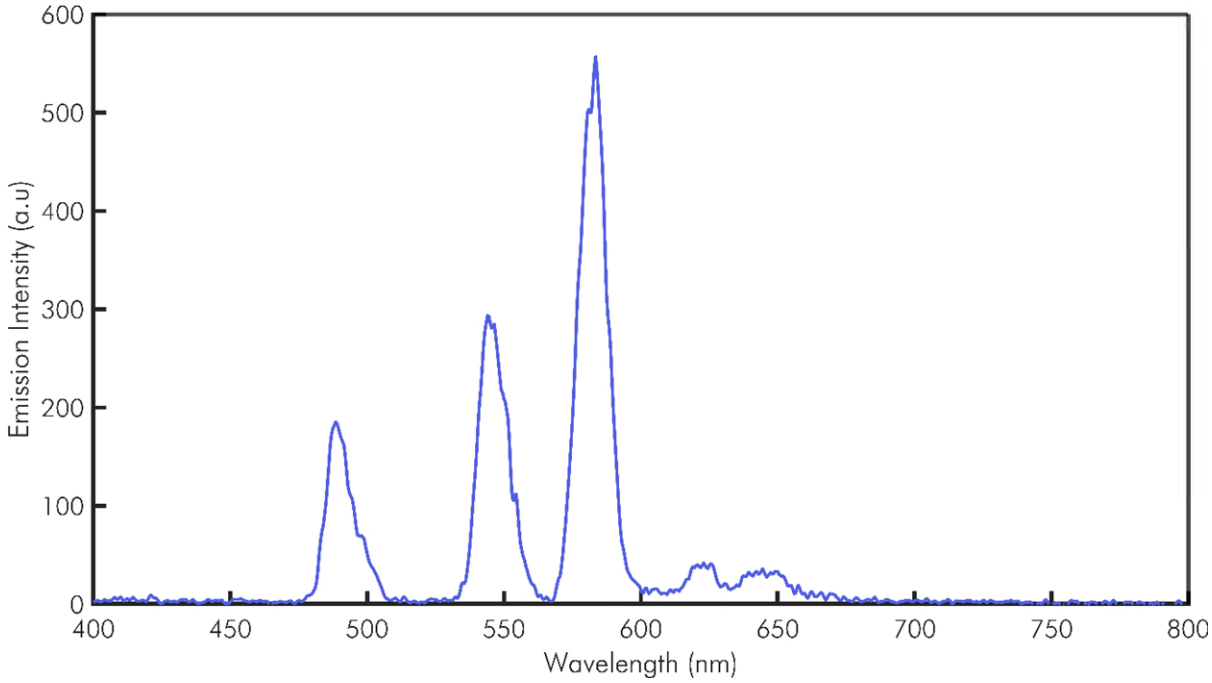

*Figure 3.15: Steady state emission spectrum of **[Na][EuTb3.1]** recorded in H_2O at 10^{-4} M. Excited at 290 nm. The emission monochromator was set to 2.5 nm bandpass.*

3.8: ELECTRON PARAMAGNETIC RESONANCE SPECTROSCOPY OF [Na][GdLu3.1]

We sought to investigate the magnetic properties of **[Na][GdLu3.1]** and **[Na][Gd$_2$3.1]** with electron paramagnetic resonance (EPR) spectroscopy. This work was carried out in collaboration with the group of Christiane Timmel at the University of Oxford. The EPR experiments were carried out by Ashley Redman.

We chose gadolinium(III) as the paramagnetic ion for the isotropic electron distribution. Lutetium(III) was used as the diamagnetic ion doesn't affect magnetic properties or cause as signal in EPR experiments.

Continuous wave EPR measurements were performed at X-band on a Bruker EMXmicro spectrometer equipped with an ER4122SHQE-W1 resonator. The temperature was held constant at 10 K using liquid helium in combination with a continuous flow cryostat (ESR900, Oxford Instruments) and temperature controller (ITC503s, Oxford Instruments). 3.8 mm o.d., 2.7 mm i.d. quartz EPR tubes were used. The samples were prepared as methanol solutions and were degassed by several freeze-pump-thaw cycles before filling with argon and sealing the tube. The sample was flash frozen in liquid nitrogen prior to insertion to the spectrometer.

Figure 3.16 shows the EPR spectrum of **[Na][GdLu3.1]** recorded in frozen methanol solution. The spectrum was recorded at 10 K due to the rapid electronic relaxation of gadolinium(III) ions. The spectrum has had a linear baseline correction applied. The multiple transitions observed imply a large zero-field splitting, splitting the otherwise 8-fold degenerate m_s states in 4 Kramer's doublets, which split in a magnetic field to an 8-level system.

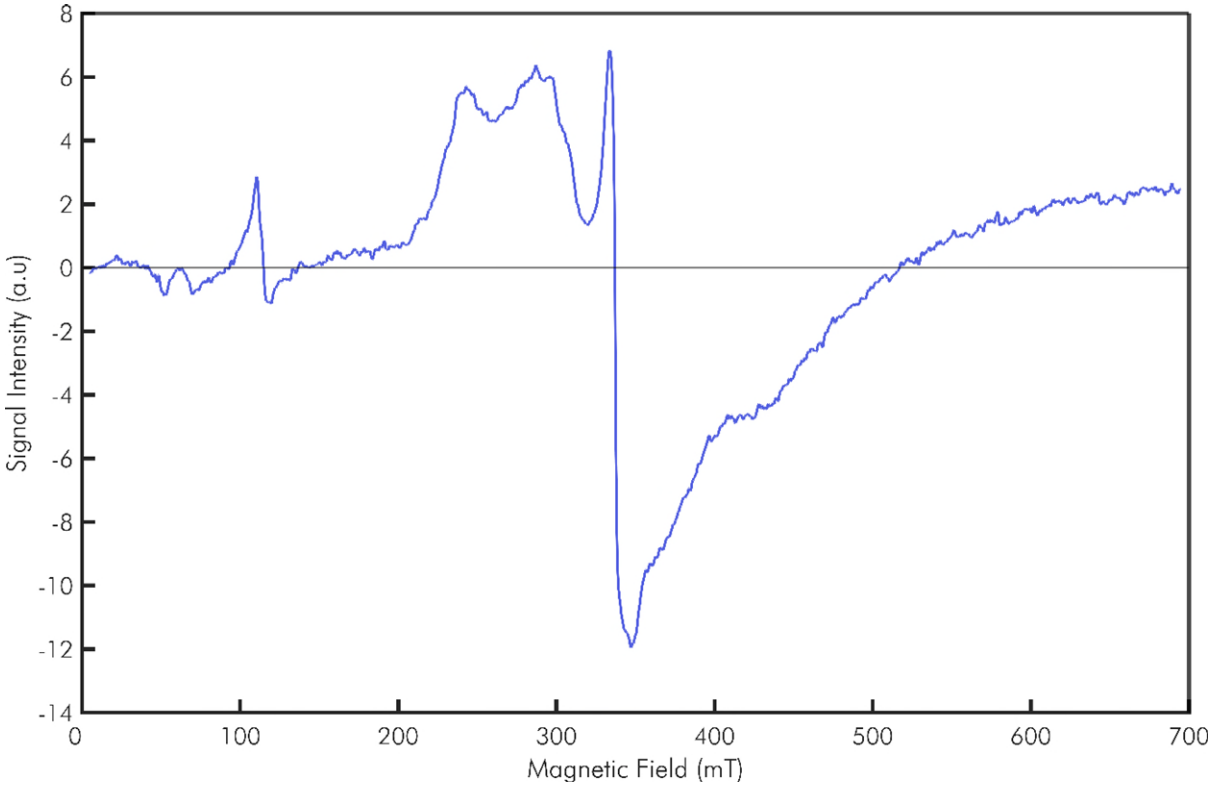

*Figure 3.16: EPR spectrum of **[Na][GdLu3.1]** in frozen methanol solution at 10 K.*

Attempts to acquire a spectrum of **[Na][$Gd_2$3.1]** were unsuccessful. There is the possibility of low temperature antiferromagnetic exchange coupling, which may render the ground state of **[Na][$Gd_2$3.1]** an EPR silent singlet ground state. A similar phenomenon is observed in a structurally related system.[8]

3.9: CONCLUSIONS

We successfully developed a covalent system for modulating lanthanide-lanthanide communication, via hydrolysis of a phenyl acetate ester. Upon hydrolysis the emission intensity increases, attributed to more efficient energy transfer from ligand centred excited states to lanthanide(III) centred excited states. Luminescence lifetimes change upon ester hydrolysis, with

terbium(III) growing shorter and europium(III) growing longer. This is attributed to increased quenching by proximate lanthanide(III) ions and decreased quenching by proximate solvent oscillators. The difference in efficiency of solvent oscillator quenching results in the opposite directions of change.

We prepared a multimetallic complex **[Na][GdLu3.1]**. The EPR spectrum of **[Na][GdLu3.1]** indicates a large zero-field splitting. The binuclear analogue **[Na][$Gd_2$3.1]** did not give rise to an EPR signal; at the low temperatures required to acquire gadolinium(III) spectra this is likely the result of antiferromagnetic coupling to the two gadolinium(III) centres.

We prepared the multimetallic complex **[Na][EuTb3.1]** from the monometallic precursor **[Na][H_3Eu3.1]**, prepared via preparative HPLC. **[Na][EuTb3.1]** displays emission from both europium(III) and terbium(III) centred excited states.

3.10: REFERENCES

1. T. J. Sørensen and S. Faulkner, *Acc. Chem. Res*. , 2018, 51, 2493 – 2501.
2. S. J. A. Pope, A. M. Kenwright, S. L. Heath and S. Faulkner, *Chem. Commun.*, 2003, 1550 – 1551
3. O. A. Blackburn, M. Tropiano, L. S. Natrajan, A. M. Kenwright and S. Faulkner, *Chem. Commun*., 2016, 52, 6111 – 6114.
4. V. Srivastava, A. Tandon and S. Ray, *Synth. Commun*., 1992, 22, 2703 – 2710
5. A. Dadabhoy, S. Faulkner and P. G. Sammes, *J. Chem. Soc. Perkin Trans. 2,* 2002, 348-357.
6. L. G. Nielson, T. J. Sørensen, *Inorg. Chem*. 2020, 59, 1, 94 – 105
7. M. Regueiro-Figueroa, D. Esteban-Gómez, A. de Blas, T. Rodríguez-Blas, and C. Platas-Iglesias, *Eur. J. Inorg. Chem*., 2010, 3586 – 3595
8. J. I. Clark, unpublished results

4. A SELF-ASSEMBLY APPROACH TO MULTIMETALLIC LANTHANIDE(III) COMPLEXES USING A SALICYLIC ACID APPENDED DO3A DERIVATIVE

Self-assembly is the spontaneous and reversible assembly of chemical species to form larger supramolecular species.[1, 2] Self-assembly is observed across a spectrum of length scales from self-assembling molecular cages through protein folding to extended solids.[3, 4] Self-assembly can be driven by a range of interactions including van der Waals interactions, hydrogen bonding, π-π interactions, dipolar interactions, and coordination bonds.[1, 5]

The majority of reported self-assembled lanthanide-containing species are homometallic i.e. they contain ions of only one lanthanide(III) metal. Examples have included helicates,[6-9] cages,[10] cubes[11, 12], wheels,[13] and more.[14-18]

The preparation of self-assembled multimetallic architectures was reported by Faulkner and co-workers through the coordination of a terbium(III) complex with a pendant isophthalate group to a bis-europium(III) complex (see section 1.14). [19] An extension of this idea to prepare d-f hybrids has been reported by Faulkner and co-workers. [20]

Sørenson and co-workers investigated the self-assembly of a range of carboxylic acid derivatives with binuclear *m*-xylyl complexes. It was found, for these systems, isophthalic acid gave the strongest binding and most efficient self-assembly. [21]

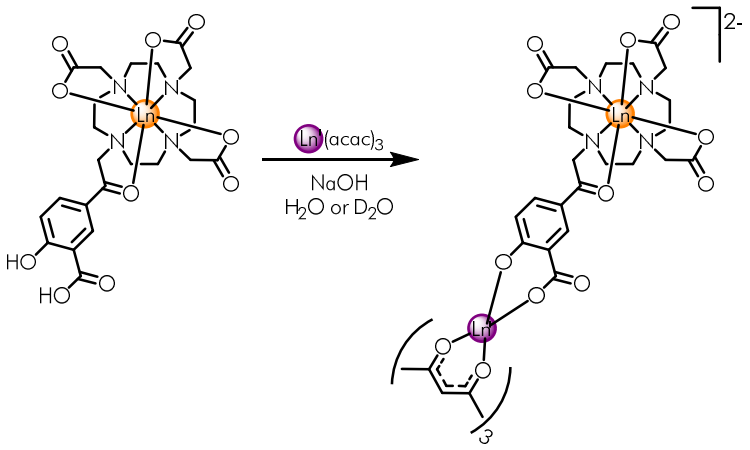

Scheme 4.1: Self-assembly of ***H_2Ln4.1*** *and* ***Ln'(acac)$_3$*** *to form* ***[Ln'(acac)3].[Ln4.1]$^{2-}$***

This chapter describes the preparation of multimetallic lanthanide complexes through a self-assembly approach. A lanthanide(III) containing DO3A derivative, with a pendant salicylic acid moiety, can self-assemble with a coordinatively unsaturated lanthanide(III) trisacetylacetonate complex. This can allow access to multimetallic complexes when different lanthanide(III) ions are used in the two components (Scheme 4.1). This chapter investigates the selective excitement of each lanthanide(III) ion and the resultant emission. Terbium(III) and europium(III) were selected for their visible emission wavelengths.

As discussed in chapter 1, long-term solution stability of multimetallic lanthanide(III) complexes requires the lanthanide chelators be kinetically inert, to prevent 'scrambling' of the lanthanide(III) ions (see section 1.12).[22] Complexes of the salicylate-appended DO3A derivative meet the requirements for kinetic inertness. Hence, the overall ternary complex is stable to 'scrambling', despite the inherent lability of lanthanide(III) trisacetylacetonate moieties.

The continuous conjugation through the salicylate moiety, between the coordinating carboxylic acid and phenolate and the coordinating ketone is expected to enable through-bond

communication between the two metal ions. This should allow Dexter exchange across the conjugated system between lanthanide ions. In the absence of Dexter exchange, energy transfer would be reliant on FRET, likely inefficient at these distance, especially given the low spectral overlap integral of weak lanthanide(III) centred transitions.[23]

4.1: SYNTHESIS OF $H_5$4.1

The proposed complexes were prepared as in Scheme 4.2. Using a modified literature procedure.[24]

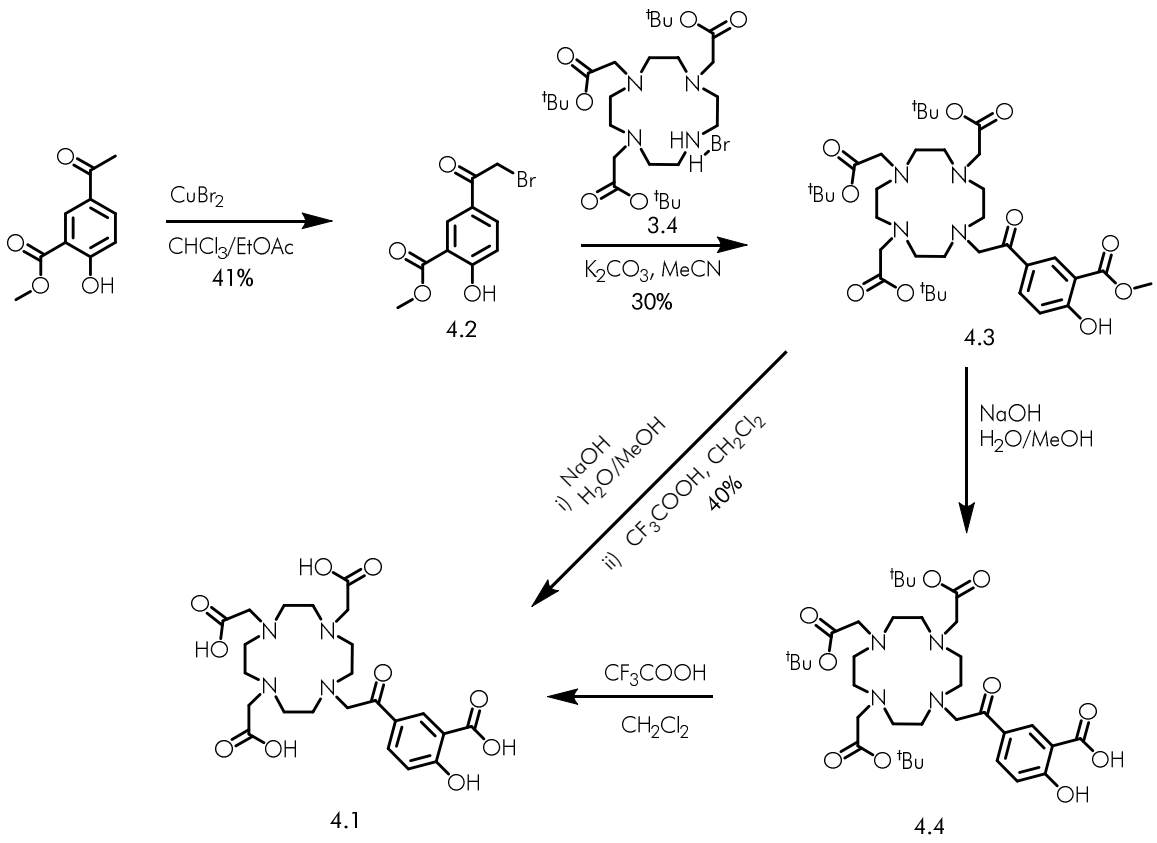

Scheme 4.2: Synthetic route to ***$H_5$4.1***

Bromination of methyl 5-acetyl salicylate, with copper(II) bromide in a 1:1 volume ratio of ethyl acetate and chloroform afforded a mixture of the starting material and the mono-, di- and tri-brominated products. Flash chromatography on silica allowed the isolation of the target mono-brominated product, **4.2**, in 41% yield. Though the copper(II) bromide was expected to be removed during workup, through filtration, it was found that bromination continued on standing of the crude product. This is attributed to a significant degree of enolisation of the phenyl ketone. Hence, purification was always carried out immediately.

N-alkylation of **3.4** with **4.2** in acetonitrile with potassium carbonate, at room temperature for 16 hours afforded crude **4.3**. Purification by flash chromatography on silica afforded pure **4.3** in 30% yield.

When attempting to hydrolyse the methyl ester of **4.3** with sodium hydroxide in methanol and water, partial hydrolysis of the *tert*-butyl esters was observed, the product was taken forward without purification. Complete hydrolysis of the *tert*-butyl esters with trifluoroacetic acid in dichloromethane at room temperature for 24 hours afforded **$H_5$4.1**. The product was recrystallisation from a concentrated methanol solution with diethyl ether thrice to afford pure **$H_5$4.1.** The 2-step procedure afforded **$H_5$4.1** in 40% yield.

Conversely, when **4.3** was treated with trifluoroacetic acid in dichloromethane to hydrolyse the *tert*-butyl esters partial hydrolysis of the methyl ester was observed. Solubility issues impaired the complete hydrolysis of the methyl ester. Hence, **4.4** was not isolated.

The complexes **$H_2Eu4.1$** and **$H_2Tb4.1$** were prepared by treatment of **$H_54.1$** with lanthanide(III) triflate salt in water and methanol, followed by heating for 16 hours. After cooling, three equivalents of sodium hydroxide (as a 1 M aqueous solution) was added, and the mixture heated for a further 24 hours. After cooling to room temperature, mixture was filtered, with excess lanthanide(III) ions expected to have precipitated as the insoluble lanthanide(III) hydroxide. The filtrate was evaporated to dryness under flowing nitrogen, with heating, to afford the crude target complexes as yellow powders. The crude complexes were purified by dialysis using FLOAT-A-LYZER G2 100-500D CE dialysis chambers to remove free lanthanide(III) ions and sodium triflate. After membrane activation, the chamber was partially filled with an aqueous solution of **$H_2Ln4.1$**. Immersion of the chamber in a large quantity distilled water (typically 2 L) allowed for purification. The external water was changed three times per day and the process typically took four days. Distilled water diffuses back across the membrane due to a salt concentration gradient. The cessation of this process indicates complete removal of salts from the complex solution. **$H_2Tb4.1$** was prepared in 94% yield, **$H_2Eu4.1$** was prepared in 72% yield.

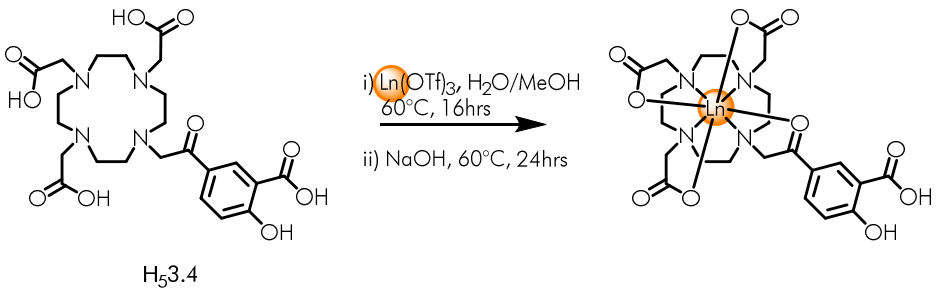

$H_53.4$

*Scheme 4.3: Synthetic scheme for the preparation of **$H_2Ln4.1$** from **$H_54.1$***

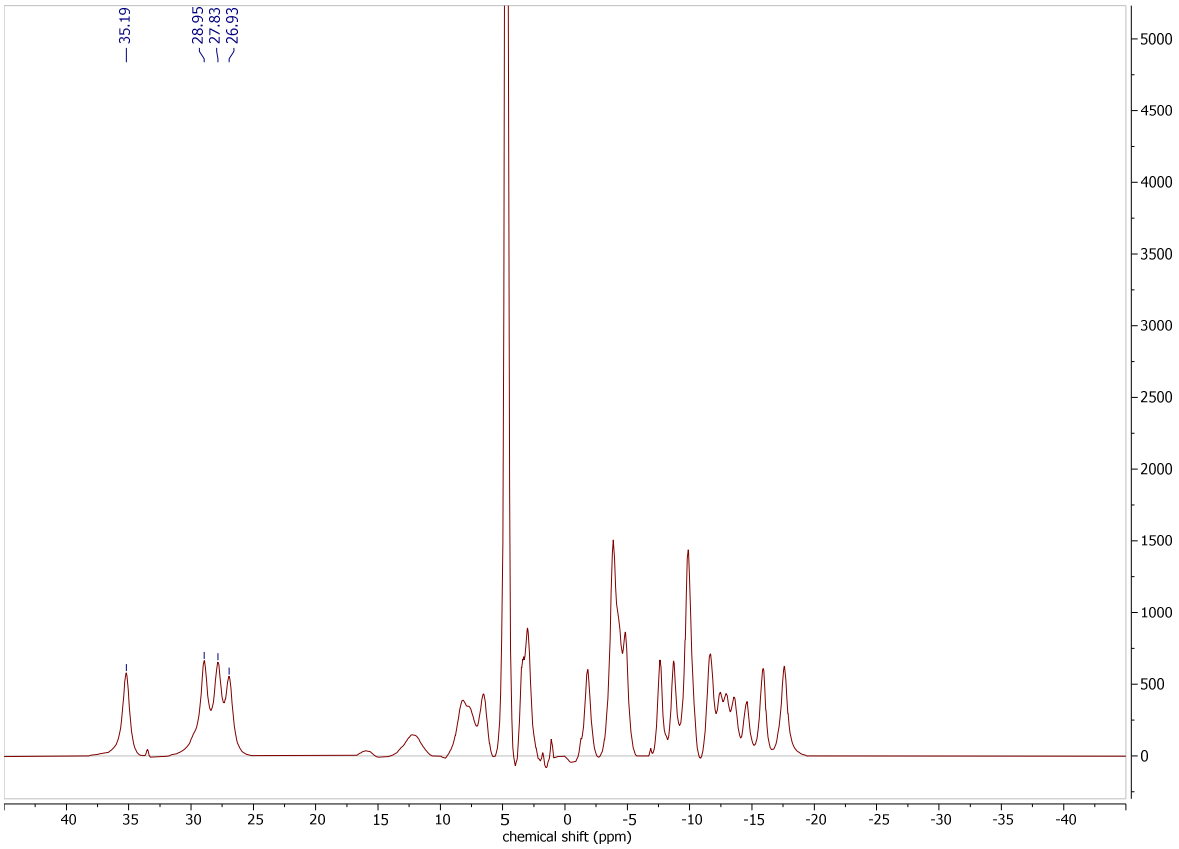

*Figure 4.1: ^{1}H NMR spectrum of **$H_2Eu4.1$** recorded in D_2O at 400 MHz*

The ^{1}H NMR spectrum of **$H_2Eu4.1$** (Figure 4.1), recorded in D_2O, shows two major resonances at 35.19 ppm and 27.83 ppm corresponding to the axial ring protons in a square antiprismatic (SAP) geometry. The lower intensity resonances in the 20 — 15 ppm region correspond axial ring protons in a twisted square antiprismatic (TSAP) geometry, indicating this is a minor part of the solution-phase structure.

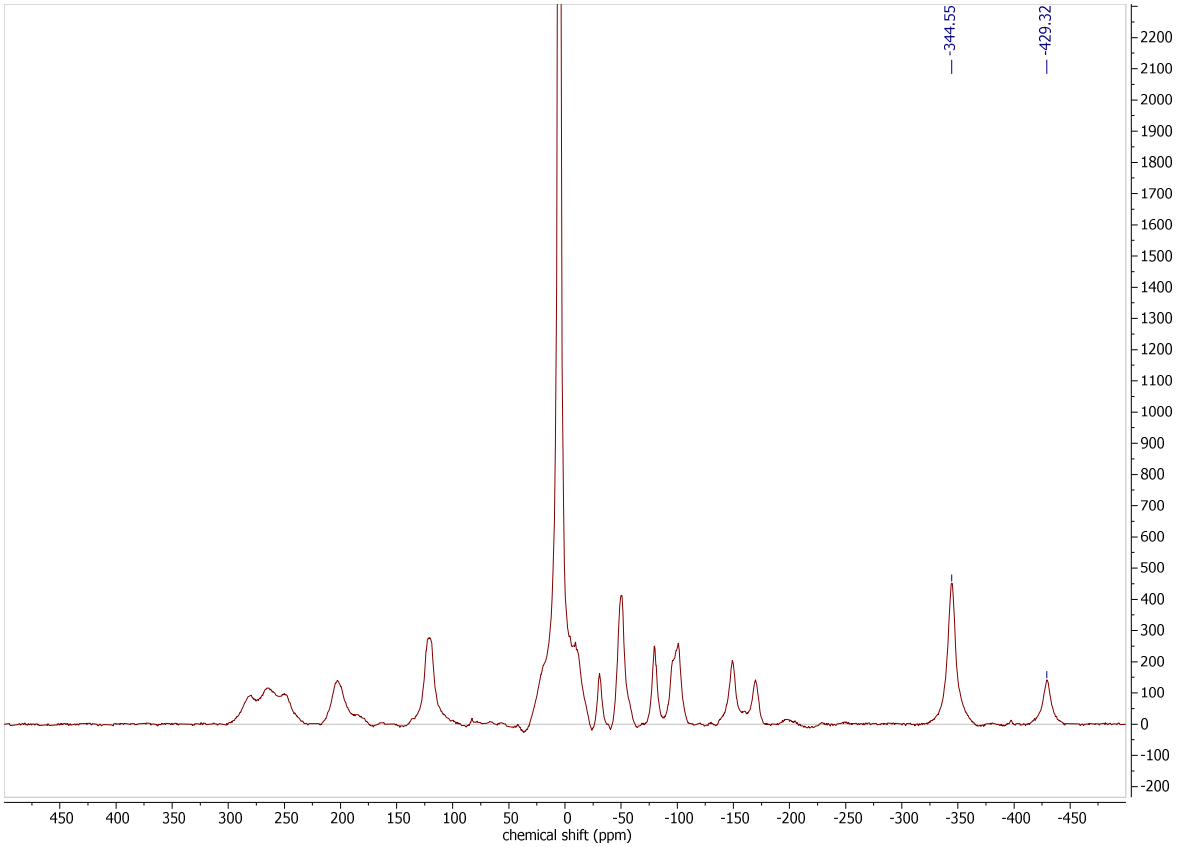

*Figure 4.2: ^{1}H NMR spectrum of **H_2Tb4.1** recorded in D_2O at 400 MHz*

Figure 4.2 shows the ^{1}H NMR spectrum of **H_2Tb4.1** recorded in D_2O. The two major resonances at -344.55 ppm and -429.32 ppm are the axial ring protons in a SAP geometry. The NMR spectra of both **H_2Tb4.1** and **H_2Eu4.1** imply the complexes exist in solution primarily as a SAP geometry.

Electrospray ionisation mass spectrometry found the $[M-H]^-$ ion for both **H_2Eu4.1** and **H_2Tb4.1**. For **$[Tb4.1]^{2-}$** no evidence of the sodium adduct, **Na_2Tb4.1**, was observed by electrospray ionisation mass spectrometry.

Both **H_2Eu4.1** and **H_2Tb4.1** were dried under high-vacuum for at least 16 hours prior to use.

[Ln'(acac)$_3$].[Ln4.1]$^{2-}$ was prepared immediately prior to use, by mixing **H_2Ln4.1** with **Ln'(acac)$_3$** in either H_2O or D_2O. 2 equivalents of sodium hydroxide was then added to facilitate self-assembly.

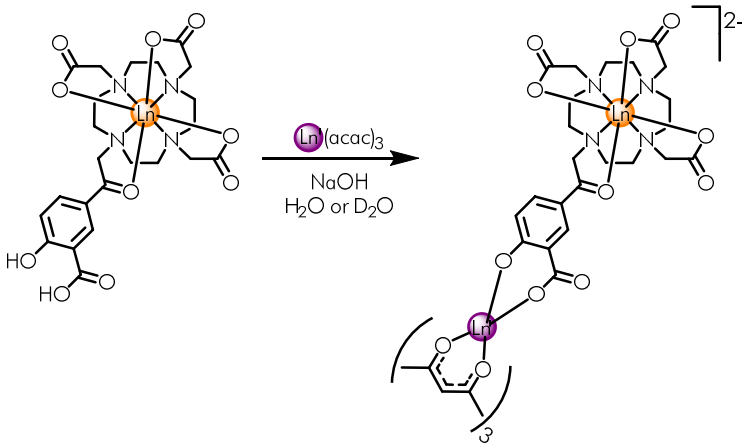

*Scheme 4.4: Self-assembly of **H_2Ln4.1** and **Ln'(acac)$_3$** to form **[Ln'(acac)3].[Ln4.1]$^{2-}$***

Attempts to characterise the formation of the self-assembled supramolecular adducts via electrospray ionisation mass spectrometry failed to identify any masses related to the adducts or the constituent parts.

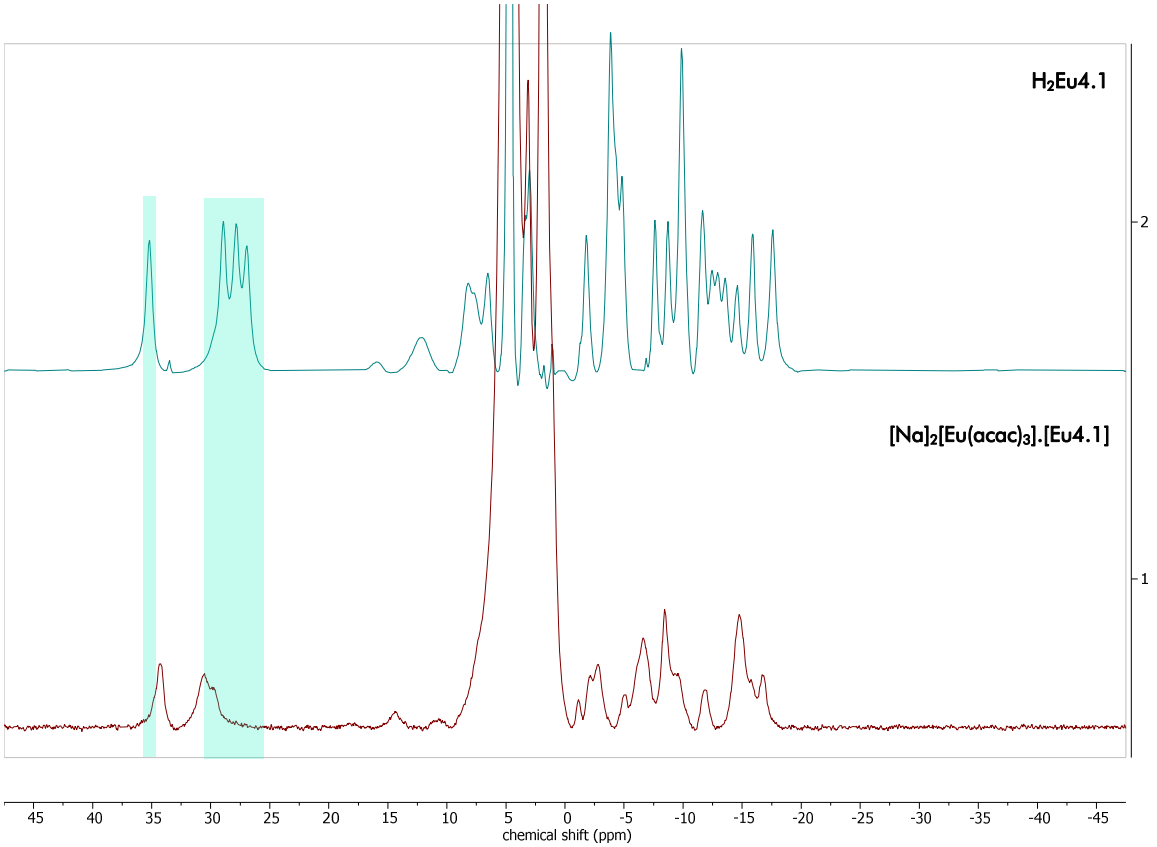

Figure 4.3: ^{1}H NMR spectra recorded at 400 MHz of top: ***H_2Eu4.1*** *in D_2O bottom:* ***$[Na]_2[Eu(acac)_3].[Eu4.1]$*** *in a 1:1 D_2O:CD_3OD mixture*

Figure 4.3 shows the ^{1}H NMR spectra of **H_2Eu4.1** in water and **$[Na]_2[Eu(acac)_3].[Eu4.1]$** in a water:methanol mixture. Upon self-assembly with **$Eu(acac)_3$** the resonances resulting from the axial ring protons in a square antiprismatic geometry (SAP) dominate compared to the peaks resulting from the axial ring protons in a twisted square antiprismatic geometry (TSAP) geometry.

Figure 4.4 shows the UV-visible absorption spectra for **H_2Tb4.1**, **$[Na]_2[Tb(acac)_3].[Tb4.1]$**, **$[Na]_2[Eu(acac)_3].[Tb4.1]$**, **$Tb(acac)_3$**, and **$Eu(acac)_3$**, recorded in H_2O at 10^{-5} M. **H_2Tb4.1** shows three absorptive bands at 214 nm, 243 nm and 309 nm. **$Eu(acac)_3$** shows a weakly absorptive band at 275 nm. **$Tb(acac)_3$** shows a weakly absorbing band at 289 nm, and a more strongly absorbing band at 200 nm. **$[Na]_2[Eu(acac)_3].[Tb4.1]$** closely resembles the spectrum of **H_2Tb4.1** with three strongly absorbing bands at 214 nm, 243 nm and 309 nm. **$[Na]_2[Tb(acac)_3].[Tb4.1]$** has an intense absorbance at 200 nm, likely due to contributions from **$Tb(acac)_3$** and two more absorbing bands at 243 nm and 309 nm.

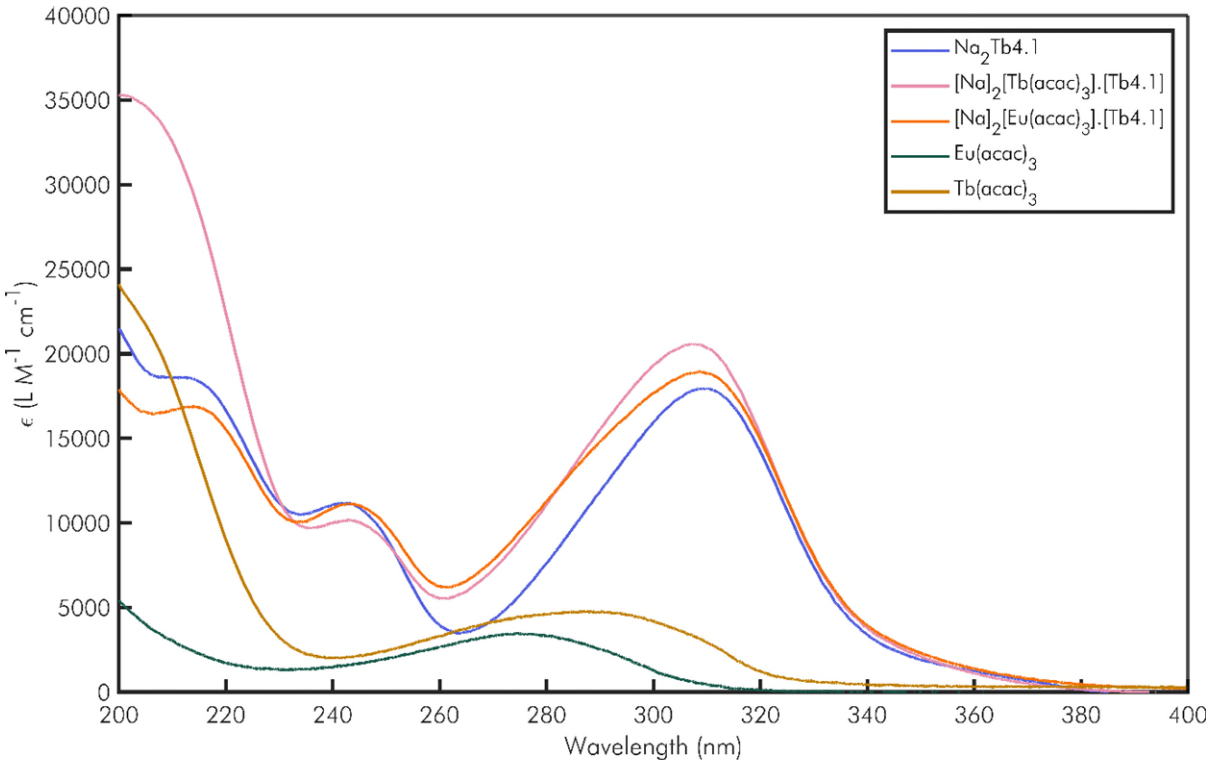

*Figure 4.4: UV-visible absorption spectra for **H_2Tb4.1** (blue), **$[Na]_2[Tb(acac)_3][Tb4.1]$** (pink), **$[Na]_2[Eu(acac)_3][Tb4.1]$** (orange), **$Tb(acac)_3$**,(green), and **$Eu(acac)_3$** (yellow) recorded in H_2O at 10^{-5} M*

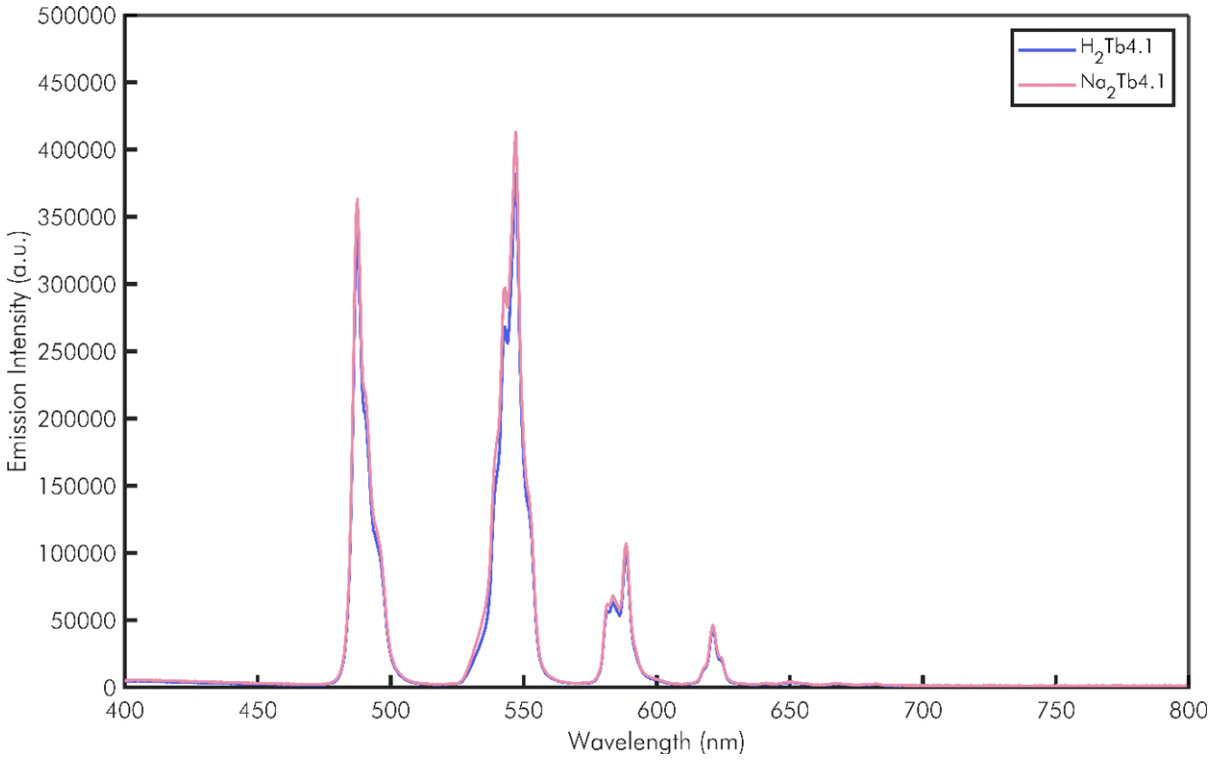

Figure 4.5:Steady state emission spectra of ***H₂Tb4.1*** *with (pink) and without (blue) sodium hydroxide added when excited at 310 nm. Emission monochromator slit was set to 1 nm bandpass.*

Figure 4.5 shows the emission spectra of **H_2Tb4.1** and **Na_2Tb4.1** both in H_2O at a concentration of 10^{-5} M. **Na_2Tb4.1** was prepared by the addition of 2 equivalents sodium hydroxide to an aqueous solution of **H_2Tb4.1**. Excitation through the ligand manifold, at λ_{ex} = 310 nm, leads to emission from terbium(III) centred excited states; there is clear energy transfer from the pendant salicylate moiety to terbium(III) centred excited states. The $^5D_4 \rightarrow {}^7F_6$ (488 nm), $^5D_4 \rightarrow {}^7F_5$ (540 nm), $^5D_4 \rightarrow {}^7F_4$ (580 nm), and $^5D_4 \rightarrow {}^7F_3$ (620 nm) transitions are observed. Sodium hydroxide was tested to enable faster self-assembly with lanthanide(III) acetylacetonates via sodium phenolate, sodium carboxylate intermediates. The addition of sodium hydroxide has no noticeable effect on the emission spectrum of **H_2Tb4.1**, indicating the carboxylate motifs do not impact energy transfer from ligand centred excited states to terbium(III) centred excited states.

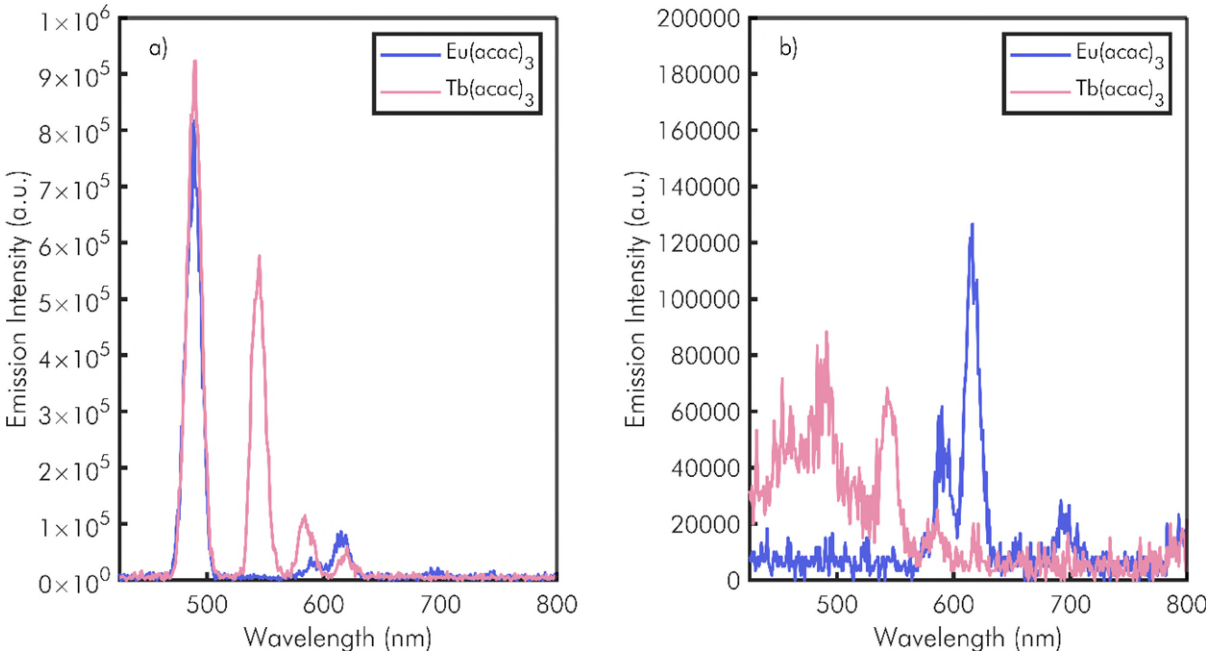

Figure 4.6: a) Time-gated emission spectra of ***Eu(acac)₃*** *(blue) and* ***Tb(acac)₃*** *(pink). a) excited at 488 nm, in D_2O at 10^{-3} M. b) Emission spectra of* ***Eu(acac)₃*** *(blue) and* ***Tb(acac)₃*** *(pink) excited at 400 nm, in D_2O at 10^{-3} M. Emission monochromator slit was set to 10 nm bandpass. A time gate of 50 μs was employed.*

Figure 4.6 shows the emission spectra of **Eu(acac)₃** and **Tb(acac)₃** when the lanthanide(III) centred excited states are directly excited. To see meaningful signal a concentration of 10^{-3} M was required. The experiments were conducted in D_2O to minimise solvent quenching and maximise signal. A time-gated measurement was employed to allow collection of data over a range of emission wavelengths including the excitation wavelength. A delay of 50 μs was used between excitation and data collection. For direct excitation of terbium(III), via the $^7F_6 \rightarrow {}^5D_4$ transition at λ_{ex} = 488 nm, significant terbium(III) centred emission is observed for **Tb(acac)₃**. **Eu(acac)₃** is weekly emissive, scattered excitation light is still visible at 488 nm. For direct excitation of europium(III), via the $^7F_0 \rightarrow {}^5L_6$ transition at λ_{ex} = 400 nm, europium(III) centred emission can be observed for **Eu(acac)₃**. For **Tb(acac)₃**, some broad emissive features between 450 nm and 550 nm are observed; these are lower in intensity than the europium(III) centred emission of **Eu(acac)₃** under the conditions. These differences in emission intensity, and hence population of corresponding lanthanide(III) centred excited states, were deemed sufficient to

selectively excite either europium(III) or terbium(III) centred excited states in the multimetallic supramolecular assemblies **[Na]$_2$[Tb(acac)$_3$].[Eu4.1]** and **[Na]$_2$[Eu(acac)$_3$].[Tb4.1]**.

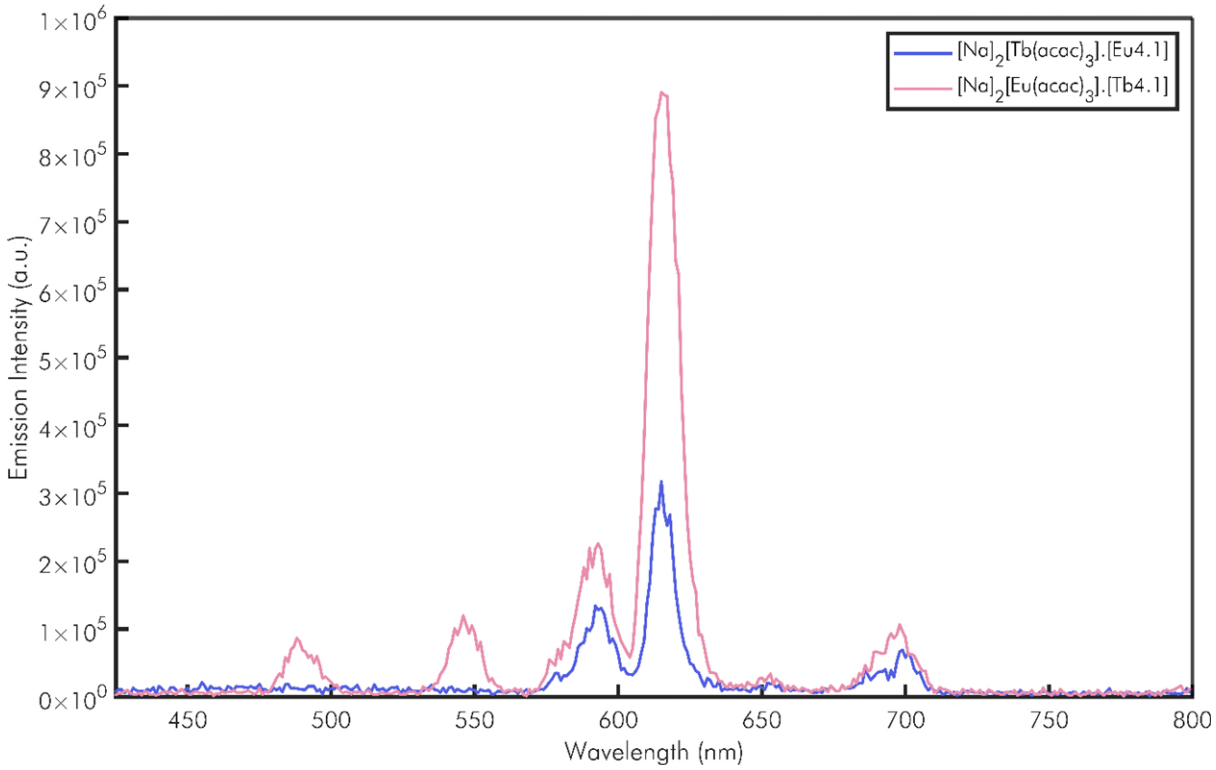

*Figure 4.7: Time-gated (50 μs) emission spectra of **[Na]$_2$[Tb(acac)$_3$].[Eu4.1]** (blue) and **[Na]$_2$[Eu(acac)$_3$].[Tb4.1]** (pink) in D_2O at 10^{-3} M with direct excitation of europium(III) at 400 nm. Emission monochromator was set to a 7 nm bandpass. Excitation monochromator was set to a 7 nm bandpass.*

Figure 4.7 shows the emission spectra of **[Na]$_2$[Tb(acac)$_3$].[Eu4.1]** and **[Na]$_2$[Eu(acac)$_3$].[Tb4.1]** when directly exciting europium(III) centred excited states at 400 nm via the $^7F_0 \rightarrow {}^5L_6$ transition. For **[Na]$_2$[Tb(acac)$_3$].[Eu4.1]** transitions characteristic of europium(III) centred emission, $^5D_0 \rightarrow {}^7F_1$ (590 nm), $^5D_0 \rightarrow {}^7F_2$ (615 nm), $^5D_0 \rightarrow {}^7F_4$ (700 nm), are also observed. Transitions at 590 nm and 615 nm are tentatively assigned as europium(III) centred, the terbium(III) centred $^5D_4 \rightarrow {}^7F_4$ and $^5D_4 \rightarrow {}^7F_3$ transitions typically overlap. No unambiguously terbium(III) centred emission transitions are observed for **[Na]$_2$[Tb(acac)$_3$].[Eu4.1]** when excited via europium(III)

centred absorption bands. No energy transfer from the **Eu4.1** motif to terbium(III) centred excited states of **$Tb(acac)_3$** is observed.

$[Na]_2[Eu(acac)_3].[Tb4.1]$, when excited via the $^7F_0 \rightarrow {}^5L_6$ transition at λ_{ex} = 400 nm to selectively excite europium(III) centred excited states (Figure 4.6), shows characteristic emission from terbium(III) centred excited states and europium(III) centred excited states. The $^5D_4 \rightarrow {}^7F_6$ (488 nm) and $^5D_4 \rightarrow {}^7F_5$ (540 nm) terbium(III) centred transitions are observed. The europium(III) centred $^5D_0 \rightarrow {}^7F_1$ (590 nm), $^5D_0 \rightarrow {}^7F_2$ (615 nm), and $^5D_0 \rightarrow {}^7F_4$ (700 nm) transitions are also observed. The terbium(III) centred $^5D_4 \rightarrow {}^7F_4$ and $^5D_4 \rightarrow {}^7F_3$ transitions may also contribute to the peaks seen at 590 nm and 615 nm respectively. These data show energy transfer from europium(III) centred excited states to terbium(III) centred excited states. As both europium(III) and terbium(III) centred transitions are observed this energy transfer is incomplete for the measured ensemble.

Figure 4.8 shows the emission spectra of **$[Na]_2[Tb(acac)_3].[Eu4.1]$** and **$[Na]_2[Eu(acac)_3].[Tb4.1]$** when excited via the $^7F_6 \rightarrow {}^5D_4$ transition, at λ_{ex} = 488 nm, to selectively excite terbium(III) centred excited states. **$[Na]_2[Eu(acac)_3].[Tb4.1]$** shows terbium(III) centred emission with the $^5D_4 \rightarrow {}^7F_6$ (488 nm) and $^5D_4 \rightarrow {}^7F_5$ (546 nm) transition clearly present. A peak at 588 nm may be attributed to either the $^5D_4 \rightarrow {}^7F_4$ (580 nm) terbium(III) centred transition, the $^5D_0 \rightarrow {}^7F_1$ (590 nm) europium(III) centred transition, or both transitions overlapping. The peak at 615 nm is likely the $^5D_0 \rightarrow {}^7F_2$ (615 nm) transition of europium(III) centred emission, the $^5D_4 \rightarrow {}^7F_6$ (620 nm) transition of terbium(III) centred emission may be broadening this peak. The europium(III) centred transition $^5D_0 \rightarrow {}^7F_4$ (700 nm) is visible in the emission spectrum of **$[Na]_2[Eu(acac)_3].[Tb4.1]$** excited at 488 nm.

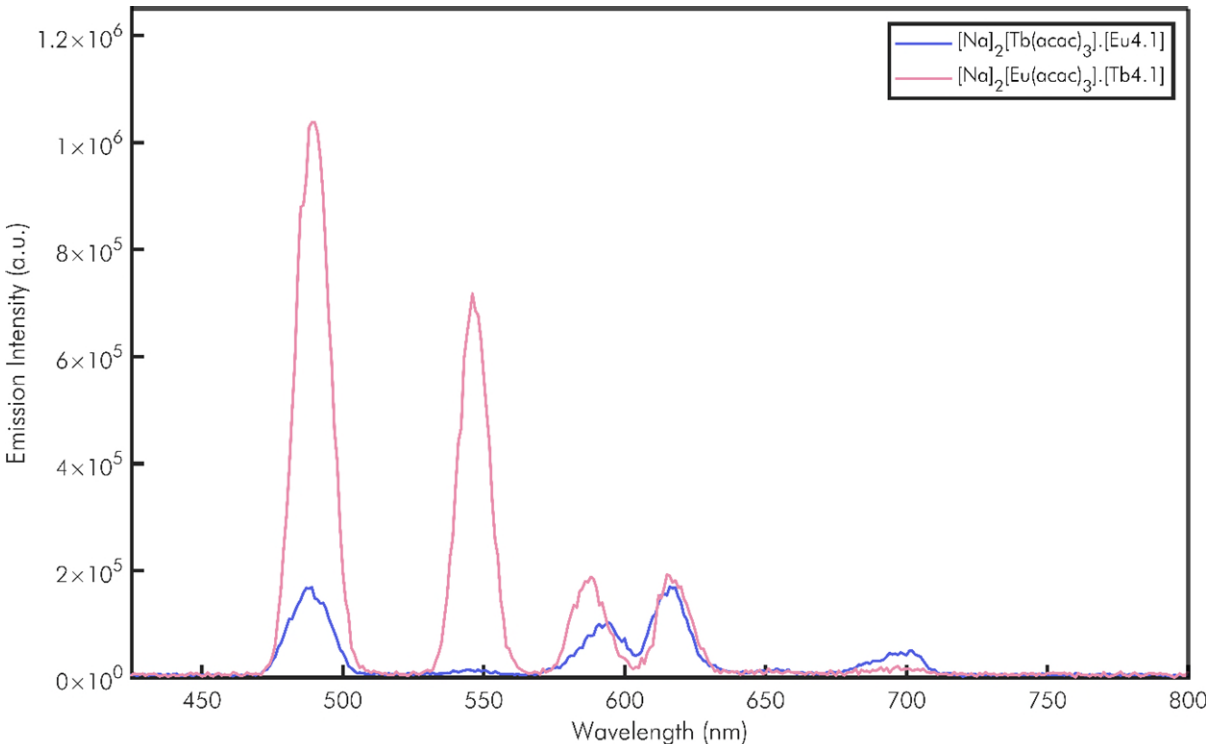

Figure 4.8: Time-gated (50 μs) emission spectra of ***[Na]$_2$[Tb(acac)$_3$].[Eu4.1]*** *(blue) and* ***[Na]$_2$[Eu(acac)$_3$].[Tb4.1]*** *(pink) in D_2O at 10^{-3} M with direct excitation of terbium(III) at 488 nm. Emission monochromator was set to a 10 nm bandpass for* ***[Na]$_2$[Tb(acac)$_3$].[Eu4.1]*** *and 7 nm bandpass for* ***[Na]$_2$[Eu(acac)$_3$].[Tb4.1].***

[Na]$_2$[Tb(acac)$_3$].[Eu4.1] shows primarily europium(III) centred emission. The peak at 488 nm being either the terbium(III) centred $^5D_4 \rightarrow {}^7F_6$ transition or an artifact from excitation at 488 nm, as seen with **Eu(acac)$_3$** (Figure 4.6). This shows energy transfer from terbium(III) centred excited states of **[Na]$_2$[Tb(acac)$_3$].[Eu4.1]** to europium(III) centred excited states. It is ambiguous whether this energy transfer is complete for the measured ensemble.

These data are weighted by how emissive a sample is, the comparative signal-to-noise of the emission of **Tb(acac)$_3$** and **H$_2$Tb4.1** show that the **Ln4.1** moiety is more emissive than the **Ln(acac)$_3$** moiety. Hence, for **[Na]$_2$[Ln'(acac)$_3$].[Ln4.1]**, one would expect to see greater emission from the **Ln4.1** moiety compared to the **Ln'(acac)$_3$** moiety, if the excited states were equally

populated. Terbium(III) complexes are generally more strongly emissive than europium(III) complexes, due to the larger energy gap between emissive and ground states.[25] Hence, one would expect terbium(III) centred excited states to contribute more strongly to the emission spectrum of **$[Na]_2[Tb(acac)_3].[Eu4.1]$** and **$[Na]_2[Eu(acac)_3].[Tb4.1]$**. Following this reasoning, it is rational to expect that **$[Na]_2[Eu(acac)_3].[Tb4.1]$** displays no europium(III) centred emission when terbium(III) centred excited states are selectively excited.

*Table 4.1: Emission lifetimes of **$[Na]_2[Tb(acac)_3].[Eu4.1]$**, **$[Na]_2[Eu(acac)_3].[Tb4.1]$**, **$Tb(acac)_3$**, and **$Eu(acac)_3$***

	τ(Eu), λ_{ex} = 400 nm, λ_{em} = 615 nm	τ(Tb), λ_{ex} = 488 nm, λ_{em} = 540 nm
$[Na]_2[Tb(acac)_3].[Eu4.1]$	0.4 ms	0.3 ms
$[Na]_2[Eu(acac)_3].[Tb4.1]$	0.4 ms	0.2 ms
$Eu(acac)_3$	0.4 ms	-
$Tb(acac)_3$	-	0.5 ms

Table 4.1 shows the lifetimes of **$[Na]_2[Tb(acac)_3].[Eu4.1]$**, **$[Na]_2[Eu(acac)_3].[Tb4.1]$**, **$Tb(acac)_3$**, and **$Eu(acac)_3$** measured in D_2O at a concentration of 10^{-5} M. Lifetimes were recorded of europium(III) centred emission by monitoring the $^5D_0 \rightarrow {}^7F_2$ at λ_{em} = 615 nm with direct excitation of europium(III) at λ_{ex} = 400 nm. For terbium(III) centred emission, lifetimes were recorded by monitoring the $^5D_4 \rightarrow {}^7F_5$ transition at λ_{em} = 540 nm, with direct excitation of terbium via the $^7F_6 \rightarrow {}^5D_4$ transition at λ_{ex} = 488 nm. Both **$[Na]_2[Tb(acac)_3].[Eu4.1]$** and **$[Na]_2[Eu(acac)_3].[Tb4.1]$** display unusually short luminescence lifetimes of terbium(III) centred emission;[26] these data suggest additional quenching mechanisms are present for **$[Na]_2[Tb(acac)_3].[Eu4.1]$** and **$[Na]_2[Eu(acac)_3].[Tb4.1]$**, attributed to energy transfer to

europium(III) centred excited states. The longest measured lifetime of terbium(III) centred emission, 0.5 ms, is in **Tb(acac)$_3$**. This decreases to 0.3 ms with self-assembly with **Na$_2$Eu4.1** to form **[Na]$_2$[Tb(acac)$_3$].[Eu4.1]**. The shortest measured lifetime of terbium(III) centred emission, 0.2 ms, is in **[Na]$_2$[Eu(acac)$_3$].[Tb4.1]**. The lifetime of europium(III) centred emission is 0.4 ms in **[Na]$_2$[Tb(acac)$_3$].[Eu4.1]**, **[Na]$_2$[Eu(acac)$_3$].[Tb4.1]**, and **Eu(acac)$_3$**.

Terbium(III) centred excited states lay higher in energy than europium(III) centred excited states.[25] Whilst energy transfer to higher-energy states, through vibrational quanta, is known, it is a less efficient and less probable phenomenon. Hence, energy transfer from terbium(III) centred excited states to europium(III) centred excited states is expected to be more efficient than energy transfer from europium(III) centred excited states to terbium(III) centred excited states. **[Na]$_2$[Eu(acac)$_3$].[Tb4.1]** displaying emission from both europium(III) and terbium(III) centred excited states when excited via a europium(III) centred transition is an example of an *'uphill'* energy transfer.

Having successfully characterised the emission of multimetallic supramolecular assemblies via direct excitation of lanthanide(III) centred excited states we sought to determine if ligand excitation would show the same characteristics. As the wavelengths required are sufficiently removed from the emission wavelengths of terbium(III) and europium(III) centred excited states, steady state emission spectra were collected i.e. no time gating between excitation light and emission measurement.

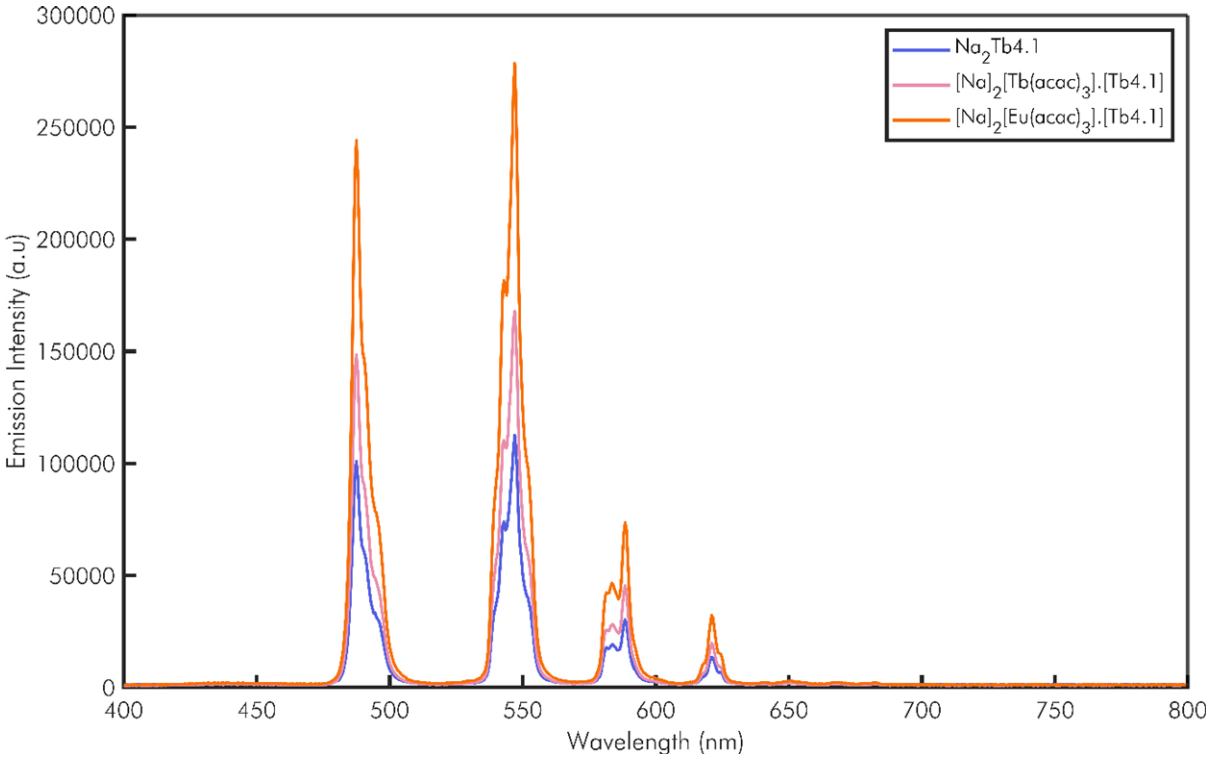

Figure 4.9: Steady state emission spectra of ***[Na]$_2$[Tb(acac)$_3$].[Tb4.1]***, ***[Na]$_2$[Eu(acac)$_3$].[Tb4.1]***, *and* ***Na$_2$Tb3.4*** *in H_2O at 10^{-4} M when excited at 308 nm. Emission monochromator slit was set to 1 nm bandpass.*

Figure 4.9 shows the emission spectra of **[Na]$_2$[Tb(acac)$_3$].[Tb4.1]**, **[Na]$_2$[Eu(acac)$_3$].[Tb4.1]**, and **Na$_2$Tb3.5** in H_2O when excited at λ_{ex} = 308 nm, via the ligand $\pi \rightarrow \pi^*$ transition. All three compounds show characteristic terbium(III) centred emission, with the $^5D_4 \rightarrow {}^7F_6$ (488 nm), $^5D_4 \rightarrow {}^7F_5$ (540 nm) , $^5D_4 \rightarrow {}^7F_4$ (580 nm), and $^5D_4 \rightarrow {}^7F_3$ (620 nm) transitions observed. No evidence of energy transfer from the ligand π^* excited states to europium(III) centred excited states is observed for **[Na]$_2$[Eu(acac)$_3$].[Tb4.1]**.

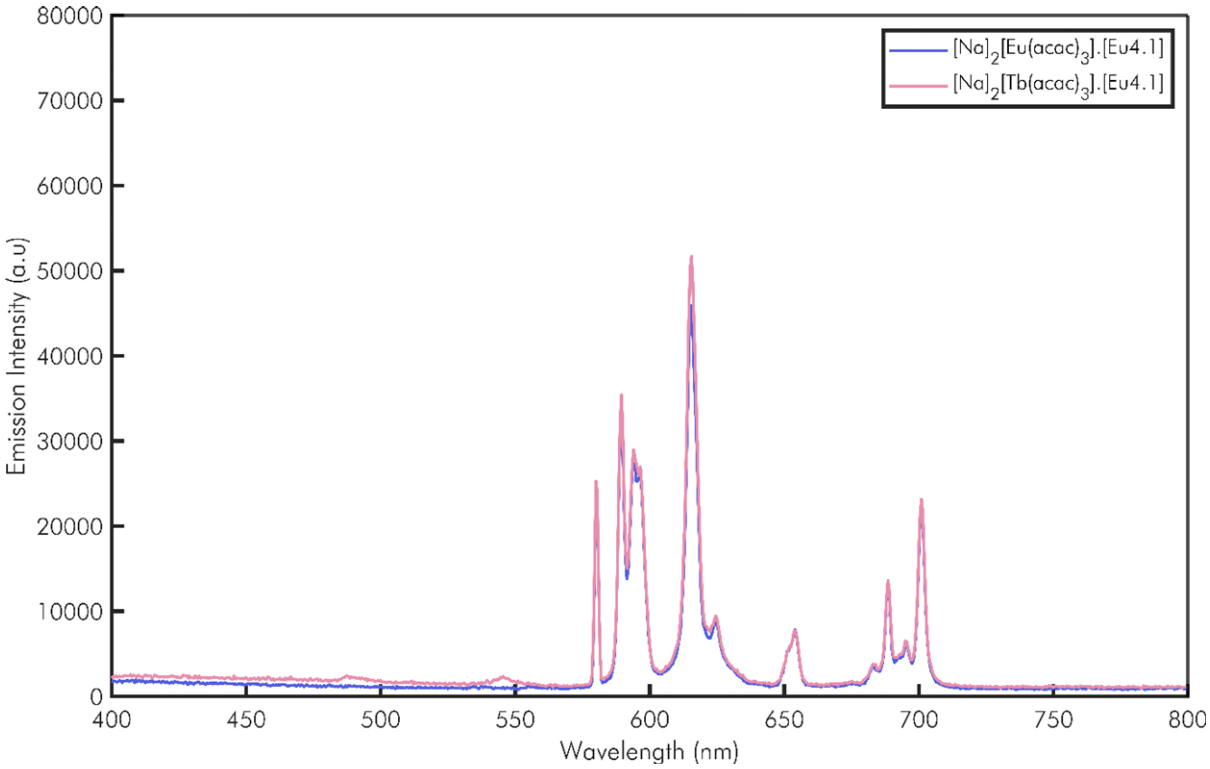

Figure 4.10: Steady-state emission spectra of ***[Na]$_2$[Eu(acac)$_3$].[Eu4.1]*** *and* ***[Na]$_2$[Tb(acac)$_3$].[Eu4.1]*** *in H_2O at 10^{-5} M, excited at 325 nm. Emission monochromator slit was set to 1 nm bandpass.*

Figure 4.10 shows the emission spectra of **[Na]$_2$[Eu(acac)$_3$].[Eu4.1]** and **[Na]$_2$[Tb(acac)$_3$].[Eu4.1]** in H_2O when excited at $\lambda_{ex} = 325$ nm, via the ligand $\pi \rightarrow \pi^*$ transition. **[Na]$_2$[Eu(acac)$_3$].[Eu4.1]** and **[Na]$_2$[Tb(acac)$_3$].[Eu4.1]** show strong characteristic europium(III) centred emission, with the $^5D_0 \rightarrow {}^7F_0$ (580 nm), $^5D_0 \rightarrow {}^7F_1$ (590 nm), $^5D_0 \rightarrow {}^7F_2$ (615 nm), $^5D_0 \rightarrow {}^7F_3$ (650 nm), and $^5D_0 \rightarrow {}^7F_4$ (700 nm) transitions observable. **[Na]$_2$[Tb(acac)$_3$].[Eu4.1]** also shows two weakly emissive peaks at 488 nm and 545 nm. These are likely the $^5D_4 \rightarrow {}^7F_6$ (488 nm) and $^5D_4 \rightarrow {}^7F_5$ (545 nm) terbium(III) centred transitions. This shows energy transfer from the ligand π^* excited state to terbium(III) centred excited states is feasible in **[Na]$_2$[Tb(acac)$_3$].[Eu4.1]** but inefficient.

Taking the data for **[Na]$_2$[Tb(acac)$_3$].[Eu4.1]** and **[Na]$_2$[Eu(acac)$_3$].[Tb4.1]** together, we only see energy transfer from ligand π^* excited states to **Ln(acac)$_3$** moiety centred excited states for **[Na]$_2$[Tb(acac)$_3$].[Eu4.1]**. This may be due to terbium(III) centred excited states being, typically,

more emissive than europium(III) centred excited states. These data were recorded in H_2O and solvent quenching effects may also impact relative quantum yields of the two lanthanide(III) centres.

4.5: SELF-ASSEMBLY OF H_2Ln4.1 WITH OTHER LANTHANIDE CONTAINING SYSTEMS

We sought to investigate the self-assembly of **H_2Tb4.1** and **H_2Eu4.1** with other lanthanide(III) containing complexes. Investigation into the self-assembly with **EuDO3A** and **TbDO3A** (Scheme 4.5) showed no indication of self-assembly. This is attributed to the salicylate motif being too bulky to coordinate to **LnDO3A**.

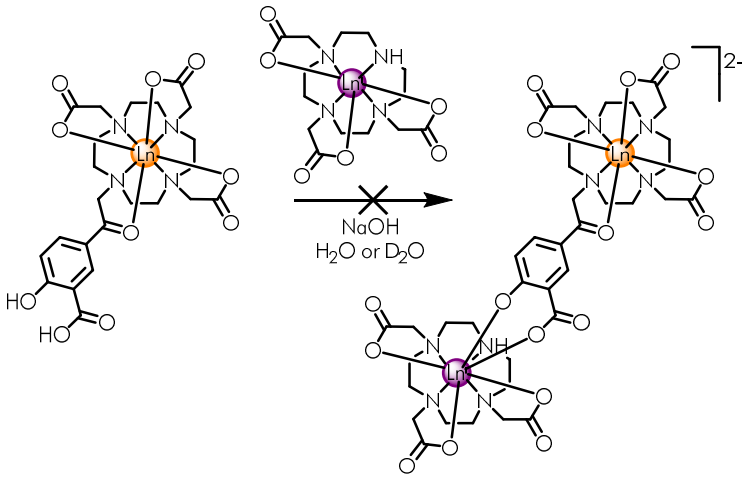

*Scheme 4.5: Proposed self-assembly of **H_2Ln4.1** with **LnDO3A***

We successfully prepared self-assembled multimetallic lanthanide complexes from **H_2Ln4.1** and **Ln'(acac)$_3$**. Direct excitation experiments proved energy transfer from europium(III) centred excited states to terbium(III) centred excited states and from terbium(III) centred excited states to europium(III) centred excited states can occur in these molecules. Excitation via ligand centred absorptions results in emission primarily from the **[Ln4.1]$^{2-}$** moiety. The possible energy transfer routes are shown in Figure 4.11. Attempts to prepared self-assembled multimetallic complexes from **H_2Ln4.1** and **Ln'DO3A** proved unsuccessful.

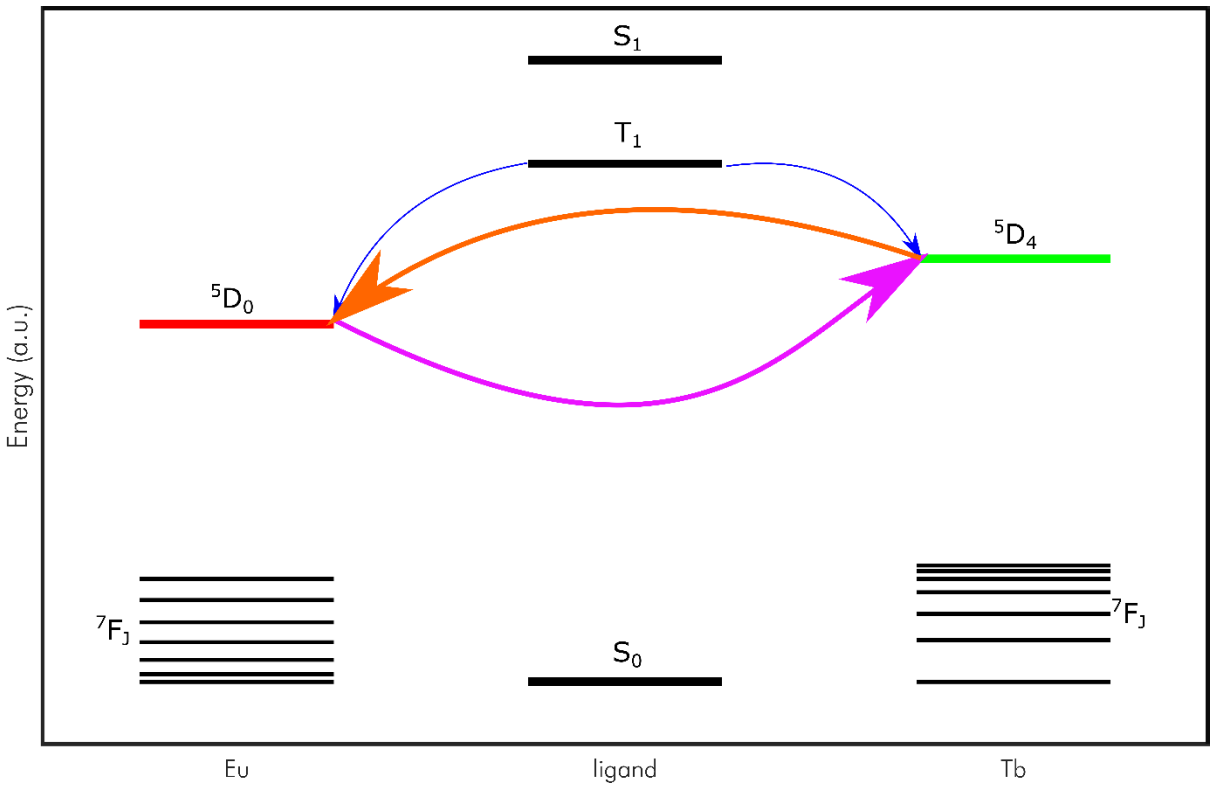

*Figure 4.11: Approximated Jablonski diagram illustrating the key energy transfer possibilities in **[Na]$_2$[Ln'(acac)$_3$].[Ln4.1]** with energy transfer from ligand centred triplet state to lanthanide(III) centred excited states (blue arrows), thermodynamically favourable energy transfer from terbium(III) centred $^5D_4$ excited states to europium(III) centred $^5D_0$ excited states (orange arrow) and the thermodynamically unfavourable energy transfer from europium(III) centred $^5D_0$ to terbium(III) centred $^5D_4$ excited state (purple arrow). Ligand centred states are estimated.*

1. G. M. Whitesides and B. Grzybowski, *Science*, 2002, 295, 2418-2421.
2. J. W. Steed and J. L. Atwood, Supramolecular chemistry, Wiley, Chichester, West Sussex, 2nd edn., 2009.
3. D. Philp and J. F. Stoddart, *Angew. Chem. Int. Ed*, 1996, 35, 1154-1196.
4. R. S. Forgan, *Chem. Sci*, 2020, 11, 4546-4562.
5. L. F. Lindoy and I. M. Atkinson, Self-assembly in supramolecular systems, Royal Society of Chemistry, Cambridge, 2000.
6. N. André, R. Scopelliti, G. Hopfgartner, C. Piguet and J.-C. G. Bünzli, *Chem. Commun*., 2002, 214-215.
7. M. Elhabiri, R. Scopelliti, J.-C. G. Bünzli and C. Piguet, *J. Am. Chem. Soc.,* 1999, 121, 10747-10762.
8. T. B. Jensen, R. Scopelliti and J.-C. G. Bünzli, *Inorg. Chem.*, 2006, 45, 7806-7814.
9. C. Piguet and J.-C. G. Bünzli, *Chem. Soc. Rev.,* 1999, 28, 347-358.
10. L.-L. Yan, C.-H. Tan, G.-L. Zhang, L.-P. Zhou, J.-C. Bünzli and Q.-F. Sun, *J. Am. Chem. Soc.,* 2015, 137, 8550-8555.
11. X.-Z. Li, C.-B. Tian and Q.-F. Sun, *Chem. Rev.*, 2022, 122, 6374-6458.
12. X.-Z. Li, L.-P. Zhou, L.-L. Yan, D.-Q. Yuan, C.-S. Lin and Q.-F. Sun *J. Am. Chem. Soc.,* 2017, 139, 8237-8244.
13. Y. Bretonnière, M. Mazzanti, J. Pécaut and M. M. Olmstead, *J. Am. Chem. Soc*., 2002, 124, 9012-9013.
14. Y. Bretonnière, M. Mazzanti, R. Wietzke and J. Pécaut, *Chem. Commun*., 2000, 1543-1544.
15. J. Hamacek and A. Vuillamy, Eur. J. *Inorg. Chem*., 2018, 2018, 1155-1166.
16. S. Swavey and R. Swavey, *Coord. Chem. Rev*., 2009, 253, 2627-2638.
17. O. A. Blackburn, M. Tropiano, L. S. Natrajan, A. M. Kenwright and S. Faulkner, *Chem. Commun*., 2016, 52, 6111-6114.
18. S. J. A. Pope, A. M. Kenwright, V. A. Boote and S. Faulkner, *Dalton Trans.*, 2003, 3780-3784.
19. J. A. Tilney, T. J. Sørensen, B. P. Burton-Pye and S. Faulkner, *Dalton Trans.*, 2011, 40, 12063-12066.
20. L. R. Hill, O. A. Blackburn, M. W. Jones, M. Tropiano, T. J. Sørensen and S. Faulkner, *Dalton Trans.*, 2013, 42, 16255-16258.
21. T. J. Sørensen, L. R. Hill and S. Faulkner, *ChemistryOpen*, 2015, 4, 509-515.
22. T. J. Sørensen and S. Faulkner, *Acc. Chem. Res.* , 2018, 51, 2493-2501.
23. J. R. Lakowicz, Principles of Fluorescence Spectroscopy, Springer US, New York, NY, 3rd. edn., 2006.
24. K. Yao, G. Karunanithy, A. Howarth, P. Holdship, A. L. Thompson, K. E. Christensen, A. J. Baldwin, S. Faulkner and N. J. Farrer, *Dalton. Trans*., 2021, 50, 8761-8767.

25. J.-C. G. Bünzli and S. V. Eliseeva, in Lanthanide Luminescence: Photophysical, Analytical and Biological Aspects, eds. P. Hänninen and H. Härmä, Springer Berlin Heidelberg, Berlin, Heidelberg, 2011, pp. 1-45.

26. A. J. Amoroso, S. J. A. Pope, *Chem. Soc. Rev.*, 2015,44, 4723-4742

5. SYNTHESIS AND PHOTOPHYSICAL CHARACTERISATION OF POLYNUCLEAR LANTHANIDE(III) COMPLEXES DERIVED FROM 5-Me-HXTA AND A NOVEL POLY-ACETIC ACID FUNCTIONALISED BENZOPHENONE DERIVATIVE

5-Me-HXTA was first reported for the preparation of polynuclear iron(III) complexes by Murch et al. who developed the complexes as models for ferritin core formation.[1, 2]

Natrajan et al. reported a series of homometallic lanthanide(III) complexes prepared with a **5-Me-HXTA** chelator.[3] The complexes of neodymium(III), samarium(III), europium(III), terbium(III), dysprosium(III), erbium(III) and ytterbium(III) were prepared. The complexes take the form of $[Ln_2(5\text{-Me-HXTA})_2]^{4-}$ with the two lanthanide(III) bridged with the phenolate oxygen atoms. Natrajan et el. report a single-crystal x-ray diffraction structure to confirm the structure in the solid state. Aqueous solution measurements suggest this structure is maintained upon dissolution. [4]

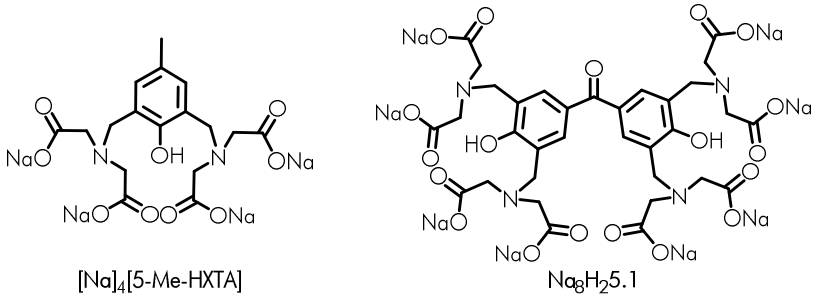

Figure 5.1: Chemical structures of ***[Na]$_4$[5-Me-HXTA]*** *and* ***Na$_8$H$_2$5.1***

We set out to extend the work of Natrajan et al.,[3,4] binuclear $[Ln_2(5\text{-Me-HXTA})_2]^{4-}$ complexes, with the preparation of tetranuclear complexes. The ligand **Na$_8$H$_2$5.1** was designed with two

septadentate chelating moieties, connected by a benzophenone linker group. It was anticipated **$Na_8H_2$5.1** could be prepared using analogous methods to **5-Me-HXTA**. Complexation of **$Na_8H_2$5.1** and **5-Me-HXTA** with lanthanide(III) ions was expected to form tetranuclear complexes of the type **$[Ln_4(5.1)(5\text{-Me-HXTA})_2]^{8-}$**.

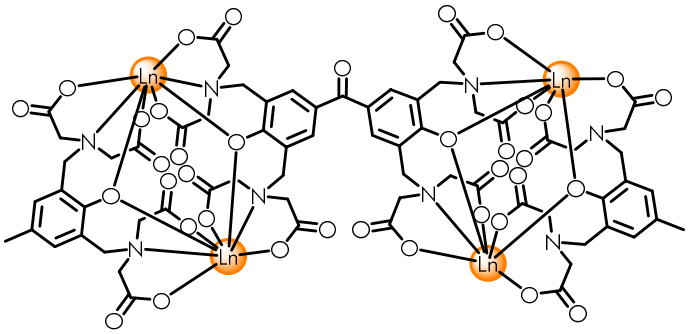

*Figure 5.2: Chemical structure of the complexes designed from **5.1** and **5-Me-HXTA***

After preparing **$Na_8H_2$5.1** and its complexes with **5-Me-HXTA**, we sought to prepare larger architectures containing only lanthanide(III) ions and **$Na_8H_2$5.1**.

5.1: SYNTHESIS OF $[Na]_4$[5-Me-HXTA] AND $Na_8H_2$5.1

$[Na]_4$[5-Me-HXTA] was prepared via a modified literature procedure.[3] A solution of 4-methylphenol (*p*-cresol) in methanol was treated with disodium iminodiacetate (1.9 equivalents) and water. The solution was heated to 60°C, and treated with paraformaldehyde (2.1 equivalents). The temperature was maintained at 60°C for 16 hours, after which an excess of methanol was added and the mixture allowed to cool to room temperature. The resultant mixture was diluted with ethanol and acetone to precipitate the target compound, which was

then collected by vacuum filtration. Washing the solid on the filter with acetone and diethyl ether afforded pure **[Na]$_4$[5-Me-HXTA]** in 52% yield.

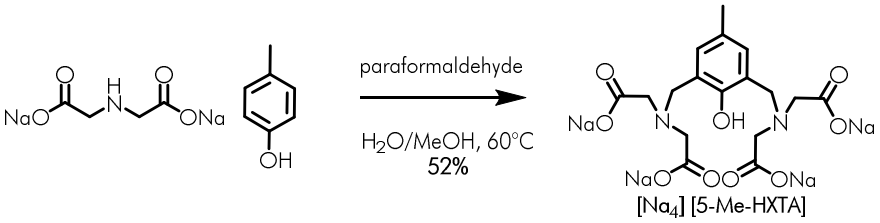

Scheme 5.1: Synthetic route to ***[Na]$_4$[5-Me-HXTA]***

Electrospray ionisation mass spectrometry found 5-Me-HXTA had been prepared as the tetrasodium salt, **[Na]$_4$[5-Me-HXTA]**, finding the $[M+H]^+$ and $[M-H]^-$ ions. The NMR data, recorded in D_2O, were consistent with this structure and matched literature reports.

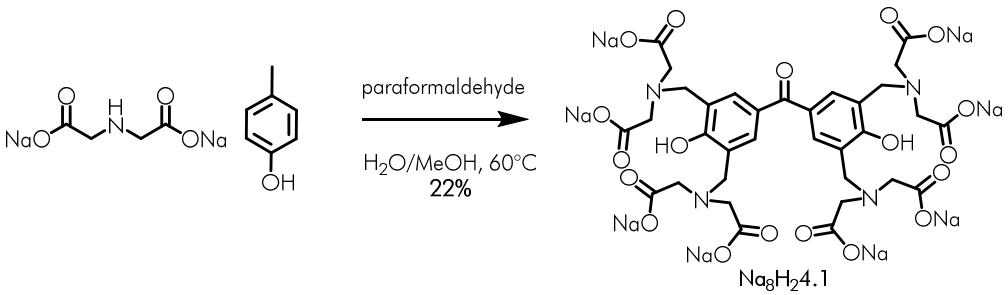

Scheme 5.2: Synthetic route to ***Na$_8$H$_2$5.1***

Na$_8$H$_2$5.1 was prepared via an analogous procedure. A solution of 4,4′-dihydroxybenzophenone in methanol was treated with disodium iminodiacetate (4.5 equivalents) and water. The solution was heated to 60°C, and treated with paraformaldehyde (4.5 equivalents). The temperature was maintained at 60°C for 24 hours, after which an excess

of methanol was added and the mixture allowed to cool to room temperature to precipitate the title compound, which was collected by vacuum filtration. Washing the solid on the filter with methanol, acetone, and diethyl ether to afforded pure **$Na_8H_2$5.1** in 22% yield.

Electrospray ionisation mass spectrometry found **5.1** had been prepared as the octasodium salt, **$Na_8H_2$5.1**, finding the $[M+H]^+$ and $[M-H]^-$ ions. NMR data, recorded in D_2O, were consistent with this structure. Despite the high mass, there are three sets of equivalent protons observed at 7.52 ppm, 3.91 ppm, and 3.31 ppm. These integrate with a 1:2:4 intensity. The phenolic protons are exchanged with the solvent and not observed.

5.3: SYNTHESIS OF $[Na]_8[Ln_4(5.1)(5\text{-Me-HXTA})_2]$

$[Na]_8[Eu_4(5.1)(5\text{-Me-HXTA})_2]$ and **$[Na]_8[Lu_4(5.1)(5\text{-Me-HXTA})_2]$** were prepared by treating a solution of **$Na_8H_2$5.1** and 2 equivalents of **$[Na]_4$[5-Me-HXTA]** in water with 4 equivalents of the parent lanthanide(III) triflate salt. The mixture was heated to 60°C for 16 hours, basified with 4 equivalents of sodium hydroxide solution (1 M in water) and heated for a further 24 hours. After cooling to room temperature, the target complexes were precipitated by the addition of acetonitrile and collected by centrifugation. The complexes were then recrystalised from water with ethanol. **$[Na]_8[Eu_4(5.1)(5\text{-Me-HXTA})_2]$** was afforded in 23% yield as a yellow solid. **$[Na]_8[Lu_4(5.1)(5\text{-Me-HXTA})_2]$** was afforded in 94% yield as an off-white solid.

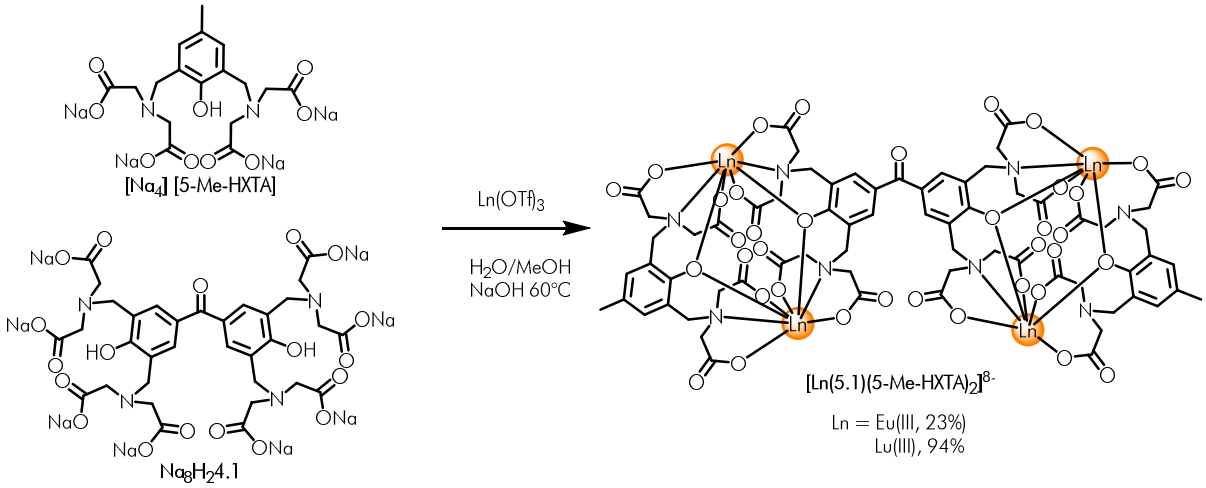

Scheme 5.3; Synthetic route to ***[Na]$_8$[Ln$_4$(5.1)(5-Me-HXTA)$_2$)]****, Ln = Eu(III), Lu(III)*

[Na]$_8$[Eu$_4$(5.1)(5-Me-HXTA)$_2$] and **[Na]$_8$[Lu$_4$(5.1)(5-Me-HXTA)$_2$]** were dried under high-vacuum prior to use to ensure any residual water was completely removed.

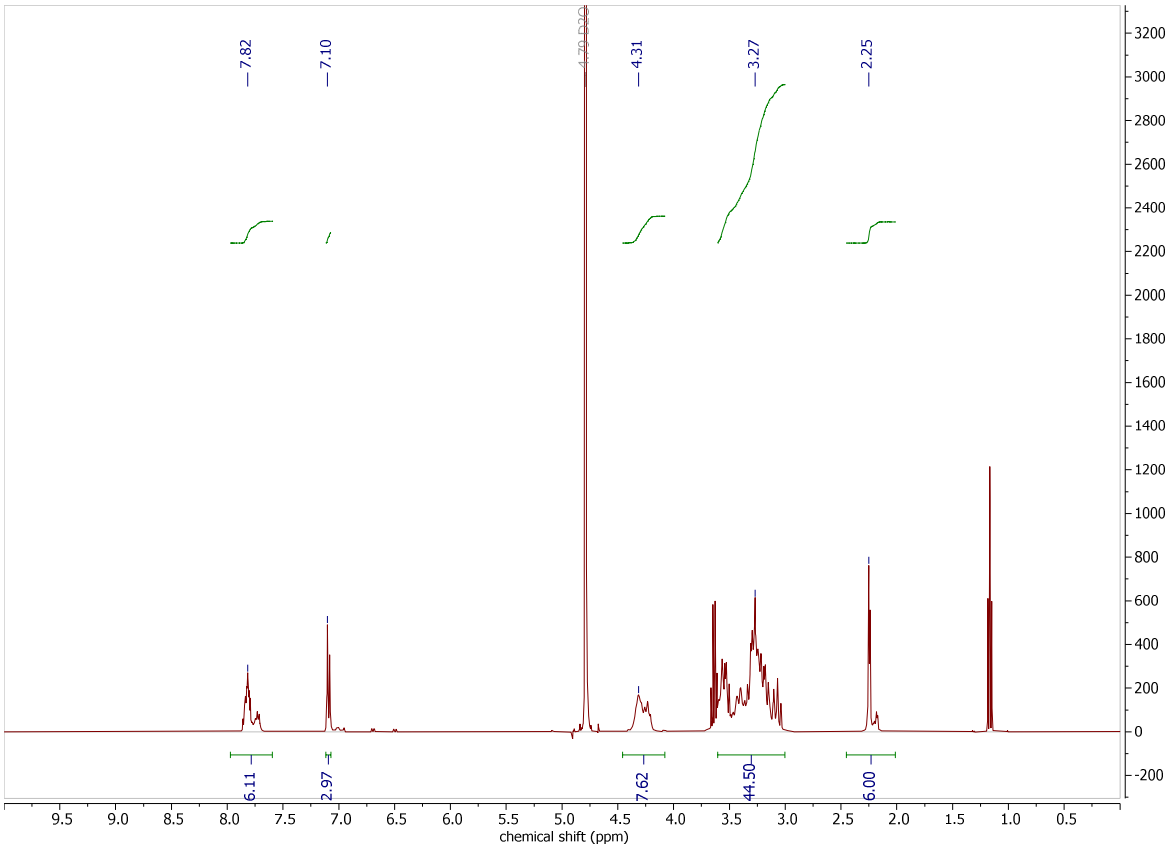

Figure 5.3: 400 MHz ^{1}H NMR spectrum of ***[Na]$_8$[Lu$_4$(5.1)(5-Me-HXTA)$_2$]*** *in D_2O*

Figure 5.3 shows the ^{1}H NMR spectrum recorded at 400 MHz in D_2O for **[Na]$_8$[Lu$_4$(5.1)(5-Me-HXTA)$_2$]**. The resonances at 1.17 and 3.65 ppm are from residual ethanol, which remained after 72 hours of drying under high vacuum. The resonance at 3.65 ppm complicates integral analysis for the methylene resonances. The ^{1}H NMR is consistent with the proposed structure and mass spectrometry data. Electrospray ionisation mass spectrometry found **[Na]$_7$[Lu$_4$(5.1)(5-Me-HXTA)$_2$]**, corresponding to an [M-Na]$^-$ adduct. An m/z = 2454.0010 was found, **[Na]$_7$[Lu$_4$(5.1)(5-Me-HXTA)$_2$]** requires /z = 2454.0034.

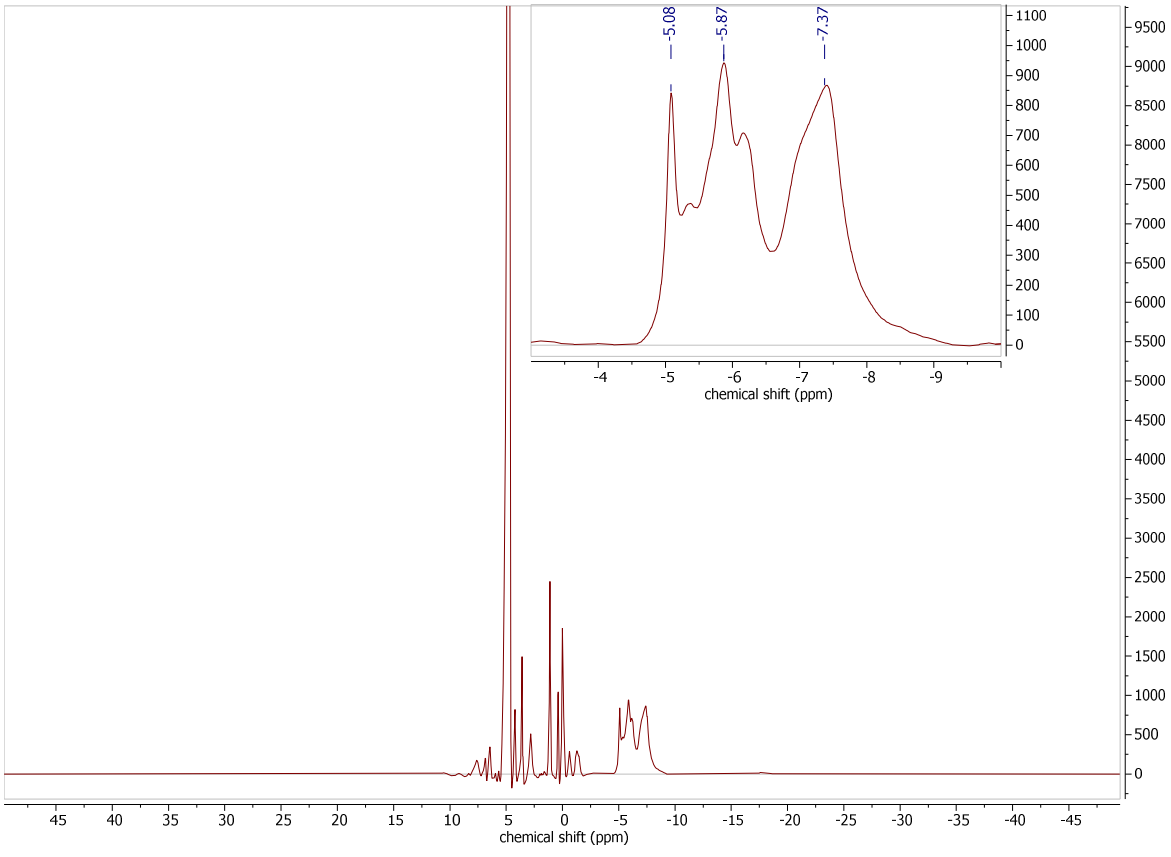

*Figure 5.4: 400 MHz ^{1}H NMR spectrum of **[Na]$_8$[Eu$_4$(5.1)(5-Me-HXTA)$_2$]** recorded in D_2O.*

Figure 5.4 shows the ^{1}H NMR spectrum of **[Na]$_8$[Eu$_4$(5.1)(5-Me-HXTA)$_2$]** recorded at 400 MHz in D_2O. Three overlapping resonances are observed at -7.37, -5.87, and -5.08 ppm. These

are likely the N-C$\underline{H_2}$-COO protons, closest to the europium(III) centre. Electrospray ionisation mass spectrometry found **[Na]$_7$[Eu$_4$(5.1)(5-Me-HXTA)$_2$]**, corresponding to an [M-Na]$^-$ adduct. An m/z = 2342.9444 was found, **[Na]$_7$[Eu$_4$(5.1)(5-Me-HXTA)$_2$]** requires /z = 2342.9355.

5.3: UV-VISIBLE SPECTROSCOPY OF [Na]$_8$[Ln$_4$(5.1)(5-Me-HXTA)$_2$]

The UV-Visible absorption spectra for **[Na]$_8$[Eu$_4$(5.1)(5-Me-HXTA)$_2$]** and **[Na]$_8$[Lu$_4$(5.1)(5-Me-HXTA)$_2$]** are shown in Figure 5.5. Four absorption maxima are observed, at 205 nm, 240 nm, 295 nm, and 333 nm. Reported literature data for **Eu$_2$(HXTA)$_2$** observe three maxima at 205 nm, 240 nm, and 300 nm. The maximum at 333 nm is assigned as the benzophenone π — π^* transition. The maximum at 300 nm is the phenolic absorption of HXTA.[3]

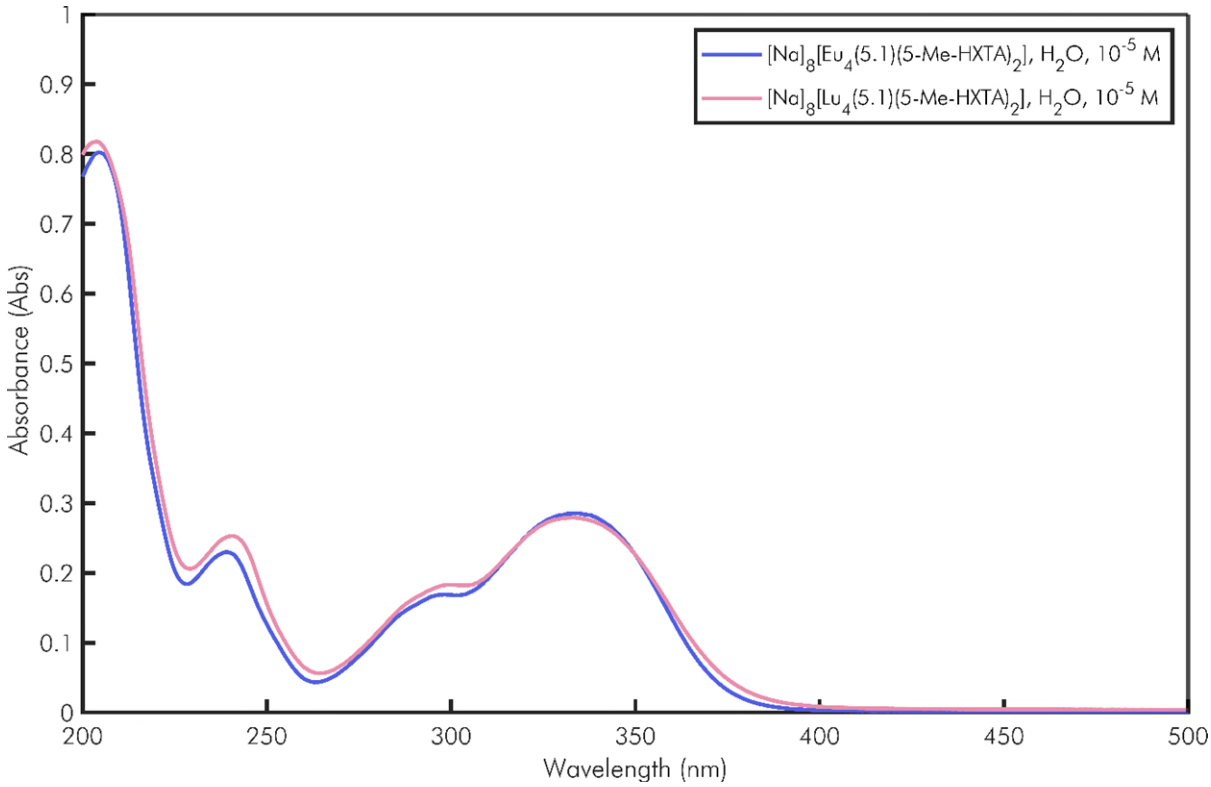

Figure 5.5: UV-visible spectra of ***[Na]$_8$[Eu$_4$(5.1)(5-Me-HXTA)$_2$]*** *(pink) and* ***[Na]$_8$[Lu$_4$(5.1)(5-Me-HXTA)$_2$]*** *(blue) in H_2O at 10^{-5} M concentration*

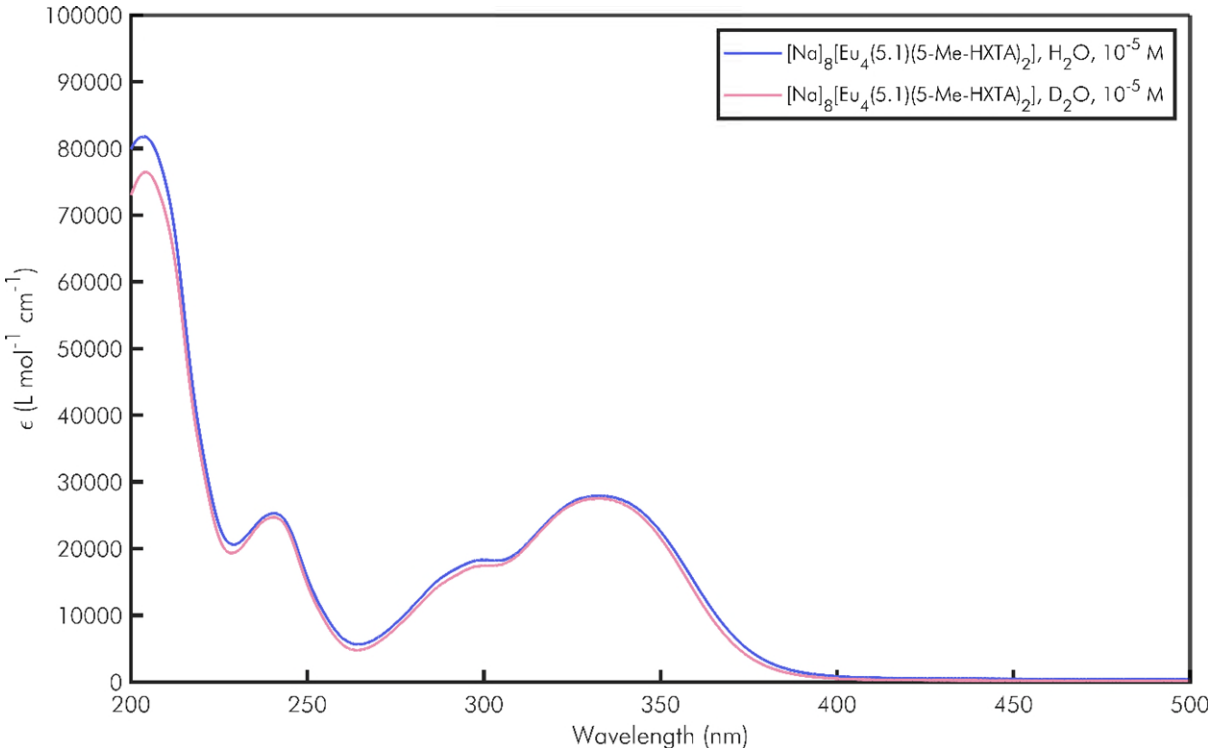

Figure 5.6: UV-visible absorption spectra of ***[Na]$_8$[Eu$_4$(5.1)(5-Me-HXTA)$_2$]*** *in H_2O (blue) and D_2O (pink) recorded at a concentration of 10^{-5} M.*

The UV-Visible absorption spectra for **[Na]$_8$[Eu$_4$(5.1)(5-Me-HXTA)$_2$]** in H_2O and D_2O are shown in Figure 5.6. There is no meaningful difference between the two spectra. The same is seen for **[Na]$_8$[Lu$_4$(5.1)(5-Me-HXTA)$_2$]** in H_2O and D_2O.

Figure 5.7 shows the emission spectra of **$[Na]_8[Lu_4(5.1)(5\text{-Me-HXTA})_2]$** in H_2O, with excitation at each of the UV-visible absorption maxima: 205 nm, 240 nm, 292 nm, and 333 nm. A broad emission spectrum, characteristic of emission from ligand centred excited states, is observed. This emission is significantly more intense when excited at 292 nm and 333 nm. These data imply excitation at λ_{ex} = 292 nm and λ_{ex} = 333 nm is more efficient at exciting ligand centred excited states. When exciting at λ_{ex} = 333 nm the emission intensity is more intense in D_2O compared to H_2O.

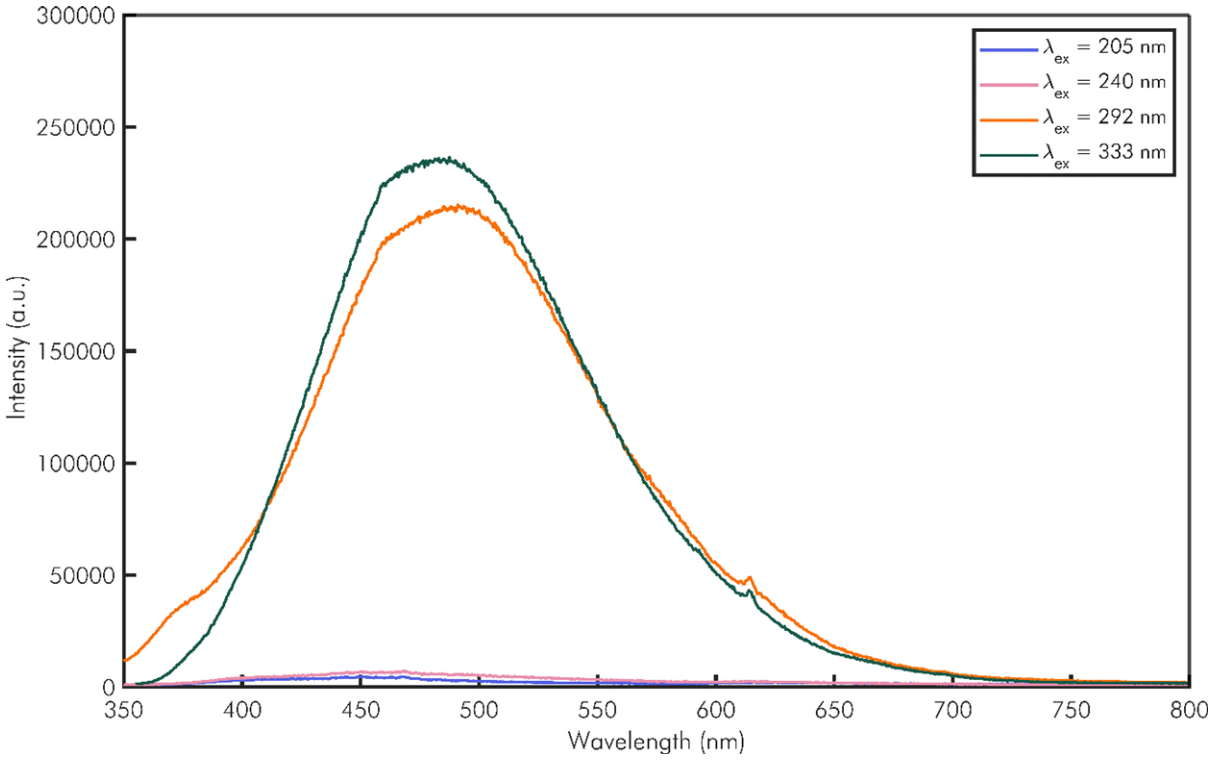

Figure 5.7: Emission spectra of ***$[Na]_8[Lu_4(5.1)(5\text{-Me-HXTA})_2]$*** *when excited at 205 nm (blue), 240 nm (pink), 292 nm (orange) and 333 nm (green). All recorded at 10^{-5} M in H_2O. Emission monochromator bandpass of 1 nm was used.*

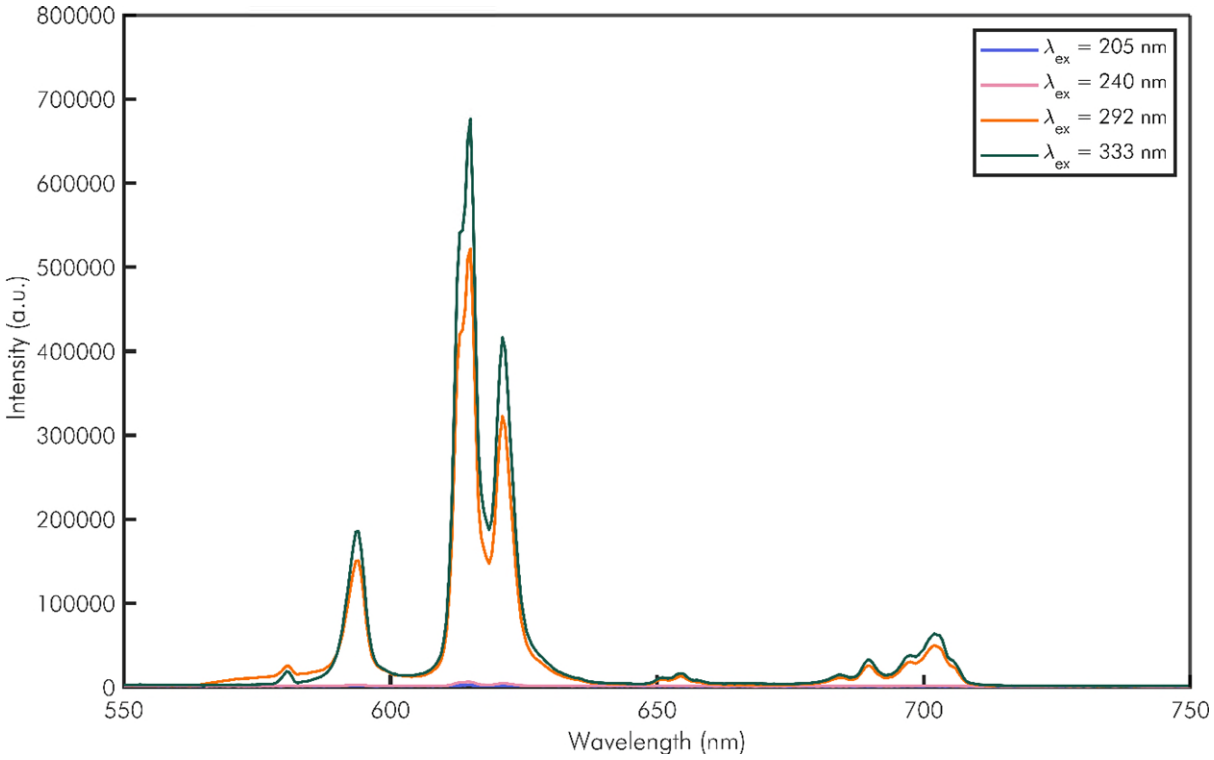

Figure 5.8: Steady state emission spectra of ***[Na]$_8$[Eu$_4$(5.1)(5-Me-HXTA)$_2$]*** *when excited at 205 nm (blue), 240 nm (pink), 292 nm (orange) and 333 nm (green). All recorded at 10^{-5} M in H_2O. Emission monochromator bandpass of 1 nm was used.*

Figure 5.8 shows the emission spectra of **[Na]$_8$[Eu$_4$(5.1)(5-Me-HXTA)$_2$]** when excited at each of the UV-visible absorption maxima: 205 nm, 240 nm, 292 nm, and 333 nm. As with **[Na]$_8$[Lu$_4$(5.1)(5-Me-HXTA)$_2$]**, excitation at λ_{ex} = 292 nm and λ_{ex} = 333 nm leaded to significantly intense emission. The observed emission is characteristic for europium(III) centred emission, with emission bands into the $^7F_0$, $^7F_1$, $^7F_2$, $^7F_3$, $^7F_4$, and $^7F_5$ levels observed. Some residual ligand centred emission is observed (λ_{em} = 490 nm). These data are consistent with excitation via benzophenone centred excited states and energy transfer to europium(III) centred excited states.

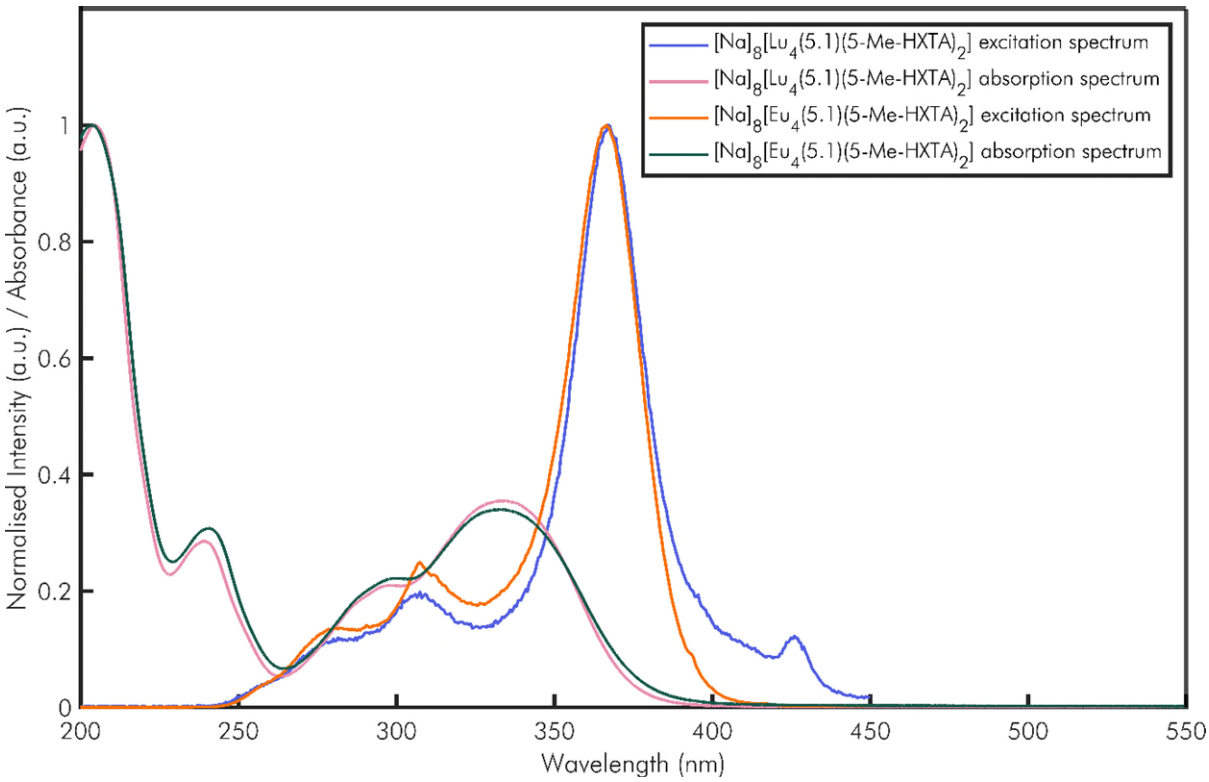

Figure 5.9: Comparison of normalised UV-visible absorption spectra for ***[Na]8[Eu4(5.1)(5-Me-HXTA)2]*** *(green) and* ***[Na]8[Lu4(5.1)(5-Me-HXTA)2]*** *(pink) and normalised luminescence excitation spectra for* ***[Na]8[Eu4(5.1)(5-Me-HXTA)2]*** *(orange) and* ***[Na]8[Lu4(5.1)(5-Me-HXTA)2]*** *(blue) all recorded in H_2O at a concentration of 10^{-5} M. For the luminescence excitation spectrum an excitation monochromator bandpass of 1 nm was used.*

Figure 5.9 shows the normalised excitation spectra and normalised UV-visible spectra for **[Na]8[Eu4(5.1)(5-Me-HXTA)2]** and **[Na]8[Lu4(5.1)(5-Me-HXTA)2]** recorded in H_2O at a concentration of 10^{-5} M. The excitation spectra were recorded by monitoring λ_{em} = 615 nm for **[Na]8[Eu4(5.1)(5-Me-HXTA)2]** and λ_{em} = 500 nm for **[Na]8[Lu4(5.1)(5-Me-HXTA)2]**. These data are in agreement with the observed emission data; population of the europium(III) centred excited states of **[Na]8[Eu4(5.1)(5-Me-HXTA)2]** and ligand centred excited states of **[Na]8[Lu4(5.1)(5-Me-HXTA)2]** occurs via absorption bands at 295 nm and 333 nm. A further strongly exciting band at 365 nm appears in the excitation spectra.

Table 5.1: Emission lifetimes in H_20 and D_2O and the calculated hydration number, q.

	$\tau(H_2O)$	$\tau(D_2O)$	q
$[Na]_8[Eu_4(5.1)(5\text{-Me-HXTA})_2]$	0.67	0.88	0.1

Table 5.1 shows the luminescence lifetimes for **$[Na]_8[Eu_4(5.1)(5\text{-Me-HXTA})_2]$** in H_2O and D_2O. The lifetimes were obtained by recording the decay in emission intensity as a function of time. Acquired data were fitted to a mono-exponential decay function. The luminescence lifetime for **$[Na]_8[Eu_4(5.1)(5\text{-Me-HXTA})_2]$** increases in D_2O compared to H_2O. When using the modified Horrocks equation,[5] the hydration number, q, is calculated as 0.1 coordinated water molecules. An error of $\pm$ 0.5q is expected with the modified Horrocks equation, this likely means that the europium(III) ions are completely coordinated by the **5.1** and **5-Me-HXTA** ligands, and there are no coordinating water molecules. The difference in lifetime is likely a function of secondary coordination sphere water molecules.

5.5: SYNTHESIS OF LARGER ARCHITECTURES WITH $Na_8H_2$5.1

Having successfully expanded the originally reported binuclear complexes of the lanthanide(III) ions with **5-Me-HXTA** to tetranuclear complexes with **5.1** as a bridging ligand we set out to explore the preparation of larger architectures. The internal angle of the two chelating sides of **$Na_8H_2$5.1** is such that the preparation of larger (potentially cyclic) architectures is feasible. We explored the preparation of such architectures by complexing different ratios of lanthanide(III) ions to **$Na_8H_2$5.1**.

For all the given ratios of lanthanide(III) ions to **$Na_8H_25.1$**, 1:1, 1:2, 1:2.3, the complexes were prepared using the same procedure. To a solution of europium(III) triflate in water was added **$Na_8H_25.1$**. The mixture was heated to reflux for 16 hours and then allowed to cool to room temperature. 8 equivalents sodium hydroxide per **$Na_8H_25.1$** was added, the mixture heated and stirred for 24 hours, allowed to cool to room temperature and filtered to remove any precipitate. The resultant solution was evaporated to dryness to afford the complexes: **Eu5.1**, **$Eu(5.1)_2$** and **$Eu(5.1)_{2.3}$**. Prepared complexes were dried under high-vacuum prior to use to ensure any residual water was removed.

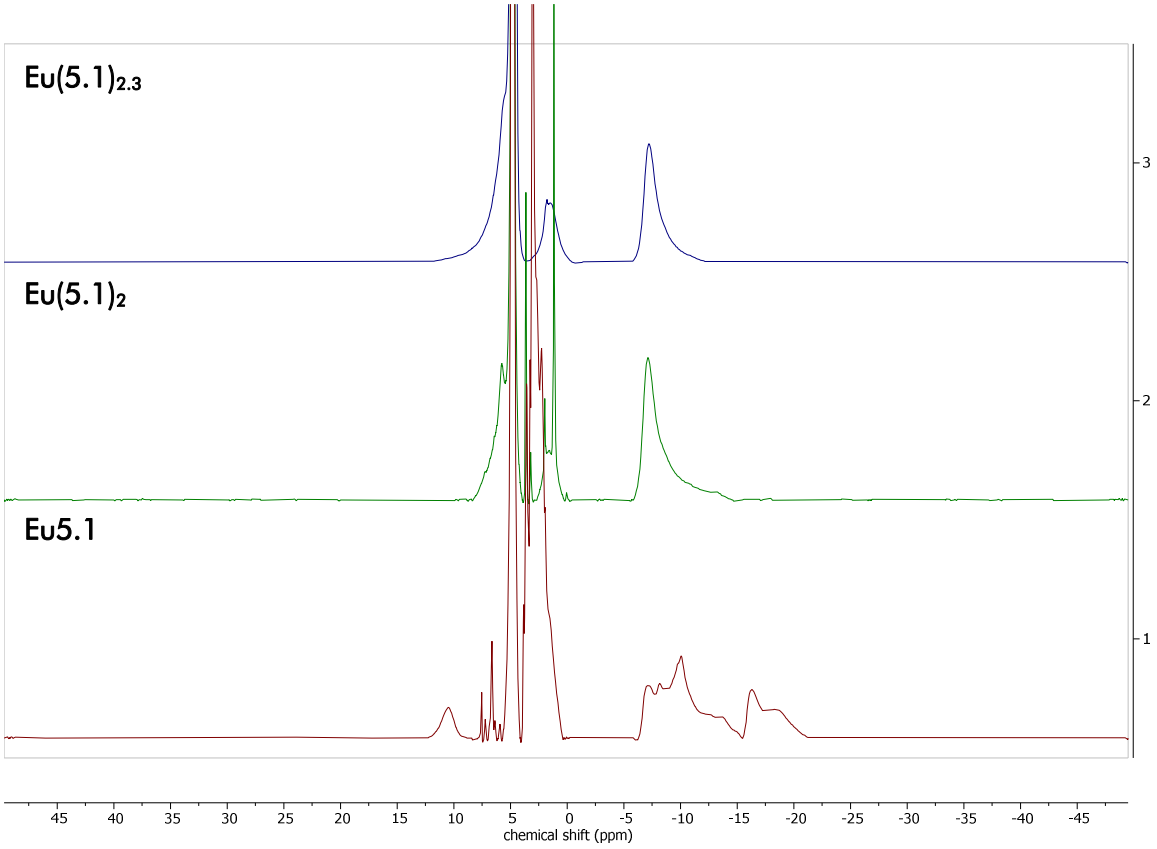

*Figure 5.10: 1H NMR spectra recorded at 400 MHz in D_2O top: **$Eu(5.1)_{2.3}$** middle: **$Eu(5.1)_2$** bottom: **Eu5.1***

Figure 5.10 shows the ^1H NMR spectra of **Eu5.1**, **$Eu(5.1)_2$**, **$Eu(5.1)_{2.3}$** in D_2O. **$Eu(5.1)_2$** and **$Eu(5.1)_{2.3}$** are very similar with a single broad resonance outside the diamagnetic window

at -7.14 ppm and -7.22 ppm respectively. **Eu5.1** shows multiple overlapping resonances at: -16.29 ppm, -10.06 ppm, -8.19 ppm, and -7.18 ppm. This suggests more structural complexity or lower symmetry for **Eu5.1** compared to **Eu(5.1)$_2$** and **Eu(5.1)$_{2.3}$**.

5.6: UV-VISIBLE AND LUMINESCENCE SPECTROSCOPY OF Eu(5.1)$_n$

Figure 5.11 shows the UV-visible absorption spectra of **Eu5.1**, **Eu(5.1)$_2$** and **Eu(5.1)$_{2.3}$** in H_2O at a concentration of 10^{-6} M. The spectra in D_2O are similar, within reasonable error. Similarly, to **[Na]$_8$[Eu$_4$(5.1)(5-Me-HXTA)$_2$]**. there are four primary absorption bands: 205 nm, 240 nm, 295 nm, and 350 nm. The lowest energy absorption band is bathochromicaly shifted compared to **[Na]$_8$[Eu$_4$(5.1)(5-Me-HXTA)$_2$]**.

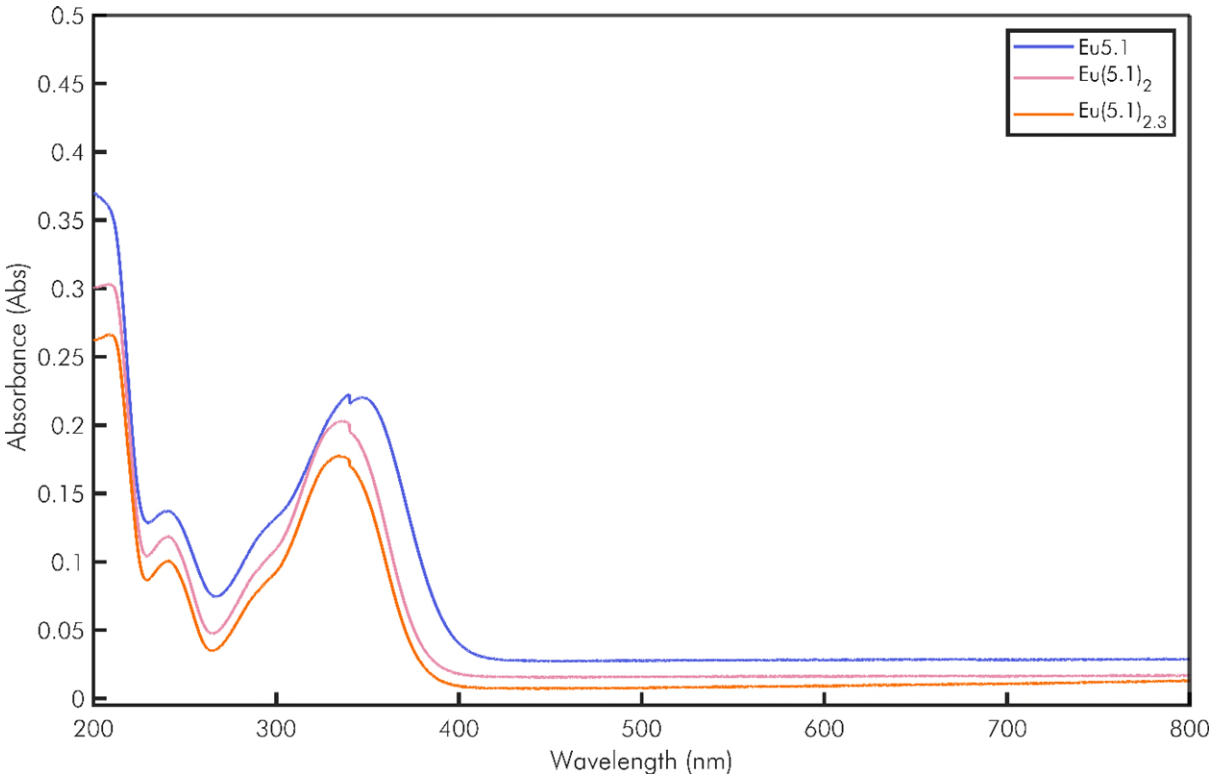

*Figure 5.11: UV-Visible absorption spectra for **Eu5.1**, **Eu(5.1)$_2$** and **Eu(5.1)$_{2.3}$** at 10^{-6} M in H_2O.*

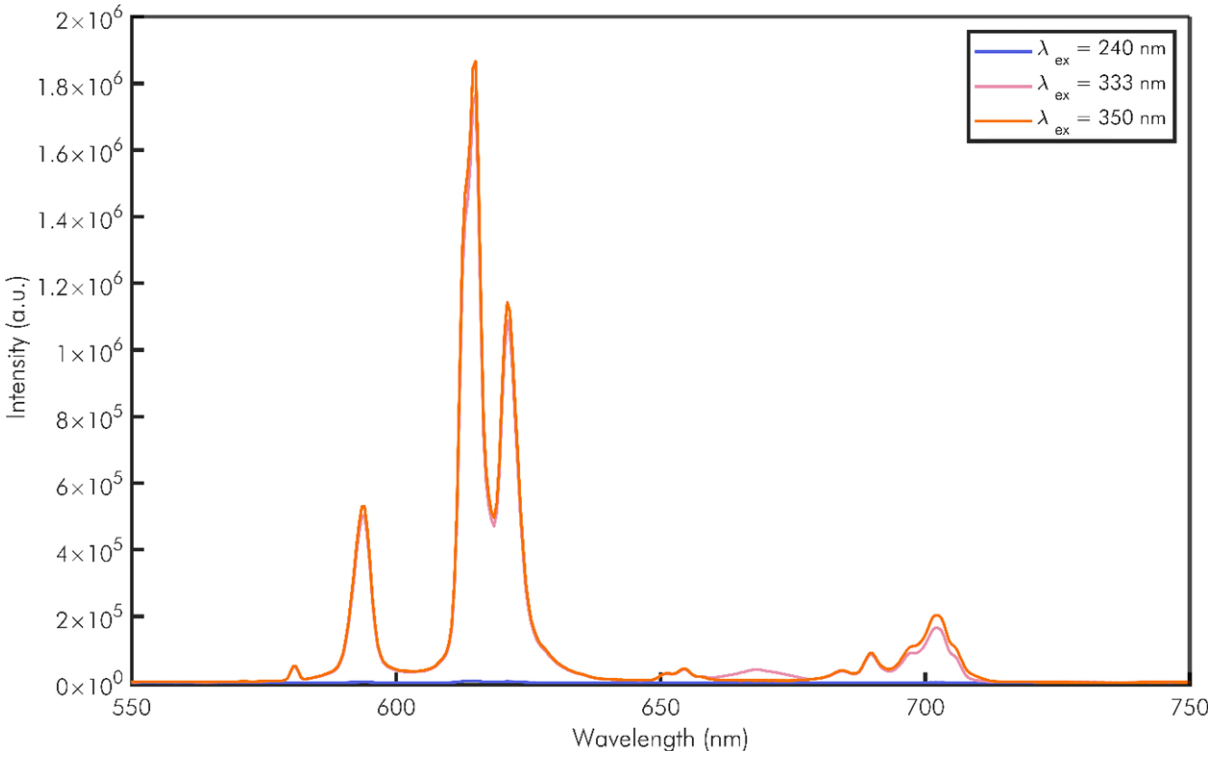

Figure 5.12: Emission spectra of ***Eu(5.1)$_2$*** *in D_2O at 10^{-6} M, when excited at 240 nm (blue), 333 nm (pink), and 350 nm (orange). Emission monochromator bandpass of 1 nm was used.*

Figure 5.12 shows the emission spectra of **Eu(5.1)$_2$** in D_2O at a concentration of 10^{-6} M with varying excitation wavelengths. Strong europium(III) centred emission is observed with excitation at λ_{ex} = 333 and λ_{ex} = 350 nm. Only weak emission is observed with excitation at λ_{ex} = 240 nm. This is consistent with **[Na]$_8$[Eu$_4$(5.1)(5-Me-HXTA)$_2$]** complexes previously discussed.

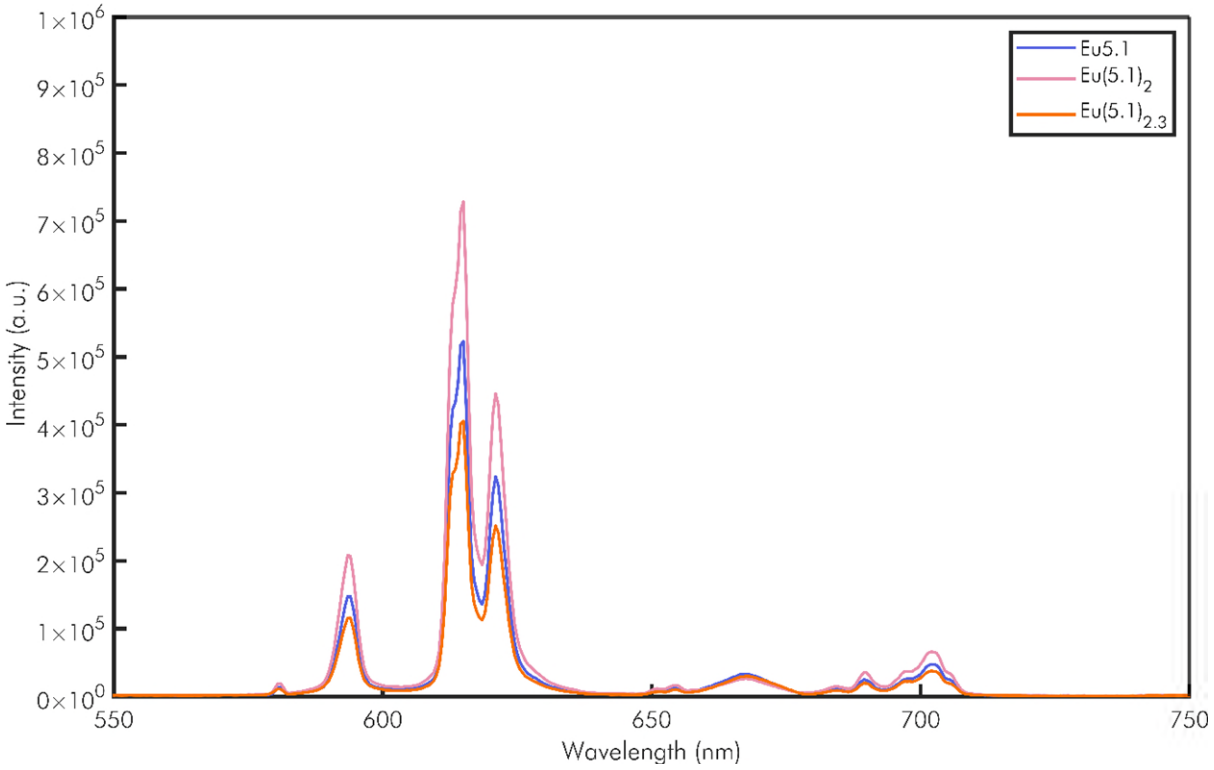

Figure 5.13: Emission spectra of ***Eu5.1*** *(blue),* ***Eu(5.1)$_2$*** *(pink), and* ***Eu(5.1)$_{2.3}$*** *(orange) when excited at 333 nm, in H_2O at a concentration of 10^{-6} M. Emission monochromator bandpass of 1 nm was used.*

Eu5.1, **Eu(5.1)$_2$**, and **Eu(5.1)$_{2.3}$** have very similar emission spectra (when excited at λ_{ex} = 333 nm, in H_2O at a concentration of 10^{-6} M) as shown in Figure 5.13. There is some small variation in emission intensity observed. The line shape, including the hypersensitive $^5D_0 \rightarrow {}^7F_2$ transition, are the same across **Eu5.1**, **Eu(5.1)$_2$**, and **Eu(5.1)$_{2.3}$** suggesting similar local coordination environments of the emissive europium(III) ion.

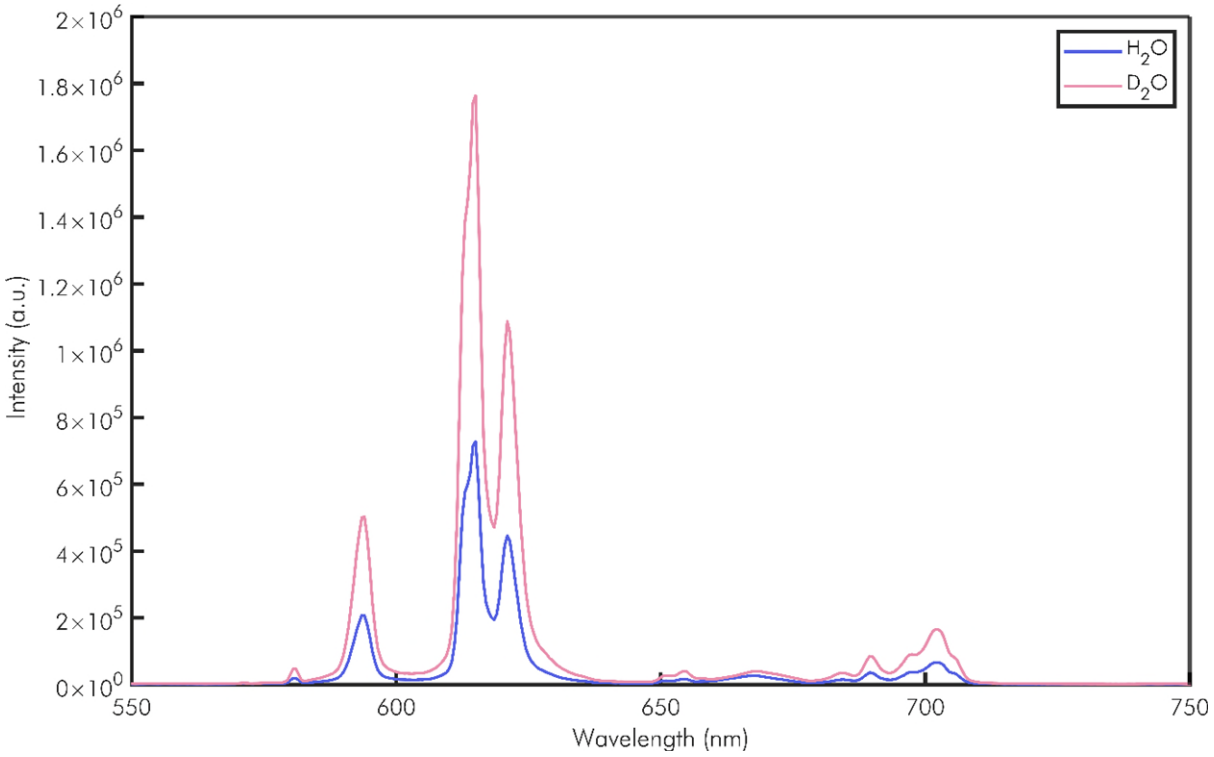

Figure 5.14: Emission spectra of ***Eu(5.1)₂*** *in H_2O (blue) and D_2O (pink) at a concentration of 10^{-6} M, excited at 333 nm. Emission monochromator bandpass of 1 nm was used.*

Emission intensity was significantly greater in D_2O compared to H_2O. Figure 5.14 shows the spectra for **Eu(5.1)₂** (excited at λ_{ex} = 350 nm, at a concentration of 10^{-6} M). **Eu5.1** and **Eu(5.1)$_{2.3}$** show similar results. These data indicate the emissive europium(III) ions are influenced by proximate solvent molecules.

Table 5.2: Measured lifetimes for ***Eu5.1****,* ***Eu(5.1)₂****, and* ***Eu(5.1)$_{2.3}$*** *in H_2O and D_2O and the calculated hydration number, q.*

	$\tau(H_2O)$	$\tau(D_2O)$	q
Eu5.1	0.82	1.10	0
Eu(5.1)₂	0.78	0.97	0
Eu(5.1)$_{2.3}$	0.72	0.87	0

Table 5.2 gives the measured lifetimes for **Eu5.1**, **Eu(5.1)$_2$**, and **Eu(5.1)$_{2.3}$** in H_2O and D_2O, at a concentration of 10^{-6} M. Lifetimes were measured by monitoring the emission intensity as a function of time at λ_{em} = 615 nm. Using the modified Horrocks equation the number of coordinated water molecules, q, can be calculated.[5] The calculated values of q imply there are no coordinated water molecules. A significant assumption of the modified Horrocks equation is that solvent quenching is the dominant quenching mechanism. Where other quenching mechanisms are significant, such as in molecules with proximate lanthanide-lanthanide connections, these assumptions can break down. As such the reported values of q are taken as inconclusive.

5.7: CONCLUSIONS

These data show that we successfully prepared two novel tetranuclear complexes from **[Na]$_4$[5-Me-HXTA]** and **Na$_8$H$_2$5.1**. The prepared complexes, **[Na]$_8$[Eu$_4$(5.1)(5-Me-HXTA)$_2$]** and **[Na]$_8$[Lu$_4$(5.1)(5-Me-HXTA)$_2$]**, were emissive when excited via ligand centred absorption bands. **[Na]$_8$[Eu$_4$(5.1)(5-Me-HXTA)$_2$]** exhibited characteristic emission from europium(III) centred excited states. Measurement of the luminescence lifetime in protic and deuterated solvent suggest a hydration number of 0, though alternative quenching pathways due to proximate lanthanide(III) ions may be impacting this result.

These data show that we successful prepared three novel complexes containing europium(III) and **Na$_8$H$_2$5.1**. The prepared complexes, **Eu5.1**, **Eu(5.1)$_2$**, and **Eu(5.1)$_{2.3}$**, were emissive when excited via ligand centred absorption bands at 333 nm and 350 nm. **Eu5.1**, **Eu(5.1)$_2$**, and **Eu(5.1)$_{2.3}$** exhibited characteristic emission from europium(III) centred excited states. Measurement of the luminescence lifetime in H_2O and D_2O suggest a hydration number of 0.

Alternative quenching pathways due to proximate lanthanide(III) ions may be impacting this result.

5.8: REFERENCES

1. B. P. Murch, F. C. Bradley, P. D. Boyle, V. Papaefthymiou and L. Que, Jr., *J. Am. Chem. Soc*, 1987, 109, 7993-8003.
2. B. P. Murch, P. D. Boyle and L. Que, Jr., *J. Am. Chem. Soc*, 1985, 107, 6728-6729.
3. L. S. Natrajan, P. L. Timmins, M. Lunn and S. L. Heath, *Inorg. Chem*., 2007, 46, 10877-10886.
4. L. S. Natrajan, A. J. L. Villaraza, A. M. Kenwright and S. Faulkner, *Chem. Commun*., 2009, 6020-6022.
5. A. Beeby, I. M. Clarkson, R. S. Dickins, S. Faulkner, D. Parker, L. Royle, A. S. de Sousa, J. A. Gareth Williams and M. Woods, *J. Chem. Soc., Perkin Trans.*, 1999, 493-504.

6. CONCLUSIONS

The overall theme of this thesis was to explore the routes to preparing, characterising and understanding multimetallic lanthanide complexes.

The preparation of bimetallic lanthanide complexes without any bridging motif, **$Ln_2$3.3**, in which an acetyl ester could be hydrolysed to introduce phenolate bridging, allowed the control of intermetallic communication pathways. The luminescence lifetimes of the bis-europium(III) and bis-terbium(III) complexes changed upon hydrolysis of the acetyl ester and increased lanthanide-lanthanide communication. The comparative sensitivity to vibrational solvent quenching led to opposite effects being observed for europium(III) and terbium(III). Future work could seek to exploit this change for sensing applications, with esterase enzymes a sensible first target.

A symmetric bis-macrocyclic ligand, **$H_7$3.1**, allowed the preparation of two multimetallic lanthanide complexes: **[GdLu3.1]**$^-$ and **[EuTb3.1]**$^-$. The EPR spectrum of **[GdLu3.1]**$^-$ was indicative of a large zero-field splitting. Comparison to the binuclear analogue **[Gd23.1]**$^-$ were not feasible, no signal was observed, likely due to low temperature antiferromagnetic coupling. **[EuTb3.1]**$^-$ displayed emission from both europium(III) and terbium(III) when excited via the ligand manifold. The ^{1}H NMR spectrum of **[EuTb3.1]**$^-$ displayed interesting properties with peaks well beyond the range expected from a europium(III) paramagnetic centre. Further work could look to investigate other pairs of lanthanide ions. Future target molecules could be prepared by varying the substituent on the bridging phenolate group.

Multimetallic lanthanide complexes were prepared by the self-assembly of a salicylate appended DO3A derivative, **H_2Ln4.1**, with lanthanide acetylacetonate complexes. Selective excitation of europium(III) and terbium(III) in the europium(III)-terbium(III) assemblies, led to emission from both europium(III) and terbium(III) centred excited states. This is the result of europium(III) to terbium(III) and terbium(III) to europium(III) energy transfer. The former being thermodynamically unfavourable. The unusually short luminescence lifetimes suggest lanthanide-lanthanide quenching is occurring. Further work should look to investigate other pairs of lanthanide ions.

Tetranuclear complexes prepared from **5-Me-HXTA** and a novel octaacetic acid benzophenone derivative, **$Na_8H_2$5.1**, displayed strong emission, characteristic of the lanthanide employed. We investigated the preparation of larger architectures from a novel octaacetic acid benzophenone derivative. Further work to prove the proposed structures using single crystal x-ray crystallography should be investigated. These ligand platforms may be useable to investigate the properties of statistical mixtures of lanthanide ions, for the screening of multimetallic complex properties.

Transition metal analogues of **[GdLu3.1]$^-$**, prepared from copper(II) and zinc(II) as a statistical mixture, were investigated as a simple $S = \frac{1}{2}$ spin system model. We found the system to be more complicated than anticipated, and focused efforts on multimetallic lanthanide complexes. Further studies could investigate the use of 1,4,7-triazacyclononane (TACN) derivatives to prepare natively 6 coordinate complexes, removing the complexity of counterion effects (Figure 6.1).

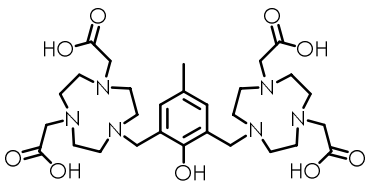

Figure 6.0.1: Proposed structure of new target ligand for copper(II)-zinc(II) complexes

More broadly, future work in the field of multimetallic lanthanide complexes should seek to investigate the behaviour of more pairs of lanthanide ions, searching for novel and unique behaviours.

Overall, this thesis describes approaches to multimetallic complexes via statistical and self-assembly approaches and the photophysical and magnetic properties of the resultant complexes.

7. EXPERIMENTAL DETAILS

7.1: GENERAL EXPERIMENTAL CONSIDERATIONS

1,4,7,10-tetraazacyclododecane was obtained from CheMaTech. Other materials were obtained from: Sigma Aldrich, Aldrich, Fisher, Fluorochem, Fluka Analytical, and Alfa Aesar. Where used, anhydrous solvents were obtained by passing through a *MBraun MPSP-800* column (degassed with nitrogen) and used immediately. $Cu(BF_4)_2.6H_2O$ and $Zn(BF_4)_2.6H_2O$ were dried for 16 hours at <1 mbar prior to use. All other materials were used as received.

Nuclear magnetic resonance spectroscopy was performed on a Bruker AVIII HD 400 spectrometer (400 MHz ^1H and 100 MHz ^{13}C experiments), a Bruker NEO 600 with broadband helium cryoprobe (600 MHz ^1H experiments and 151 MHz ^{13}C experiments) or a Bruker AVIII HD 500 (variable temperature experiments) and spectra are calibrated using the solvent peak. Chemical shift (δ) values are given in parts per millions (ppm) relative to tetramethyl silane (TMS). Results are described as singlet (s), doublet (d), triplet (t), multiplet (m), and broad (br).

Low resolution mass spectrometry was performed on an Agilent 6120 or a Waters LCT Premier XE. LCMS was performed on a Waters LCT Premier. High resolution accurate mass spectra were recorded to four decimal places using Thermo Exactive High-Resolution Orbitrap FTMS or Waters BioAccord (with loop injection).

Flash chromatography was performed on silica gel (Geoduran, 60 Å pore size, 230-400 mesh, 40-63 μm obtained from Merck) or alumina (activated, neutral, Brockmann Grade I, 58 Å pore

size, 60 mesh obtained from Alfa Aesar). Where multiple solvents have been used volume ratios and volume percentages have been used to describe the mixtures.

Thin layer chromatography was performed on silica coated (60G F245) aluminium-backed plates (obtained from Merck) or alumina coated aluminium-backed plates with 254 nm fluorescent indicator (obtained from Merck) and plates were visualised using UV-light (254 and 365 nm) or potassium permanganate stain.

Where reactions have been carried out under argon, a balloon filled with argon were fitted to oven dried glassware with rubber septa. Where noted, standard Schlenk techniques were employed for more sensitive reactions. For these reactions Schlenk flasks were cycled onto an argon Schlenk line and standard techniques employed. No reagents or products necessitating glovebox use were employed during synthesis.

Centrifugation was conducted at 3750 rpm for 10 minutes at 4°C.

Electron paramagnetic resonance (EPR) spectra in Chapter 2 were recorded by Ashley Redman and Filip Ivanovic at X-band on a Bruker Biospin EMXmicro spectrometer using either a ER-4122SHQE or dual-mode ER-4116DM resonator. The spectra were frequency corrected to 9.75 GHz. EPR spectra in Chapter 3 were recorded by Ashley Redman at the X-band on a Bruker Biospin EMXmicro spectrometer equipped with an ER4122SHQE-W1 resonator. The temperature was held constant at 10 K using liquid helium in combination with a continuous-flow cryostat (ESR900, Oxford Instruments) and temperature controller (ITC503s, Oxford Instruments).

UV-visible absorption spectra were obtained using a Jasco V-770 UV-Visible/NIR spectrophotometer. Luminescence spectra were obtained using a Horiba Fluorolog 3-12 fluorimeter. Unless noted uncorrected spectra were used. Where noted, normalisation was conducted in MATLAB R2021b. Time-resolved and time-gated measurements were recorded using a Horiba Fluorolog 3-12 fluorimeter.

Luminescence lifetimes were obtained by fitting time-resolved decay data to an exponential function in Origin 2023. Unless otherwise noted a mono-exponential decay was employed. A Levenberg Marquardt fitting algorithm, native to Origin 2023, was employed.

Table 7.1

Time	Solvent A water	Solvent B acetonitrile
0	95	5
5	95	5
7	5	95
8	5	95
10	95	5
11	95	5

High performance liquid chromatography (HPLC) was carried out on an Agilent Infinity II 1260 fitted with a preparatory pump (G7161A), prep sampler (G7157A), VWD (G7114A), fraction collector (G1364E) and a 1 mL sample loop. Samples were purified with sample detection at 254 nm. An Agilent 5 Prep C18 (p/N 446905-702, 50 × 21.2 mm, 5 μL) column was used,

with injection volumes between 50 μL and 750 μL. Solvent A is water and solvent B is acetonitrile, changing as shown in Table 7.1 Fractions were manually collected based on the PDA response at 254 nm.

Table 7.2

Time	Solvent A Water + 0.1% formic acid	Solvent B Acetonitrile + 0.1% formic acid
0	95	5
1	95	5
6	50	50
6.5	0	100
7	0	100
7.5	95	5
10	95	5

Liquid chromatography mass spectrometry (LCMS) was carried out on a Agilent 1260 Infinity II® fitted with a Quat. Pump (G7111A), autosampler (G7129A), Column oven (G7130A), DAD (G7115A) and mass spectrometer (G6125B). The photodiode array acquired data at 254 nm. Solvent A is water + 0.1% formic acid, solvent B is acetonitrile + 0.1% formic acid, changing as shown in Table 7.2.

2.2

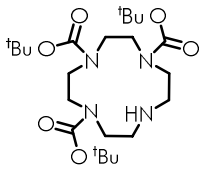

2.2

Prepared according to a literature procedure.[1]

To a stirring, ice-cold solution of 1,4,7,10-tetraazacyclododecane (2.0010 g, 11.62 mmol) and triethylamine (6.5 mL, 4.72 g, 46.6 mmol, 4 equiv.) in chloroform (45 mL) was added, dropwise, a solution of di-*tert*butyl-dicarboxylate (7.76 g, 35.6 mmol, 3 equiv.) in chloroform (35 mL) over 16 hours, the solution was allowed to warm to room temperature over the addition. After addition the mixture was stirred for a further 24 hours at room temperature. After stirring the mixture was diluted with chloroform (100 mL) and then washed with water and brine. The organic layer was then dried over magnesium sulphate, filtered and the filtrate evaporated to dryness under reduced pressure to afford a pale-yellow-white solid. The product was purified by column chromatography (silica, isocratic, diethyl ether) to afford the title compound as a white solid (2.266 g, 4.79 mmol, 41%). ^{1}H NMR (400 MHz, DMSO-d6) δ/ppm 3.54(m, 4H, CH_2 ring), 3.17(m, 4H, CH_2 ring), 2.63(m, 4H, CH_2 ring), 1.36 (m, 27H, ^{t}Bu). ^{13}C NMR (151 MHz, DMSO-d6) δ/ppm 155.08, 154.98, 78.71, 78.59, 51.20, 50.88, 50.05, 49.77, 49.39, 49.30, 48.83, 45.28, 44.20, 30.89, 28.79, 28.57, 28.48. LRMS *m/z* $(ESI)^+$ 473.8 ($[M+H]^+$ 97%), 945.5 ($[2M+H]^+$ 98%), 967.4 ($[2M+Na]^+$, 100%). HRMS $(ESI)^+$ [Found *m/z* = 473.3330, $C_{23}H_{45}O_6N_4$ requires $[M+H]^+$ *m/z* = 473.3334].

2.3

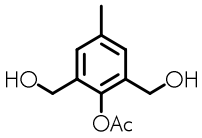

2.3

To a stirring solution of 2,6-bis(hydroxymethyl)-4-methylphenol (5.0381 g, 29.95 mmol) in isopropanol (120 mL) was added acetic anhydride (7.5 mL, 8.10 g, 79.34 mmol, 2.65 eq.). The pH was adjusted to pH 8 and the solution was stirred at room temperature for 1 hour, diluted with water then the isopropanol removed under reduced pressure. The residue was diluted with water (125 mL) and extracted to ethyl acetate (3 × 100 mL). The combined ethyl acetate layers were washed with water (100 mL) and brine (100 mL), the organic layer was dried with magnesium sulphate, filtered and the filtrate dried under reduced pressure. The product was purified by column chromatography (silica, gradient, ethyl acetate:pentane 0:1 → 4:6, 4% ethyl acetate steps) to afford the title compound as a clear oil (1.3532 g, 6.44 mmol, 21%). ^{1}H NMR (400 MHz, $CDCl_3$) δ/ppm 8.19 (s, 1H, O<u>H</u> phenol), 7.05 (d, J = 2.2 Hz, 1H, Ar<u>H</u>), 6.96 (d, J = 2.3 Hz, 1H, Ar<u>H</u>), 5.12 (s, 2H, C<u>H</u>$_2$), 4.75 (s, 2H, C<u>H</u>$_2$), 3.05 (s, br, 1H, O<u>H</u>), 2.27 (s, 3H, COC<u>H</u>$_3$), 2.12 (s, 3H, Ar-C<u>H</u>$_3$). ^{13}C NMR (101 MHz, $CDCl_3$) δ/ppm 173.02 (ArO<u>C</u>(O)CH_3), 152.07 (<u>Ar</u>OC(O)CH_3), 131.44 (<u>Ar</u>H), 129.96 (<u>Ar</u>H), 127.07 (<u>Ar</u>CH_2OH), 122.09 (<u>Ar</u>CH_2OH), 63.47 (Ar<u>C</u>H_2OH), 62.68 (Ar<u>C</u>H_2OH), 20.98 (ArOC(O)<u>C</u>H_3), 20.33 (Ar<u>C</u>H_3). LRMS $(ESI)^+$ *m/z* = 233.014 (100%) ($[M+Na]^+$). HRMS $(ESI)^+$ [Found *m/z* = 233.0783, $C_{11}H_{14}O_4Na$ $[M+Na]^+$ requires *m/z* = 233.0784].

2.4

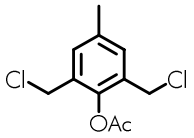

2.4

To a stirring solution of **2.3** (3.45 g, 16.4 mmol) in dichloromethane (35 mL) under argon was added thionyl chloride (17.8 mL, 27.88 g, 234.4 mmol, 14 eq.) dropwise. After stirring, under argon, at room temperature for 72 hours the reaction mixture was poured over ice and stirred for 1 hour. The water/dichloromethane mixture was made neutral by slow addition of sodium hydroxide solution (2 M, aqueous) and separated. The product was extracted from the biphasic mixture with dichloromethane (3 × 200 mL) and the organic layers combined. The combined organic layers were washed with water (200 mL) and brine (200 mL), dried over magnesium sulphate, filtered and the filtrate evaporated to dryness under reduced pressure to yield a pale-yellow solid. The product was purified by column chromatography (silica, gradient, pentane:ethyl acetate, 1:0 → 9:1, 1% ethyl acetate steps) to yield a white solid (2.4049 g, 9.73 mmol, 59.3%). ^{1}H NMR (600 MHz, $CDCl_3$) δ/ppm 7.27 (s, 2H, Ar<u>H</u>), 4.49 (s, 4H, C<u>H</u>$_2$Cl), 2.43 (s, 3H, ArC<u>H</u>$_3$), 2.38 (s, 3H, COC<u>H</u>$_3$). ^{13}C NMR (151 MHz, $CDCl_3$) δ/ppm 168.97 (Ar), 145.11 (Ar), 136.75 (Ar), 131.67 (Ar), 130.25 (Ar), 41.15 (Ar<u>C</u>H$_2$Cl), 20.78 (C(O)<u>C</u>H$_3$, 20.63 (Ar<u>C</u>H$_3$). LRMS (ESI)$^+$ *m/z* = 268.977 (38.23%), 270.982 (30.81%), 272.988 (7.92%) ([M+Na]$^+$, Cl_2 isotope distribution pattern), 301.005 (43.10%) 303.007 (35.01%) 305.014 (9.13%) ([M+Na+CH_3OH]$^+$ Cl_2 isotope distribution pattern) 514.960 (93.93%) 516.953 (100.00%) 518.969(81.50%) 520.987 (31.02%) 522.004 (7.49%) ([2M+Na]$^+$, Cl_4 isotope distribution pattern). HRMS (ESI$^+$) [Found *m/z* = 269.0107, $C_{11}H_{12}O_2{}^{35}Cl_2$ requires [M+Na]$^+$ *m/z* = 269.0107].

2.5

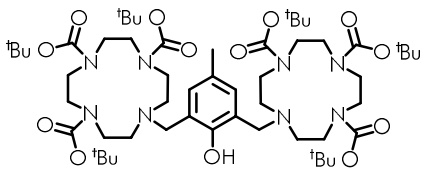

2.5

To a stirring suspension of **2.2** (1.1484 g, 2.43 mmol, 1 equiv.) and potassium carbonate (837.2 mg, 6.06 mmol, 2.5 equiv.) in acetonitrile (15 mL) was added a solution of **2.4** (309 mg, 1.25 mmol, 0.5 equiv.) in acetonitrile (10 mL) dropwise and the mixture heated to reflux. After heating to reflux for 72 hours the mixture was cooled to room temperature and filtered under vacuum. The filtrate was evaporated to dryness under reduced pressure to yield the title compound as a brown solid (0.928 g, 0.86 mmol, 71%). ^{1}H NMR (400 MHz, DMSO-d6) δ/ ppm 6.88 – 6.75 (m, 2H, Ar<u>H</u>), 3.32 (s, 32H, C<u>H</u>$_2$ rings), 2.25 – 2.01 (m, 4H, ArC<u>H</u>$_2$N), 1.43 – 1.32 (m, 57H, ^{t}Bu). ^{13}C NMR (101 MHz, DMSO-d6) δ 54.88, 28.22, 27.97. LRMS (ESI)$^{+}$ *m/z* 1077.74 ([M+H]$^{+}$ 100%) 593.40 ([M+2H]$^{+}$ 42%). HRMS (ESI)$^{+}$ [Found: *m/z* = 1077.7132, $C_{55}H_{97}O_{13}N_8$, [M+H]$^{+}$ requires *m/z* = 1077.7170];

H2.1

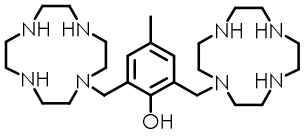

H2.1

To a stirring solution of **2.5** (869.6 mg, 0.789 mmol) in dichloromethane (6 mL) was added trifluoroacetic acid (2 mL) and the resultant solution stirred at room temperature for 90 minutes. After stirring, the solution was evaporated to dryness under reduced pressure. The residue was dissolved in dichloromethane, then evaporated to dryness under reduced pressure, twice. The residue was dissolved in methanol, then dried under reduced pressure, thrice to afford the product. The product was purified by reprecipitation from a concentrated methanol solution by diethyl ether thrice to afford the title compound as an oily black solid (324.4 mg, 0.680 mmol, 86%). ^{1}H NMR (400 MHz, DMSO-d6) δ/ppm 7.52 – 6.70 (m, 2H, ArH), 4.37 – 2.63 (m, 36H, ring CH_2 and $ArCH_2N$), 2.41 – 2.08 (m, 3H, CH_3). ^{13}C NMR (126 MHz, MeOD-d4) δ/ppm 151.30, 132.28, 131.78, 131.36, 128.10, 125.13, 120.28, 117.95, 115.62, 52.36, 51.02, 44.42, 44.31, 43.14, 42.14, 42.09, 41.93, 41.82, 19.58, 19.15. LRMS $(ESI)^+$ m/z = 477.40 ($[M+H]^+$, 100%). HRMS $(ESI)^+$ [Found m/z = 477.4016 $C_{25}H_{49}N_8O$ $[M+H]^+$ requires m/z = 477.4024]

$[Cu_2$2.1$][NO_3]_3$

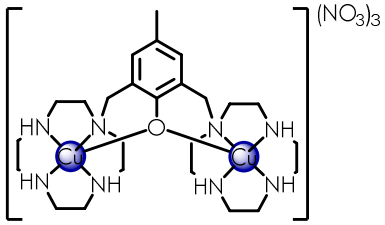

$[Cu_2$2.1$][NO_3]_3$

To a stirring solution of **H2.1** (50 mg, 0.105 mmol) in methanol (2.1 mL) was added copper(II) nitrate hexahydrate (71.0 mg, 0.199 mmol) and the resultant solution heated to reflux for 16 hours. After cooling to room temperature, the pH was adjusted to 5 by addition of sodium hydroxide solution (1 M aqueous), then the solvent removed under reduced pressure to afford the crude product as a dark green-black solid. The residue was dissolved in methanol (2 mL)

and the product was precipitated by addition of diethyl ether (12 mL), then collected by centrifugation. The residue was then dissolved in methanol (3 mL) and the product was precipitated by addition of diethyl ether (11 mL), then collected by centrifugation. The residue was dissolved in methanol (3.5 mL) and the product was precipitated by addition of diethyl ether (10.5 mL), then collected by centrifugation. The residue was washed with diethyl ether and dried under vacuum to afford a green solid (59.1 mg, 0.075 mmol, 75%). The products were not observed by either electrospray ionisation nor MALDI mass spectrometry.

General method for ratio tests of **$[Cu_nZn_{2-n}2.1][NO_3]_3$**

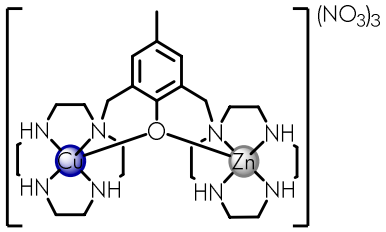

$[Cu_nZn_{2-n}2.1][NO_3]_3$

To a stirring solution of **H2.1** in water (0.5 M, 125 μL, 0.06 mmol) was added copper(II) nitrate hexahydrate as an aqueous soltution and zinc(II) nitrate hexahydrate as an aqueous solution. The resultant solution was diluted with methanol to a total volume of 2.1 mL. The resultant solution was stirred at room temperature for 16 hours. After stirring the mixture was diluted with methanol (2 mL) and the product precipitated with diethyl ether (24 mL). The solid product was collected by centrifugation. The products were not observed by either electrospray ionisation nor MALDI mass spectrometry.

$[Cu_{0.5}Zn_{1.5}2.1][NO_3]_3$ (25 mol% Cu(II))

Copper(II) nitrate hexahydrate (0.5 M in water, 50.3 μL, 0.03 mmol) and zinc(II) nitrate hexahydrate (0.5 M in water, 201 μL, 0.1 mmol) were used. Afforded the title compound as a green solid (11.5 mg, 30%).

$[Cu_{0.2}Zn_{1.8}2.1][NO_3]_3$ (10 mol% Cu(II))

Copper(II) nitrate hexahydrate (0.5 M in water, 25 μL, 0.01 mmol) and zinc(II) nitrate hexahydrate (0.5 M in water, 226 μL, 0.1 mmol) were used. Afforded the title compound as a green solid (11.7 mg, 31%).

$[Cu_{0.166}Zn_{1.834}2.1][NO_3]_3$ (8.3 mol% Cu(II))

Copper(II) nitrate hexahydrate (0.05 M in water, 240 μL, 0.01 mmol) and zinc(II) nitrate hexahydrate (0.5 M in water, 239 μL, 0.1 mmol) were used. Afforded the title compound as a green solid (8 mg, 21%).

$[Cu_{0.08}Zn_{1.92}2.1][NO_3]_3$ (4 mol% Cu(II))

Copper(II) nitrate hexahydrate (0.05 M im water, 100 μL, 0.01 mmol) and zinc(II) nitrate hexahydrate (0.5 M in water, 241 μL, 0.1 mmol) were used. Afforded the title compound as a brown solid (9.1 mg, 24%).

$[Cu_{0.02}Zn_{1.98}2.1][NO_3]_3$ (1 mol% Cu(II))

Copper(II) nitrate hexahydrate (0.05 M in water, 25 μL, 0.001 mmol) and zinc(II) nitrate hexahydrate (0.5 M in water, 249 μL, 0.1 mmol) were used. Afforded the title compound as a brown solid (11.2 mg, 30%).

$[Cu_2 2.1][BF_4]_3$

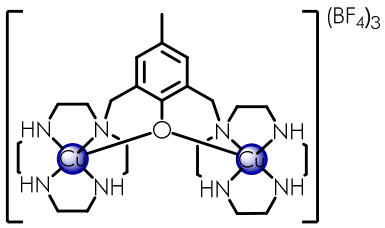

$[Cu_2 2.1][BF_4]_3$

Synthesis carried out using standard Schlenk techniques on an argon-equipped Schlenk line. To a stirring of **H2.1** (0.05 M in dry acetonitrile, 1.5 mL, 0.08 mmol) was added copper(II) tetrafluoroborate (0.1 M in dry acetonitrile, 1.5 mL, 0.2 mmol) and the resultant solution stirred at room temperature for 24 hours. After stirring the solution was diluted with dry toluene (7 mL) and the title compound precipitated. The solid was collected by canula filtration to afford the title compound which was dried under high-vacuum for 16 hours. This afforded the title compound as a black solid (30.7 mg, 0.04 mmol, 47%). The product was stored under argon prior to preparation of EPR samples for characterisation.

$[Cu_{0.02}Zn_{1.98}2.1][BF_4]_3$ (1 mol% Cu(II))

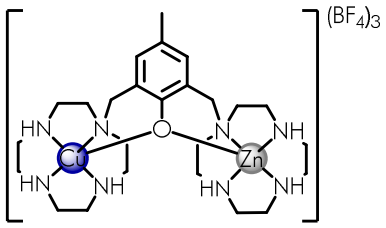

$[Cu_{0.02}Zn_{1.98}2.1][BF_4]_3$

Synthesis carried out using standard Schlenk techniques on an argon-equipped Schlenk line. To a stirring solution of **H2.1** (0.05 M in dry acetonitrile, 1.5 mL, 0.08 mmol) was added zinc(II) tetrafluroborate (0.1 M in dry acetonitrile, 1.45 mL, 0.1 mmol) and copper(II) tetrafluoroborate (0.025 M in dry acetonitrile, 60 μL, 0.001 mmol). The result solution was stirred at room temperature for 24 hours. After stirring the solution was diluted with dry toluene (14 mL) and the title compound precipitated. The solid was collected by canula filtration and dried under high-vacuum for 16 hours, to afford the title compound as an orange-brown solid. The product was stored under argon prior to preparation of EPR samples for characterisation.

3.4

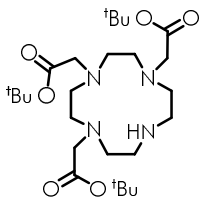

3.4

Prepared according to a modified literature procedure.[2]

To a stirring suspension of 1,4,7,10-tetraazacyclododecane (5.1145 g, 29.7 mmol) was added sodium hydrogen carbonate (8.2271 g, 97.9 mmol) and the resultant suspension cooled to 0°C. To this was added *tert*-butylbromoacetate (14.5 mL, 98.2 mmol) dropwise and the mixture stirred at 0 °C for 3 hours, then allowed to warm to room temperature and stirred for a further 32 hours. After stirring the mixture was filtered and the filtrate evaporated to dryness under reduced pressure to yield a brown solid. The residue was triturated in room temperature toluene (125 mL) and filtered, the solid was washed with room temperature toluene and diethyl ether and dried on the filter to yield the title compound as its hydrobromide salt as a white powder (6.9068 g, 11.6 mmol, 39%). ^{1}H NMR (600 MHz, DMSO-d6) δ/ppm 8.85 (s, 2H, N$\underline{H}_2$Br), 3.35 (s, 2H, NC$\underline{H}_2$COO^{t}Bu), 3.31 (s, 4H, NC$\underline{H}_2$COO^{t}Bu), 3.01 – 2.93 (m, 4H, C$\underline{H}_2$ ring), 2.87 – 2.82 (m, 4H, C$\underline{H}_2$ ring), 2.74 – 2.69 (m, 4H, C$\underline{H}_2$ ring), 2.69 – 2.65 (m, 4H, C$\underline{H}_2$ ring), 1.46 – 1.40 (m, 27H, ^{t}Bu). ^{13}C NMR (151 MHz, DMSO-d6) δ/ppm 171.05, 170.90, 170.48, 84.41, 81.82, 81.67, 81.06, 80.98, 56.53, 54.83, 54.14, 52.49, 52.15, 51.43, 50.18, 49.52, 48.86, 47.73, 46.00, 42.29, 28.34, 28.31, 28.23, 28.19. LRMS (ESI)$^{+}$ *m/z* = 515.29 ([M+H]$^{+}$ 100%). HRMS (ESI)$^{+}$ [Found *m/z* = 515.3800, $C_{26}H_{51}O_6N_4$ [M+H]$^{+}$ requires *m/z* = 515.3803].

3.5

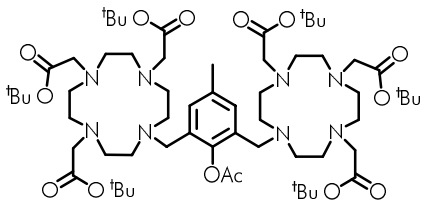

3.7

To a stirring solution of **3.4** (3.5401 g, 6.88 mmol, 1.95 eq.) in acetonitrile (40 mL) was added sodium carbonate (1.6094 g, 15.18 mmol, 5 eq.) and **2.4** (0.7516 g, 3.04 mmol, 1 eq.) and the resultant suspension allowed to stir at room temperature for 72 hours. After which the

suspension was filtered and the filter cake washed with acetonitrile (50 mL) and chloroform (50 mL). The filtrate was evaporated to dryness under reduced pressure to afford the crude product. The product was purified by column chromatography (silica, gradient, CH_2Cl_2:acetone:iPrOH:MeOH, 47.5:47.5:5:0 → 47:47:6:0 → 46:46:8:0 → 45:45:10:0 → 45:45:8:2 → 45:45:6:4 → 45:45:4:6 → 45:45:2:8 → 45:45:0:10 → 42.5:42.5:0:15 → 40:40:0:20 → 35:35:0:30 → 30:30:0:40) to afford the pure title compound as a yellow powder (1.0617 g, 0.88 mmol, 29%). ^{1}H NMR (600 MHz, $CDCl_3$) δ 7.51 (s, 2H, Ar-H), 3.75 – 2.20 (m, 54 H, CH_2), 1.85 (s, 10, CH_2), 1.44 (m, 57 H, ^{t}Bu). ^{13}C NMR (151 MHz, $CDCl_3$) δ 173.89 (Ar), 172.83 (Ar), 170.67 (Ar), 169.54 (C(O)Me), 147.45 (Ar), 136.35 (Ar), 131.65 (Ar-H), 82.89 (C(O)O^{t}Bu), 82.50 (C(O)O^{t}Bu), 81.83 (C(O)O^{t}Bu), 58.36 (CH_2), 56.59 (CH_2), 55.98 (CH_2), 53.39 (CH_2) , 51.51 (CH_2), 50.07 (CH_2), 49.37 (CH_2), 47.66 (CH_2), 28.38 (^{t}Bu), 28.34 (^{t}Bu), 28.21 (^{t}Bu), 28.20 (^{t}Bu), 27.99 (^{t}Bu), 21.20 (Me), 20.82 (OAc CH_3) LRMS (ESI)$^+$ 602.313 ([M+2H]$^{2+}$, 100%), 1203.759 ([M+H]$^+$, 66%), 1285.682 ([M+2MeCN+H]$^+$, 42%) HRMS (ESI)$^+$ [Found *m/z* = 1203.8224, $C_{63}H_{110}N_8O_{14}$ [M+H]$^+$ requires *m/z* = 1203.8214].

$H_6$3.3

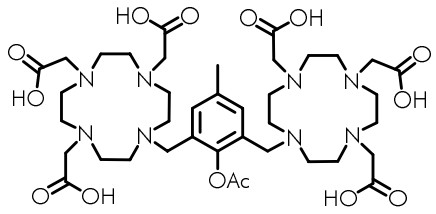

$H_6$3.3

To a stirring solution of **3.5** (834.4 mg, 0.69 mmol) in dichloromethane (7.5 mL) was added trifluoroacetic acid (7.5 mL) and the resultant mixture allowed to stir at room temperature for 48 hours. After which the mixture was diluted with dichloromethane (15 mL) and evaporated to dryness under reduced pressure. The resultant residue was dissolved in dichloromethane

(30 mL), and evaporated to dryness under reduced pressure, twice. The resultant residue was dissolved in methanol (30 mL), and evaporated to dryness under reduced pressure, thrice. The resultant solid was dissolved in methanol (40 mL) and portioned into 8 × 5 mL aliquots. To each aliquot, diethyl ether (40 mL) was added and the resultant solid collected by centrifugation. The supernatant was decanted, the solid dissolved in a minimum of methanol (5 – 10 mL) and precipitated by addition of diethyl ether (35 – 40 mL) to a total volume of 45 mL, the solid collected by centrifugation and the supernatant decanted, twice more. The solid was then suspended in diethyl ether (45 mL), the solid collected by centrifugation and the supernatant decanted to afford the title compound as a brown powder (507.7 mg, 0.59 mmol, 84%). ^{1}H NMR (400 MHz, $CDCl_3$) δ 7.50 (s, 2H, Ar-H), 4.15 – 2.7 (m, 50 H), 2.46k (s, 3 H), 2.27 (s, 3H). ^{13}C NMR (151 MHz, D_2O) δ 176.72, 174.57, 173.02, 171.95, 169.94, 169.76, 169.28, 146.24, 146.01, 140.08, 139.77, 133.11, 56.42, 56.28, 55.15, 54.85, 53.86, 53.38, 52.81, 51.65, 50.88, 50.55, 49.06, 48.55, 47.88, 46.70, 46.61, 46.40, 42.36, 20.43, 20.32, 20.15, 8.25. LRMS (ESI)$^+$ 434.163 ([M+2H]$^{2+}$, 97%), 867.322 ([M+H]$^+$, 100%), 889.378 ([M+Na]$^+$, 58%). HRMS (ESI)$^+$ [Found m/z = 867.4450, $C_{39}H_{62}N_8O_{14}$ [M+H]$^+$ requires m/z = 867.4458].

$H_7$3.1

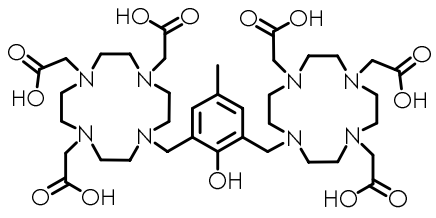

$H_7$3.1

To a stirring solution of **3.5** (508 mg) in methanol (4 mL) was added sodium carbonate (196.3 mg) and water (1.5 mL). After stirring at room temperature for 16 hours, further methanol was added to precipitate residual sodium carbonate and the mixture filtered. The filtrate was

evaporated to dryness under reduced pressure. The resultant residue was dissolved in dichloromethane (3 mL) and trifluoroacetic acid (3 mL) and stirred at room temperature for 48 hours. After stirring the resultant solution was diluted with dichloromethane and evaporated to dryness under reduced pressure. The resultant residue was dissolved in dichloromethane and evaporated to dryness under reduced pressure twice. After which the resultant residue was dissolved in methanol and evaporated to dryness under reduced pressure thrice. The target compound was prepared from recrystallisation from concentrated methanol solution with diethyl ether thrice, with the resultant fine solid collected by centrifugation each time. The target compound was afforded as a white solid (151.9 mg, 0.18 mmol, 44%). ^{1}H NMR (600 MHz, D_2O) δ 7.54 (s, 2H, ArH), 3.40 (m, 50H, CH_2). ^{13}C NMR (101 MHz, D_2O) δ 193.65, 150.94, 145.58, 144.73, 144.07, 135.05, 133.31, 57.75, 53.51, 53.36, 51.58, 51.30, 50.24, 49.04, 47.90, 42.56, 19.30. HRMS (ESI)$^+$ [Found m/z = 825.4357, $C_{37}H_{61}N_8O_{13}$ $[M+H]^+$ requires m/z = 825.4353)] [Found m/z = 847.4155, $NaC_{37}H_{60}N_8O_{13}$ $[M+Na]^+$ requires m/z = 847.4172)].

$Eu_2$3.3

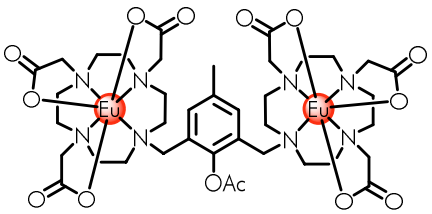

$Eu_2$3.3

To a stirring solution of **$H_6$3.3** (48.3 mg, 0.06 mmol) in acetonitrile (0.6 mL) and methanol (2.4 mL) was added europium(III) triflate (66.9 mg, 0.11 mmol, 2 equiv.). After stirring at room temperature for 21 hours the resultant solution was evaporated to dryness under flowing nitrogen. The resultant solid was dissolved in water (3 mL) and purified by dialysis (FLOAT-A-LYZER G2 500 - 1000D CE) for 96 hours. After dialysis, the resultant solution was evaporated

to dryness under flowing nitrogen. The resultant solid was dried under high vacuum for 24 hours affording a yellow solid (36.3 mg, 0.03 mmol, 56%). ^{1}H NMR (400 MHz, CD_3OD) δ 45.29, 44.04, 42.42, 28.30, 24.71, 5.04, 3.37, 2.33, 2.12, 1.36, -7.99, -9.56, -12.36, -13.70, -16.21, -17.49, -20.82, -21.35, -25.02, -29.77.

$Tb_2$3.3

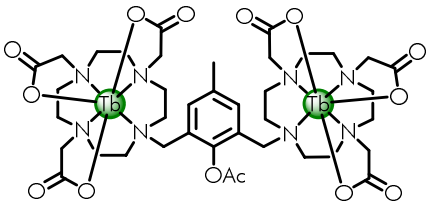

$Tb_2$3.3

To a stirring solution of **$H_6$3.3** (52.8 mg, 0.06 mmol) in acetonitrile (0.6 mL) and methanol (2.4 mL) was added terbium(III) triflate (69.7 mg, 0.11 mmol). After stirring at room temperature for 21 hours the resultant solution was evaporated to dryness under flowing nitrogen. The resultant solid was dissolved in water (3mL) and purified by dialysis (FLOAT-A-LYZER G2 500 - 1000D CE) for 96 hours. After dialysis, the resultant solution was evaporated to dryness under flowing nitrogen. The resultant solid was dried under high vacuum for 24 hours affording a yellow solid (25.3 mg, 0.02 mmol, 35%). ^{1}H NMR (400 MHz, CD_3OD) δ 119.49, 114.74, 109.56, 14.53, 6.42, 3.34, 2.02, 1.45, -80.85, -95.27, -107.05.

[Na][Eu23.1]

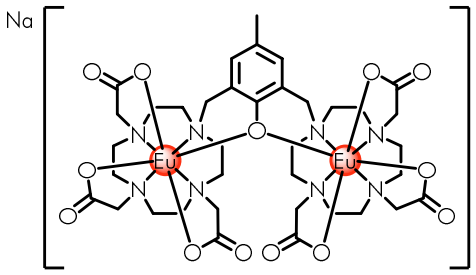

[Na][$Eu_2$3.1]

To a stirring solution of H73.1 (30.5 mg, 0.04 mmol) in water (1.8 mL) and methanol (1.8 mL) was added europium(III) triflate (55.8 mg, 0.09 mmol) and the mixture stirred at 60°C for 16 hours. Sodium hydroxide (1 M in water, 254 μL) was added and the mixture stirred at 60°C for a further 24 hours. The mixture was cooled to room temperature and filtered. The filtrate was evaporated to dryness under flowing nitrogen, whilst held at 50°C. The product was dialysed (FLOAT-A-LYZER G2 500 - 1000D CE) for 120 hours with three water changes, after which the solution was evaporated to dryness under flowing nitrogen, whilst held at 50°C to afford the title compound as a pale, yellow solid (7.4 mg, 0.01 mmol, 18%). ^{1}H NMR (400 MHz, D_2O) δ 48.72, 38.22, 37.47, 36.41, 35.56, 33.93, 22.19, 19.71, 16.32, 13.29, 10.99, 9.92, 8.18, -20.02, -22.23, -23.53, -26.71, -29.35. HRMS $(ESI)^-$ [found m/z = 1123.2209, $Eu_2C_{37}H_{53}N_8O_{13}$ $[M]^-$ requires m/z = 1123.2162].

[Na][Tb23.1]

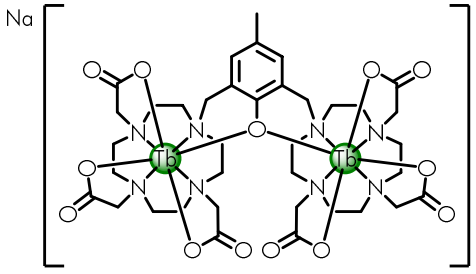

[Na][$Tb_2$3.1]

To a stirring solution of **$H_7$3.1** (30.0 mg, 0.04 mmol) in water (1.8 mL) and methanol (1.8 mL) was added terbium(III) triflate (55.4 mg, 0.09 mmol) and the mixture stirred at 60°C for 16 hours. Sodium hydroxide (1 M in water, 254 μL) was added and the mixture stirred at 60°C for a further 24 hours. The mixture was cooled to room temperature and filtered. The filtrate was evaporated to dryness under flowing nitrogen, whilst held at 50°C. The product was dialysed (FLOAT-A-LYZER G2 500 - 1000D CE) for 120 hours with three water changes, after which the solution was evaporated to dryness under flowing nitrogen, whilst held at 50°C to afford the title compound as a pale, pink solid (10.4 mg, 0.01 mmol, 24%). ^{1}H NMR (400 MHz, D_2O) δ 351.81, 311.16, 262.31, 217.31, 192.59, 186.33, 137.75, 83.87, -139.76, -142.65, -159.54, -186.67, -189.44, -199.43, -202.76, -230.38, -248.68, -265.03, -328.89, -357.92, -401.58, -422.22, -437.99. HRMS $(ESI)^-$ [found m/z = 1135.2300, $Eu_2C_{37}H_{53}N_8O_{13}$ $[M]^-$ requires m/z = 1135.2312].

[Na][$Gd_2$3.1]

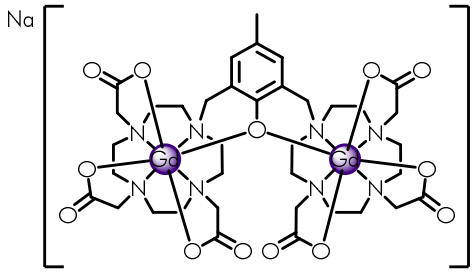

[Na][$Gd_2$3.1]

To a stirring solution of **$H_7$3.1** (33 mg, 0.04 mmol) in ethanol (400 μL) and water (400 μL) was added gadolinium(III) triflate (52.5 mg, 0.087 mmol). The resultant solution was heated to 50 °C for 16 hours, after which sodium hydroxide solution (1 M in water, 280 μL) was added and the solution heated to 50 °C for a further 2 hours. After cooling to room temperature, the solvent was removed under reduced pressure. The product was dialysed (FLOAT-A-LYZER G2 500 - 1000D CE) for 24 hours with three water changes. After removing the solvent, the product was obtained as a pale brown solid (0.5 mg, 0.043 μmol, 1%).

[Na][H_3Lu3.1]

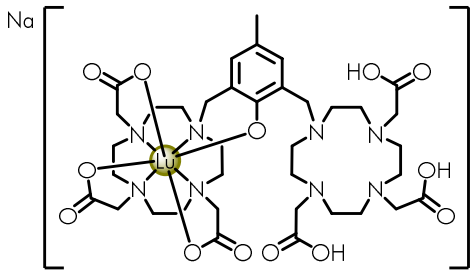

[Na][H_3Lu3.1]

To a stirring solution of **$H_7$3.1** (14 mg, 0.017 mmol) in methanol (100 μL) and water (100 μL) was added lutetium(III) triflate (11.8 mg, 0.019 mmol). The resultant solution heated to 60°C for 48 hours. After which sodium hydroxide (1 M in water, 119 μL) was added and the resultant solution heated to 60°C for 24 hours. After cooling to room temperature, the solvent was removed under reduced pressure. The desired product was purified by HPLC to afford the title compound as a pale brown solid (6.4 mg, 0.006 mmol, 37%). ^{1}H NMR (400 MHz, D_2O) δ/ ppm 7.16 (s, 1H), 7.04 (s, 1H), 4.10 – 2.39 (m, 48H), 2.24 (s, 3H).

[Na][GdLu3.1]

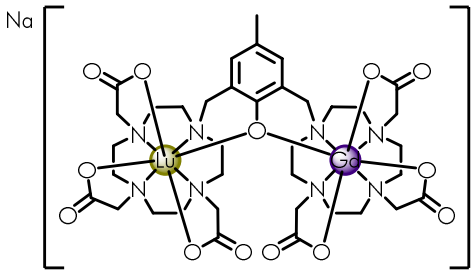

[Na][$Tb_2$3.1]

To a stirring solution of **[Na][H_3Lu3.1]** (6.4 mg, 0.006 mmol) in water (94 μL) and methanol (100 μL) was added a 0.5 M aqueous solution of gadolinium (III) triflate (12.2 μL, 0.006 mmol) and the resultant solution was heated to 60°C for 48 hours. After cooling, sodium hydroxide (1 M in water, 19.3 μL) was added, then the solution heated to 60°C for 24 hours. After cooling

to room temperature, the solution was filtered then the filtrate was dried under reduced pressure to afford the product as a brown solid (1 mg, 0.0009 mmol, 14%). The product was not observed with any mass spectrometry techniques available to us (ESI or MALDI).

$H_3Eu3.1$

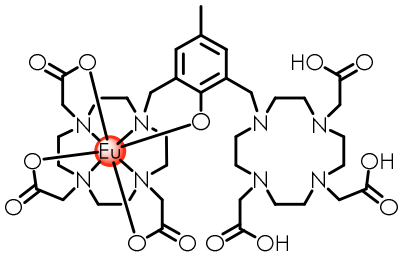

$H_3Eu_2$3.1

To a stirring solution of **$H_7$3.1** (39.3 mg, 0.05 mmol) in water (300 mL) and methanol (300 mL) was added europium(III) triflate (27.9 mg, 0.5 mmol). The resultant solution was heated to 60°C for 48 hours, after which sodium hydroxide (1 M in water, 242 μL) was added and the resultant solution stirred at 60°C for 3 hours. After cooling to room temperature, the solution was filtered and the filtrate evaporated to dryness under flowing nitrogen whilst held at 50°C. The resultant solid was purified by HPLC to afford the title compound as a yellow solid (21 mg, 0.02 mmol, 45%). ^{1}H NMR (400 MHz, D_2O) δ 47.72, 38.71, 34.11, 13.42, -6.79, -8.25, -13.99, -14.84, -16.41, -22.10. HRMS $(ESI)^+$ [Found m/z = 974.343, $C_{38}H_{59}EuN_7O_{13}$ $[M+H]^+$ requires m/z = 974.3378].

[Na][EuTb3.1]

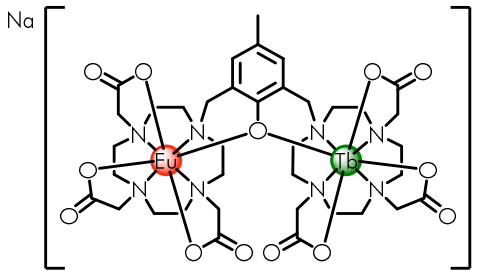

[Na][EuTb3.1]

To a stirring solution of **H_3Eu3.1** (14.4 mg, 0.01 mmol) in water (500 μL) and methanol (500 μL) was added terbium(III) triflate (12.7 mg, 0.02 mmol) The resultant solution was heated to 60°C for 48 hours, after which sodium hydroxide (1 M in water, 70 μL) was added and the resultant solution stirred at 60°C for 3 hours. After cooling to room temperature, the solution was filtered and the filtrate evaporated to dryness under flowing nitrogen whilst held at 50°C to afford the title complex as a white powder (16.6 mg, 0.01 mmol, 99%). ^{1}H NMR (400 MHz, D_2O) δ 98.85, 84.37, 70.45, 34.16, 31.24, 19.22, 13.65, -38.73, -45.96, -54.58, -85.97, -89.94, -96.80, -100.61, -112.95. HRMS (ESI)$^-$ [Found: *m/z* = 1129.2240, $C_{37}H_{53}N_8O_{13}EuTb$ [M-Na]- requires *m/z* = 1129.2203]

4.2

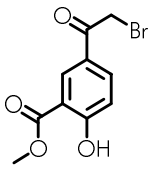

4.2

Prepared according to a modified literature procedure.[3]

To a stirring solution of methyl 5-acetylsalicylate (503.7 mg, 2.59 mmol) in chloroform (10 mL) and ethyl acetate (10 mL) was added copper (II) bromide (1.1691 g, 5.23 mmol) and the resultant suspension heated to reflux for 16 hours. After cooling to room temperature, the mixture was filtered through celite and the filtrate evaporated to dryness under reduced pressure. The product was purified by column chromatography (silica, gradient, dichloromethane:pentane, 1:1 → 8:2, 10% dichloromethane steps) to afford the title compound as a white powder (294.3 mg, 1.07 mmol, 41%) ^{1}H NMR (600 MHz, $CDCl_3$) δ/ppm 11.33 (s, 1H, ArO<u>H</u>), 8.52 (d, J = 2.3 Hz, 1H, Ar<u>H</u>), 8.10 (dd, J = 8.8, 2.3 Hz, 1H, Ar<u>H</u>), 7.06 (d, J = 8.8 Hz, 1H, Ar<u>H</u>), 4.39 (s, 2H, C<u>H</u>$_2$Br), 4.01 (s, 3H, OC<u>H</u>$_3$). ^{13}C NMR (151 MHz, $CDCl_3$) δ/ppm 189.28 (Aryl <u>C</u>H), 169.89 (<u>C</u>(O)OCH$_3$), 165.86 (<u>C</u>(O)CH$_2$Br), 136.08 (Aryl <u>C</u>), 132.20 (Aryl <u>C</u>H), 125.65 (Aryl <u>C</u>), 118.45 (Aryl <u>C</u>H), 112.38 (Aryl <u>C</u>), 52.83 (O<u>C</u>H$_3$), 30.24 (<u>C</u>H$_2$Br). HRMS (ESI)$^-$ [Found: *m/z* = 270.9622, $C_{10}H_8BrO_4$ ([M-H]$^-$) requires *m/z* = 270.6911]; LRMS (ESI)$^-$ *m/z* = 271.000 (95.4%), 272.900 (100%) ([M-H]$^-$, Br$_1$ isotope pattern), 564.900, 566.90 ([M+Na-2H]$^-$, Br$_1$ isotope pattern).

4.3

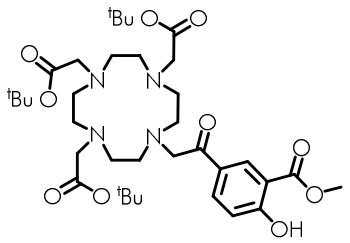

4.3

To a stirring solution of **3.4** (3.3954 g, 5.7 mmol) in acetonitrile (50 mL) was added potassium carbonate (4.2948 g, 31 mmol) and **4.2** (1.6622 g, 6.1 mmol) and the resultant suspension stirred at room temperature for 16 hours. After 16 hours, the reaction mixture was filtered and

the filtrate was evaporated to dryness under reduced pressure. The title compound was purified by column chromatography (silica, gradient, CH_2Cl_2/acetone (1:1) : MeOH, 1:0 → 95:5, 0.5% MeOH steps) to afford the title compound as a brown solid (1.2154 g, 1.7 mmol, 30%). ^{1}H NMR (400 MHz, $CDCl_3$) δ 11.24 (s, 1H, ArOH), 8.42 (d, J = 2.3 Hz, 1H, ArH), 8.02 (dd, J = 8.8, 2.2 Hz, 1H, ArH), 7.03 (d, J = 8.8 Hz, 1H, ArH), 4.00 (s, 6 H, CH_2 arm), 3.53 – 2.04 (m, 32, CH_2 ring), 1.44 (s, 30H, ^{t}Bu, Me).^{13}C NMR (101 MHz, $CDCl_3$) δ 197.38, 172.84, 169.89, 165.59, 134.78, 130.68, 118.28, 112.04, 81.92, 81.89, 59.85, 55.67, 52.86, 27.92, 27.90, 27.83. HRMS (ESI)$^+$ [Found *m/z* = 707.4226 $C_{36}H_{59}N_4O_{10}$ $[M+H]^+$ requires *m/z* = 707.4226], [Found *m/z* = 729.4042 $NaC_{36}H_{58}N_4O_{10}$ $[M+Na]^+$ requires *m/z* =729.4045]

4.1

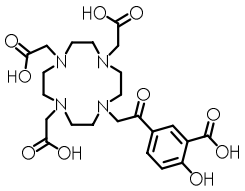

4.1

To a stirring solution of **4.3** (1.1754 g, 1.7 mmol) in ethanol (15 mL) was added sodium hydroxide (985.5 mg, 9.3 mmol) and water (15 mL). The resultant solution was stirred at room temperature for 16 hours. Ethanol was added and the solution was concentrated under reduced pressure. The resultant suspension was filtered and the filtrate evaporated to dryness. The resultant oil was dissolved in dichloromethane (16 mL) and trifluoroacetic acid (16 mL) was added dropwise. The resultant solution was stirred for 48 hours, after which the solvent was removed under reduced pressure. The resultant residue was dissolved in dichloromethane and evaporated to dryness under reduced pressure twice. The resultant residue was dissolved in

methanol and evaporated to dryness under reduced pressure thrice. The resultant solid was dissolved in methanol and precipitated with diethyl ether thrice to afford the title compound as a yellow solid (350.8 mg, 0.7 mmol, 40%). ^{1}H NMR (400 MHz, D_2O) δ 8.09, 7.80, 7.78, 7.78, 6.75, 6.73, 3.82, 3.78, 3.77, 3.66, 3.56, 3.54, 3.50, 3.46, 3.36, 3.32, 3.19, 2.95, 2.94. ^{13}C NMR (101 MHz, D_2O) δ 174.50, 172.95, 169.89, 133.98, 131.68, 131.60, 117.38, 53.25, 51.60, 47.78, 42.27. HRMS $(ESI)^+$ [Found m/z = 525.2193 $C_{23}H_{33}N_4O_{10}$ $[M+H]_+$ requires m/z = 525.2191]

H_2Eu4.1

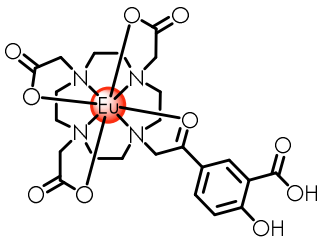

H_2Eu4.1

To a stiring solution of **$H_5$4.1** (47.6 mg, 0.09 mmol) in water (0.9 mL) and ethanol (0.9 mL) was added europium(III) triflate (83.1 mg, 0.14 mmol). The resultant solution was stirred at 60°C for 16 hours, after which sodium hydroxide (1 M in water, 300 μL) was added and the solution stirred for a further 24 hours. After cooling to room temperature, the mixture was filtered and the filtrate evaporated to dryness under flowing nitrogen, whilst held at 50°C. The resultant residue was dissolved in water and purified by dialysis (FLOAT-A-LYZER G2 100 - 500D CE) for 96 hours, with 3 water changes per day. After dialysis the solution was evaporated to dryness under flowing nitrogen, whilst held at 50°C, then dried under high-vacuum to afford the title compound as a yellow solid (44.0 mg, 0.07 mmol, 72%).^{1}H NMR (400 MHz, D_2O) δ

35.19, 28.95, 27.83, 26.93, 12.18, 8.20, 6.54, 3.41, 2.99, -1.81, -3.86, -4.83, -7.62, -8.71, -9.88, -11.65, -12.44, -12.94, -13.59, -14.61, -15.89, -17.59. HRMS $(ESI)^-$ [Found m/z = 673.1037, $C_{23}H_{28}N_4O_{10}Eu$ $[M-H]^-$ requires m/z = 673.1037]

H_2Tb4.1

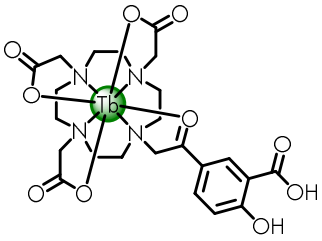

H_2Eu4.1

To a stiring solution of **$H_5$4.1** (52.8 mg, 0.1 mmol) in water (0.9 mL) and ethanol (0.9 mL) was added terbium(III) triflate (83.5 mg, 0.1 mmol). The resultant solution was stirred at 60°C for 16 hours, after which sodium hydroxide (1 M in water, 300 μL) was added and the solution stirred for a further 24 hours. After cooling to room temperature, the mixture was filtered and the filtrate evaporated to dryness under flowing nitrogen, whilst held at 50°C. The resultant residue was dissolved in water and purified by dialysis (FLOAT-A-LYZER G2 100 - 500D CE) for 96 hours, with 3 water changes per day. After dialysis the solution was evaporated to dryness under flowing nitrogen, whilst held at 50°C, then dried under high-vacuum to afford the title compound as a yellow solid (64.5 mg, 0.1 mmol, 94%). ^{1}H NMR (400 MHz, D_2O) δ 280.00, 264.62, 249.87, 202.49, 120.60, -30.84, -50.04, -79.74, -100.52, -149.23, -169.69, -344.55, -429.33. HRMS $(ESI)^-$ [Found m/z = 679.1060, $C_{23}H_{28}N_4O_{10}Tb$ $[M-H]^-$ requires m/z = 679.1064]

$[Na]_4$[5-Me-HXTA]

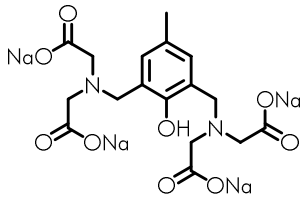

$[Na]_4$[5-Me-HXTA]

Prepared according to a modified literature procedure.[4]

To a stirring solution of 4-methylphenol (2.1279 g, 19.7 mmol) in methanol (40 mL) was added disodium iminodiacetate (6.5202 g, 36.8 mmol) and water (40 mL) and the mixture heated to 60°C. Paraformaldehyde (1.2639 g, 42.1 mmol) was added, and the mixture stirred at 60°C for 16 hours. Methanol (120 mL) was added and the solution allowed to cool to room temperature. The mixture was diluted with ethanol (400 mL) and acetone (200 mL) and allowed to precipitate for 1 hour. The resultant solid was filtered and washed on the filter with acetone (2 × 100 mL) and diethyl ether (3 × 100 mL) and dried on the filter to afford the title compound as a fine white powder (4.9438 g , 10.2 mmol, 52%). ^{1}H NMR (400 MHz, D_2O) δ/ppm 7.02 (s, 2H, C<u>H</u> aryl), 3.84 (s, 4H, Ar-C<u>H$_2$</u>-N), 3.30 – 3.22 (s, 8H, N-C<u>H$_2$</u>-COONa), 2.23 (s, 3H C<u>H$_3$</u>). ^{13}C NMR (101 MHz, D_2O) δ/ppm 177.40 (<u>C</u>OONa), 153.63 (Ar<u>C</u>-OH), 131.76 (Ar<u>C</u>-H), 128.65 (Ar<u>C</u>), 115.76 (Ar<u>C</u>), 57.38 (N-<u>C</u>H$_2$-COONa), 54.95 (Ar-<u>C</u>H$_2$-N), 19.29 (<u>C</u>H$_3$). HRMS *m/z* (ESI$^-$) [Found: 463.0705, $C_{17}H_{18}N_2Na_4O_9$ requires [M-Na]$^-$ 463.0711] (ESI$^+$) [Found: 487.0679, $C_{17}H_{18}N_2Na_4O_9$ requires [M+H]$^+$ 487.0679]. LRMS: (ESI$^+$) 464.979 (100%, [M-Na+2H]$^+$), 486.940 (63%, [M+H]$^+$).

$Na_8H_2$5.1

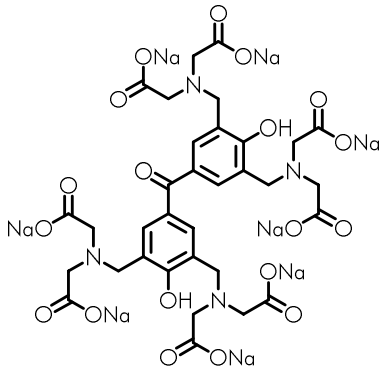

$Na_8H_2$5.1

To a stirring solution of 4,4′-dihydroxybenzophenone (2.0287 g, 9.5 mmol) in methanol (40 mL) was added disodium iminodiacetate (7.5939 g, 42.9 mmol) and water (40 mL) and the mixture heated to 60°C. Paraformaldehyde (1.2509 g, 41.7 mmol) was added, and the mixture stirred at 60°C for 24 hours. Methanol (120 mL) was added and the solution allowed to cool to room temperature. The resultant solid was filtered and washed on the filter with methanol (1 × 100 mL), acetone (2 × 100 mL) and diethyl ether (3 × 100 mL) and dried on the filter to afford the title compound as a fine yellow powder (1.9983 g, 2.1 mmol, 22%).^{1}H NMR (400 MHz, D_2O) δ 7.52 (s, 4H, C<u>H</u> aryl), 3.91 (s, 8H, Ar-C<u>H_2</u>-N), 3.31 (s, 16H, N-C<u>H_2</u>-COONa) ^{13}C NMR (101 MHz, D_2O) δ 175.71, 134.99, 123.87, 57.35, 56.50. HRMS: *m/z* (ESI^-) [Found: 947.0806, $C_{33}H_{30}N_4Na_8O_{19}$ requires $[M\text{-}Na]^-$ 947.0794] (ESI^+) [Found: 971.0737, $C_{33}H_{30}N_4Na_8O_{19}$ requires $[M+H]^+$ 971.0759]

$[Na]_8[Lu(5\text{-}Me\text{-}HXTA)_2(5.1)]$

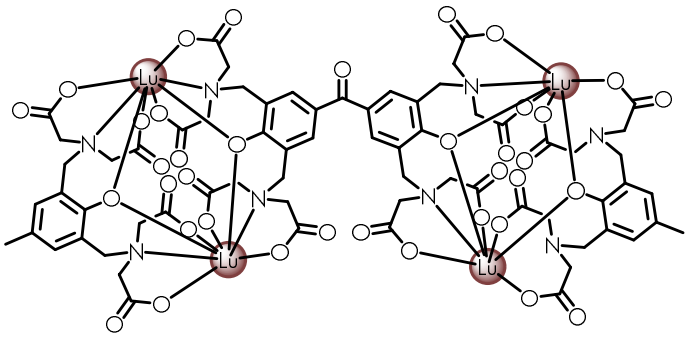

$[Lu_4(5\text{-}Me\text{-}HXTA)_2(5.1)]^{8+}$

To a stirring solution of **$[Na]_4[5\text{-}Me\text{-}HXTA]$** (98.5 mg, 0.20 mmol) and **$Na_8H_25.1$** (100.4 mg, 0.10 mmol) in water was added lutetium(III) triflate (250.8 mg, 0.40 mmol) and the resultant solution heated to 60°C for 16 hours, after which NaOH (1 M in water, 300 μL) was added and heating continued a further 24 hours. After cooling to room temperature, acetonitrile (5 mL) was added and the solid collected by centrifugation affording the title compound as an off-white solid (221.1 mg, 0.09 mmol, 87%). ^{1}H NMR (400 MHz, D_2O) δ 7.82 (m, 6H), 7.10 (m, 3H), 4.31 (m, 8H), 3.27 (m, br, 44 H), 2.25 (m, 6H). HRMS: *m/z* (ESI^-) [Found: 2454.0010, $C_{67}H_{62}Lu_4N_8O_{37}Na_8$ requires $[M]^-$ 2454.0034].

$[Na]_8[Eu(5\text{-Me-HXTA})_2(5.1)]$

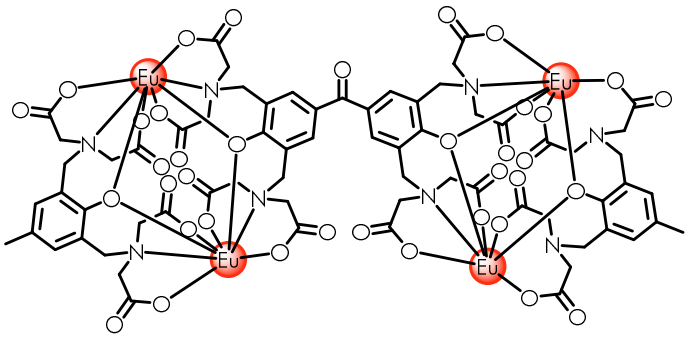

$[Eu_4(5\text{-Me-HXTA})_2(5.1)]^{8+}$

To a stirring solution of **$[Na]_4$[5-Me-HXTA]** (98.4 mg, 0.20 mmol) and **$Na_8H_2$5.1** (98.6 mg, 0.10 mmol) in water was added europium(III) triflate (244.4 mg, 0.41 mmol) and the resultant solution heated to 60°C for 16 hours, after which sodium hydroxide (1 M in water, 300 μL) was added and heating continued a further 24 hours. After cooling to room temperature, acetonitrile (5 mL) was added and the solid collected by centrifugation affording the title compound as a yellow solid (51.2 mg, 0.022 mmol, 21%). ^{1}H NMR (400 MHz, D_2O) δ 3.58, 2.82, 1.11, 0.38, 0.00, -0.15, -5.08, -5.34, -5.87, -6.19, -7.37. HRMS: *m/z* (ESI^-) [Found: 2342.9444, $C_{67}H_{62}Eu_4N_8O_{37}Na_8$ requires $[M\text{-}Na]^-$ 2342.9355].

General Method for **Eu(5.1)$_n$**

To a stirring solution of **$Na_8H_2$5.1** in water was added europium(III) triflate. The resultant solution was heated to 60°C for 16 hours, after which sodium hydroxide (1 M in water, 200 μL) was added and the mixture heated for 60°C for a further 24 hours. After cooling to room temperature, the solvent was removed by evaporation under flowing nitrogen whilst heated to 50°C.

Eu5.1

$Na_8H_2$5.1 (50.6 mg, 0.05 mmol) and europium(III) triflate (30.3 mg, 0.05 mmol) were used. The method above afforded the title compound as a yellow solid (54.9 mg, 0.05 mmol, 99%). ^{1}H NMR (400 MHz, D_2O) δ 10.49, -7.18, -8.19, -10.06, -16.29.

Eu(5.1)$_2$

$Na_8H_2$5.1 (50.2 mg, 0.05 mmol) and europium(III) triflate (60.1 mg, 0.1 mmol) were used. The method above afforded the title compound as a yellow solid (48.6 mg, 0.04 mmol, 80%). ^{1}H NMR (400 MHz, D_2O) δ 3.63, 3.22, 1.98, 1.16, -7.14.

Eu(5.1)$_{2.3}$

$Na_8H_2$5.1 (52.3 mg, 0.05 mmol) and europium(III) triflate (70.8 mg, 0.1 mmol) were used. The method above afforded the title compound as a yellow solid (59.9 mg, 0.05 mmol, 94%). ^{1}H NMR (400 MHz, D_2O) δ 1.78, -7.22.

1. M. Woods, G. E. Kiefer, S. Bott, A. Castillo-Muzquiz, C. Eshelbrenner, L. Michaudet, K. McMillan, S. D. K. Mudigunda, D. Ogrin, G. Tircsó, S. Zhang, P. Zhao and A. D. Sherry, *J. Am. Chem. Soc.* , 2004, 126, 9248-9256.
2. A. Dadabhoy, S. Faulkner and P. G. Sammes, *J. Chem. Soc., Perkin Trans. 2*, 2002, 348-357.
3. K. Yao, G. Karunanithy, A. Howarth, P. Holdship, A. L. Thompson, K. E. Christensen, A. J. Baldwin, S. Faulkner and N. J. Farrer, *Dalton. Trans.,* 2021, 50, 8761-8767.
4. L. S. Natrajan, P. L. Timmins, M. Lunn and S. L. Heath, *Inorg. Chem*., 2007, 46, 10877-10886

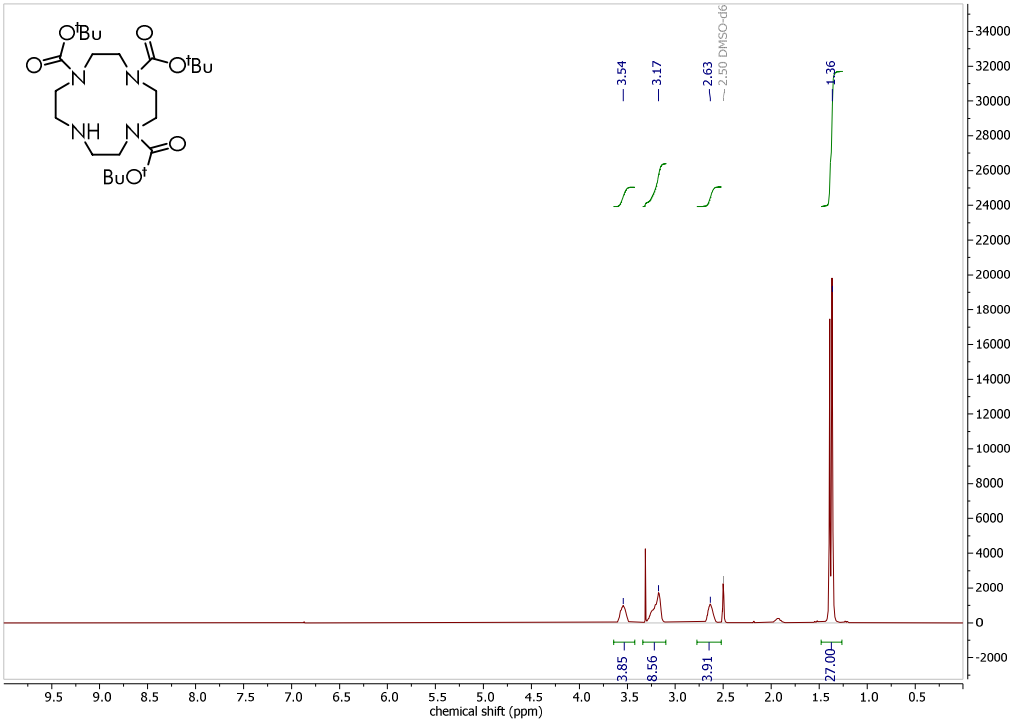

*Figure 8.1: [1]H NMR spectrum of **2.2** recorded at 400 MHz in DMSO-d6*

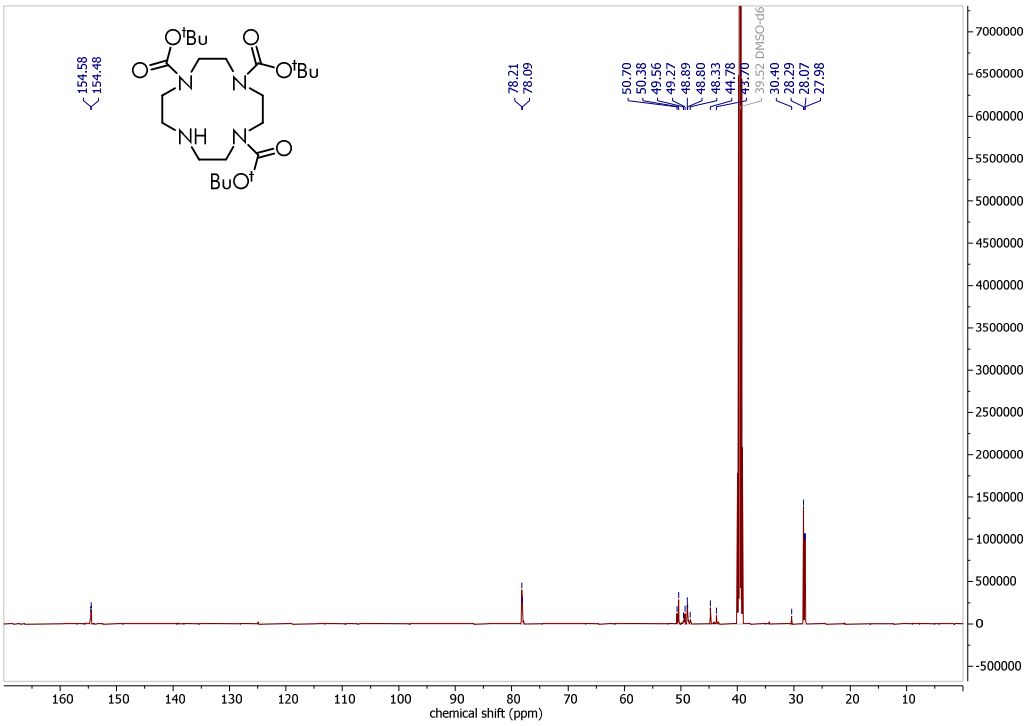

*Figure 8.2: [13]C NMR spectrum of **2.2** recorded at 150 MHz in DMSO-d6*

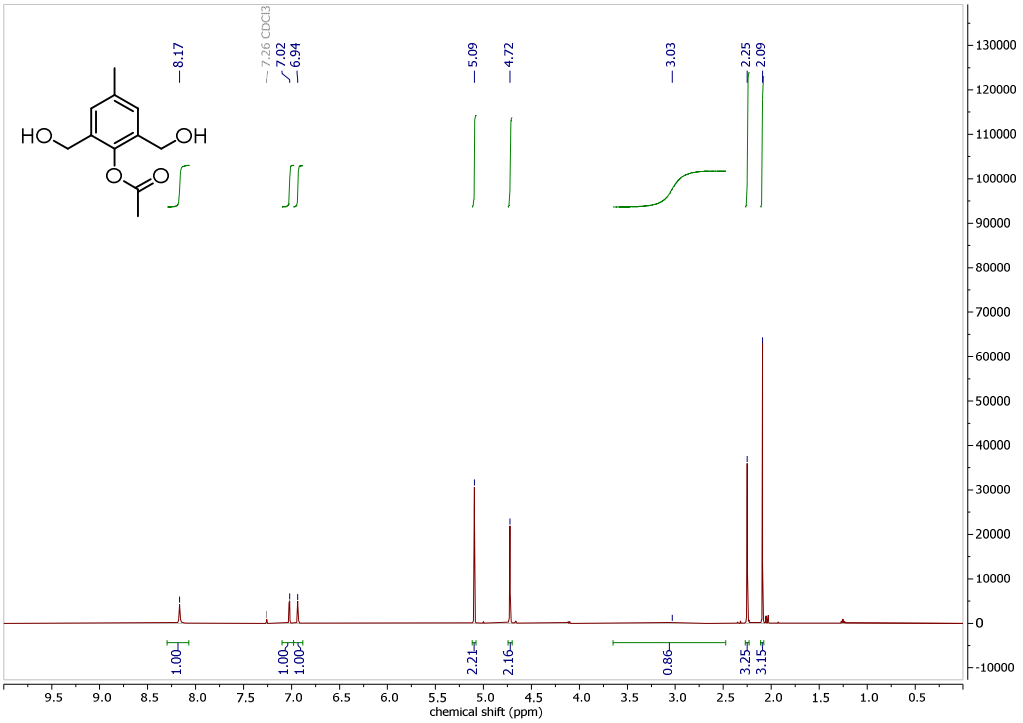

*Figure 8.3: ^{1}H NMR spectrum of **2.3** recorded at 400 MHz in $CDCl_3$*

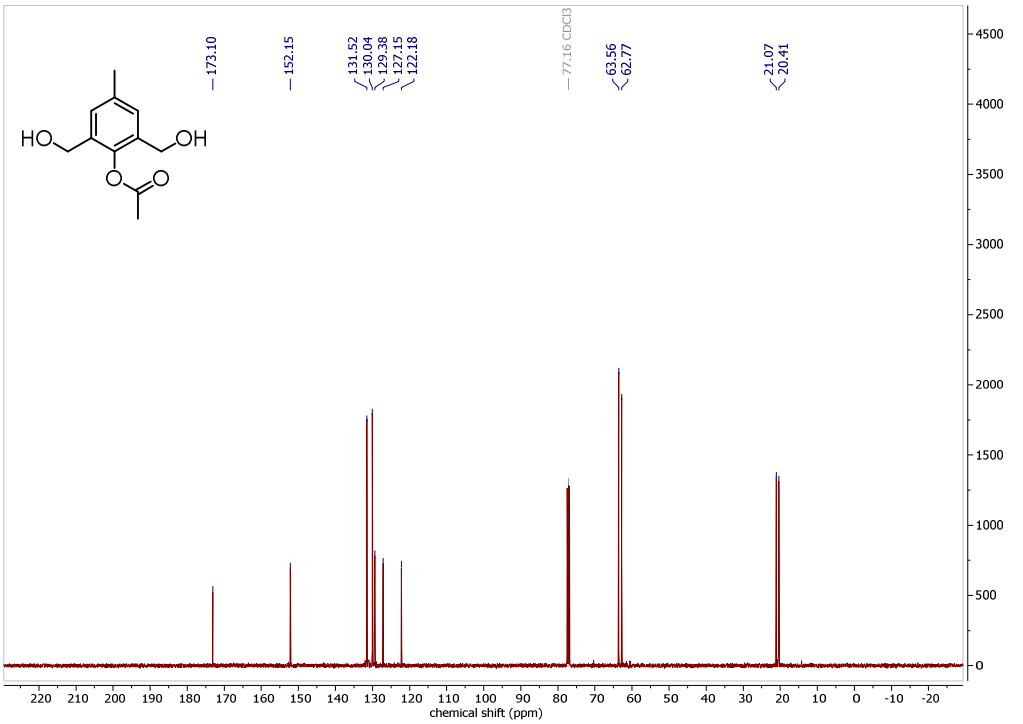

*Figure 8.4: ^{13}C NMR spectrum of **2.3** recorded at 100 MHz in $CDCl_3$*

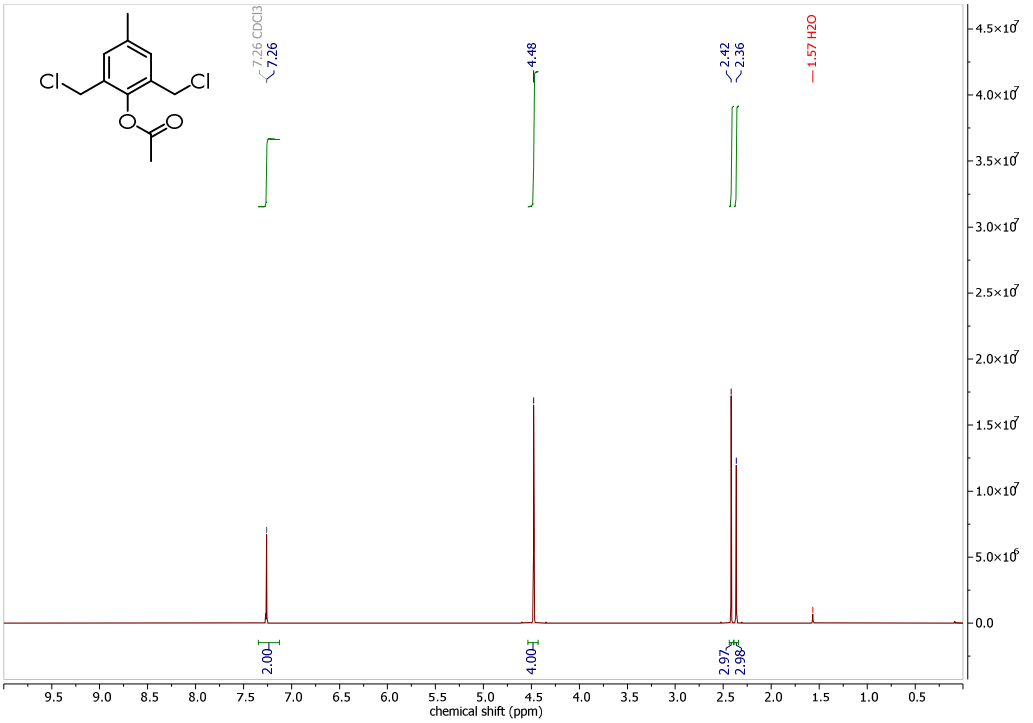

*Figure 8.5: [1]H NMR spectrum of **2.4** at 600 MHz in $CDCl_3$*

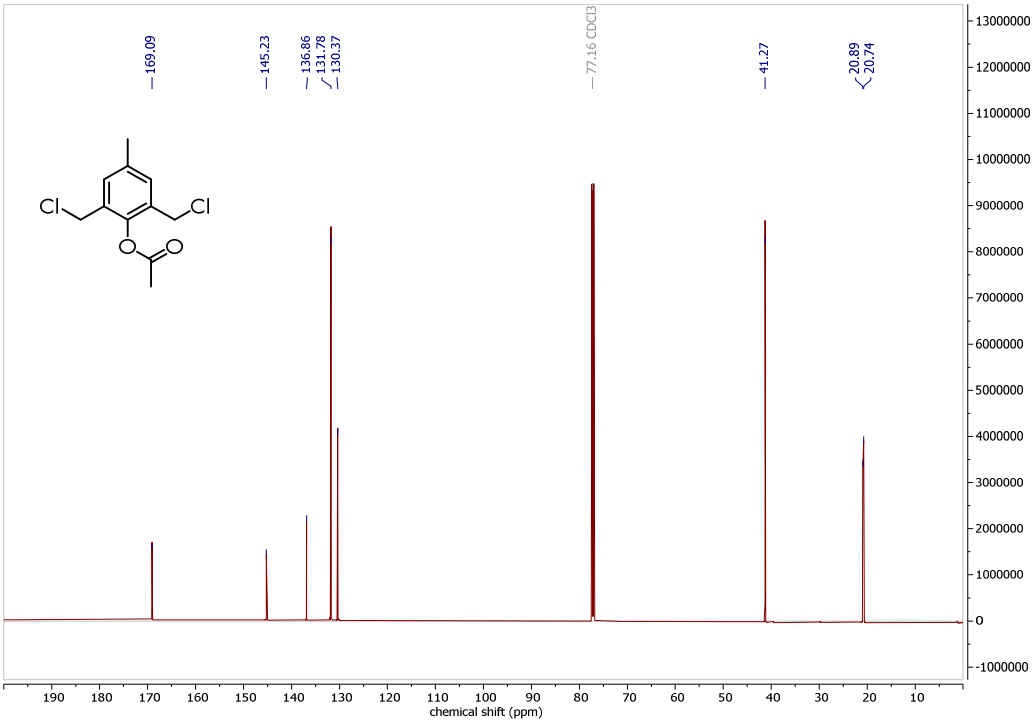

*Figure 8.6: [13]C NMR spectrum of **2.4** recorded at 150 MHz in $CDCl_3$*

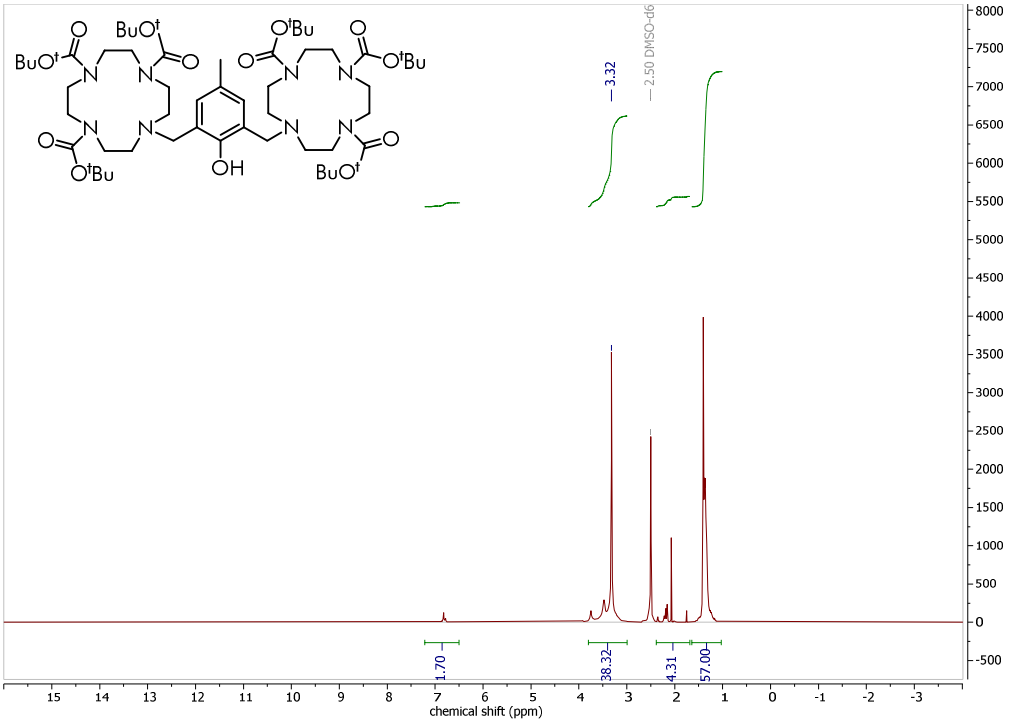

*Figure 8.7: ^{1}H NMR spectrum of **2.5** recorded at 400 MHz in DMSO-d*

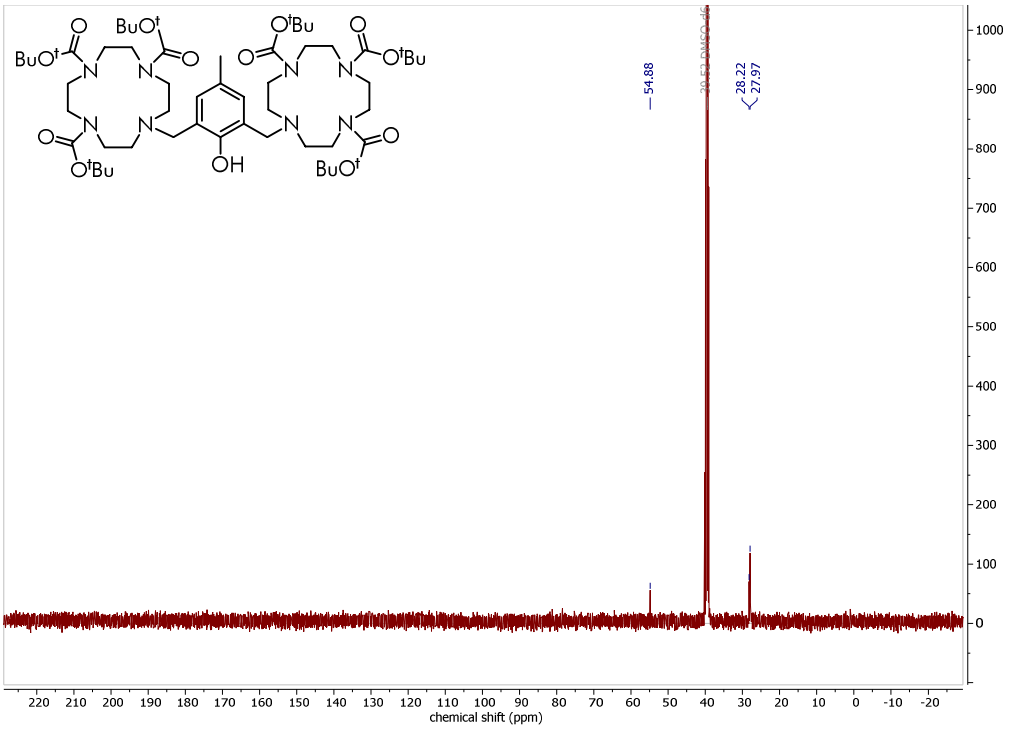

*Figure 8.8: ^{1}H NMR spectrum of **2.5** recorded at 400 MHz in DMSO-d6*

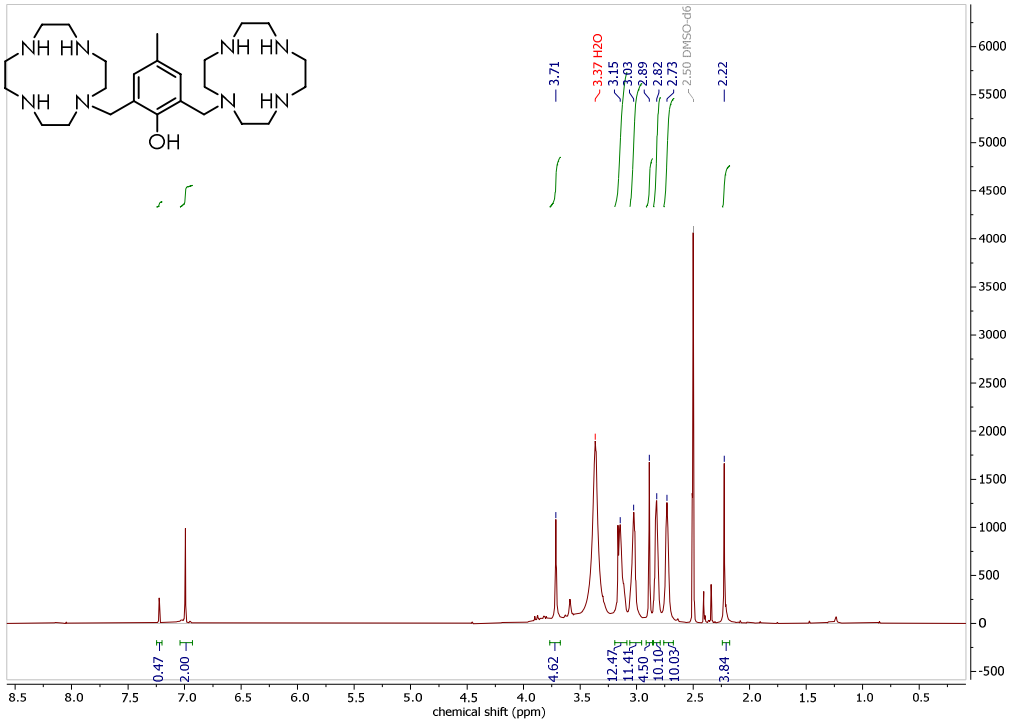

*Figure 8.9: [1]H NMR spectrum for **H2.1** recorded at 500 MHz in DMSO-d6.*

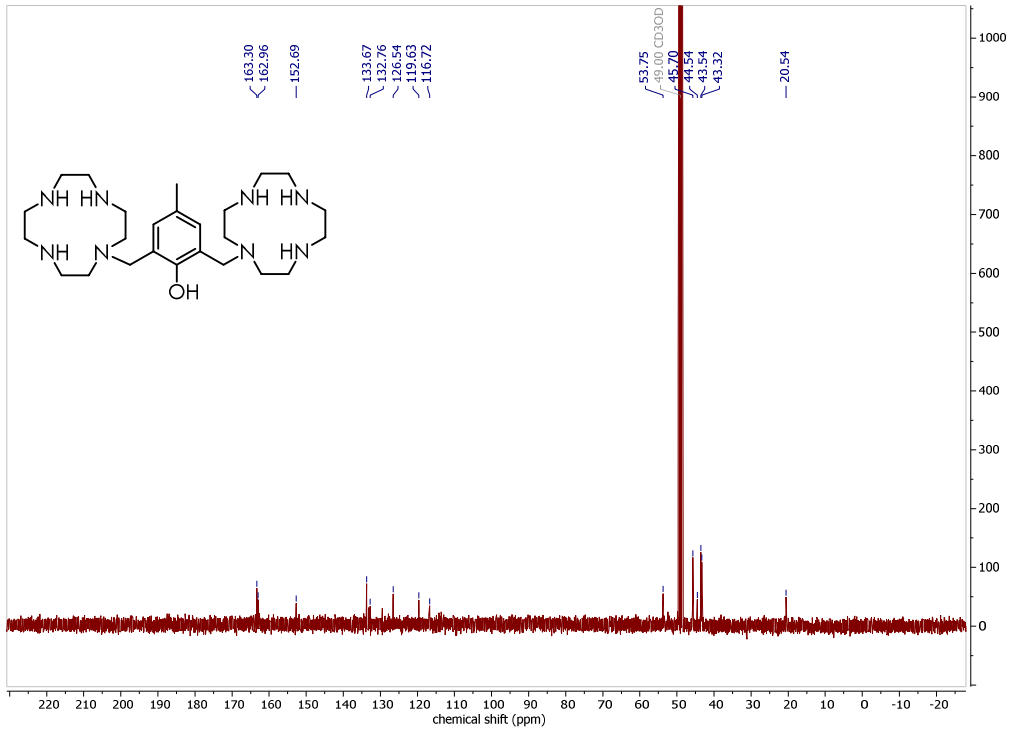

*Figure 8.10: [13]C NMR spectrum of **H2.1** in CD_3OD at 100 MHz*

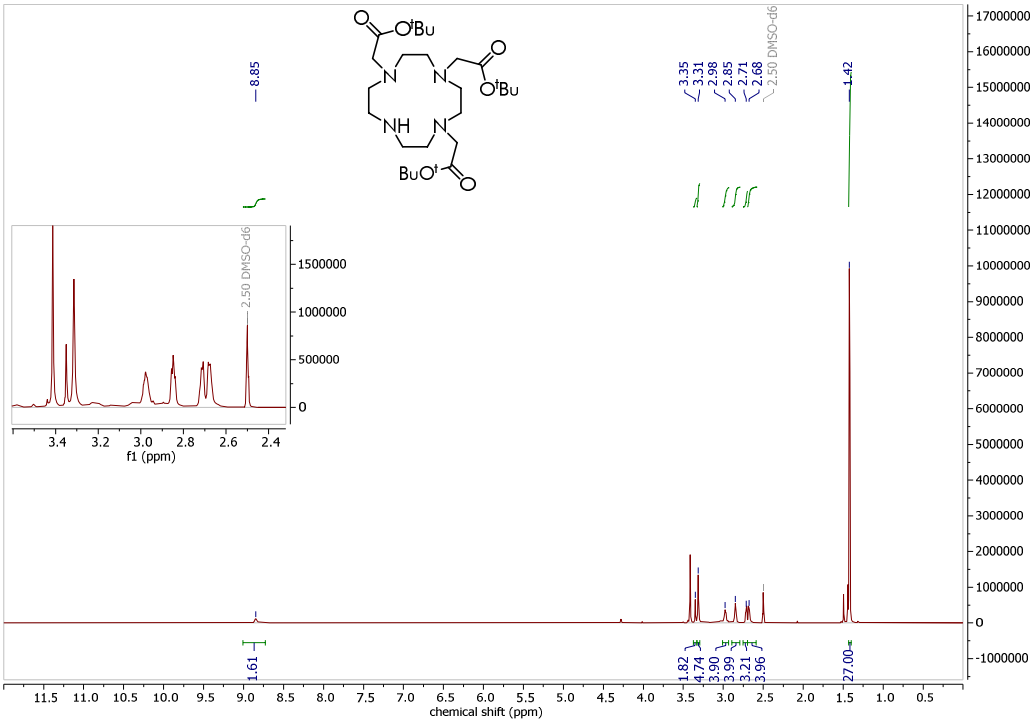

*Figure 8.11: ^{1}H NMR spectrum of **3.4** recorded at 600 MHz in DMSO-d6*

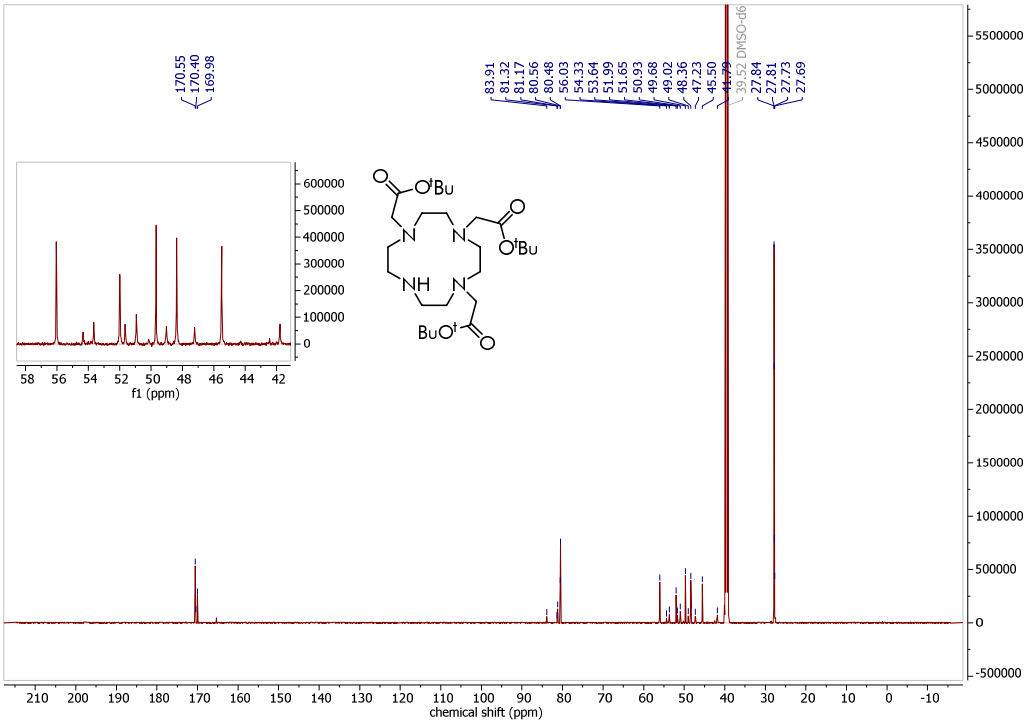

*Figure 8.12: ^{13}C NMR spectrum of **3.4** recorded at 150 MHz in DMSO-d6*

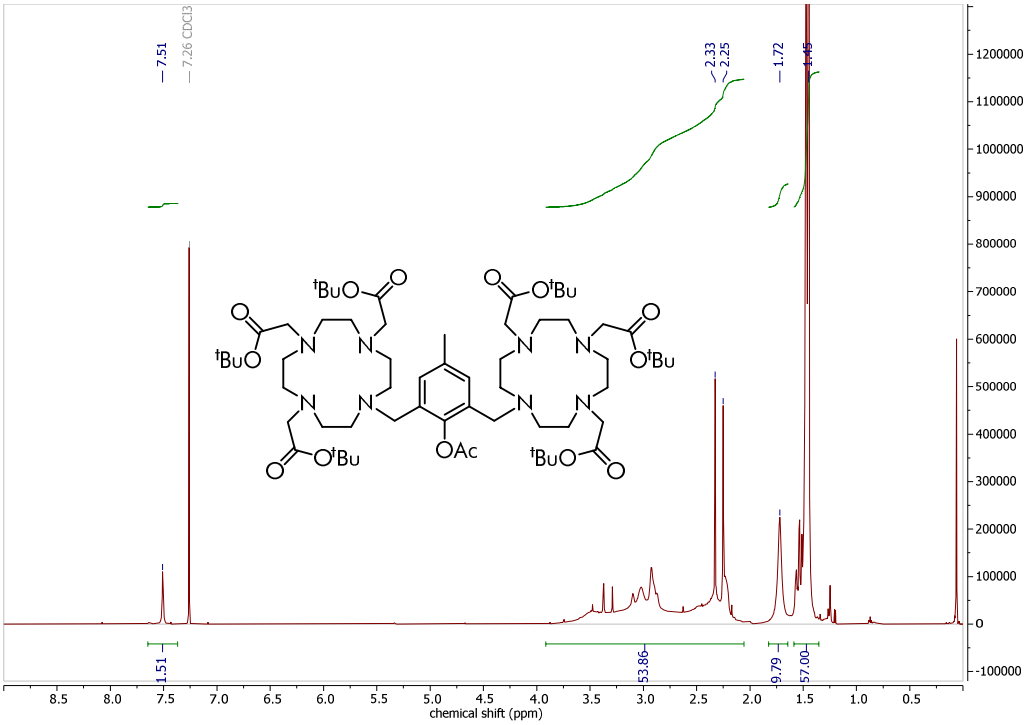

*Figure 8.13: ^{1}H NMR spectrum of **3.5** in $CDCl_3$ at 400 MHz*

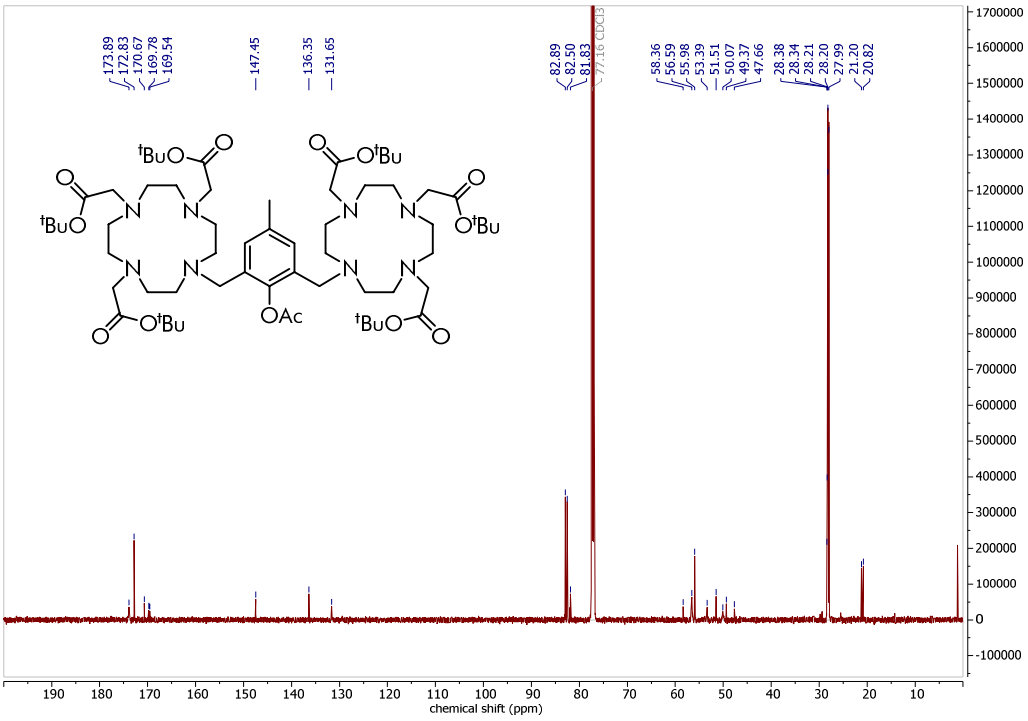

*Figure 8.14: ^{13}C NMR spectrum of **3.5** in $CDCl_3$ at 151 MHz*

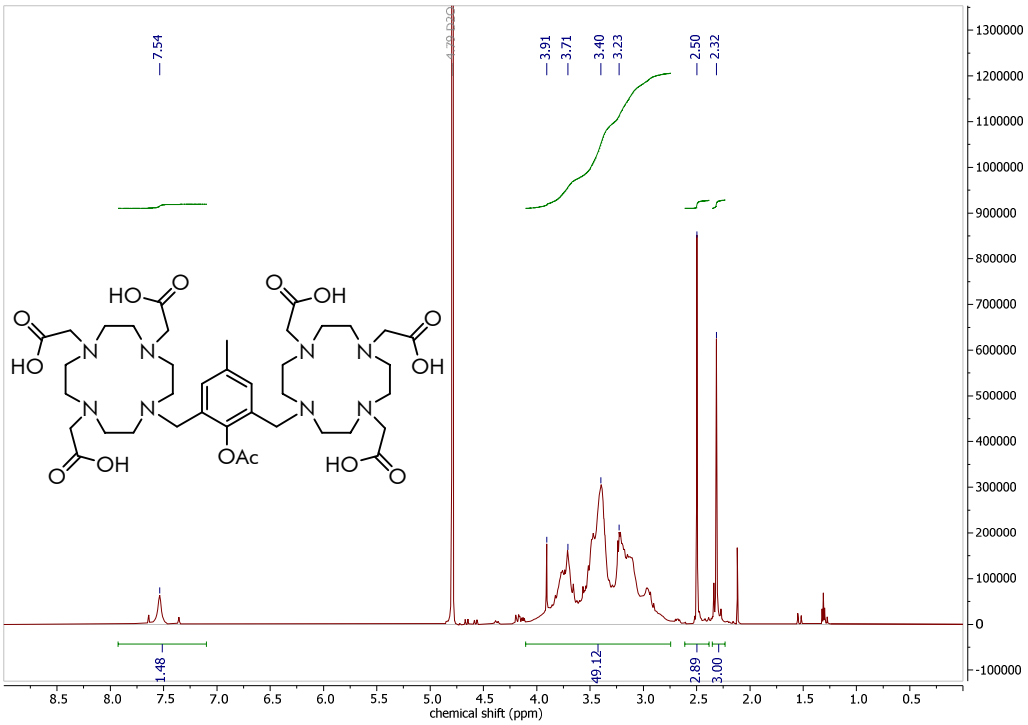

*Figure 8.15: ^{1}H NMR spectrum of **$H_6$3.3** in D_2O at 600 MHz*

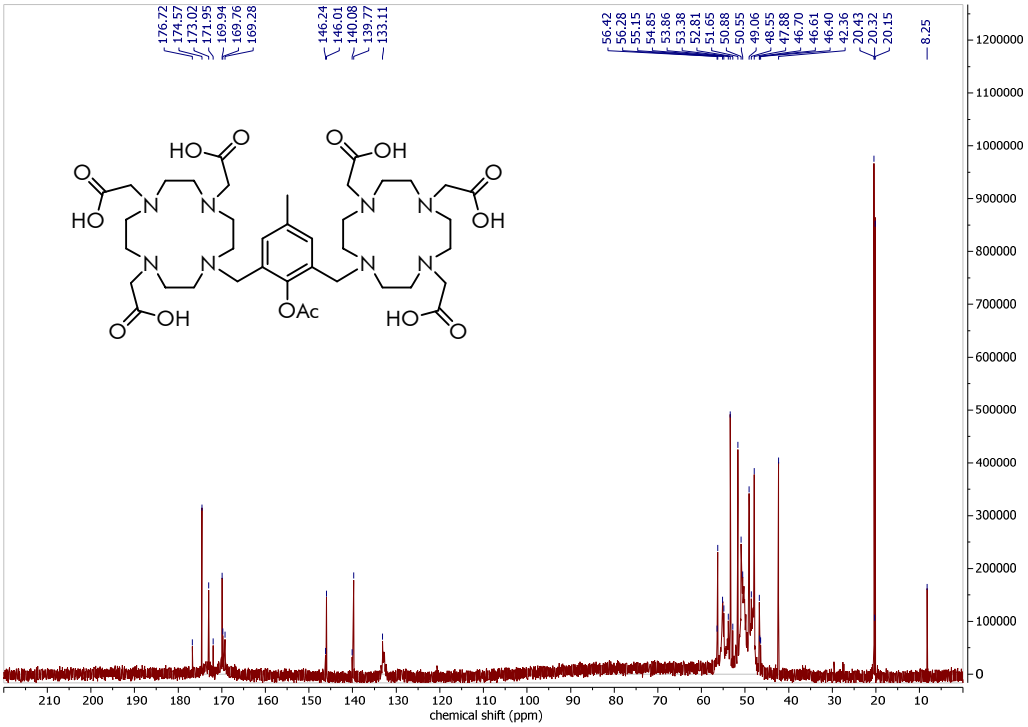

*Figure 8.16: ^{13}C NMR spectrum of **$H_6$3.3** in D_2O*

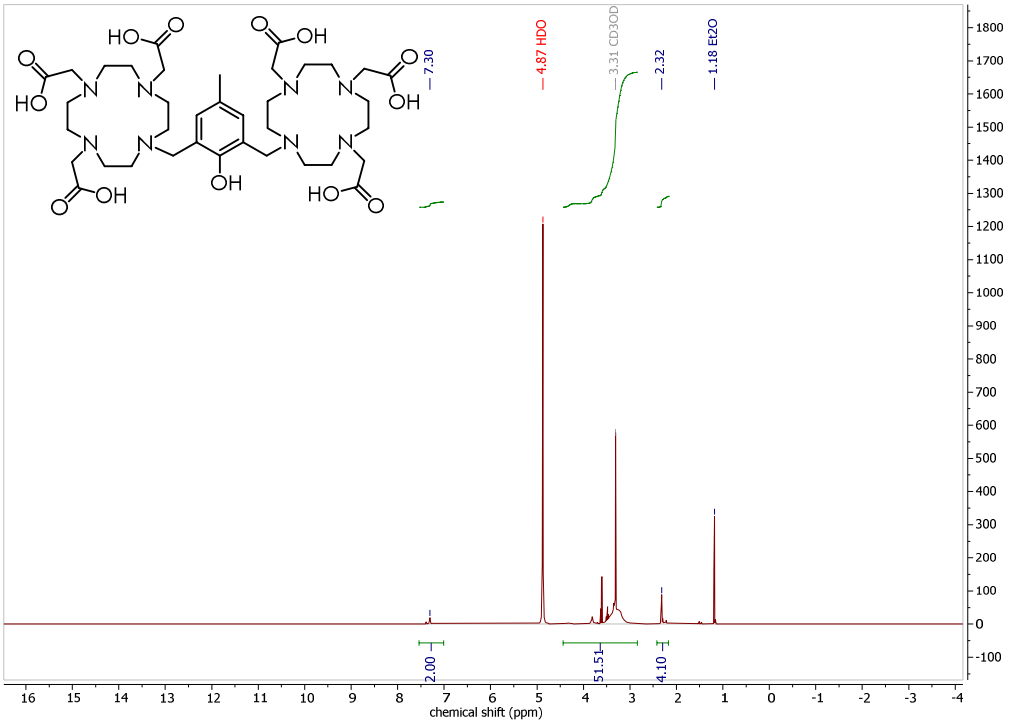

*Figure 8.17: ^{1}H NMR spectrum of **$H_7$3.1** recorded in CD_3OD at 500 MHz*

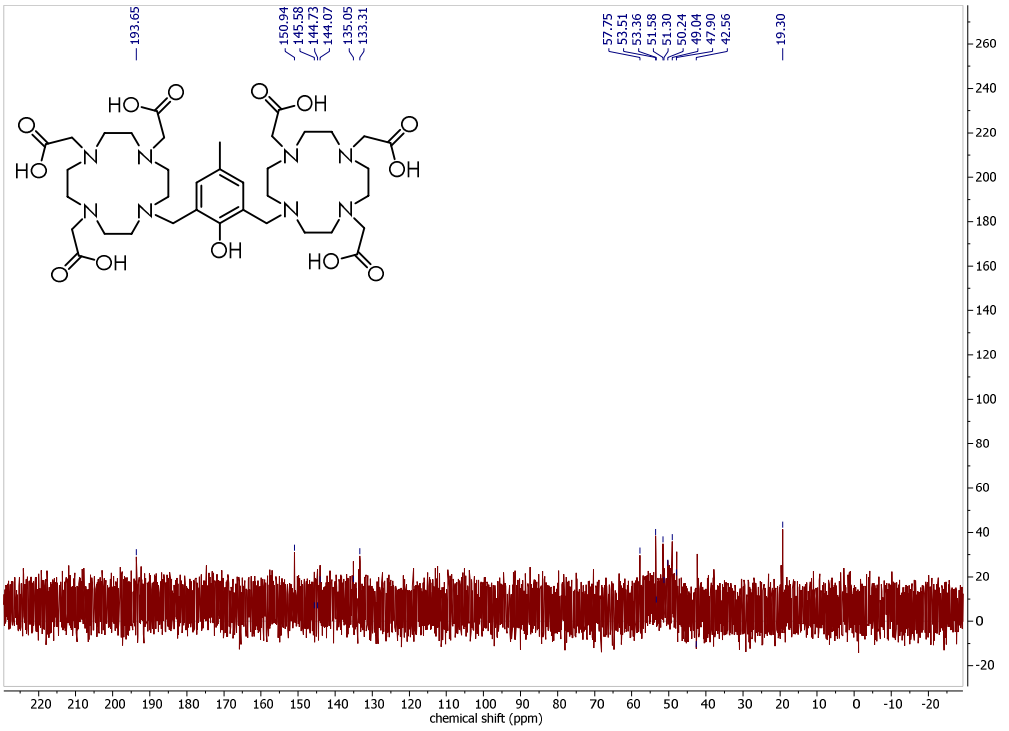

*Figure 8.18: ^{13}C NMR spectrum of **$H_7$3.1** recorded inD_2O at 400 MHz*

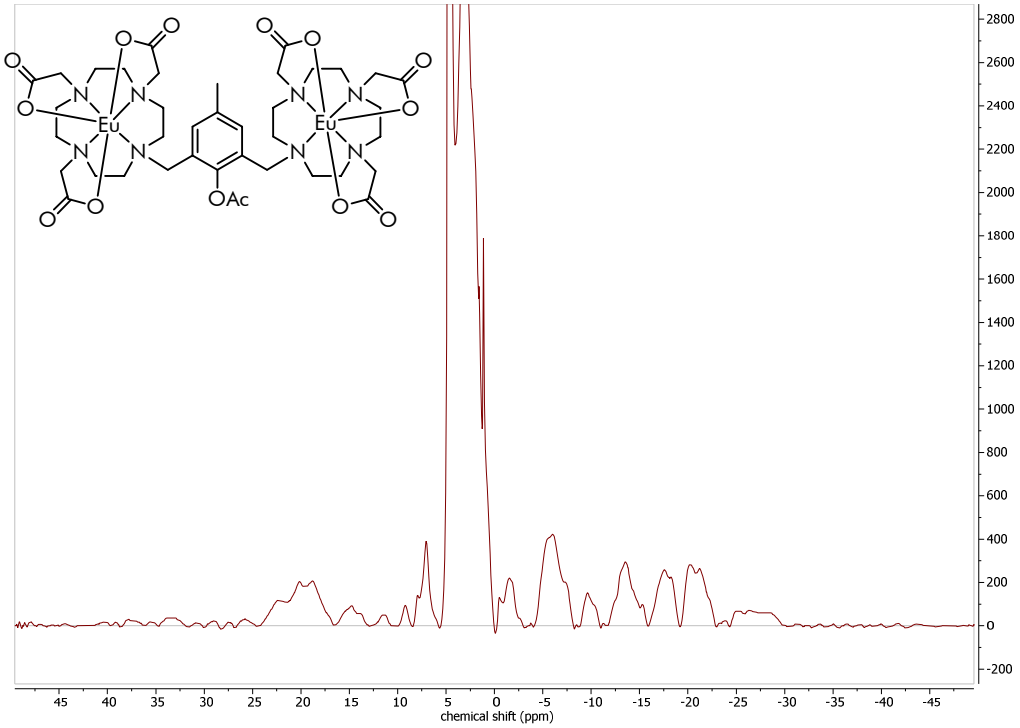

Figure 8.19 ^{1}H NMR spectrum of ***Eu$_2$3.3*** *recorded at 400 MHz in D_2O*

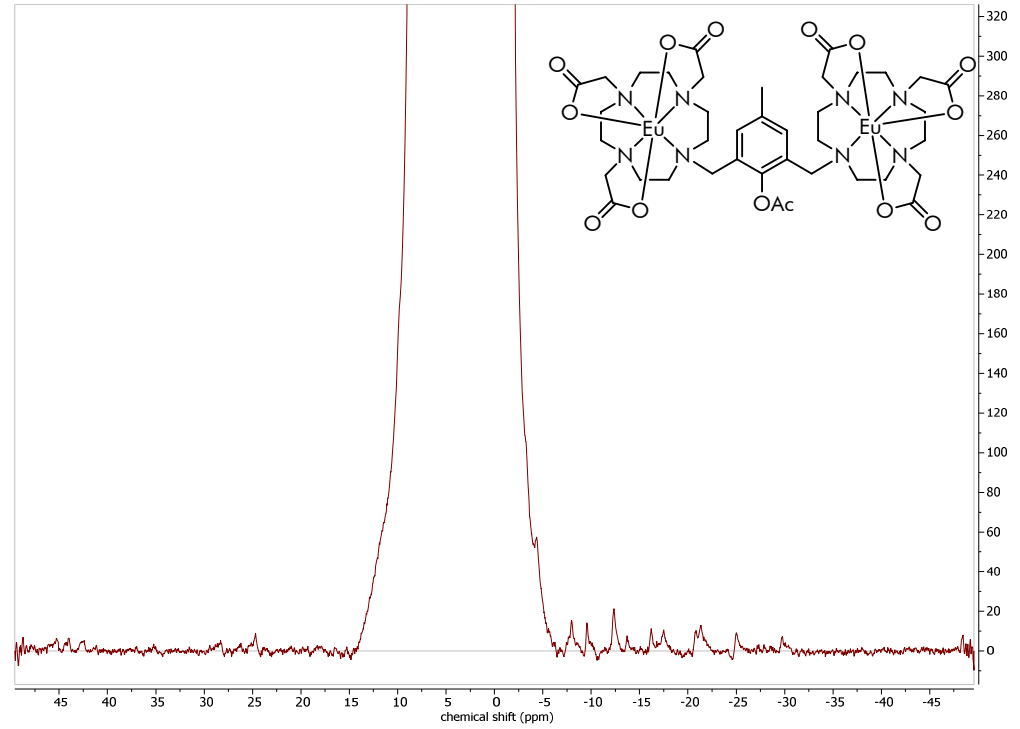

Figure 8.20 ^{1}H NMR spectrum of ***Eu$_2$3.3*** *recorded at 400 MHz in CD_3OD*

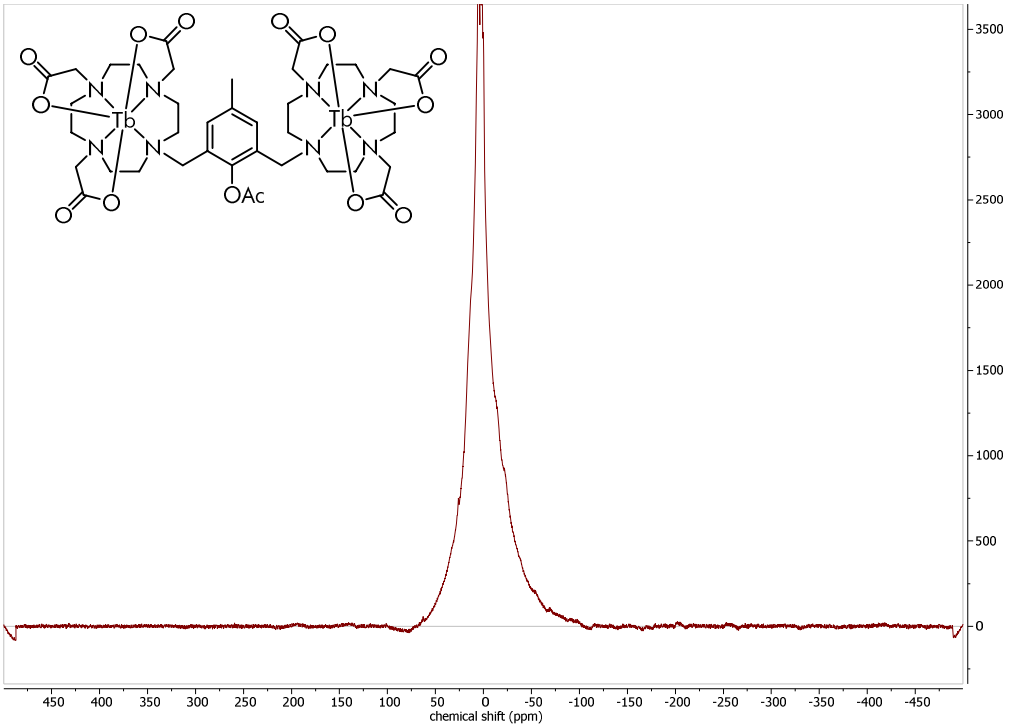

*Figure 8.21: ^{1}H NMR spectrum of **$Tb_2$3.3** recorded at 400 MHz in D_2O*

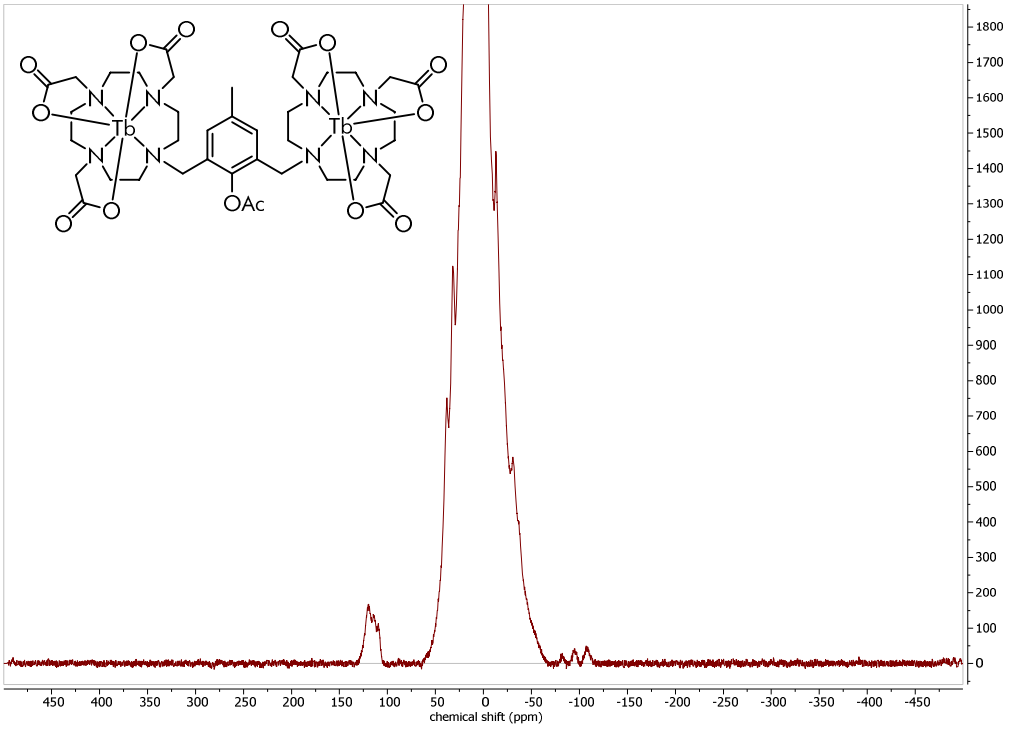

*Figure 8.22^{1}H NMR spectrum of **$Tb_2$3.3** recorded at 400 MHz in CD_3OD*

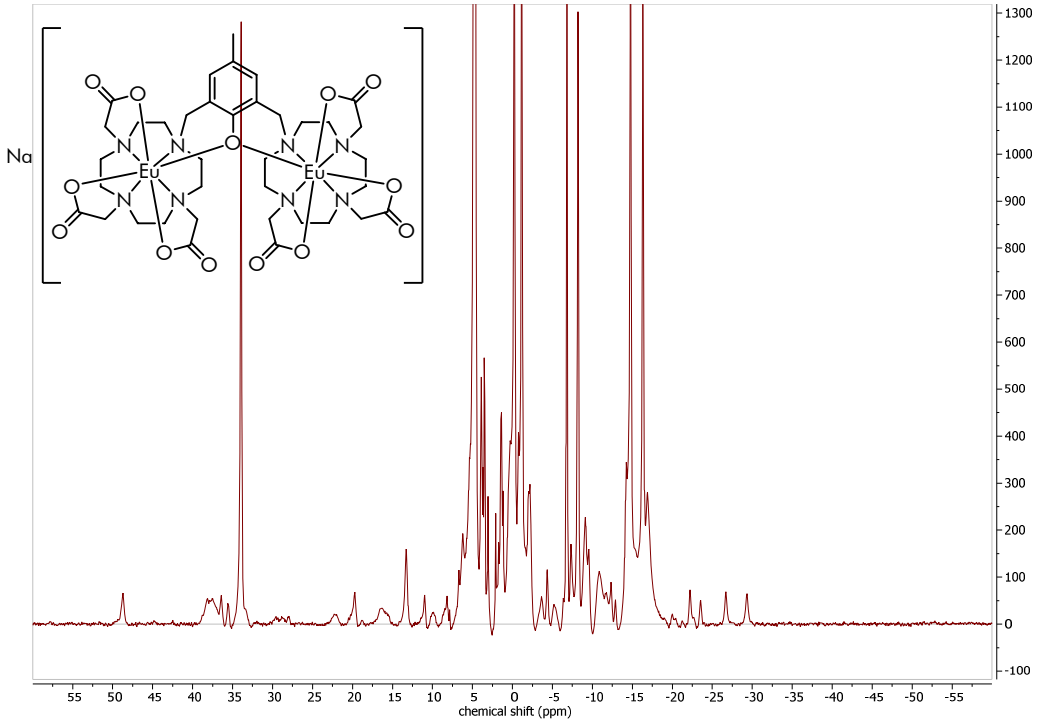

*Figure 8.23 ^{1}H NMR spectrum of **[Na][Eu$_2$3.1]** recorded at 400 MHz in D_2O*

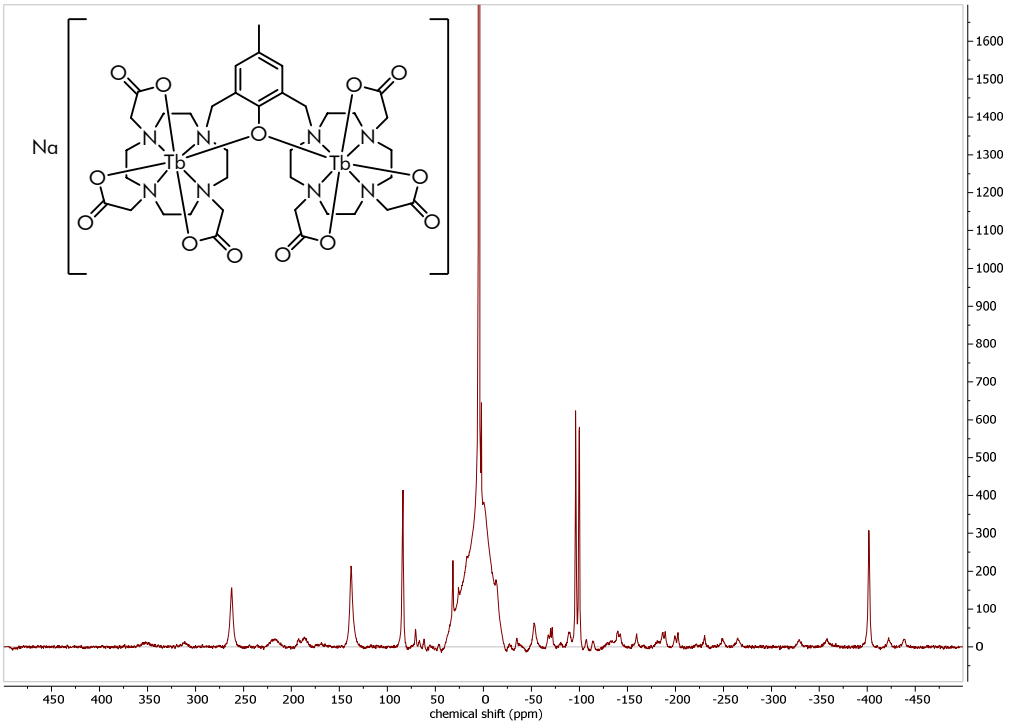

*Figure 8.24: ^{1}H NMR spectrum of **[Na][Tb$_2$3.1]** recorded at 400 MHz in D_2O*

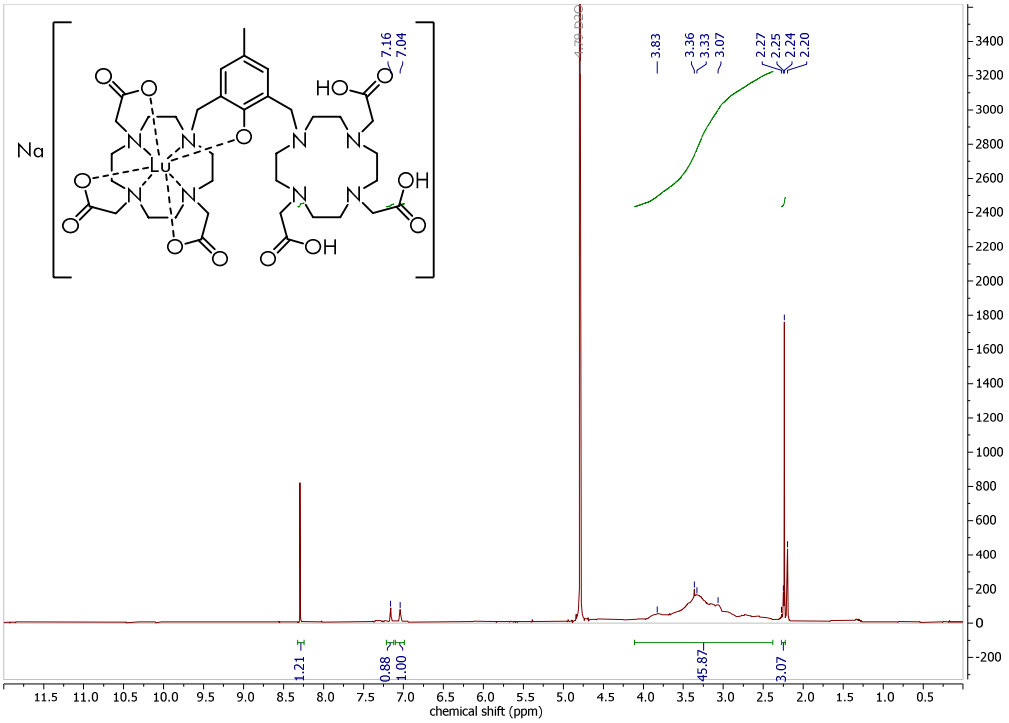

*Figure 8.25: ^{1}H NMR spectrum of **$H_3Lu3.1$** recorded at 400 MHz in D_2O*

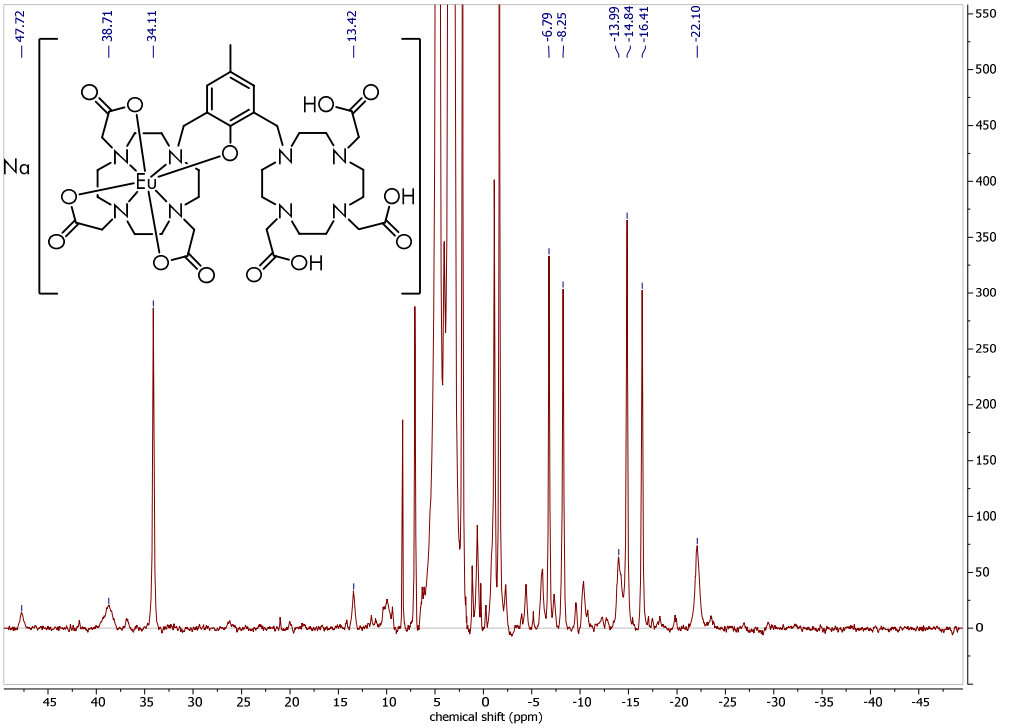

*Figure 8.26: ^{1}H NMR spectrum of **$H_3Eu3.1$** in H_2O at 400 MHZ*

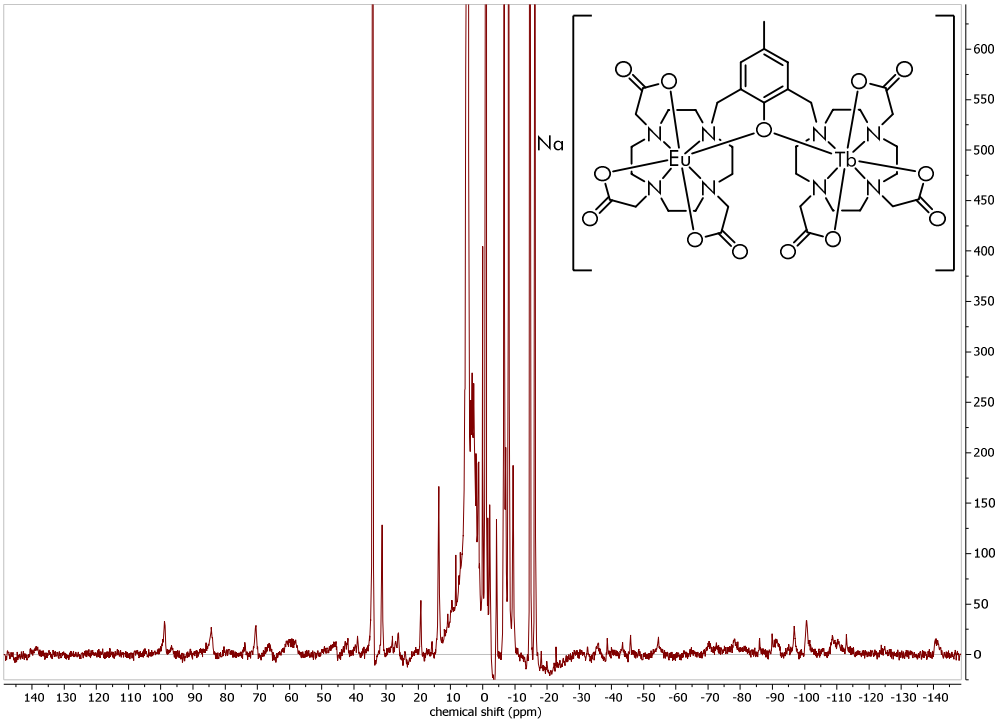

*Figure 8.27: ^1H NMR spectrum of **[Na][EuTb3.1]** in D_0O and 400 MHz.*

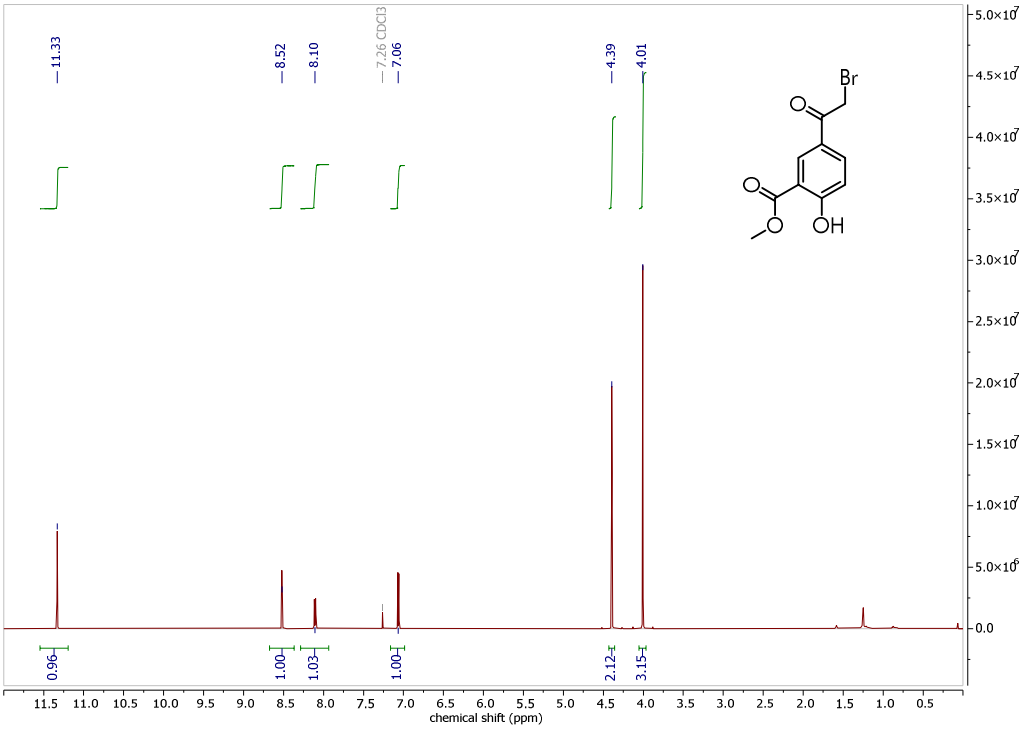

*Figure 8.28: ^1H NMR spectrum of **4.2** recorded at 600 MHz in $CDCl_3$*

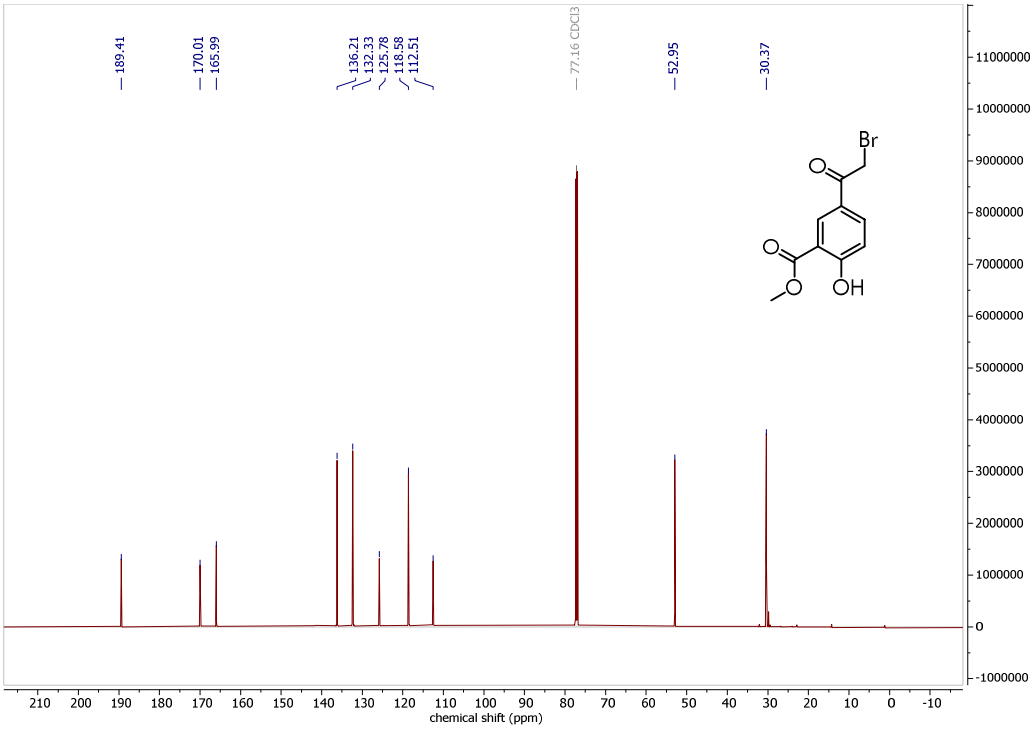

*Figure 8.29: ^{13}C NMR spectrum of **4.2** recorded at 150 MHz in $CDCl_3$*

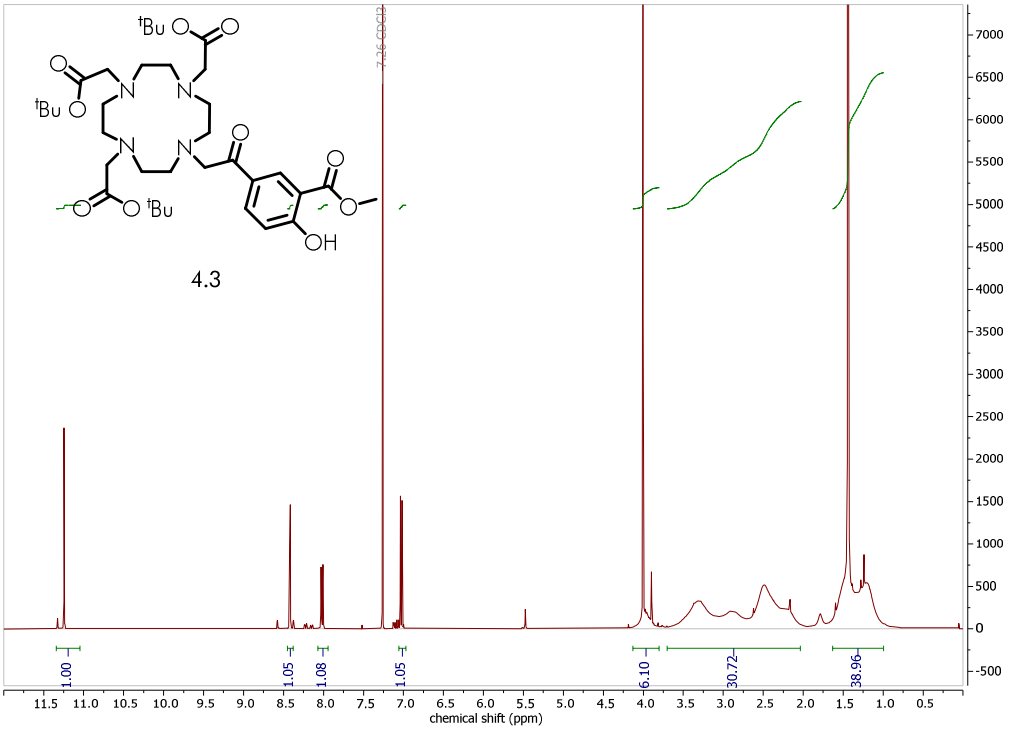

*Figure 8.30: ^{1}H NMR spectrum of **4.3** recorded at 400 MHz in $CDCl_3$*

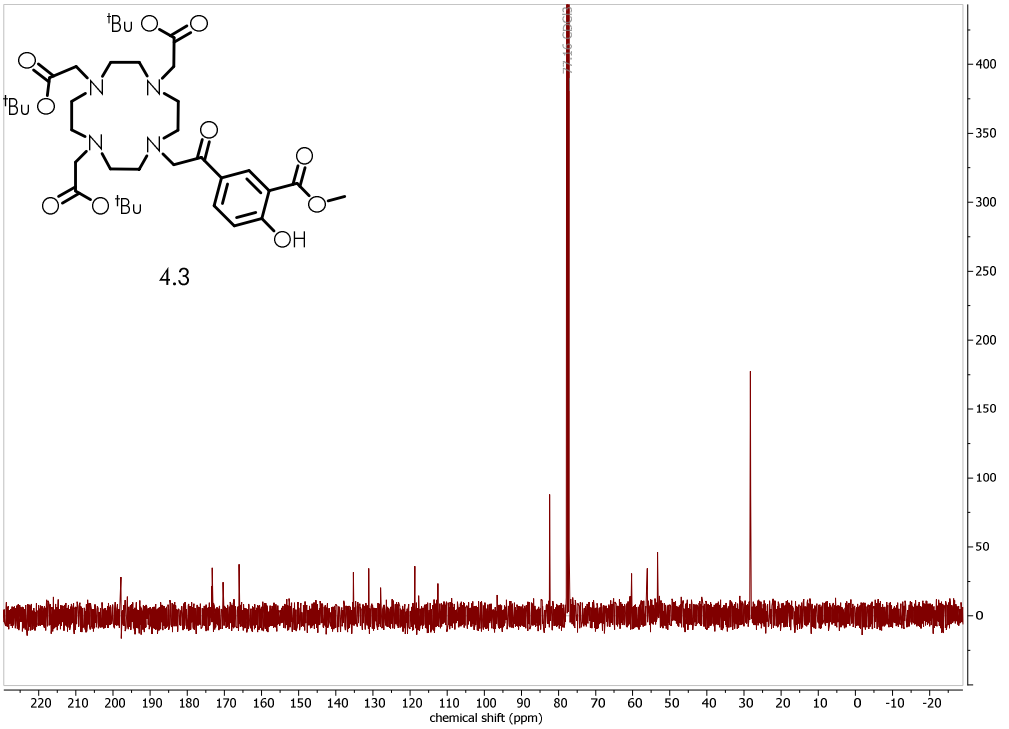

*Figure 8.31: ^{13}C NMR spectrum of **4.3** recorded at 100 MHz in $CDCl_3$*

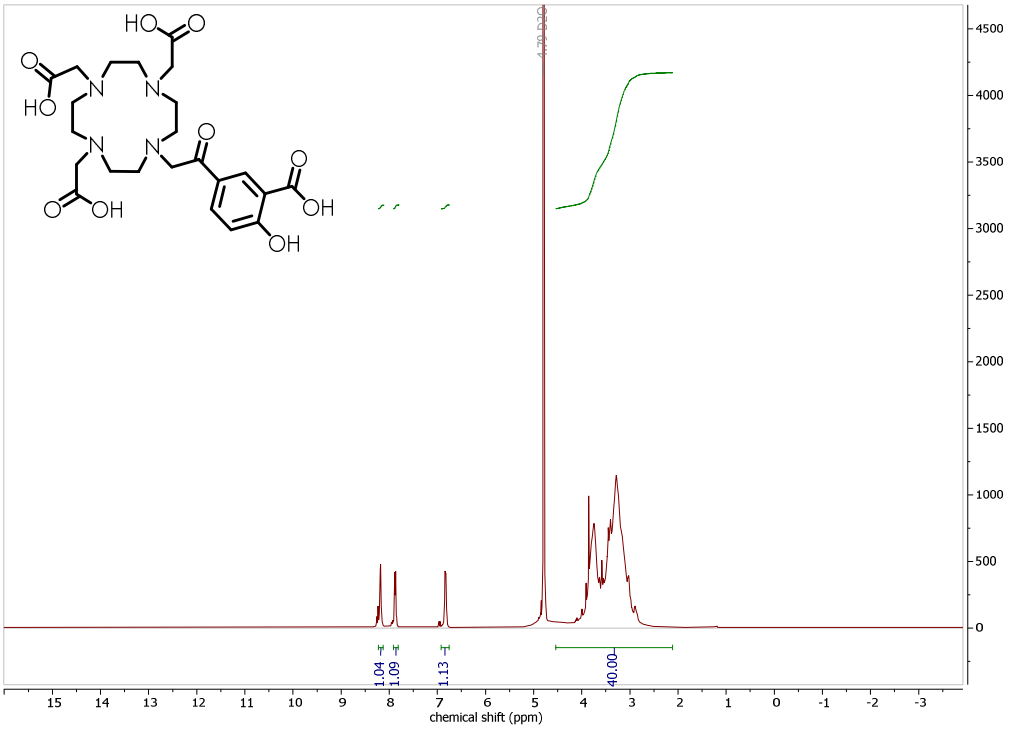

*Figure 8.32: ^{1}H NMR spectrum of **$H_2$4.1** recorded at 400 MHz in D_2O*

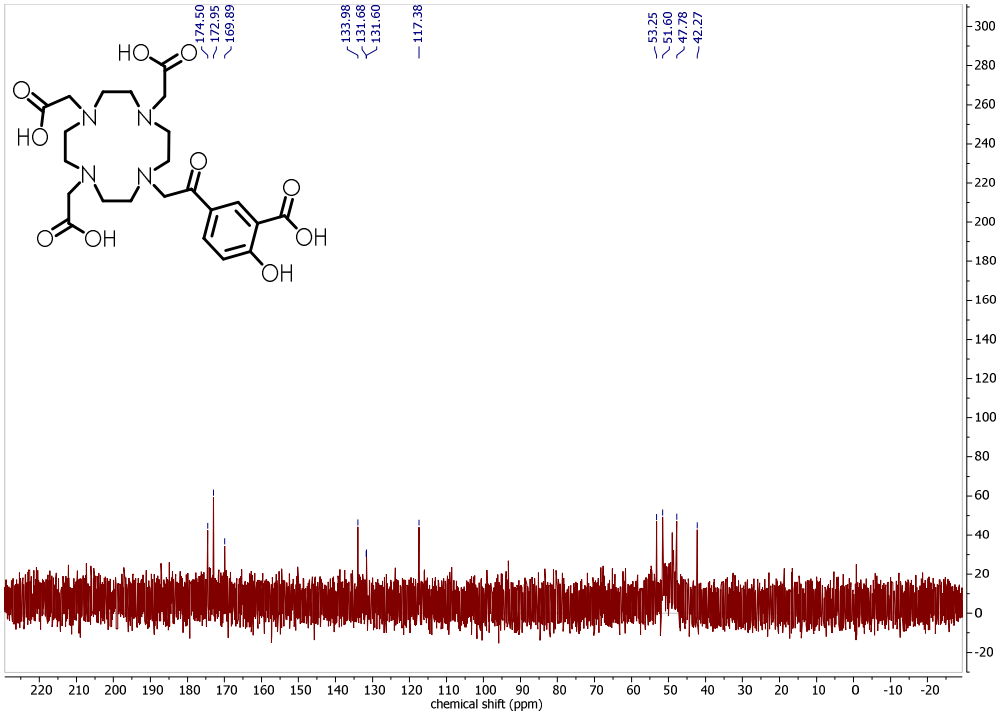

*Figure 8.33: ^{13}C NMR spectrum of **$H_2$4.1** recorded at 100 MHz in D_2O*

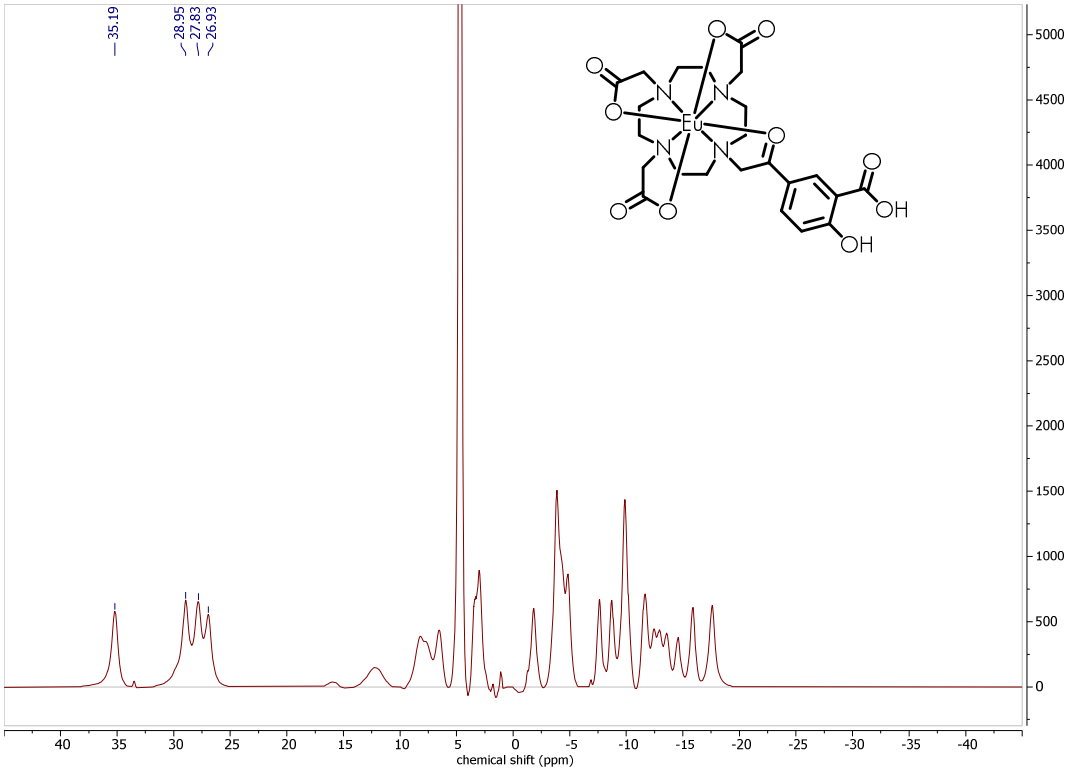

*Figure 8.34: ^{1}H NMR spectrum of **H_2Eu3.4** recorded in D_2O at 400 MHz*

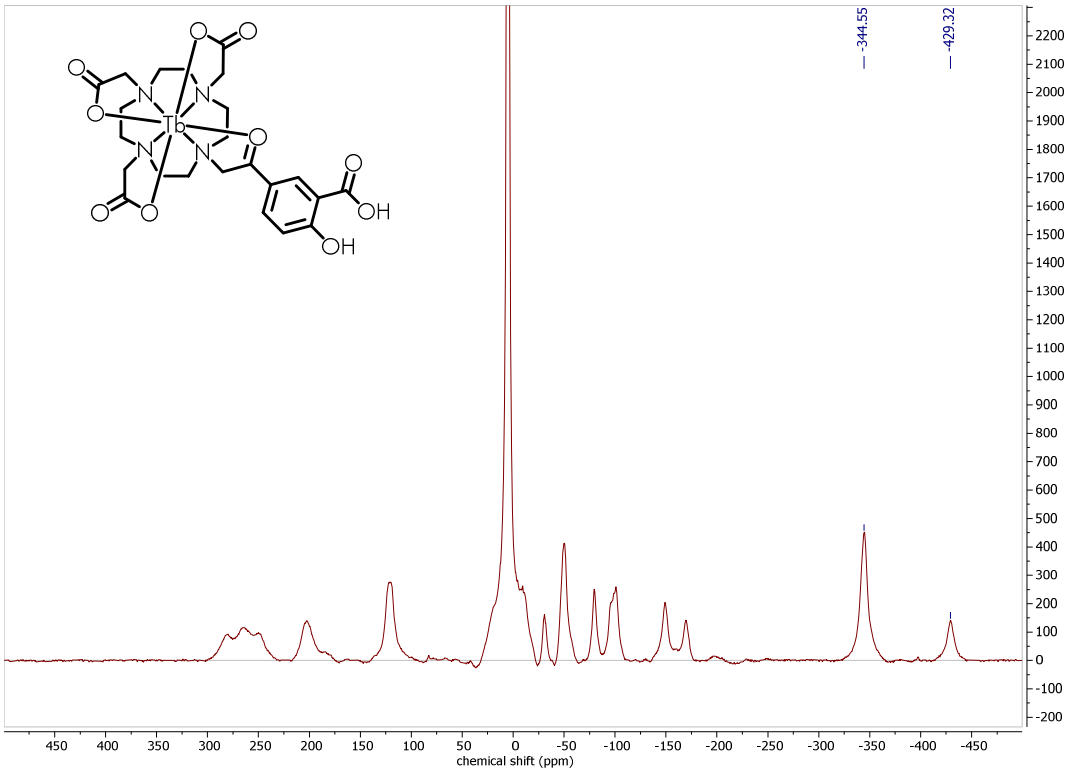

*Figure 8.35: ^1H NMR spectrum of **$H_2Tb3.4$** recorded in D_2O at 400 MHz*

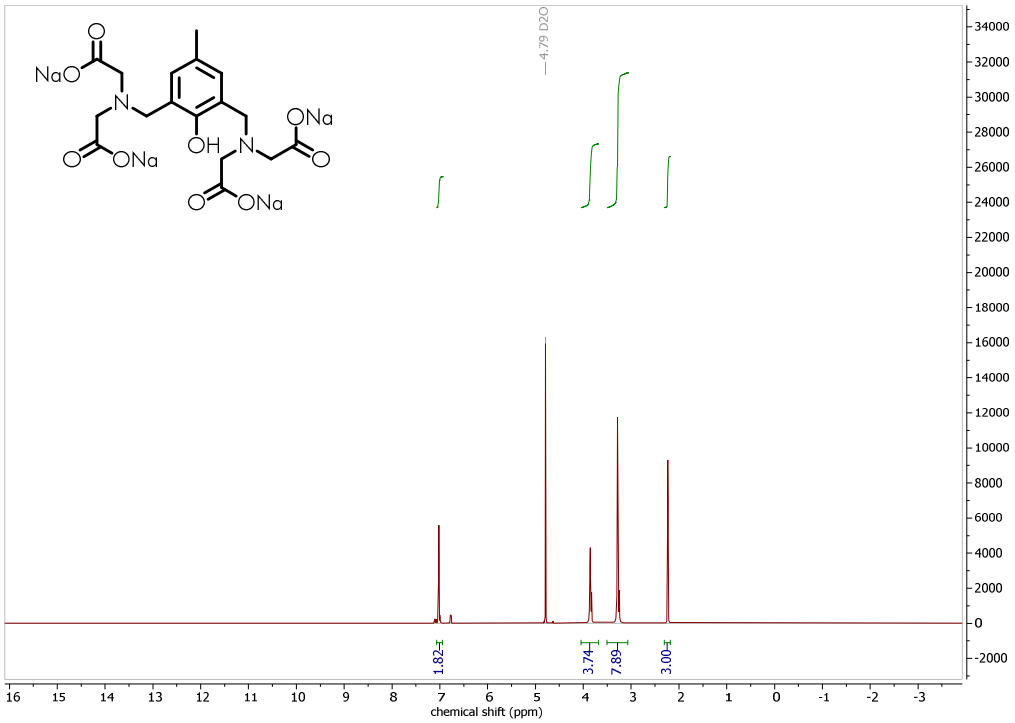

*Figure 8.36: ^1H NMR spectrum of **[Na]$_4$[5-Me-HXTA]** recorded at 400 MHz in D_2O*

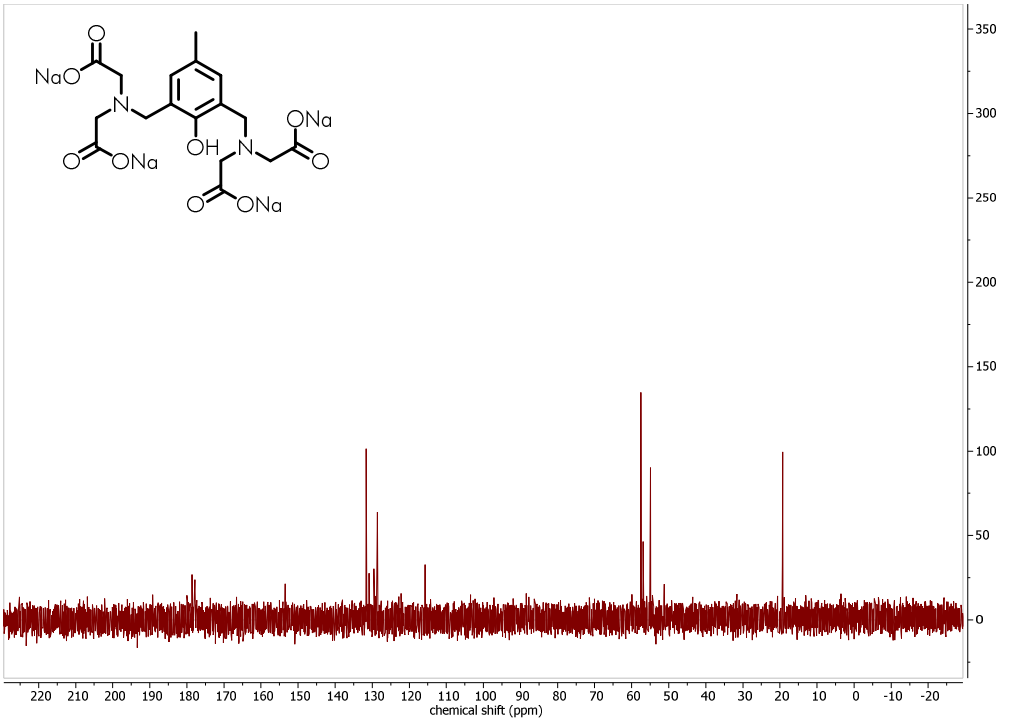

*Figure 8.37: ^{13}C NMR spectrum of **[Na]$_4$[5-Me-HXTA]** recorded at 100 MHz in D_2O*

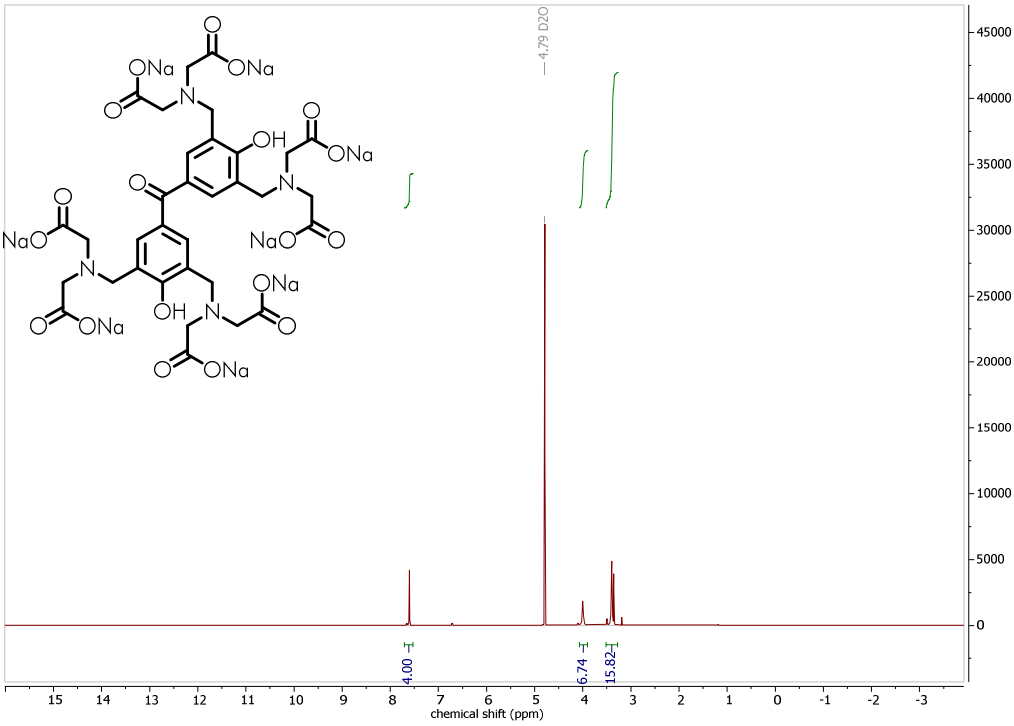

*Figure 8.38: ^{1}H NMR spectrum of **$Na_8H_2$4.1** recorded at 400 MHz in D_2O*

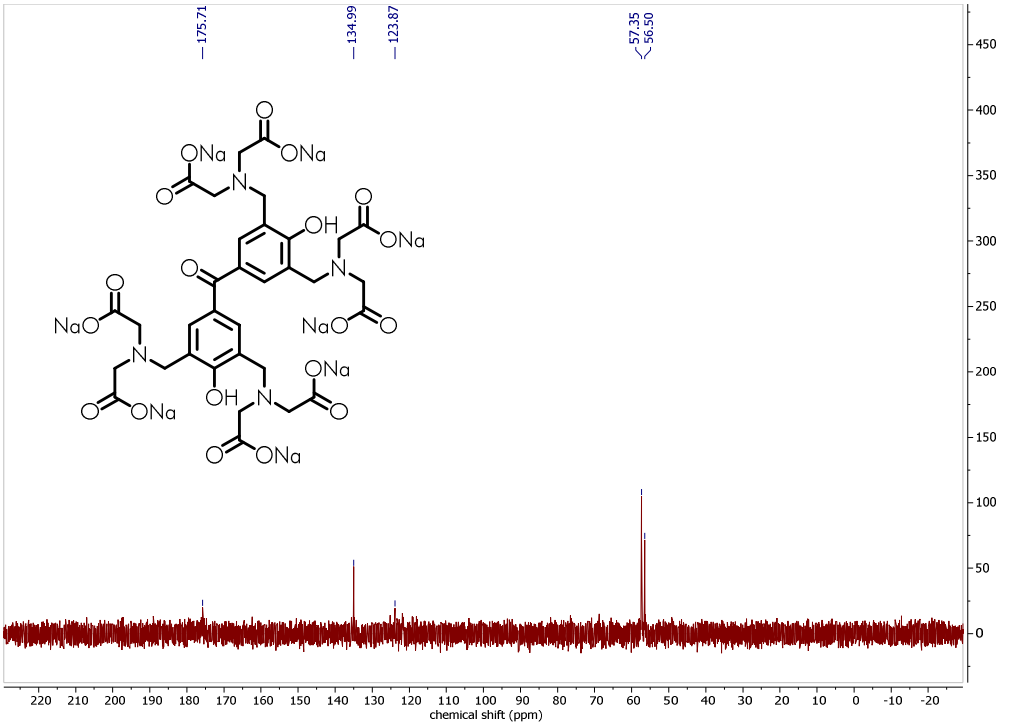

Figure 8.39: ^{13}C NMR spectrum of ***$Na_8H_24.1$*** *recorded at 100 MHz in D_2O*

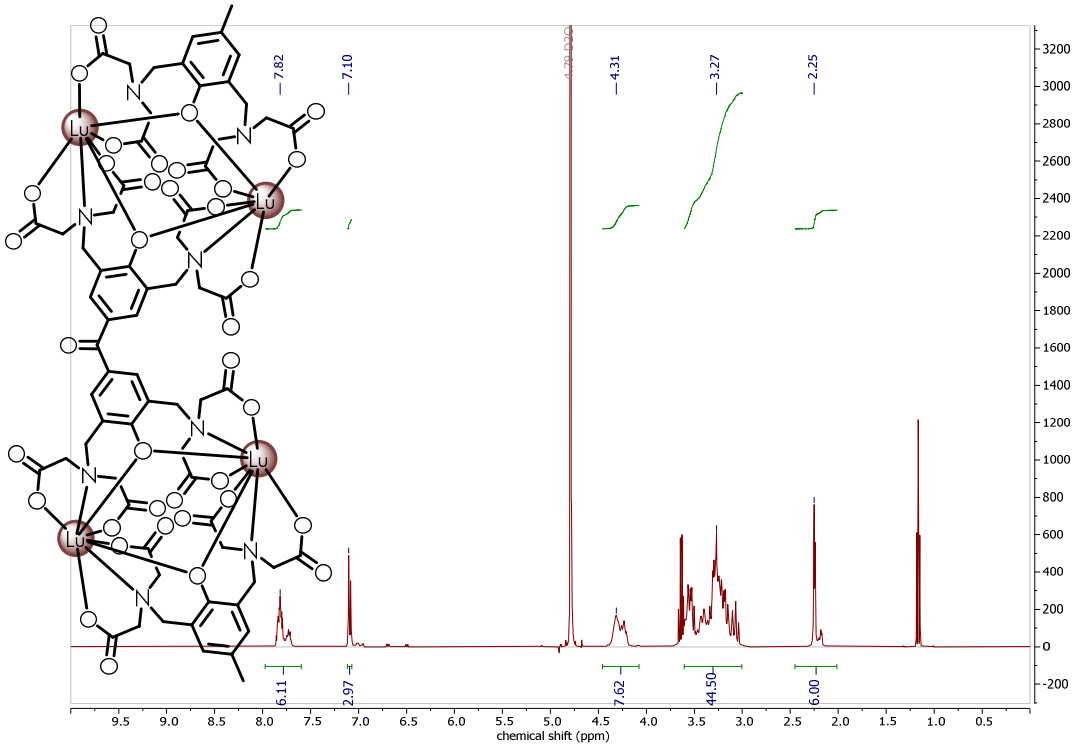

Figure 8.40: 400 MHz ^1H NMR spectrum of ***$[Na]_8[Lu_4(5\text{-}Me\text{-}HXTA)_2(5.1)]$*** *in D_2O*

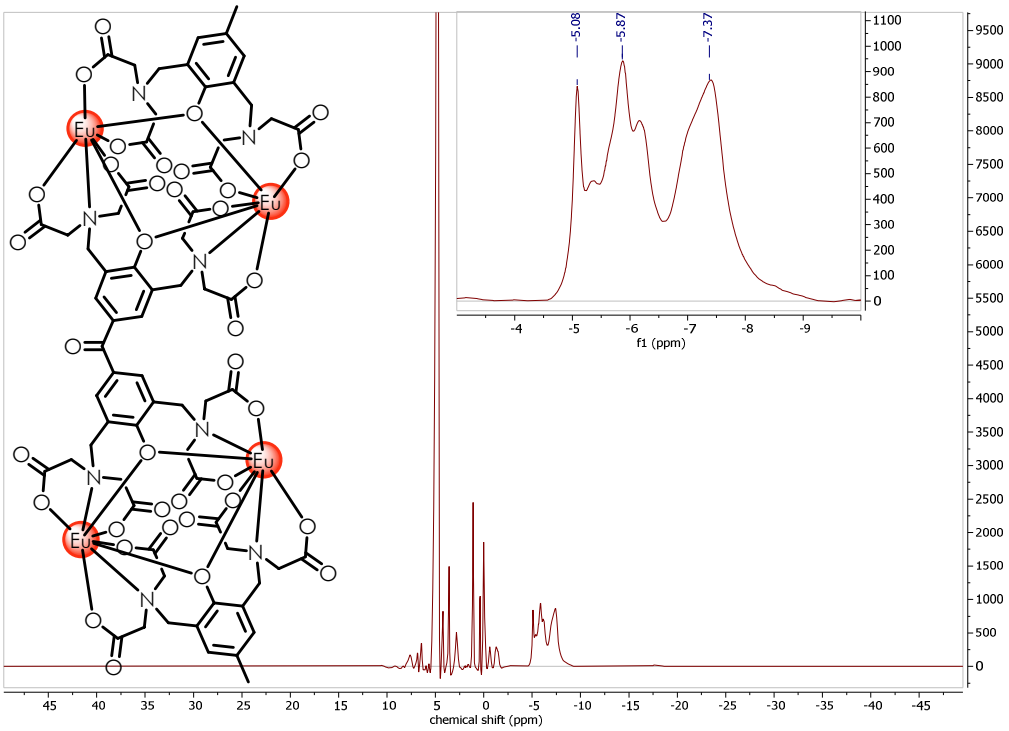

Figure 8.41: 400 MHz ^{1}H NMR spectrum of ***[Na]$_8$[Eu$_4$(5-Me-HXTA)$_2$(5.1)]*** *recorded in D_2O.*

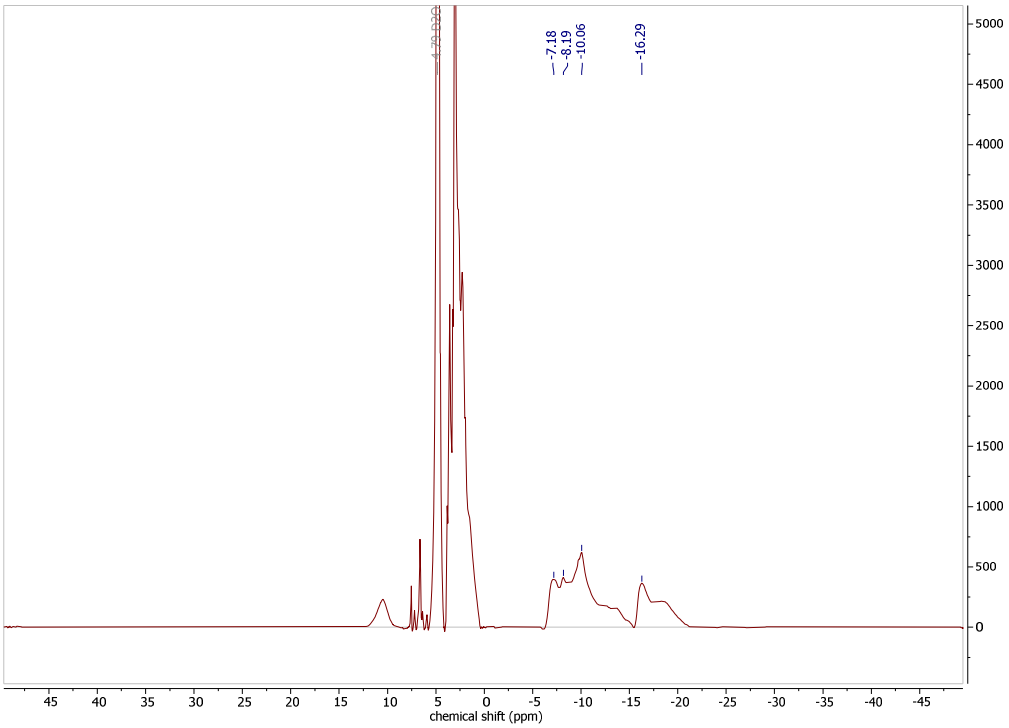

Figure 8.42: ^{1}H NMR spectrum of ***Eu5.1*** *recorded at 400 MHz in D_2O*

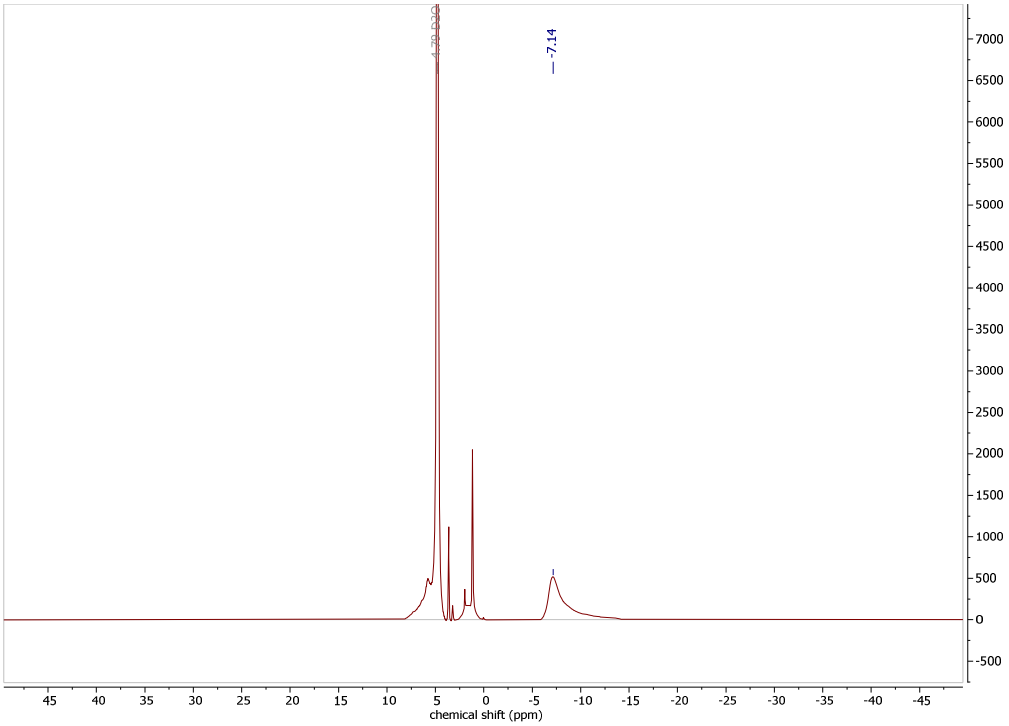

*Figure 8.43: ^{1}H NMR spectrum of **Eu(5.1)$_2$** recorded at 400 MHz in D_2O*

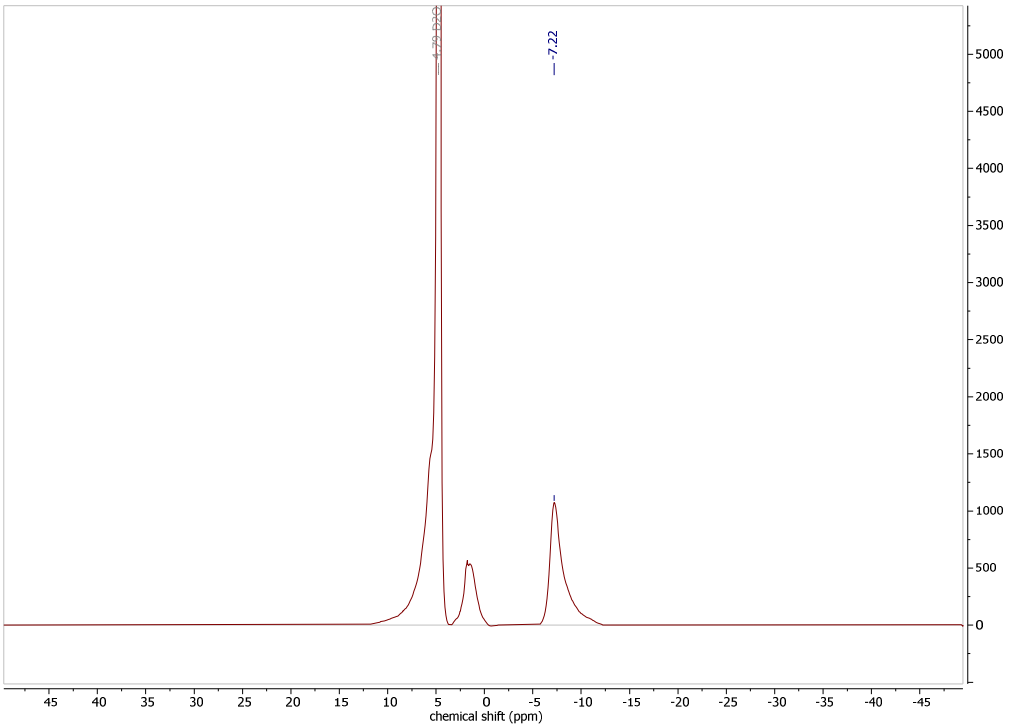

*Figure 8.44: ^{1}H NMR spectrum of **Eu(5.1)$_{2.3}$** recorded at 400 MHz in D_2O*

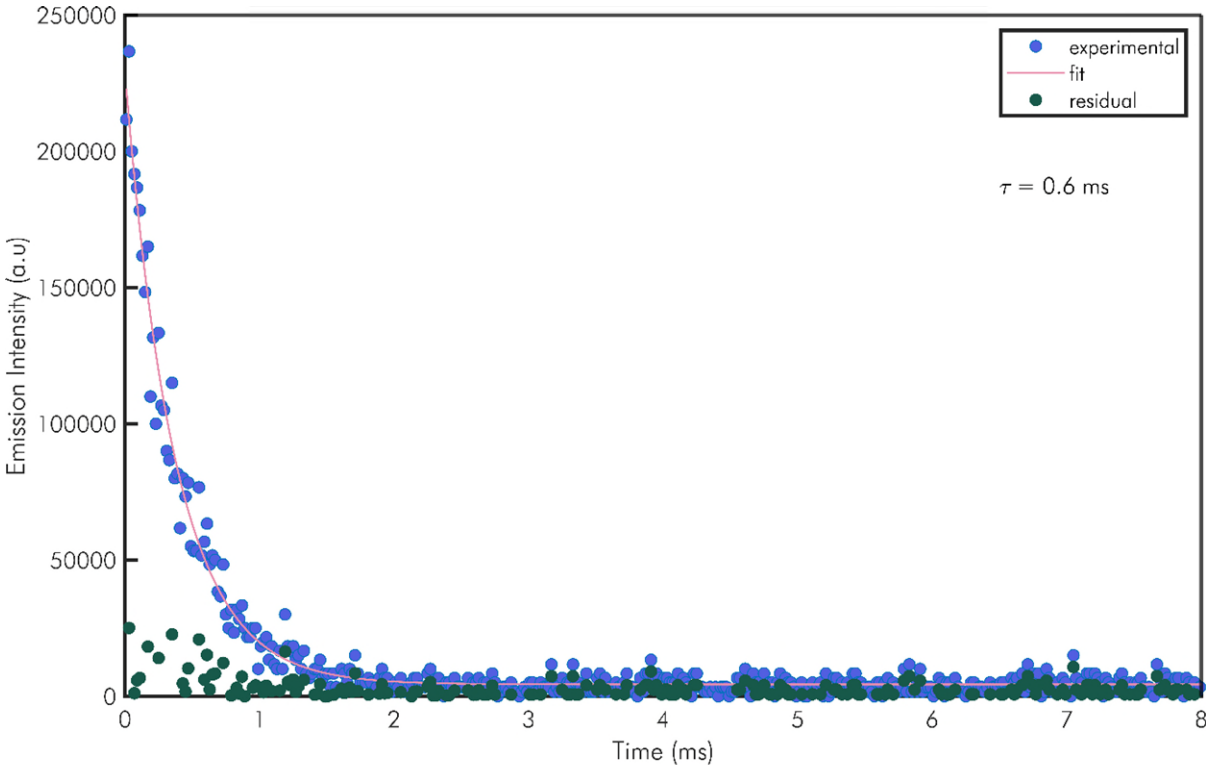

Figure 9.1 Time resolved emission spectroscopy of ***Eu$_2$3.3*** *in H_2O (10^{-5} M). λ_{em} = 617 nm. λ_{ex} = 270 nm*

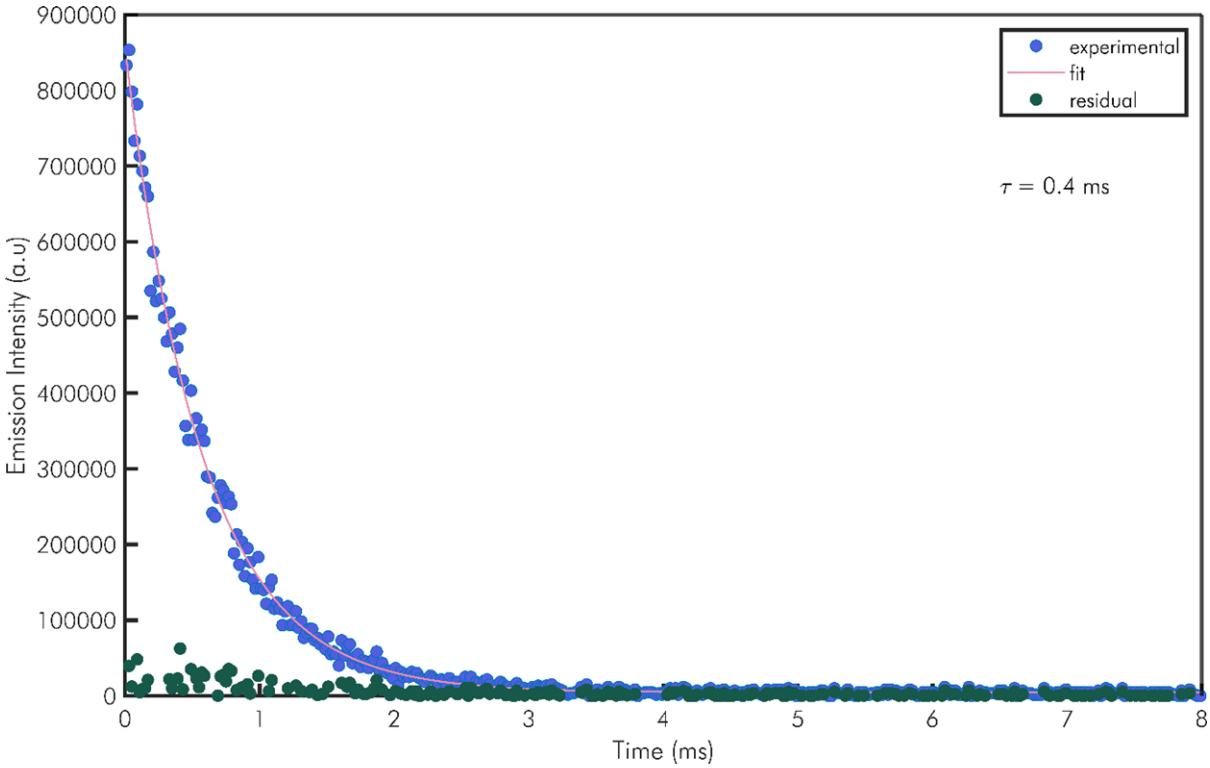

Figure 9.2 Time resolved emission spectroscopy of ***[Na][Eu$_2$3.1]*** *in H_2O (10^{-5} M). λ_{em} = 617 nm. λ_{ex} = 270 nm*

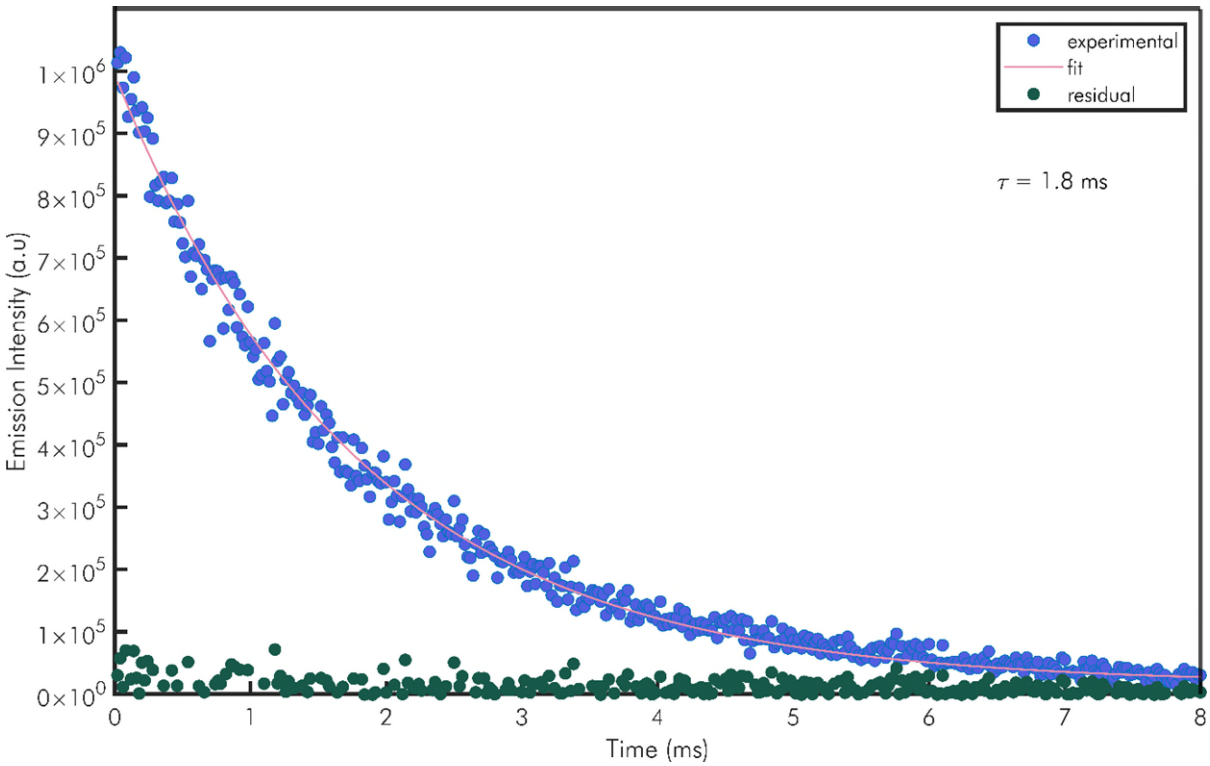

Figure 9.3 Time resolved emission spectroscopy of ***$Tb_2$3.3*** *in H_2O (10^{-6} M). λ_{em} = 546 nm. λ_{ex} = 270 nm*

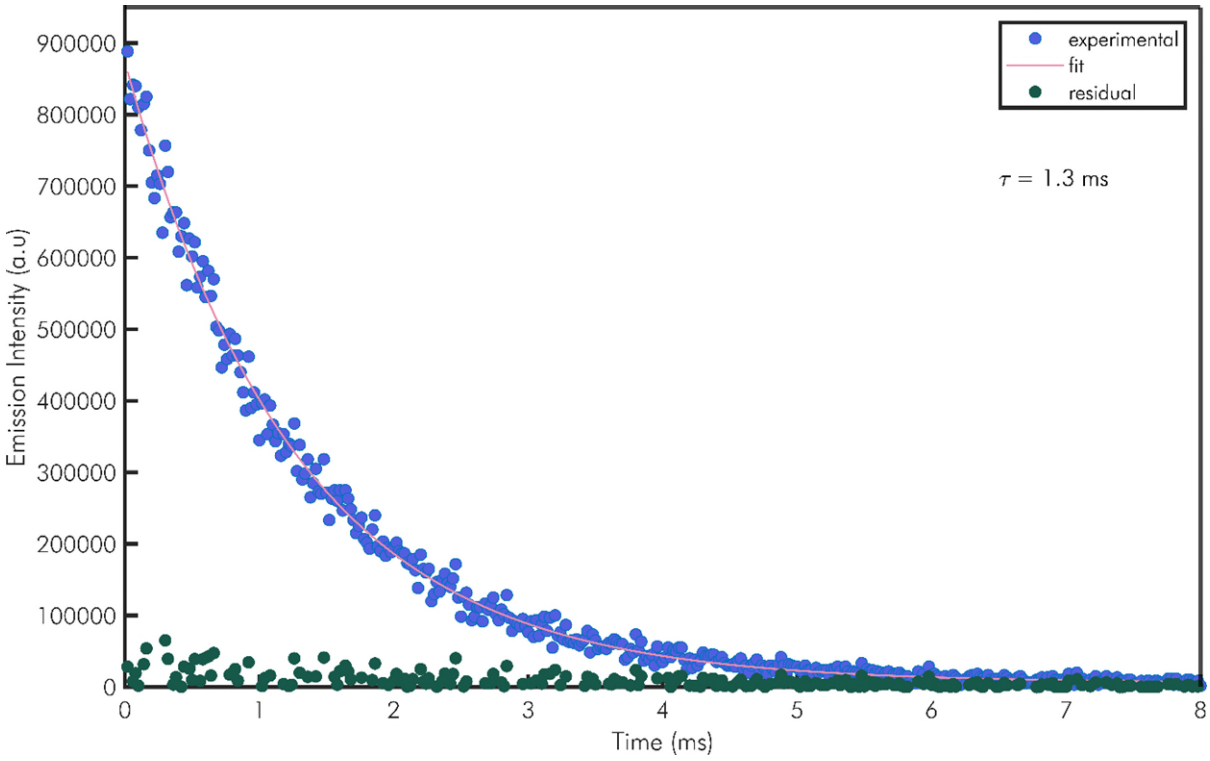

Figure 9.4 Time resolved emission spectroscopy of ***[Na][$Tb_2$3.1]*** *in H_2O (10^{-6} M). λ_{em} = 546 nm. λ_{ex} = 270 nm*

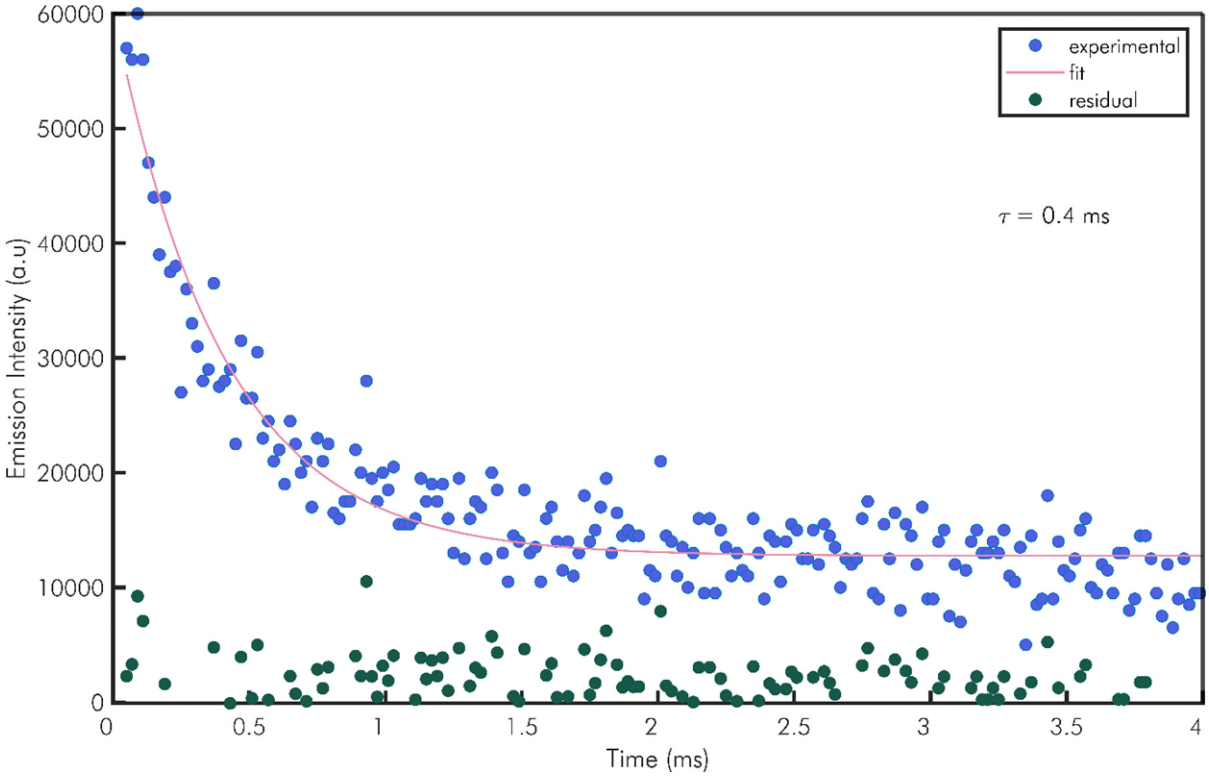

Figure 9.5 Time resolved emission spectroscopy of **Eu(acac)$_3$** *in D_2O (10^{-3} M). λ_{em} = 615 nm. λ_{ex} = 400 nm.*

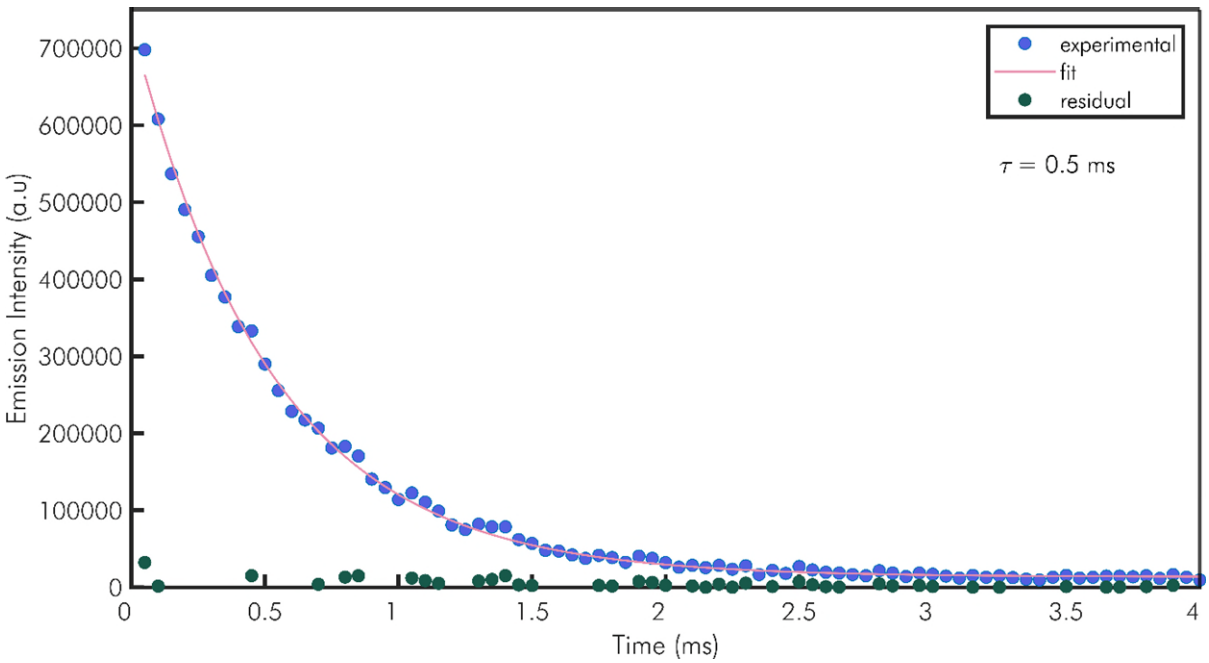

Figure 9.6 Time resolved emission spectroscopy of **Tb(acac)$_3$** *in D_2O (10^{-3} M). λ_{em} = 540 nm. λ_{ex} = 488 nm.*

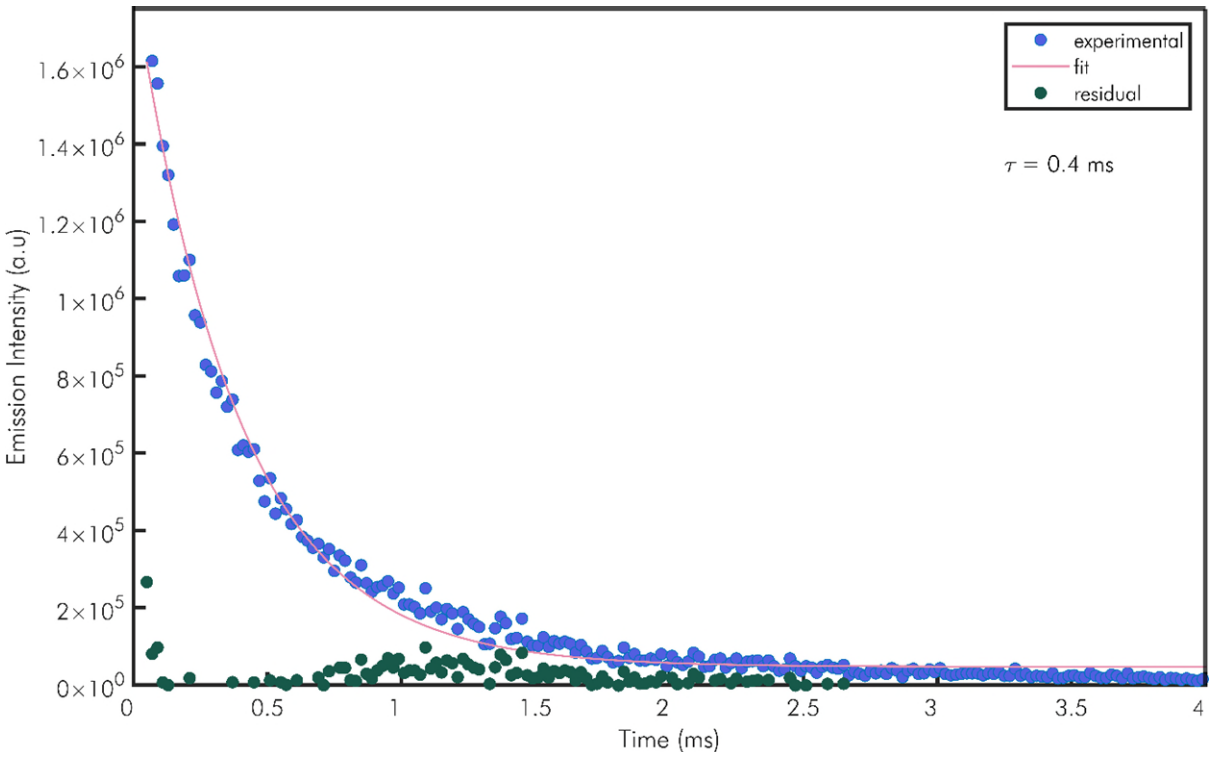

Figure 9.7 Time resolved emission spectroscopy of ***[Na]$_2$[Eu(acac)$_3$].[Tb4.1]*** *in D_2O (10^{-3} M). λ_{em} = 615 nm. λ_{ex} = 400 nm*

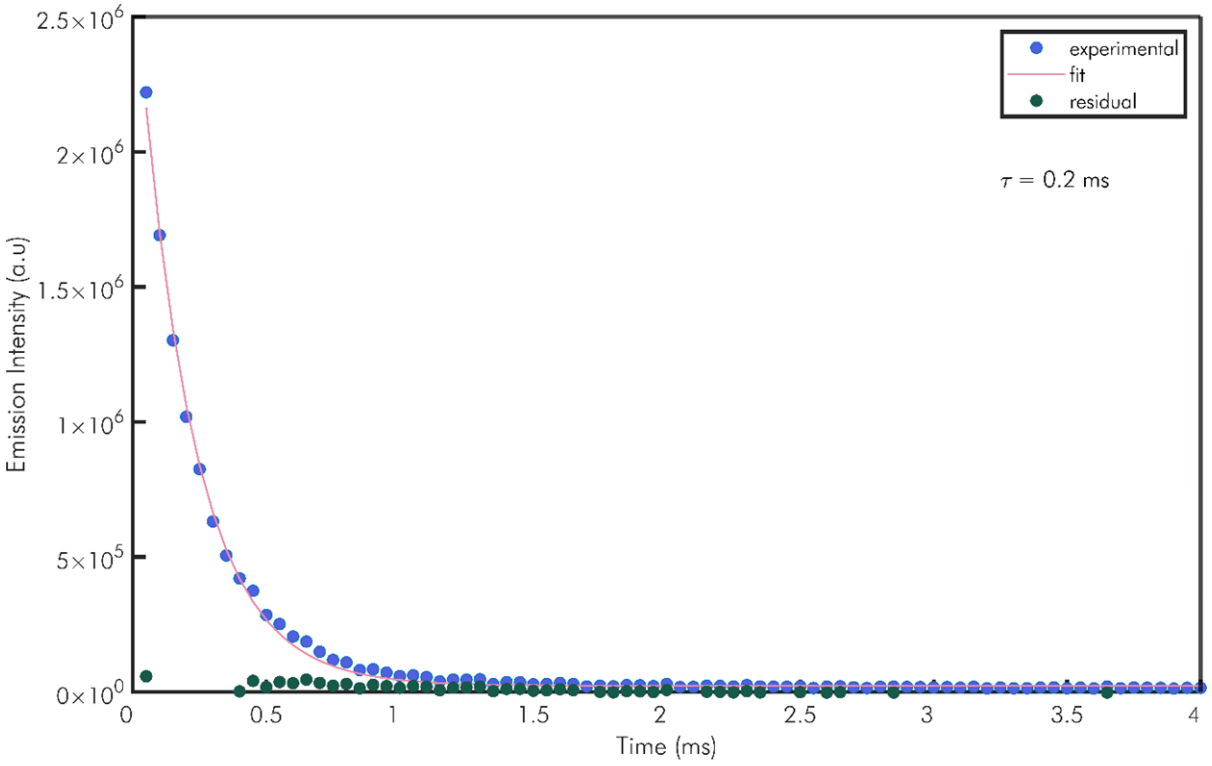

Figure 9.8 Time resolved emission spectroscopy of ***[Na]$_2$[Eu(acac)$_3$].[Tb4.1]*** *in D_2O (10^{-3} M). λ_{em} = 540 nm. λ_{ex} = 488 nm*

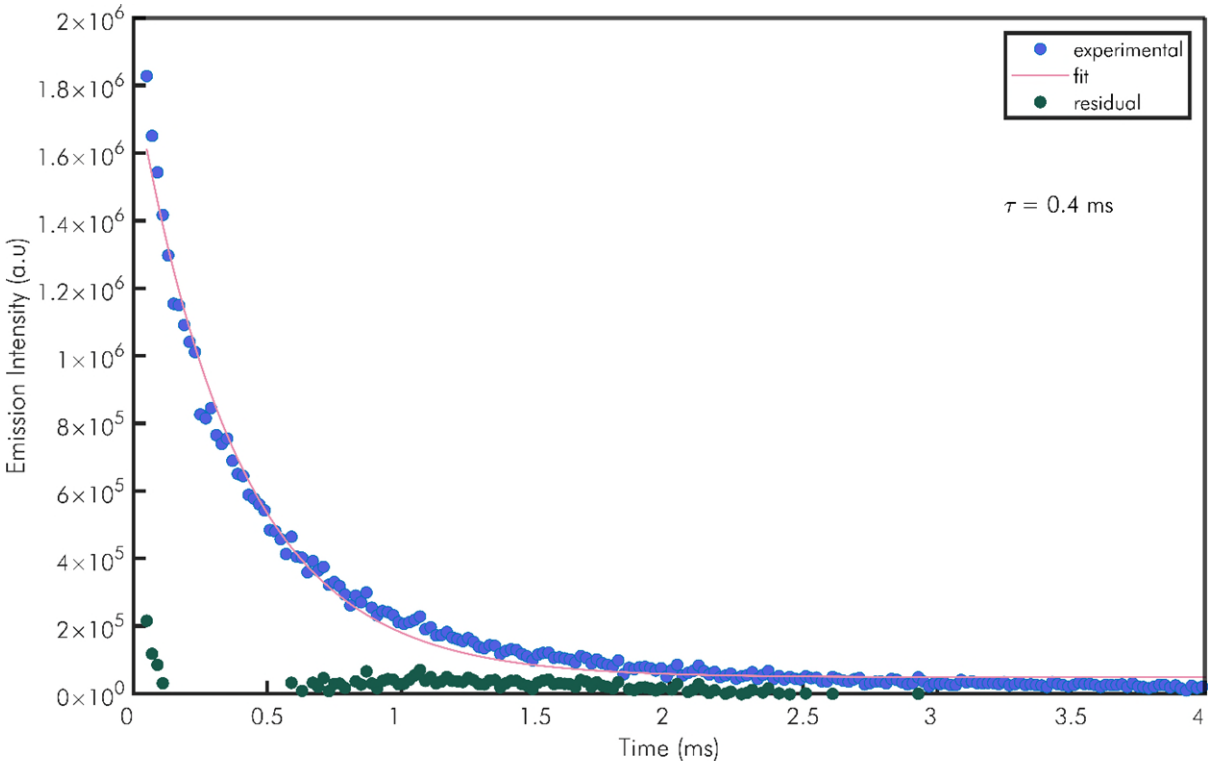

Figure 9.9 Time resolved emission spectroscopy of ***[Na]$_2$[Tb(acac)$_3$].[Eu4.1]*** *in D_2O (10^{-3} M). λ_{em} = 615 nm. λ_{ex} = 400 nm*

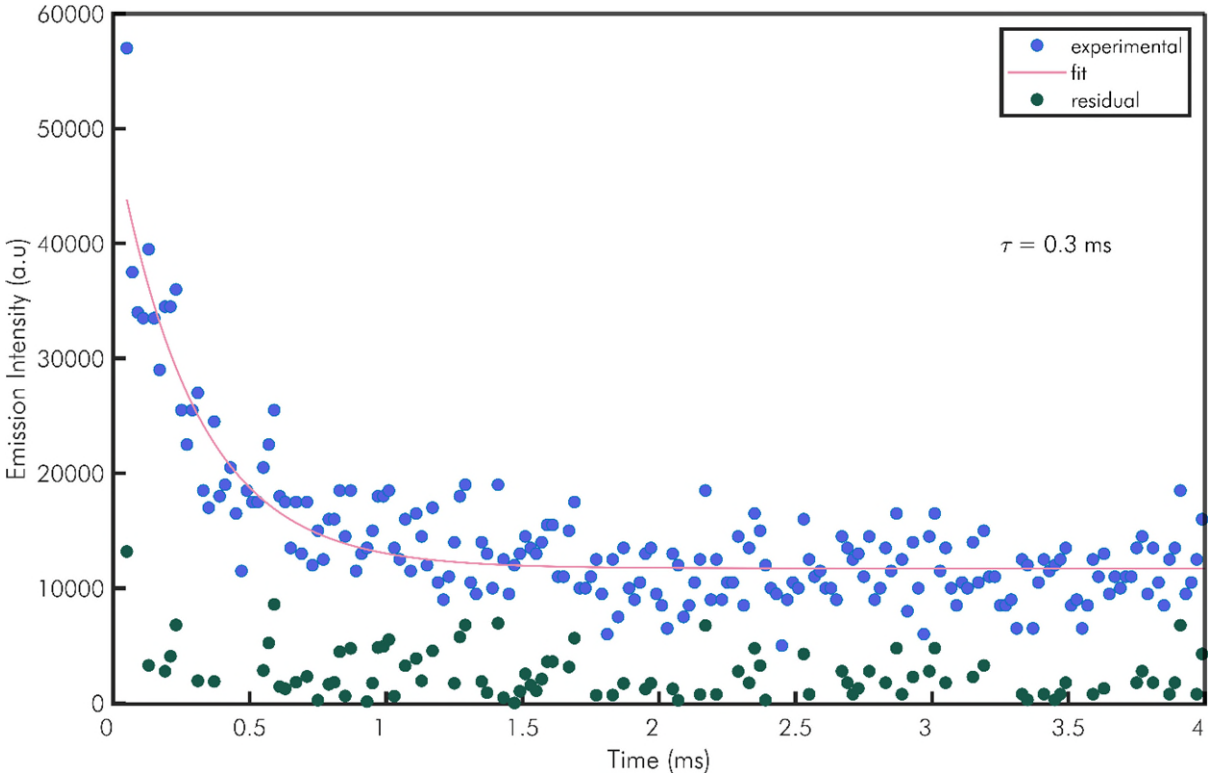

Figure 9.10 Time resolved emission spectroscopy of ***[Na]$_2$[Tb(acac)$_3$].[Eu4.1]*** *in D_2O (10^{-3} M). λ_{em} = 540 nm. λ_{ex} = 488 nm*

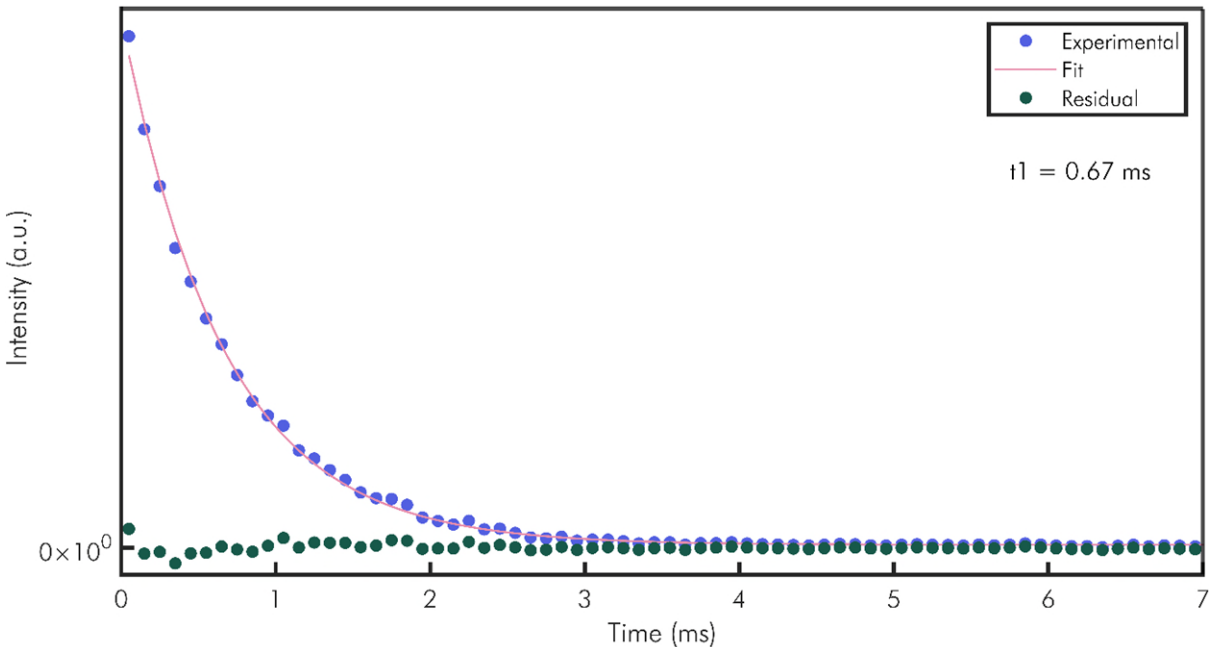

Figure 9.11: Time resolved emission spectroscopy of ***[Na]$_8$[Eu$_4$(5-Me-HXTA)$_2$(5.1)]*** *in H_2O (10^{-5} M). λ_{em} = 615 nm. λ_{ex} = 333 nm.*

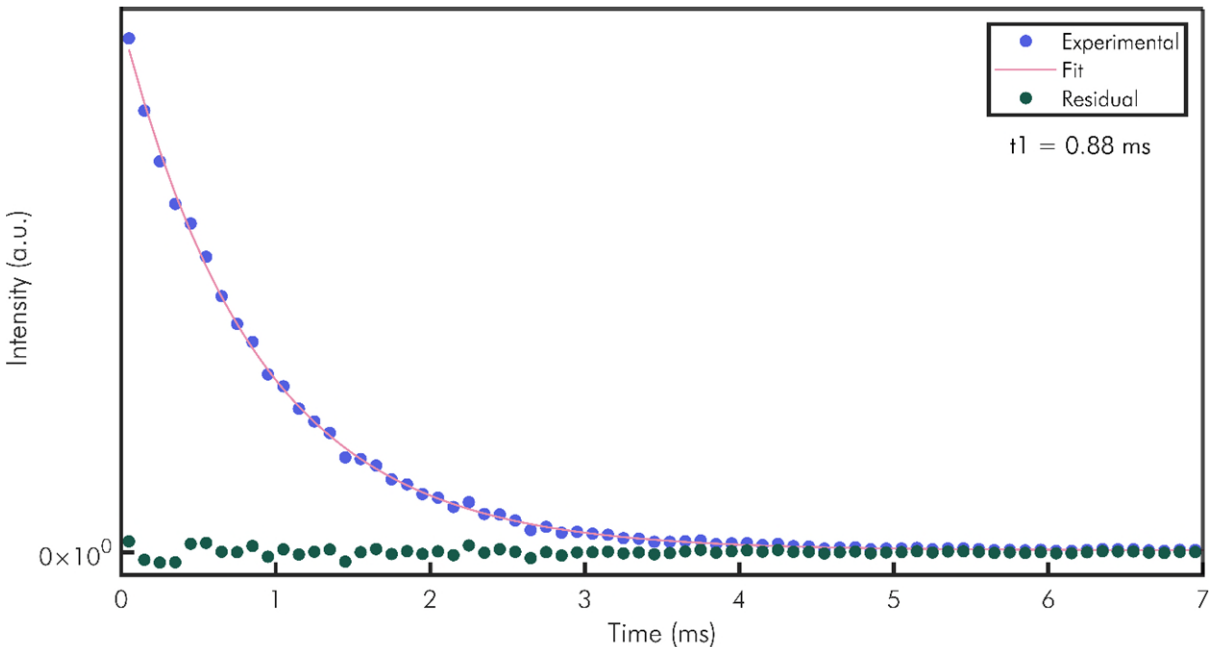

Figure 9.12: Time resolved emission spectroscopy of ***[Na]$_8$[Eu$_4$(5-Me-HXTA)$_2$(5.1)]*** *in D_2O (10^{-5} M). λ_{em} = 615 nm. λ_{ex} = 333 nm.*

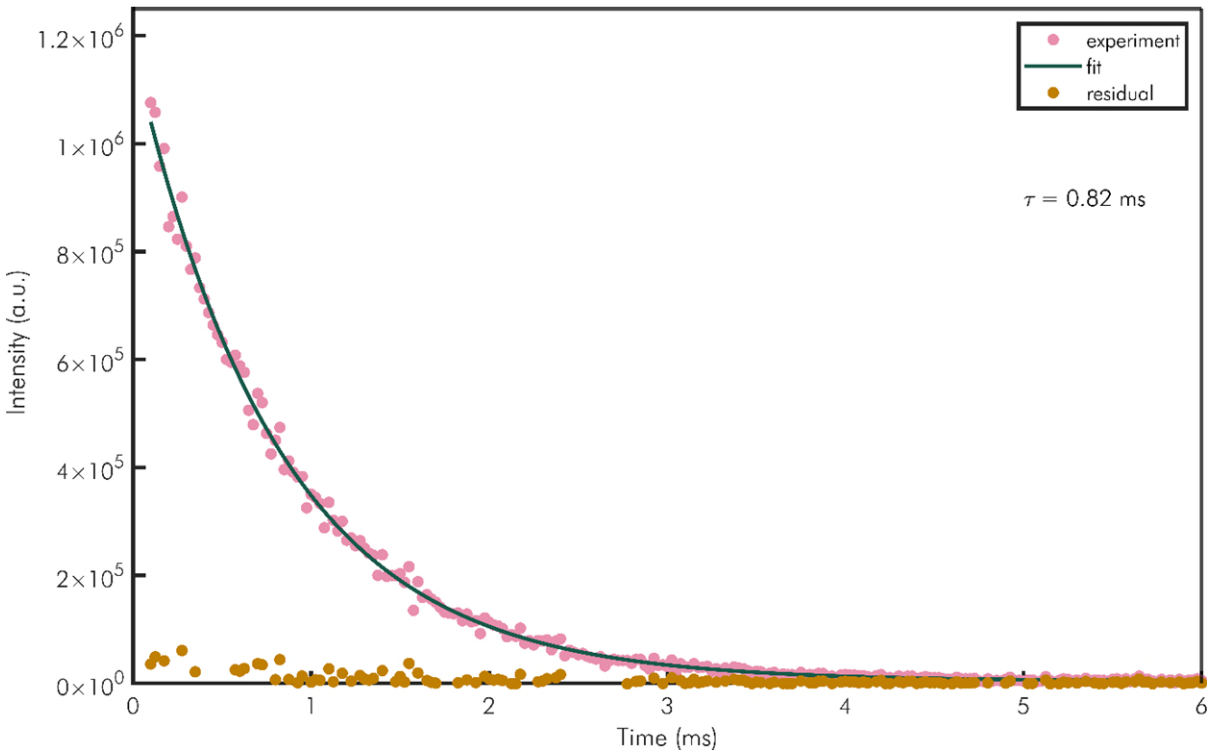

Figure 9.13: Time resolved emission spectroscopy of ***Eu(5.1)*** *in H_2O (10^{-6} M). λ_{em} = 615 nm. λ_{ex} = 350 nm.*

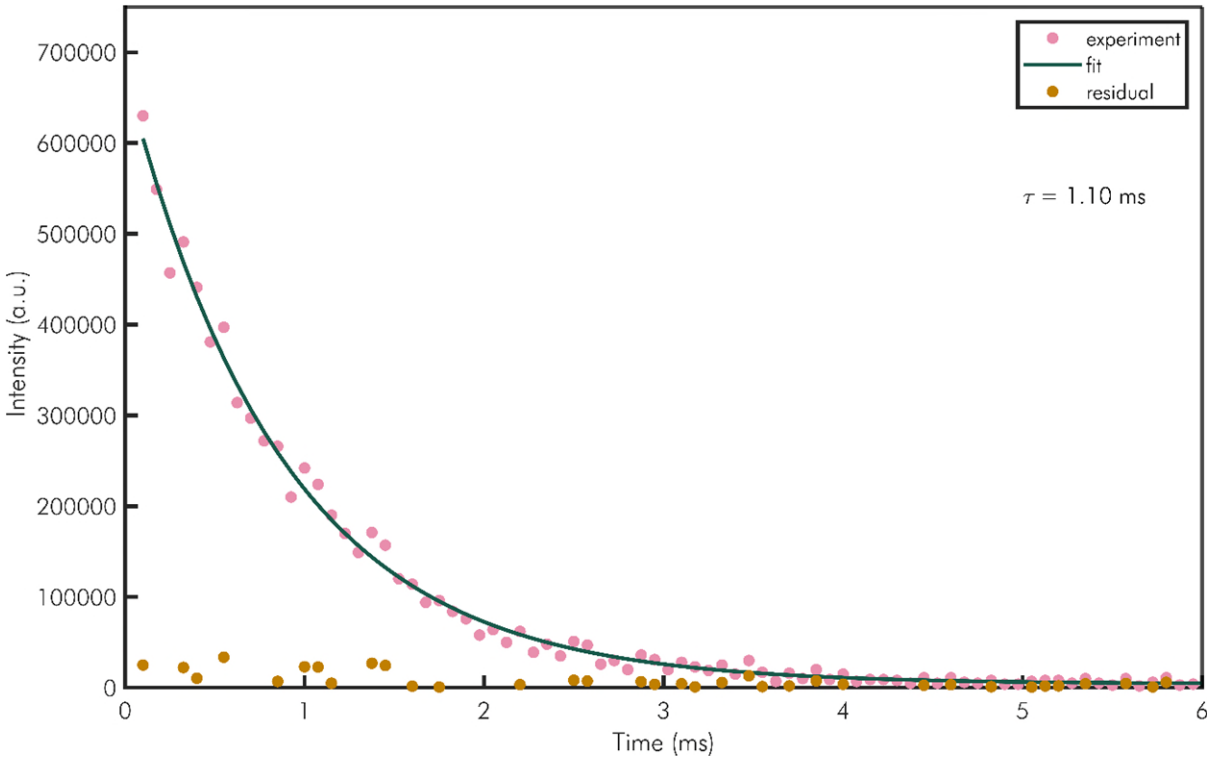

Figure 9.14 Time resolved emission spectroscopy of ***Eu(5.1)*** *in D_2O (10^{-6} M). λ_{em} = 615 nm. λ_{ex} = 350 nm.*

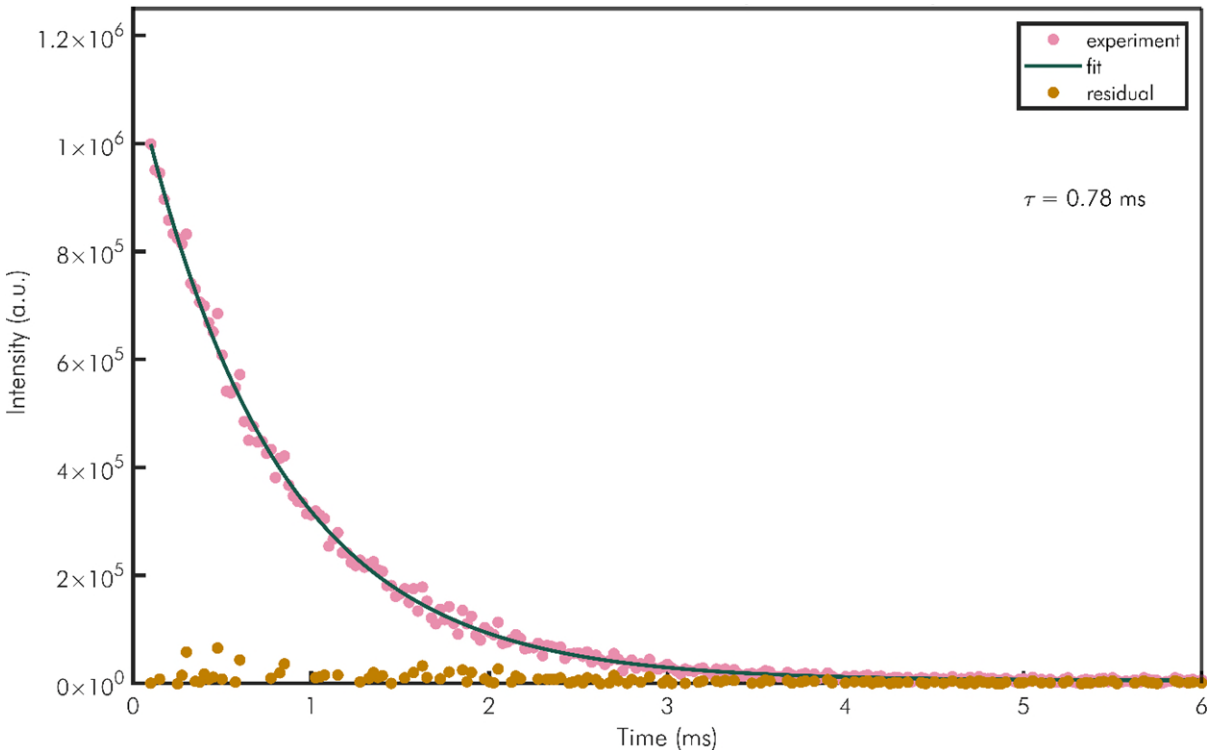

Figure 9.15 Time resolved emission spectroscopy of ***Eu(5.1)₂*** *in H_2O (10^{-6} M). λ_{em} = 615 nm. λ_{ex} = 350 nm.*

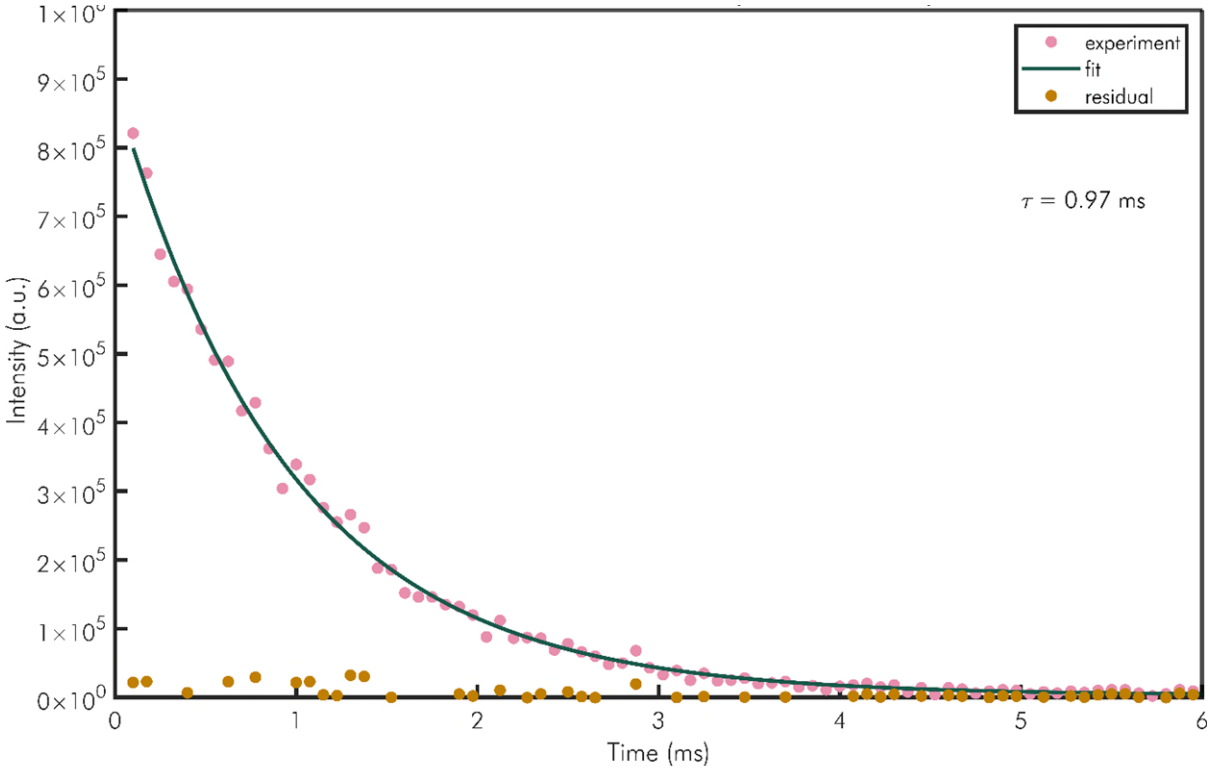

Figure 9.16 Time resolved emission spectroscopy of ***Eu(5.1)₂*** *in D_2O (10^{-6} M). λ_{em} = 615 nm. λ_{ex} = 350 nm.*

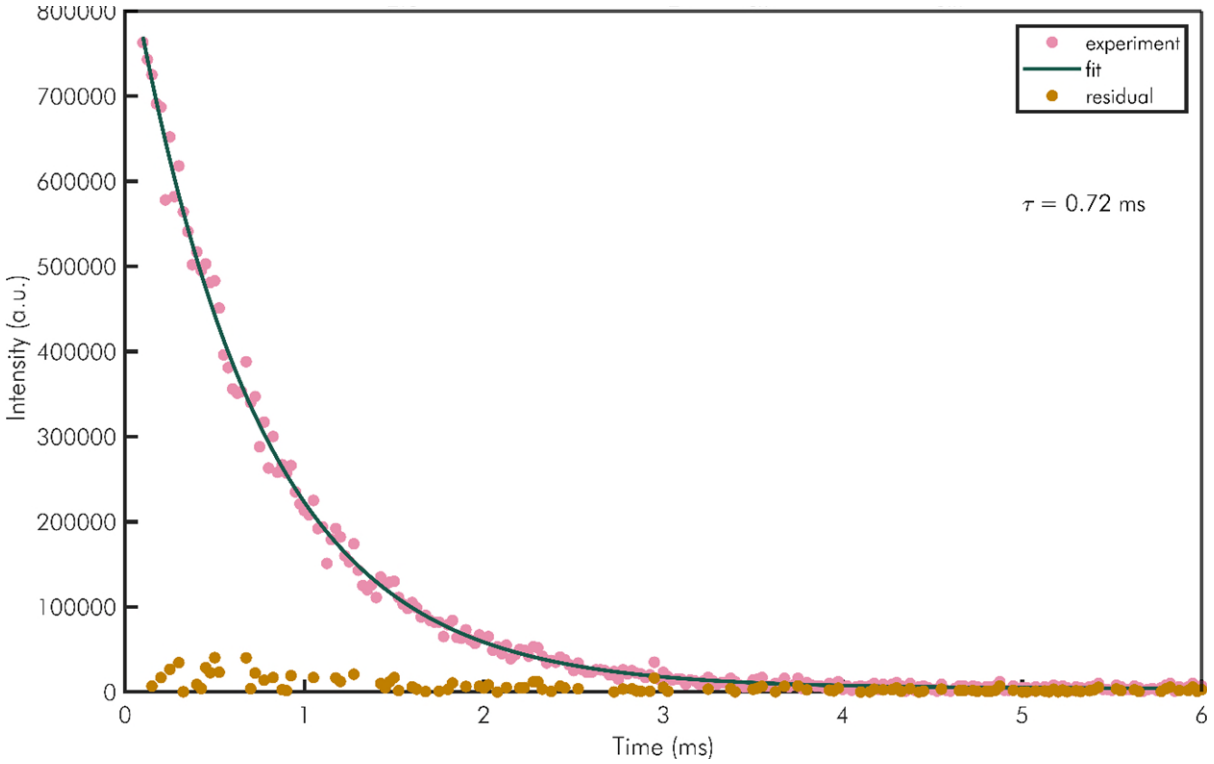

Figure 9.17 Time resolved emission spectroscopy of ***Eu(5.1)$_{2.3}$*** *in H_2O (10^{-6} M). λ_{em} = 615 nm. λ_{ex} = 350 nm.*

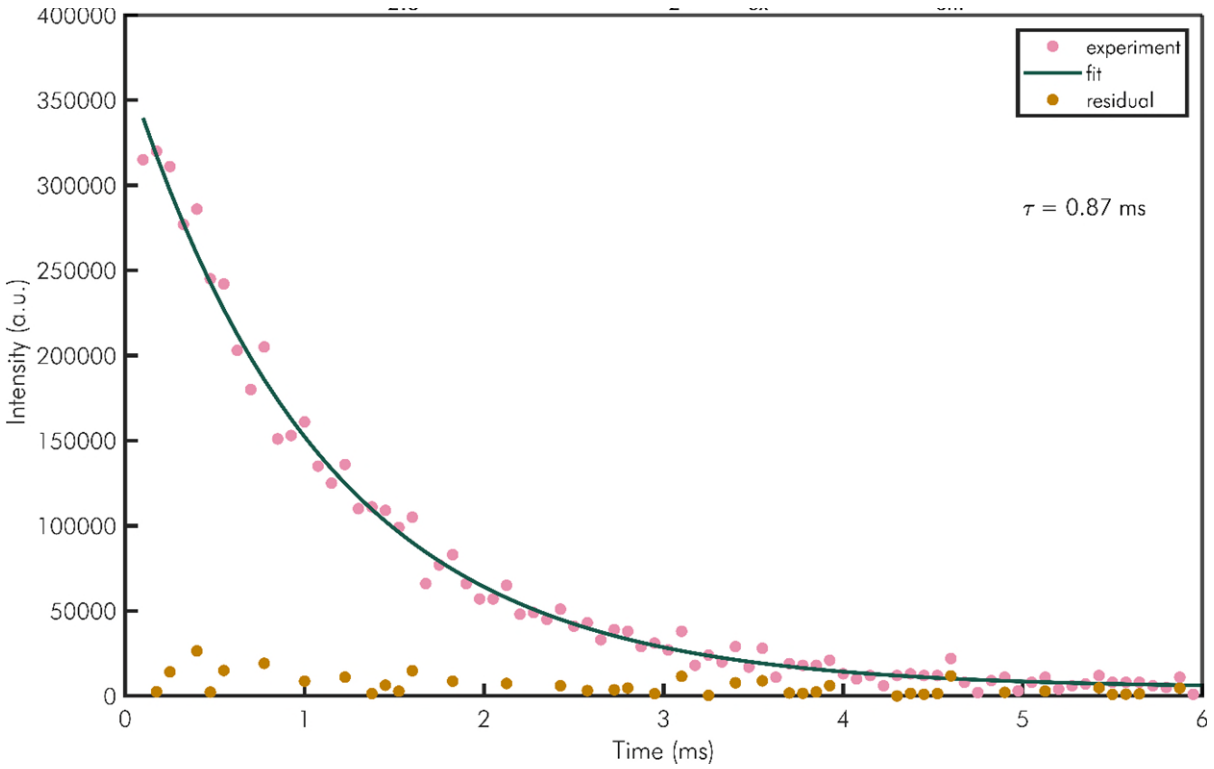

Figure 9.18: Time resolved emission spectroscopy of ***Eu(5.1)$_{2.3}$*** *in D_2O (10^{-6} M). λ_{em} = 615 nm. λ_{ex} = 350 nm.*